Écoulements diphasiques et transferts thermiques associés dans les technologies solaires à concentration

Samuel Mer

Écoulements diphasiques et transferts thermiques associés dans les technologies solaires à concentration

Présentée par : **Samuel Mer**

En vue de l'obtention de : **l'Habilitation à Diriger des Recherches**
Spécialité : *Sciences de l'Ingénieur - Énergétique et Génie des Procédés*

Délivrée par **l'Université de Perpignan Via Domitia**

Préparée au sein du **Laboratoire PROMES-CNRS, UPR8521**
et de **Ecole Doctorale n°305 – Energie et Environnement**

Soutenue publiquement le **4 juillet 2025** devant le jury composé de :

Jérôme BELLETTRE *Pr, Univ. Nantes – LTEN*	Président
Michel GRADECK *Pr, Univ. Loraine – LEMTA*	Rapporteur
Véronique ROIG *Pr, Toulouse INP – IMFT*	Rapporteure
Stéphane VINCENT *Pr, Univ. Paris-Est – MSME*	Rapporteur
Lounès TADRIST *Pr, Univ. Aix-Marseille – IUSTI*	Examinateur
Gilles FLAMANT *DR-E, CNRS – PROMES*	Examinateur
Adrien TOUTANT *MCF-HDR, Univ. Perp. – PROMES*	Examinateur

Remerciements

La rédaction de ce mémoire est l'occasion de faire le point sur mon parcours dans le monde de la recherche. Je tiens à en profiter pour remercier les personnes, passionnantes et très souvent passionnées, qui ont déjà marqué ma jeune carrière.

En premier lieu, je tiens à remercier mes directeurs de thèse, Jean-Paul Thibault et Christophe Corre, qui m'ont donné le goût de la recherche durant mes années grenobloises. J'ai beaucoup appris à leurs côtés, et je les remercie pour l'autonomie qu'ils m'ont laissée dans mon travail de thèse.

Mon passage à l'IMFT a certainement été décisif pour la suite de mon parcours. C'est notamment durant ces années de post-doctorat que j'ai commencé à travailler sur les écoulements diphasiques, à l'échelle où je les étudie aujourd'hui. Mes compétences numériques ont également profité de l'environnement local pour faire un grand bond. Pour tout cela, je tiens à remercier vivement Jacques Magnaudet, Véronique Roig, Thomas Bonometti, Olivier Praud, Hervé Neau et Annaïg Pedrono.

Le jeu des concours m'a fait atterrir en Catalogne, au laboratoire PROMES. Merci aux collègues pour l'accueil qu'ils m'ont réservé. Mention spéciale à Adrien Toutant : mon intégration au laboratoire a grandement profité de ton dynamisme. Merci pour ton appétit scientifique débordant et notre collaboration fructueuse. Je tiens aussi à remercier Gilles Flamant et Françoise Bataille – qui ont également œuvré à mon intégration – d'une part pour leur énergie communicative et d'autre part pour avoir creusé le sillon de la mécanique des fluides à PROMES. Mes activités de recherche et d'enseignement ont également bénéficié du dynamisme et de l'implication de plusieurs collègues que je souhaite remercier. Je pense notamment à Maxime Perrier-Muzet, Nathalie Mazet, Régis Olives, Martin Rosalie...

Un grand merci aux doctorants et postdoctorants avec qui j'ai eu la chance de travailler depuis mon recrutement à PROMES. Vous m'avez, malgré vous, formé à l'encadrement de la recherche et avez activement contribué aux contenus de ce mémoire. Votre implication est une réelle source de motivation pour moi. Par ordre chronologique, merci donc à : Salim Hamidi, Ronny Gueguen, Edouard Butaye, Israël Aguilera-Cortes, Alexandre Labat, Kelana Bachir-Brahim, Julien Djeumegni et Thibaut Devos.

Je tiens évidemment à remercier les membres du jury pour avoir pris le temps d'évaluer mon travail et pour la qualité des échanges qui en sont ressortis. C'est un réel honneur pour moi de vous avoir rassemblés dans ce jury.

Enfin, je tiens à remercier ma compagne Noémie. Merci d'avoir accepté de me suivre à Toulouse puis à Perpignan, merci pour ton soutien si précieux et pour tout ce que nous avons construit ensemble. À Anicet et Zélie, mes deux *asticots*, merci pour votre malice et la perspective que vous donnez à la vie. J'oserais même conclure en vous remerciant de me tenir éveillé, au sens propre comme au figuré.

Résumé

La transition énergétique, imposée par les enjeux climatiques contemporains, stimule le développement de technologies solaires à concentration (CST) toujours plus performantes et adaptées aux besoins. Dans la plupart de ces dispositifs, les phénomènes d'écoulement et de transfert thermique jouent un rôle déterminant. Les travaux présentés dans ce manuscrit s'inscrivent dans ce contexte, à l'interface entre recherche appliquée et recherche fondamentale, et reposent une démarche articulant expérimentation, modélisation physique et simulation numérique haute performance.

Le premier volet du manuscrit est consacré à l'étude des écoulements bouillants horizontaux eau-vapeur. Ces écoulements sont au cœur des technologies de génération directe de vapeur (GDV), une voie prometteuse pour l'hybridation solaire de procédés industriels consommateurs de vapeur. Des simulations thermohydrauliques ont permis d'évaluer l'effet de l'inclinaison d'un récepteur sur son fonctionnement. Parallèlement, un dispositif expérimental dédié a été développé. Il a permis de constituer une base de données originale couvrant différents régimes d'écoulement bouillant, représentatifs des récepteurs GDV. Ces données permettront l'évaluation et l'amélioration des modèles numériques utilisés dans le dimensionnement de ces systèmes.

Le deuxième axe explore l'utilisation de lits fluidisés comme fluides de transfert thermique (HTF) dans les CST. Grâce à leur aptitude à fonctionner à des températures supérieures à celles des fluides actuels et à favoriser un stockage thermique efficace, les particules fluidisées apparaissent comme un HTF prometteur pour les applications à *haute température*. Les régimes d'écoulement intervenant dans un récepteur solaire à lit fluidisé en circulation ascendante ont été caractérisés expérimentalement, d'abord à température ambiante, puis sous irradiation solaire concentrée. Les transferts thermiques associés à chacun ont également été évalués, apportant des éléments de compréhension aux couplages entre dynamique et thermiques dans ces écoulements.

Enfin, le troisième chapitre est dédié à la modélisation résolue d'écoulements fluide-particules anisothermes. L'approche développée repose sur des méthodes numériques avancées, notamment une formulation monofluide des équations de conservation, un suivi d'interface par *Front-Tracking*, une pénalisation visqueuse pour la phase solide et un modèle de collisions de type *sphères molles*. Cette modélisation vise à approfondir la compréhension des interactions thermohydrauliques fines entre fluide et particules. À moyen terme, ces travaux permettront d'enrichir les modèles macroscopiques intégrés dans les outils de simulation utilisés largement dans l'industrie pour la conception et l'optimisation de composants.

L'ensemble de ces travaux ouvre de nombreuses perspectives de recherche, allant de l'amélioration des modèles de fermeture sur lesquels reposent les outils de simulation numérique industriels, à la caractérisation expérimentale fine des écoulements, en passant par l'optimisation de procédés solaires à concentration.

Table des matières

Préambule

L'objectif de ce document est de faire le point sur les activités de recherche que j'ai menées et encadrées depuis mon recrutement en tant que Maître de Conférences au sein du laboratoire PROcédés et Matériaux pour l'Energie Solaire (PROMES) et du département des Sciences Physiques pour l'Ingénieur (SPI) de l'Université de Perpignan Via Domitia (UPVD) en septembre 2019.

Bien que ce mémoire soit un travail individuel, l'ensemble des travaux et résultats de recherche qu'il présente a été obtenu dans le cadre de projets collaboratifs. Ces travaux impliquent très souvent d'autres chercheurs, des doctorants, des stagiaires, ainsi que des personnels d'appui technique à la recherche. En préambule de chaque chapitre, je prendrai soin de rappeler brièvement le contexte des travaux présentés ainsi que les principaux contributeurs. Sans dresser ici la liste exhaustive de toutes les personnes impliquées, je souhaite tout de même les remercier chaleureusement pour la richesse scientifique et humaine de nos échanges.

Dans un souci de mise en contexte, avant de détailler mes travaux actuels, je retracerais rapidement dans ce préambule les différentes thématiques de recherche sur lesquelles j'ai travaillé. Celles-ci ont réellement débuté en 2013 lorsque j'ai entrepris un doctorat au sein du Laboratoire des Écoulements Géophysiques et Industriels (LEGI) entre 2013 et 2016. À la suite de cela, j'ai réalisé deux postdoctorats, sur deux sujets différents, à l'Institut de Mécaniques des fluides de Toulouse (IMFT) avant d'être recruté en tant que maitre de conférences à l'UPVD et au laboratoire PROMES.

Travaux de thèse - de 2013 à 2016

Titre	Stockage d'ergol cryogénique pour l'exploration spatiale : étude expérimentale, modélisation et optimisation d'un dispositif de contrôle thermodynamique à échappement
Encadrants	Jean-Paul Thibault (LEGI) et Christophe Corre (LMFA)
Laboratoire	Laboratoire LEGI – *Groupe : EDT*
Jury	*Président du jury :* N. Mordant (LEGI) – *Rapporteurs :* C. Colin (IMFT), L. Tadrist (IUSTI) – *Examinateur & invités :* J.L. Harion (Mines de Douai), B. (CNES), F. Mathey (ALAT)

Les futures missions d'exploration spatiale nécessitent le stockage d'ergols cryogéniques sur de longues durées. Sous l'effet d'entrées thermiques résiduelles, l'ergol se vaporise et le réservoir s'auto-pressurise, pouvant entraîner la rupture du réservoir pour des missions suffisamment longues. Cette thèse s'intéresse à un système de contrôle, appelé *Thermodynamic Venting System (TVS)* et représenté sur la figure 1, reposant sur l'injection d'un jet sous-refroidi dans le réservoir (contenant de l'ergol en phase liquide et vapeur). L'injection entraîne la condensation

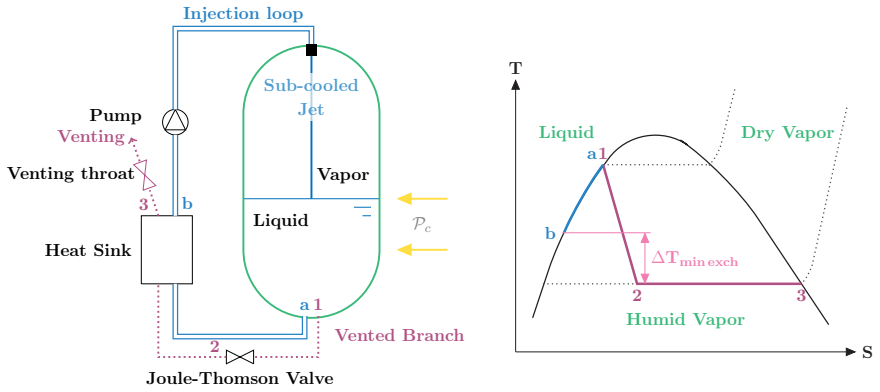

FIGURE 1 – Gauche : représentation schématique d'un système de contrôle TVS pour un réservoir soumis à une entrée thermique $\mathcal{P}_c$. Droite : description du système TVS dans le diagramme $T-S$.

de la vapeur, la déstratification du bain liquide et par conséquent une baisse de pression dans le réservoir. L'étude expérimentale, réalisée sur le banc expérimental décrit à la figure 2, a permis de développer une technique originale d'isolation active générant une condition de paroi à flux de chaleur net nul. Une base de données expérimentales, d'auto-pressurisation et de contrôle TVS incluant la stratification thermique du fluide mesurée grâce à la canne présentée à la figure 2, a été constituée avec ce nouveau dispositif [60, 61]. Elle a notamment permis de valider un modèle

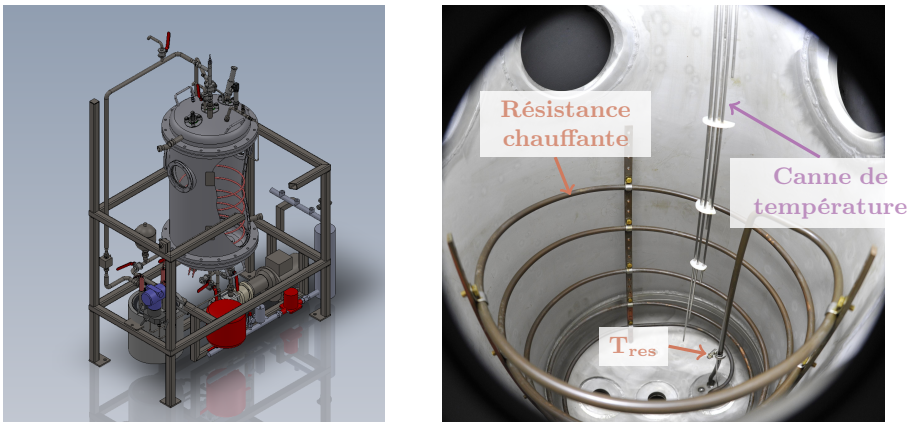

FIGURE 2 – Gauche : vue CAO du dispositif expérimental. Droite : photo de l'intérieur du réservoir montrant la résistance chauffante, ainsi que le capteur de température T_{res} qui y est fixé, et la canne de température mesurant la stratification verticale de température au sein du fluide (liquide et vapeur).

thermodynamique homogène capable de prédire, avec une bonne fiabilité et à un coût modeste, l'évolution de la température et de la pression dans le réservoir. Ce modèle a été étendu afin de décrire le comportement de tous les éléments constitutifs du système TVS. Un outil de dimensionnement du système complet a ainsi été développé et couplé à une plateforme d'optimisation pour maximiser les performances d'un système TVS, dont le test est prévu dans une future mission de démonstration de la NASA, en partenariat avec le CNES [57]. Enfin, une étude numérique a mis en évidence, pour notre cas d'étude, les limites des modèles de changement de phase disponibles dans les solveurs CFD commerciaux. Une modélisation prédictive du changement de phase a été implémentée dans un code de recherche, puis validée sur un cas académique unidimensionnel en vue d'une future intégration dans un code de calcul haute performance.

Post-doctorat I (24 mois) - de 2017 à 2018

Titre	Hydrodynamique de cavités immergées
Collaborateurs	Olivier Praud, Jacques Magnaudet et Véronique Roig
Laboratoire	Institut de Mécanique des Fluides de Toulouse – *Groupe : ASI*
Collab. indus.	Naval Group & Electricité de France

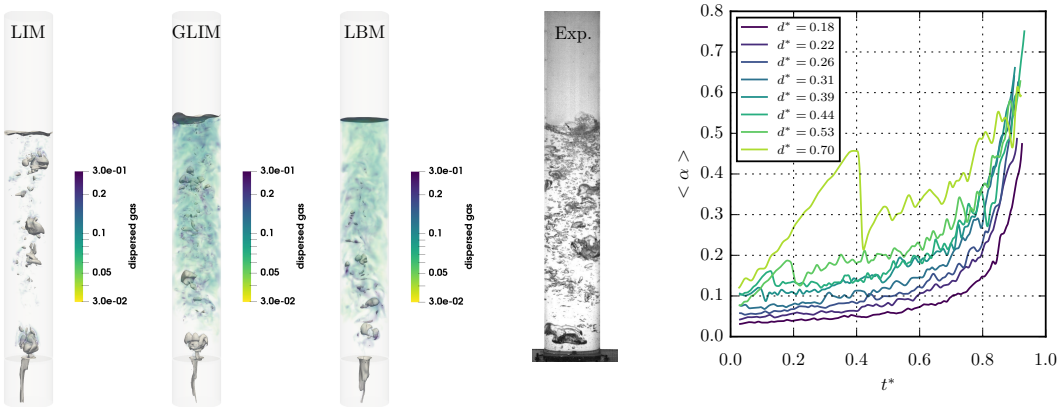

(a) (b)

FIGURE 3 – (a) Comparaison des différents modèles multi-échelles de NEPTUNE_CFD avec une vidange expérimentale. (b) Évolution de la fraction volumique moyenne d'air dans la colonne fluide $\langle \alpha \rangle$ pour différents diamètres normalisés de l'orifice de décharge.

Les écoulements gaz-liquide, multi-échelles, faisant intervenir des essaims de bulles de forte poly-dispersité, sont omniprésents dans bon nombre de procédés industriels (tels que les colonnes à bulles, pour n'en citer qu'un). Afin d'étudier ce type d'écoulements sur une configuration simplifiée, l'écoulement oscillant se produisant lors de la vidange d'une bouteille d'eau a été sélectionné. Cet écoulement met en jeu une physique complexe avec une large gamme d'échelles spatio-temporelles et donne lieu à de nombreuses transitions de régimes [58]. En effet, périodiquement, des bulles sont créées au goulot, typiquement de l'ordre du diamètre de l'orifice, se détachent et remontent dans la colonne d'eau jusqu'à la surface libre. Lors de leur ascension, ces grosses bulles se fragmentent pour créer un essaim de plus petites bulles, une partie de celles-ci pouvant ensuite re-coalescer avec les plus grosses. Expérimentalement, l'utilisation simultanée d'un capteur de pression et d'une technique d'ombroscopie, pour suivre le déplacement de l'in-

terface liquide au sommet de la bouteille, a permis d'évaluer l'évolution du taux de vide moyen dans la bouteille durant la vidange (voir Fig. 3b). On observe que ce dernier dépend fortement du diamètre de l'orifice de décharge et du volume de la première structure gazeuse remontant dans la bouteille. Pour les orifices les plus larges, cette structure est une bulle de Taylor. Numériquement, les modèles multi-échelles récemment implémentés dans NEPTUNE_CFD – où les plus petites inclusions gazeuses sont modélisées en sous-maille, tandis que les plus grosses sont pleinement résolues et autorisées à se déformer – ont été évalués et discutés par confrontation aux données expérimentales (voir Fig. 3a extraite de [59]). De plus, la prise en compte des forces capillaires dans NEPTUNE_CFD a été validée, en étroite collaboration avec les développeurs d'EdF, par confrontation à des résultats de vidange de bouteille issus de simulations numériques directes mises en place avec JADIM, un code de recherche développé à l'IMFT reposant sur une méthode Volume Of Fluid (VOF).

Post-doctorat II (6 mois) - en 2019

Titre	Modélisation d'écoulements diphasiques visqueux en configuration instable dans une conduite verticale
Collaborateurs	Thomas Bonometti et Jacques Magnaudet
Laboratoire	Institut de Mécanique des Fluides de Toulouse – *Groupe : F&P*

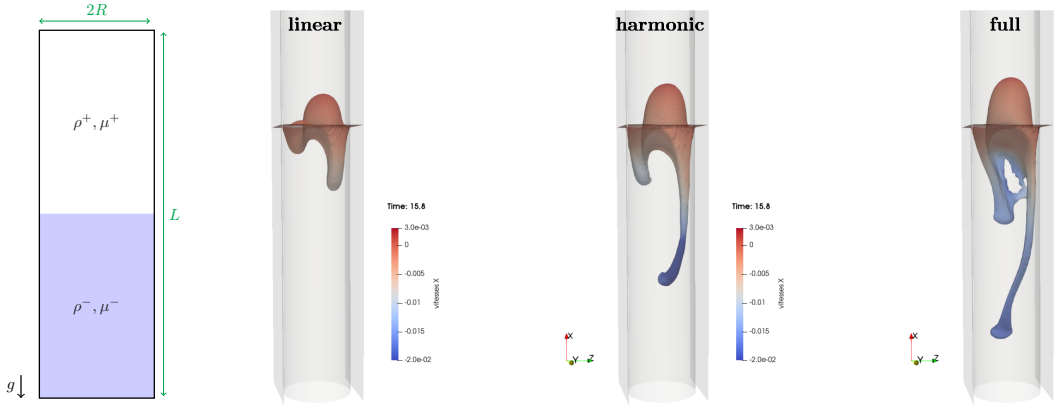

(a) (b)

FIGURE 4 – (a) Schéma de la configuration de calcul. (b) Influence du modèle de contraintes visqueuses sur la dynamique d'inversion des deux phases pour une initialisation asymétrique, un rapport de viscosité $\mu^+/\mu^- = 100$ et un nombre de Reynolds $Re = \dfrac{\rho^+ D\sqrt{g\frac{(\rho^+-\rho^-)}{\rho^+}D}}{\mu^+} \approx 1$.

Les écoulements intervenant dans les cheminées magmatiques sont multiphasiques et font intervenir des fluides de densité et de viscosité variables. On retrouve des configurations d'écoulement similaires dans les procédés d'extraction secondaire du pétrole, où des fluides peu visqueux sont injectés pour augmenter la capacité de captage des puits. À ce jour, la distribution des fluides dans les conduites d'extraction reste souvent mal connue [45], bien qu'elle soit capitale pour l'optimisation des procédés de pompage. Une configuration idéalisée consiste à étudier dans un tube vertical l'écoulement de deux fluides de masse volumique et de viscosité différentes, placés initialement en configuration instable l'un au-dessus de l'autre (voir Fig. 4a). Des expériences de

laboratoire [3] et des analyses de stabilité linéaire [74, 46] montrent que la configuration d'écoulement sélectionnée par le 'système' – échange des fluides axisymétrique, avec fluide visqueux au centre ou en périphérie du tube, ou asymétrique – et le débit d'extraction dépendent fortement du rapport de viscosités et de la déformation initiale de l'interface. L'objectif de ce travail était de réaliser des simulations numériques directes, avec le code JADIM développé à l'IMFT, qui repose sur une approche VOF, de cet écoulement pour une large gamme de propriétés fluides afin de dresser une cartographie de l'écoulement et d'extraire les processus primordiaux qui le pilotent. Nous cherchions en particulier à identifier l'influence sur la configuration d'écoulement choisie : du rapport de viscosités, du rapport de densités, des effets capillaires, de la déformation initiale de l'interface et du modèle de prise en compte des contraintes visqueuses à l'interface. La géométrie cylindrique du tube est représentée par une méthode IBM [5] sur un maillage cartésien. Cela relaxe les contraintes en pas de temps par rapport à un maillage cylindrique pour lequel de toutes petites mailles apparaissent sur l'axe. On constate sur la Fig. 4b que la dynamique d'échange dépend fortement de ce dernier. Du fait de ma réussite au concours de MCF à Perpignan, j'ai dû quitter prématurément ce projet en août 2019. Avant cela, afin de collecter une base de données expérimentales pour la validation des calculs, j'ai mis en place un banc expérimental représentatif de la configuration de calcul. Les résultats préliminaires obtenus durant l'été 2019 étant prometteurs, une deuxième expérience plus aboutie a été mise en place et est actuellement exploitée dans le cadre de la thèse d'Hadrien Bruhier à l'IMFT. La confrontation des résultats issus de celle-ci avec les résultats numériques fait l'objet d'un article récemment soumis [54] ArXiv .

En tant que Maître de conférence à l'UPVD depuis 2019

Ces différentes expériences m'ont permis de développer une expertise dans les écoulements diphasiques, les transferts thermiques et la thermodynamique. Mes recherches tirent profit à la fois de la complémentarité des approches numériques et expérimentales que je développe, ainsi que de la richesse des trois domaines scientifiques auxquels elles appartiennent : la mécanique des fluides, la thermique et le génie des procédés.

Depuis mon arrivée au laboratoire PROMES, le sujet d'application de mes recherches a évolué pour se concentrer sur les technologies solaires à concentration. Je développe des méthodes expérimentales et numériques pour caractériser, comprendre et modéliser les écoulements diphasiques et les transferts thermiques associés dans ces procédés.
Pour rendre compte de ce travail, le reste du manuscrit est structuré de la manière suivante. Dans le chapitre 1, j'introduirai les technologies solaires à concentration (CST) et leur rôle potentiel dans la transition énergétique. Dans le chapitre 2, je présenterai les travaux associés à une thématique de recherche que j'ai initiée au laboratoire sur les écoulements bouillants dans les Récepteurs Solaires (RS) à Génération Directe de Vapeur (GDV). Dans les deux chapitres suivants, je détaillerai les travaux que nous menons concernant les écoulements gaz-particules dans les CST. Au chapitre 3, je présenterai la caractérisation expérimentale des régimes d'écoulement de lit fluidisé et des transferts thermiques associés, dans un RS en circulation ascendante. Pour décortiquer les mécanismes de transferts à la petite échelle intervenant dans ces écoulements, nous développons, avec A. Toutant, un outil pour la simulation résolue des écoulements fluide-particules dans le code *open source* `Trio_CFD`. Je présenterai les travaux associés à cette thématique dans le chapitre 4 avant de dresser des conclusions et de proposer quelques perspectives pour ce travail.

Chapitre 1

Les Technologies Solaires à Concentration

Sommaire

1.1 Contexte énergétique

Le dérèglement climatique constitue l'un des enjeux majeurs de notre siècle. Les différents rapports du GIEC ont maintenant clairement établi que les activités humaines sont responsables de l'augmentation de la température moyenne de la surface du globe d'environ 1.1° C par rapport à la période préindustrielle (1800-1850)[43]. En effet, depuis la révolution industrielle, les activités économiques ne cessent de se développer, notamment grâce aux énergies fossiles émettrices de CO_2. Afin de satisfaire les accords de la COP21 de Paris, visant à limiter le réchauffement à +1.5° C, il est maintenant urgent d'augmenter la part des énergies renouvelables (EnR) dans le mix énergétique mondial.

L'énergie hydroélectrique est la source d'EnR la plus utilisée dans le monde [42]. Elle représente environ 16% de la production mondiale d'électricité. En 2022, la production hydroélectrique mondiale a atteint 4 300 TWh, ce qui représente 51, 2% de la production électrique issue d'EnR. L'énergie éolienne est la seconde EnR la plus utilisée mondialement. Son développement est en forte croissance et, en 2022, elle représentait environ 25% de la production mondiale d'électricité issue d'EnR (soit 2 000 TWh). En troisième position des EnR, on retrouve l'énergie solaire – photovoltaïque (PV) ou thermique. Le marché des centrales PV est en pleine expansion, surtout avec la baisse des coûts des panneaux solaires. Elle couvre environ 3% de la production mondiale d'électricité, avec un potentiel énorme pour l'avenir. L'agence IRENA estime que la capacité mondiale d'énergie solaire photovoltaïque a dépassé les 1 200 TWh en 2022 [42]. Enfin, la biomasse et la géothermie complètent l'offre des EnR existantes. La biomasse est utilisée pour produire de la chaleur, de l'électricité et des biocarburants. Enfin, bien que moins répandue que les autres EnR, la géothermie est utilisée dans certains pays – notamment l'Islande, l'Indonésie et les États-Unis – pour produire de la chaleur. Ces sources d'énergies renouvelables jouent un

rôle essentiel dans la transition énergétique et la décarbonation des économies, bien qu'elles représentent encore une part plus modeste comparée aux énergies fossiles dans le mix énergétique mondial.

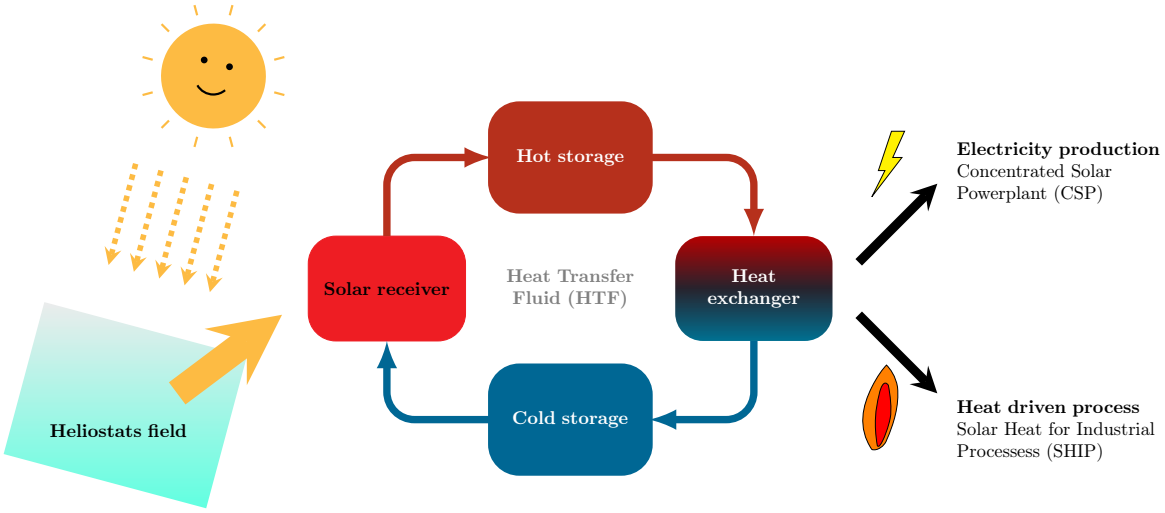

FIGURE 1.1 – Schéma présentant la chaine de conversion de l'énergie dans les technologies solaires à concentration (CST).

Bien qu'absentes de la liste précédente – car sous-exploitées actuellement – les technologies solaires à concentration (*Concentrated Solar Technologies (CST)* en anglais) apparaissent comme une solution pertinente pour décarboner le mix énergétique mondial et certains procédés industriels. Début 2024, on compte 114 centrales CSP (produisant de l'électricité, voir plus bas) en fonctionnement dans le monde pour une puissance totale installée de 6,6 GW [64]. Les CST permettent de produire de la chaleur en concentrant le rayonnement solaire à l'aide d'un champ de miroirs (héliostats) focalisant l'énergie sur un récepteur solaire. Cette chaleur, évacuée par un fluide caloporteur (*Heat Transfer Fluid (HTF)* en anglais), peut être directement utilisée dans un procédé industriel ; on parle alors de *Solar Heat for Industrial Process (SHIP)*, ou convertie en électricité via un cycle thermodynamique. Dans ce dernier cas, on parle de Centrale Solaire à Concentration (*Concentrated Solar Powerplant (CSP)* en anglais). L'un des principaux atouts des CST réside dans l'utilisation de la chaleur comme vecteur énergétique (voir Fig. 1.1), ce qui permet un stockage simple, économique et durable. Cette flexibilité offre un approvisionnement énergétique pilotable. Ceci est un avantage clé par rapport à l'énergie solaire photovoltaïque (PV), qui dépend directement de l'ensoleillement instantané et dont le stockage repose sur la mise en place de batteries électriques coûteuses d'un point de vue économique et environnemental. Pour la production d'électricité (CSP), le stockage facilite d'une part la gestion du réseau électrique – où production et demande doivent constamment être équilibrées – mais présente d'autre part un intérêt économique, puisque l'électricité peut être produite au moment des pics de consommation et donc vendue à un prix élevé.

1.2 Techniques de concentration du rayonnement solaire

Les différents systèmes de concentration solaire sont présentés sur la Fig. 1.2. Sur la première ligne, on présente les concentrateurs linéaires, tandis que la deuxième présente les concentrateurs

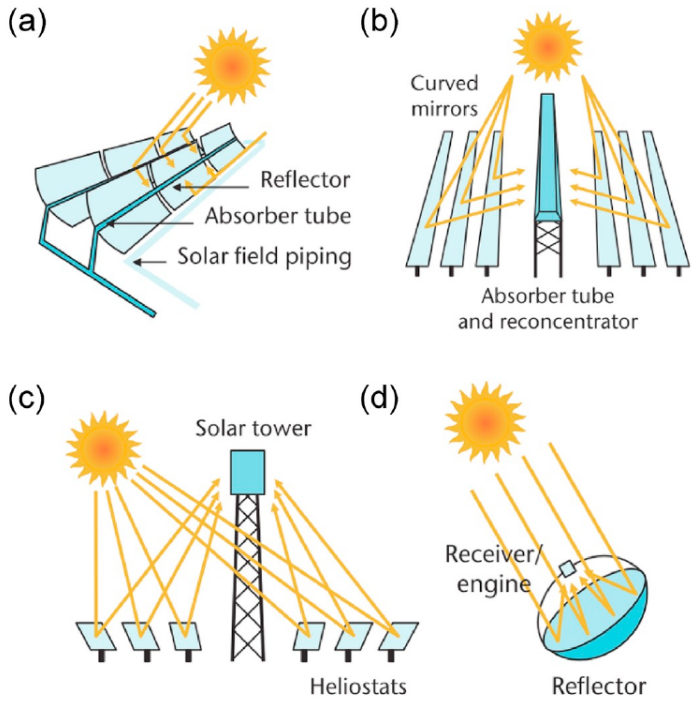

FIGURE 1.2 – Les principales techniques de concentration du rayonnement solaire (extrait de [13]). Les concentrateurs linéaires sont présentés sur la première ligne tandis que les ponctuels apparaissent sur la seconde : (a) cylindro-parabolique, (b) linéaire Fresnels, (c) à tour (d) parabolique.

ponctuels. Comme leur nom l'indique, les concentrateurs ponctuels concentrent le rayonnement en un seul point et permettent donc d'atteindre de plus hauts facteurs de concentration que les concentrateurs linéaires. Ils sont ainsi plus adaptés aux applications dites *"haute température"* ($T \gtrsim 400°C$), tandis que leurs homologues linéaires conviennent mieux aux applications à plus basse température.

Dans les centrales à tour, un champ de miroirs – aussi appelés héliostats – est positionné au pied d'une tour. En orientant les héliostats pour qu'ils suivent l'orientation du soleil, le rayonnement solaire est concentré vers une surface réceptrice positionnée en haut de la tour – le récepteur. Ce dernier s'échauffe et un fluide de transfert thermique (HTF) évacue la chaleur pour la valoriser ensuite. Actuellement, les fluides les plus répandus sont les sels fondus – mélange de nitrate de sodium et de nitrate de potassium. Ces fluides ne peuvent opérer que jusqu'à 565°C. Au-delà, leurs propriétés physico-chimiques se dégradent. Or, pour produire de l'électricité à partir de la chaleur, la loi de Carnot indique que, pour augmenter l'efficacité des cycles thermodynamiques, il faut accroître la différence de température entre la source chaude et la source froide. Ainsi, une tendance actuelle de développement du CSP consiste à augmenter la température de sortie du récepteur solaire en utilisant des fluides alternatifs.

La seule centrale solaire à concentration commerciale française produisant de l'électricité sur le réseau est installée à Llo en Cerdagne. Elle utilise des collecteurs linéaires de Fresnel pour concentrer le rayonnement solaire. En ajustant l'orientation des différentes rangées de miroirs, on reproduit la concentration d'un collecteur cylindro-parabolique à moindres frais mais sur un récepteur fixe. Le rayonnement est concentré sur un tube situé à quelques mètres au-dessus des

rangées de miroirs. À Llo, le fluide de transfert est de l'eau sous-refroidie. Sous l'effet du rayonnement solaire, la paroi du tube récepteur chauffe et l'eau évacue la chaleur par convection. Au-delà de la saturation (fonction de la pression de fonctionnement du champ solaire – 70 *bar* à Llo), un écoulement bouillant se met en place. Différents régimes d'écoulement apparaissent (poche-bouchon, stratifié, stratifié à vagues, annulaire...) en fonction des paramètres de contrôle. La vapeur produite peut être stockée dans des accumulateur de vapeur [69] avant d'être valorisée dans un cycle de Rankine pour produire de l'électricité [62]. Cependant, une filière parallèle et prometteuse, visant la décarbonation de l'industrie, consiste à valoriser directement la vapeur produite dans des procédés industriels qui la requièrent [49] (agroalimentaire, papeterie, extraction de pétrole...). Dans ce secteur, l'essentiel des besoins se situe à des niveaux de température intermédiaires (inférieurs à 250°C), pour lesquels l'utilisation d'un mélange eau/vapeur comme HTF est tout à fait adaptée.

1.3 Positionnement de mes recherches dans ce contexte

Les tendances de développement des CST se concentrent actuellement sur deux volets principaux : (i) solariser des procédés industriels pour les décarboner et (ii) augmenter la température de sortie des récepteurs solaires pour accroître le rendement de conversion électrique des centrales CSP. Dans les deux cas, un verrou scientifique associé au développement des récepteurs solaires (RS) se situe dans la compréhension et la maîtrise des écoulements et des transferts thermiques associés à ce composant clé. Ainsi, mes travaux de recherche visent à caractériser, comprendre et modéliser les écoulements diphasiques dans les récepteurs solaires par des approches numériques et expérimentales.

Pour le point (i), l'essentiel des besoins concerne des niveaux de température modérés pour lesquels une technique de concentration linéaire est adaptée. De plus, de nombreux procédés industriels requièrent de la vapeur pour fonctionner. Dans les RS GDV, cette vapeur est directement produite dans le champ solaire, minimisant ainsi le nombre d'échangeurs de chaleur et le besoin en HTF standard (dont l'impact écologique n'est pas toujours négligeable). Dans le chapitre 2, nous détaillerons un axe de recherche portant sur l'étude des écoulements bouillants dans les RS GDV horizontaux ou faiblement inclinés.

Pour le point (ii), les températures cibles sont de l'ordre de 700 à 800°C, soit bien au-delà de ce que peuvent supporter les HTF actuellement utilisés. Le développement de RS à air pressurisé [29, 52] ou utilisant des particules fluidisées [4, 31, 32, 50] comme HTF permettra d'atteindre ces niveaux de température. Dans les chapitres 3 et 4, je détaillerai deux axes de recherche distincts qui s'intéressent aux RS gaz-particules à deux échelles différentes. D'abord, à celle du récepteur solaire à l'aide d'approches expérimentales (voir chapitre 3) pour étudier les régimes d'écoulement dans les récepteurs et quantifier les échanges de chaleur globaux dans ces derniers. Pour comprendre les mécanismes de transfert (de quantité de mouvement et thermiques) à la plus petite échelle, je détaille dans le chapitre 4 les travaux que nous menons sur la modélisation résolue des écoulements fluide-particules avec le code *open source* `Trio_CFD`.

Chapitre 2

Écoulements bouillants dans les récepteurs à Génération Directe de Vapeur horizontaux

Sommaire

Préambule

Cette thématique de recherche faisait partie du projet d'intégration que j'ai présenté lors de l'entretien préalable à mon embauche, en vue de structurer mes activités au sein du laboratoire. Initiée en septembre 2019, elle constitue une nouvelle orientation pour l'unité, visant à combler le vide existant entre les études à l'échelle centrale, menées par Q. Falcoz en collaboration avec la centrale eLLO, et celles à l'échelle locale, développées par A. Toutant en lien avec le CEA. Dans ce cadre, nous avons progressivement construit un outil de simulation thermohydraulique, reposant sur les outils du génie nucléaire français, à travers trois stages de master successifs (H. Vernier en 2020, E. Butaye en 2021, L. Jaunasse en 2022). La thématique a pris un tournant expérimental avec le lancement, en 2022, du projet européen TOPCSP [77], qui finance la thèse d'I. Aguilera ainsi que son accompagnement. La mise en place du banc expérimental ConBo *n'aurait pas été possible sans les contributions respectives des services techniques (H. Duval, J.-J. Huc, H. Hernandez) et administratifs (C. Rocher, A. Leroyer, S. Puig) que je remercie vivement.*

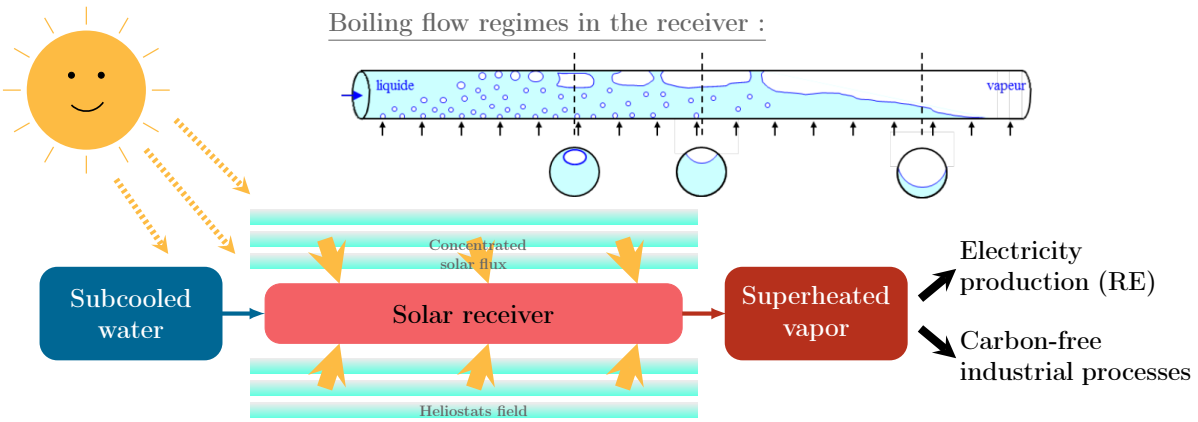

FIGURE 2.1 – Représentation schématique d'un récepteur solaire à Génération Directe de Vapeur horizontal. Les régimes d'écoulement pouvant apparaître dans le récepteur sont également représentés.

2.1 Contexte

Nous nous intéressons ici à un objet technologique encore mal compris : les récepteurs solaires horizontaux à Génération Directe de Vapeur. Nous étudierons ces derniers à une échelle d'étude intermédiaire, permettant une bonne représentativité du procédé et une analyse fine des mécanismes physiques mis en jeu. Notre approche combine une étude expérimentale sur le dispositif CONBO avec la modélisation et la simulation numérique des écoulements bouillants en jeu.

D'un point de vue applicatif, il est primordial de pouvoir prédire les régimes d'écoulement dans les RS GDV pour deux raisons. Tout d'abord, le débit de vapeur produite en dépend directement. De plus, les contraintes thermomécaniques exercées sur le tube récepteur, qui ont un impact direct sur sa durée de vie, varient également en fonction des régimes. En effet, lorsqu'une partie du tube récepteur s'assèche, des points chauds peuvent apparaître en raison de la mauvaise évacuation de la chaleur par la vapeur. Ceux-ci engendrent des phénomènes de dilatations différentielles du récepteur et donc des contraintes thermomécaniques sur celui-ci. Les résultats obtenus permettent d'optimiser un procédé de décarbonation de l'industrie et d'améliorer la compréhension des écoulements bouillants dans ce contexte.

2.1.1 Objectifs et méthode

Dans ce contexte, les objectifs scientifiques de cet axe de recherche sont de : (i) caractériser les différents régimes d'écoulement susceptibles d'intervenir dans les RS GDV ; (ii) comprendre les phénomènes physiques régissant ces régimes ainsi que leurs transitions ; (iii) améliorer la modélisation des écoulements bouillants dans les approches Euler-Euler afin de faciliter leur prédiction et leur contrôle.

Pour atteindre ces objectifs, le travail entrepris repose sur deux axes complémentaires, associant approche expérimentale et modélisation numérique :

1. Le banc expérimental CONBO a été conçu, grâce au soutien du projet TOPCSP, pour l'étude des écoulements bouillants eau-vapeur en conduite horizontale ou faiblement incli-

née. Son instrumentation offre un accès simultané à la puissance thermique injectée, aux températures du fluide et du solide en différents points, et les régimes d'écoulement sont identifiés grâce à une boîte de visualisation.

2. Les capacités des outils de modélisation Euler-Euler, développés initialement pour des applications haute pression dans l'industrie nucléaire, sont évaluées afin de vérifier leur aptitude à reproduire les régimes d'écoulement à basse pression et mieux comprendre le fonctionnement des RS GDV.

2.1.2 Positionnement de nos travaux par rapport à l'état de l'art

Au plan international, la plupart des travaux expérimentaux concernant les régimes d'écoulement en tube sont limités soit à des écoulements eau-air sans changement de phase [75], soit à des études avec des fluides frigorigènes [82, 2, 20], dont les propriétés physiques diffèrent grandement de celles de l'eau. Quelques études d'ébullition eau-vapeur existent pour des canaux millimétriques [36] ou des thermosiphons [85]. Quel que soit le fluide, la majorité de ces études s'intéresse à des tubes de diamètre limité – où le confinement joue un rôle important –, alors que les diamètres des récepteurs solaires sont de l'ordre de $50-70\,\text{mm}$, ce qui réduit significativement le confinement. Enfin, bon nombre d'entre elles concernent des configurations d'écoulement verticales, pour lesquelles la gravité n'impose pas de stratification entre le liquide et sa vapeur.

Actuellement, dans la communauté de la *« mécanique des fluides diphasiques »*, les travaux faisant référence pour les applications GDV sont ceux de [2, 20]. Dans ces études, les régimes d'écoulement et l'efficacité des transferts thermiques associés sont analysés pour des fluides frigorigènes et des récepteurs de diamètre $\leq 11\,\text{mm}$ et de longueur de l'ordre du mètre. Ces écoulements sont également étudiés dans la communauté du *« solaire à concentration »*, mais sur des dispositifs de plus grande taille ($L \geq 10\,\text{m}$, $D_{in} \geq 40\,\text{mm}$) et en eau, pour être plus représentatifs de l'échelle d'une centrale [38, 53]. Cependant, ces dispositifs, à l'échelle du pilote industriels, sont toujours chauffés par voie solaire et disposent d'une instrumentation bien plus limitée que dans l'approche précédente, ne permettant pas une analyse détaillée des régimes.

Dans la section 2.3, nous présenterons le dispositif expérimental ConBo que nous avons développé pour caractériser et cartographier les régimes d'écoulement à l'œuvre dans ces procédés. Pour ce faire, nous nous positionnons à une échelle intermédiaire entre les approches *« mécanique des fluides »* et *« solaire à concentration »*.

Du point de vue numérique, les simulations rapportées dans la littérature [66, 67] reposent sur l'approche stationnaire disponible dans le code commercial `Fluent`. Cependant, les régimes d'écoulement peuvent être hautement instationnaires, ce qui interroge la légitimité de cette approche. L'outil de modélisation 3D instationnaire, détaillé dans la section 2.2, permet l'étude approfondie des régimes, de leurs instationnarités et de leurs mécanismes de transition.

Les outils mis en œuvre sont issus de l'expérience en thermohydraulique développée dans le génie nucléaire français. Ils reposent sur l'expertise acquise par cette communauté et font référence dans la littérature. Cependant, les configurations d'écoulement dans le domaine nucléaire concernent généralement des écoulements verticaux à haute pression. Or, l'approche moyennée – dite Euler-Euler – utilisée pour la partie fluide repose sur de nombreux modèles de fermeture pour représenter les transferts (de masse, de quantité de mouvement et d'énergie).

Ces modèles restent à valider pour des configurations horizontales et à basse pression (on se compare ici au niveau de pression dans les centrales nucléaires), comme celles des RS GDV. L'outil de modélisation mis en place a été validé par confrontation à des données issues de la

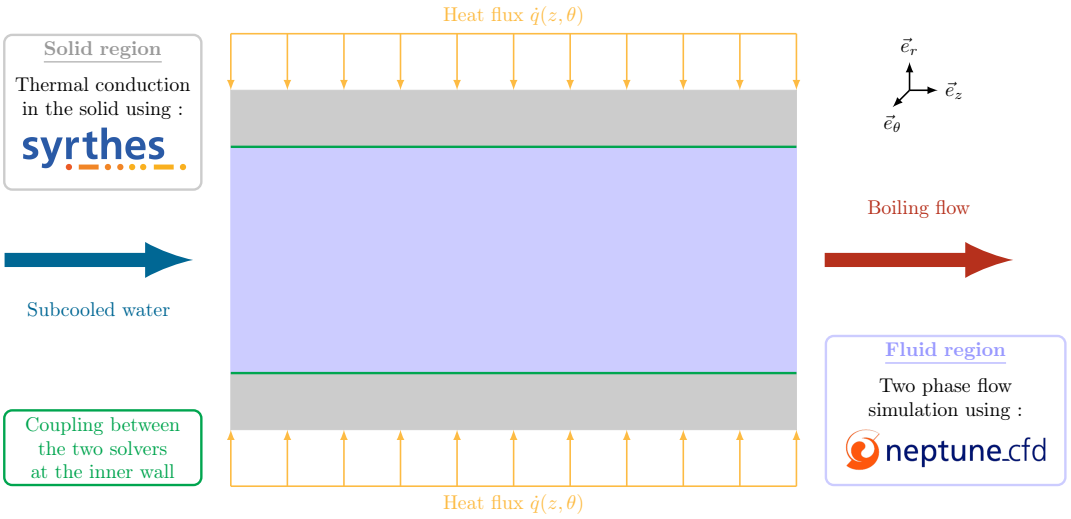

FIGURE 2.2 – Représentation schématique de notre outil de simulation thermohydraulique pour un cas de calcul représentatif d'un récepteur solaire GDV. Le couplage entre les solveurs fluide (NEPTUNE_CFD) et solide (SYRTHES) est mis en évidence.

littérature et a été utilisé, par exemple, pour étudier l'effet de l'inclinaison du récepteur sur la production de vapeur et le champ de température dans le récepteur.

Les simulations couplées associées à cet axe de recherche mobilisent plusieurs codes de calcul massivement parallèles. Leur mise en œuvre est relativement complexe et nécessite un accès aux ressources des supercalculateurs nationaux (CINES, IDRIS).

2.2 Modélisation thermohydraulique des récepteurs GDV

Au travers de trois stages de M2, un outil de modélisation thermohydraulique des écoulements bouillants a été mis en place. Cet outil tire profit de l'expérience développée par l'industrie nucléaire française, et notamment agglomérée dans le logiciel de simulation NEPTUNE_CFD™ EDF. Ce code numérique repose sur une extension à n phases du modèle à deux fluides [44], aussi appelé modèle *Euler-Euler*.

Initialement développé pour les écoulements dispersés – faisant intervenir une phase porteuse liquide et de petites inclusions de vapeur monodisperses – des travaux récents ont introduit de nouveaux modèles pour traiter des configurations impliquant différents régimes d'écoulement diphasiques [35, 15, 18, 25, 63, 12]. Sans entrer dans les détails, ces modèles différencient le traitement de la phase vapeur en fonction de la taille des inclusions (à la manière des modèles de turbulence LES). Ainsi, les plus grosses inclusions, résolues sur le maillage du domaine de calcul, sont autorisées à se déformer et intègrent les forces capillaires s'exerçant à l'interface.

À l'inverse, les plus petites inclusions sont modélisées en sous-maille – en supposant un diamètre constant – et sont soumises à des forces de transfert de quantité de mouvement telles que la traînée, la portance, la masse ajoutée ou encore la dispersion turbulente. Cette différenciation de traitement selon la taille suppose que la méthode soit capable de détecter dynamiquement la taille caractéristique des inclusions dans le domaine de calcul, et d'imposer des modèles de fermeture pertinents pour ces différentes échelles. La capacité de ces méthodes à reproduire des

transitions de régimes, pour des écoulements avec ou sans changement de phase, est évaluée dans [40, 59, 39, 16, 7].

Outre ces modèles multirégimes, la validité des résultats numériques repose également sur la capacité de l'outil à prendre en compte : (i) la turbulence dans les écoulements diphasiques eau/vapeur ; (ii) les échanges de chaleur et de masse à la paroi (modèle d'ébullition [48, 27, 23, 71]) ; (iii) les transferts de chaleur et de masse entre l'eau et les différentes échelles d'inclusion de vapeur.

Les transferts thermiques couplés dans la paroi du tube récepteur sont pris en compte via le logiciel de conduction thermique 3D Syrthes™ EDF (voir Fig. 2.2). Dans nos simulations, la puissance thermique entrante est décrite comme un flux de chaleur surfacique $q(\theta, z)$ appliqué à la surface extérieure du tube. Le champ de température dans le solide est couplé à la résolution fluide grâce au partage, entre les deux solveurs, de la température de paroi interne du tube (représentée par la ligne verte sur la Fig. 2.2).

Cet outil a tout d'abord été validé par confrontation à des données de la littérature sur un cas d'ébullition de fréon dans un tube en serpentin [83]. Les simulations présentées dans [7] démontrent la capacité de l'outil à reproduire les transitions de régimes pour un fluide frigorigène à basse pression.
Depuis, il a permis d'étudier numériquement l'effet de l'inclinaison d'un récepteur GDV sur les régimes d'écoulement et la production de vapeur [1]. Pour ce faire, un cas de calcul reprenant un module du champ solaire de la centrale de Llo (longueur $L = 67\,\text{m}$, diamètre intérieur $d_{in} = 77,9\,\text{mm}$, diamètre extérieur $d_{out} = 88,9\,\text{mm}$) a été mis en place. Dans ces simulations, une distribution de flux solaire concentré réaliste – non homogène sur une section transverse [62] – a été imposée sur la surface externe du récepteur.

Sur la Fig. 2.3, on montre l'influence de l'inclinaison du récepteur sur son fonctionnement. Le champ solaire de la centrale de Llo n'étant pas plat, cette étude vise à optimiser son fonctionnement. Sur la figure, les cas bleus (resp. rouges) correspondent à des configurations d'écoulement descendant (resp. montant), le trait noir représentant une configuration horizontale. On observe que les configurations descendantes maximisent la production de vapeur, au prix de plus fortes différences de température dans le récepteur, et donc de contraintes thermomécaniques accrues. Pour les configurations montantes, les évolutions de α_v et $\ddot{x}$ sont plus bruitées, traduisant la présence d'un régime stratifié à vagues. Pour les configurations descendantes, l'écoulement est stratifié sans vagues, ce qui provoque l'apparition de points chauds en partie haute du tube – en contact avec la phase vapeur.

Pour plus de détails sur cette étude numérique, le lecteur est invité à consulter la publication incluse page 23 de ce chapitre.

2.3 Étude expérimentale avec le dispositif ConBo

En parallèle des simulations, nous avons développé, dans le cadre du projet TOPCSP, le banc expérimental ConBo – pour COnvective BOiling flow loop – permettant l'étude des régimes d'écoulement dans cette configuration. Celui-ci représente un effort expérimental considérable. Sa mise en service et sa calibration ont été achevées en février 2025. Nous détaillerons dans cette section le dispositif expérimental, son instrumentation, ainsi que les premiers résultats

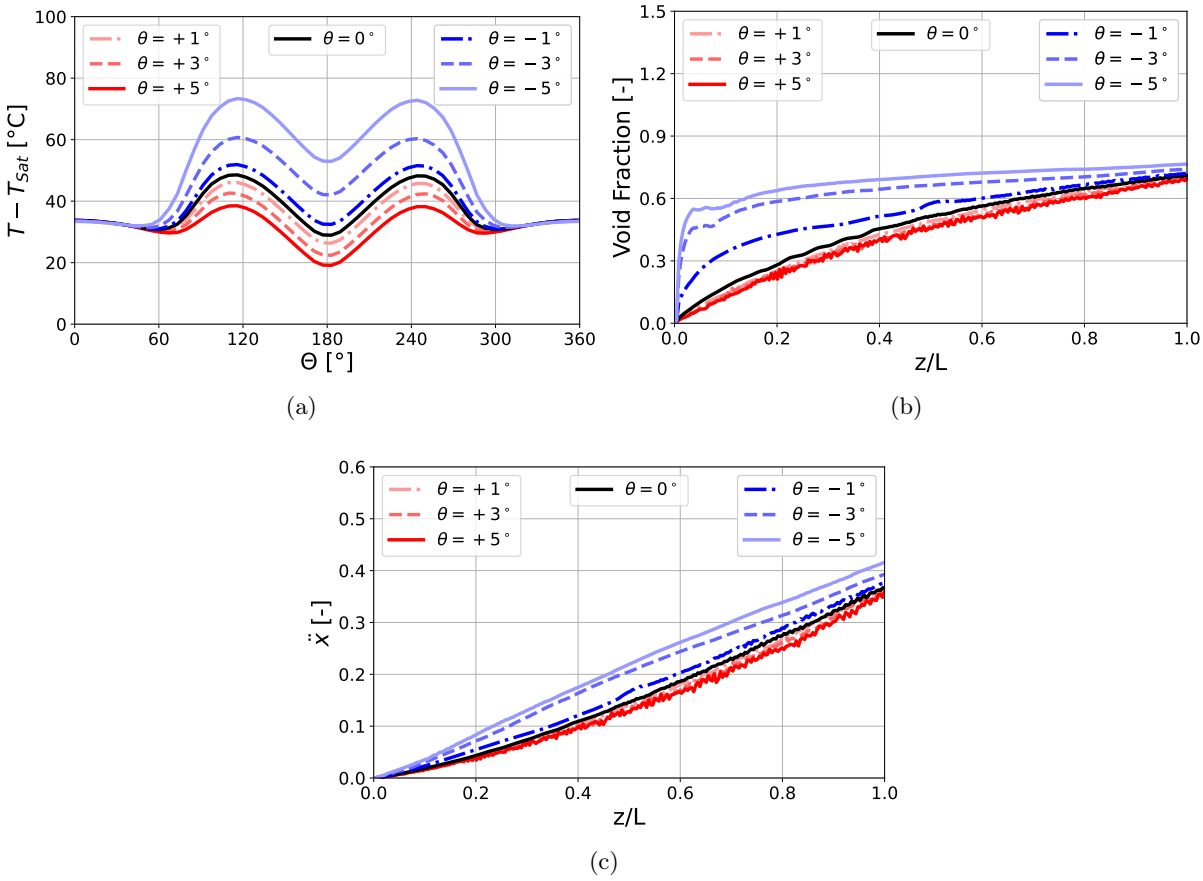

(a) (b)

(c)

FIGURE 2.3 – Effet de l'inclinaison d'un récepteur solaire sur : (a) la température de paroi extérieure dans une section transverse en sortie de récepteur ($\Theta = 0°$ correspond au point bas du tube) ; (b) l'évolution de la fraction volumique de vapeur ($\alpha_v = V_v/V$) le long du récepteur ; (c) l'évolution du titre dynamique $\ddot{x} = \dot{m}_v/\dot{m}$ le long du récepteur. Pour cette simulation, le fluide entre à saturation avec un débit massique $G = 600\,\mathrm{kg{\cdot}s^{-1}{\cdot}m^{-2}}$, le flux incident est anisotrope sur la surface externe du tube pour reproduire la concentration solaire et correspond à une puissance totale injectée $\mathcal{P}_{in} = 620\,kW$.

préliminaires obtenus avec celui-ci.

2.3.1 Le banc expérimental et son instrumentation

Le circuit hydraulique de CONBO , représentant les principaux éléments de la boucle, est schématisé sur la Fig. 2.4. Nous décrivons ci-dessous l'ensemble des éléments du circuit et leur fonctionnement.

La Section d'Essai (TS sur la Fig. 2.4), reproduisant le récepteur solaire, est un tube en Inox duplex. Ce dernier est chauffé par induction. L'inducteur, tressé autour de la TS, est composé de fil de Litz™ID Partner [41]. Son efficacité dépasse 97% . Il est alimenté par un générateur dédié pouvant délivrer une puissance électrique maximale de 22 kW. La puissance injectée peut

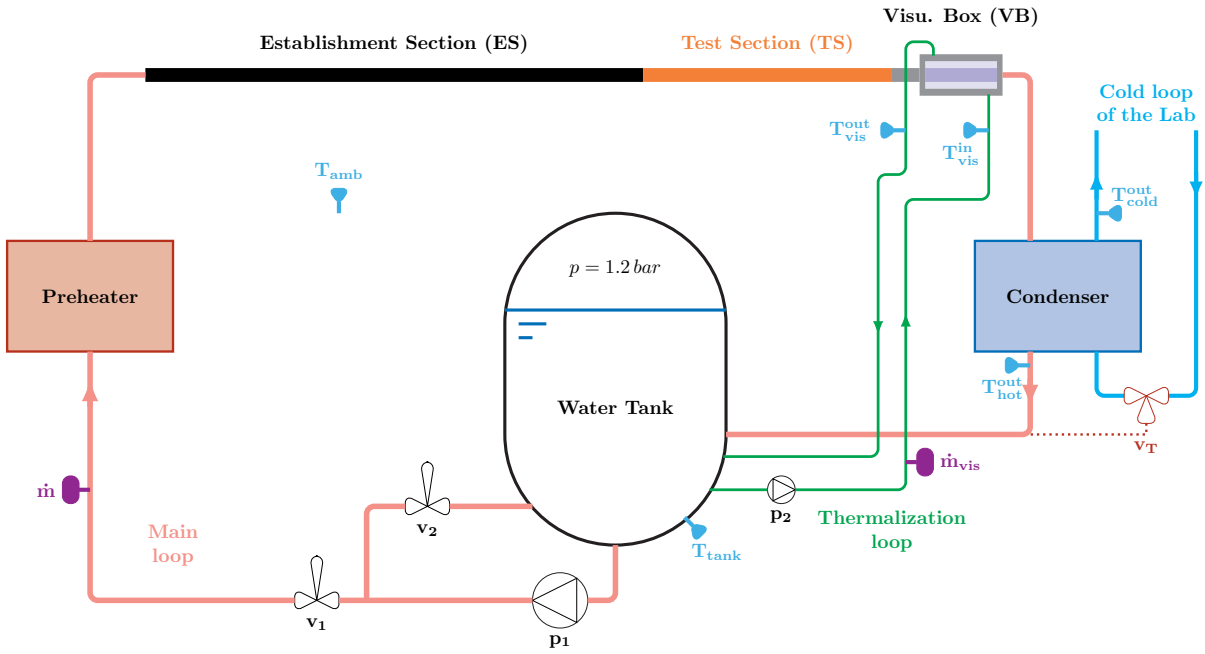

FIGURE 2.4 – Représentation schématique de la boucle hydraulique de ConBo. La boucle principale alimente en eau sous-refroidie la section d'essai (TS). La boucle de thermalisation maintient en température la boîte de visualisation. Enfin, le condenseur de la boucle principale est refroidi par la boucle froide du laboratoire. La section d'essai TS mesure 1 m de long, avec un diamètre interne $D^{in}_{\mathrm{TS}} = 50\,\mathrm{mm}$ et une épaisseur de 5,5 mm. La section d'établissement ES a une longueur $L = 20 \times D^{in}_{\mathrm{TS}}$.

être régulée, soit en puissance, soit pour maintenir une température de consigne sur la paroi extérieure de la TS, à l'aide d'un PID.

En aval de la TS se trouve la Boîte de Visualisation (VB sur la Fig. 2.4) permettant la visualisation des régimes d'écoulement en fonction des paramètres de contrôle. Cette dernière est rétroéclairée par un panneau de LED et les régimes d'écoulement (RE) sont filmés avec une caméra rapide en face avant.

La boucle fluide principale est alimentée par un réservoir d'eau déminéralisée. Une pompe principale ($\mathbf{p_1}$) permet de forcer l'écoulement dans celle-ci. Le débit circulant est ajusté manuellement à l'aide des vannes de réglage $\mathbf{v_1}$ et $\mathbf{v_2}$ (voir Fig. 2.4).

Avant d'atteindre la TS, l'écoulement s'établit dans une section d'établissement (ES sur la Fig. 2.4). Un préchauffeur d'une puissance maximale $\mathcal{P}_{pre} = 10,5\,\mathrm{kW}$ permet de fixer la température d'entrée dans la TS.

Les sections d'établissement, d'essai et la boîte de visualisation sont montées sur une potence dont l'inclinaison est rendue possible par un pivot central.

Une fois sorti de la VB, l'écoulement diphasique est ramené à l'état sous-refroidi dans un condenseur. Sa source froide provient de la boucle thermorégulée du laboratoire, dans laquelle de l'eau pressurisée circule à $\sim 20°\mathrm{C}$. La circulation de la source froide dans le condenseur est contrôlée passivement par une vanne thermostatique ($\mathbf{v_T}$ sur la Fig. 2.4).

Enfin, la VB est maintenue en température, pour limiter la recondensation de la vapeur, par une boucle de thermalisation dans laquelle circule l'eau préchauffée provenant du réservoir. Le

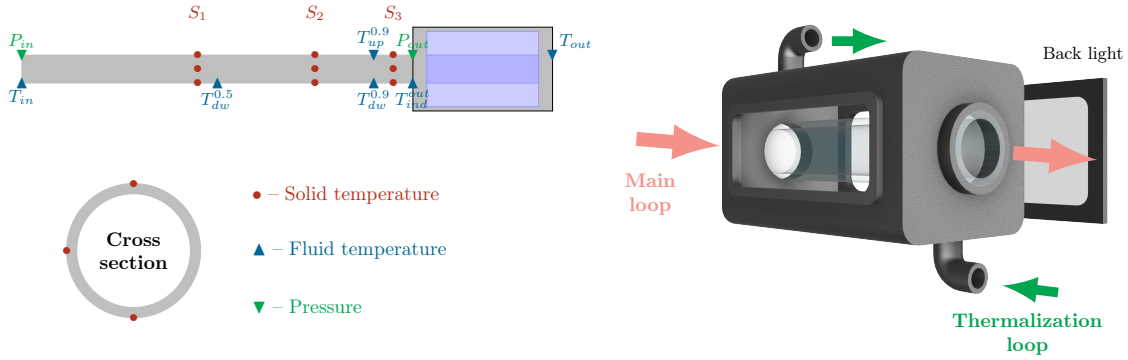

FIGURE 2.5 – Gauche : représentation schématique de l'instrumentation en place sur la Section d'Essai (TS sur la Fig. 2.4) de CONBO. Droite : vue CAO de la boîte de visualisation permettant l'observation des régimes d'écoulement en sortie de TS.

débit circulant dans cette boucle est imposé par un circulateur noté **p2** sur la Fig. 2.4.

Les campagnes expérimentales débutent par une phase de préchauffe où l'eau déminéralisée présente dans le réservoir circule dans la boucle principale et est chauffée jusqu'à 90°C par le préchauffeur. La boucle de thermalisation est ensuite mise en route. L'air résiduel est purgé en point haut des deux circuits en pressurisant légèrement le réservoir à $1,2$ bar. Les essais peuvent ensuite commencer.

Pour conclure, les paramètres de contrôle de CONBO sont listés ci-après avec leur gamme de variation :

- ▷ le débit massique dans la boucle principale $\dot{m} \in [0, 0.2]\,\mathrm{kg.s^{-1}}$
- ▷ le sous-refroidissement du fluide en entrée de TS $\Delta T_{sub} \in [-10, 0]°\mathrm{C}$
- ▷ la puissance de chauffe de l'inducteur $\mathcal{P}_{in} \in [0, 22]\,\mathrm{kW}$
- ▷ l'inclinaison de la section d'essai $\Theta \in [-5, 5]°$.

L'instrumentation actuelle de CONBO combine de la métrologie *classique* – avec des capteurs de débit, de pression, de température et d'inclinaison – et du diagnostic optique pour visualiser les régimes d'écoulement par ombroscopie, et en extraire des données quantitatives pour les régimes qui le permettent.

La Fig. 2.5 détaille l'instrumentation de la section d'essai (TS sur la Fig. 2.4) et montre une vue 3D de la boîte de visualisation (VB), tandis que les capteurs assurant la gestion et le contrôle de la boucle sont représentés sur la Fig. 2.4.

Le débit circulant dans la boucle principale $\dot{m}$ est mesuré par un débitmètre Coriolis, tandis qu'un débitmètre électromagnétique donne accès à celui circulant dans la boucle de thermalisation $\dot{m}_{\mathrm{vis}}$. Les températures de contrôle ($T_{\mathrm{tank}}, T_{\mathrm{amb}}, T_{\mathrm{vis}}^{\mathrm{in}}, T_{\mathrm{vis}}^{\mathrm{out}}, T_{\mathrm{cold}}^{\mathrm{out}}, T_{\mathrm{hot}}^{\mathrm{out}}$ représentées sur la Fig. 2.4) de la boucle sont mesurées par des thermocouples chemisés. Afin d'augmenter la précision des bilans thermiques et des calculs de flux échangés, les mesure de température effectuées sur la TS sont effectuées avec des $PT100$. Ainsi, les températures de la paroi – mesurées en position haute, intermédiaire et basse sur trois sections représentées sur la Fig. 2.5 – sont mesurés par des éléments sensibles collés sur la surface extérieure du tube. La mesure des températures fluides dans la section d'essai ($T_{\mathrm{in}}, T_{\mathrm{dw}}^{0.5}, T_{\mathrm{dw}}^{0.9}, T_{\mathrm{up}}^{0.9}, T_{\mathrm{ind}}^{\mathrm{out}}, T_{\mathrm{out}}$) est réalisée via des sondes $PT100$ chemisées.

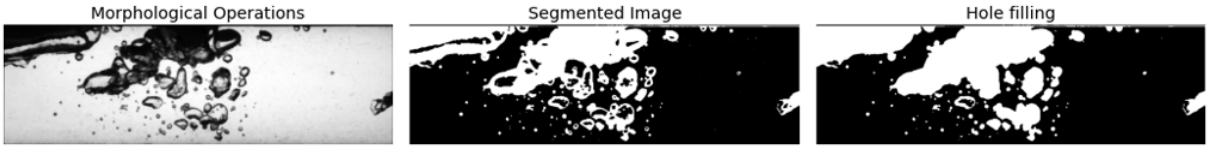

Figure 2.6 – Illustration du traitement d'image réalisé pour déterminer la projection de la fraction volumique de vapeur. L'image est normalisée, les contours des bulles sont détectés, puis les zones correspondantes sont remplies.

La pression en sortie de la SE est mesurée à l'aide d'un capteur de pression absolue, tandis que la perte de charge dans la SE est déterminée à l'aide d'un capteur de pression différentielle. Enfin, l'inclinaison de la potence soutenant la TS et la VB est mesurée par un inclinomètre. Les signaux issus de l'ensemble de ces capteurs sont numérisés par des modules d'acquisition Texas Instruments.

En plus de tous ces capteurs, la VB permet la visualisation des régimes d'écoulement. Comme le montre la Fig. 2.5, cette dernière est une boîte en inox équipée de deux hublots plans sur ses faces latérales. Le tube de la section d'essai se prolonge à l'intérieur de celle-ci par un tube en verre de même diamètre, donnant ainsi un accès optique à l'écoulement diphasique sortant de la TS. Cette boîte est rétroéclairée en face arrière par un panneau de LED, et une caméra rapide permet l'enregistrement haute fréquence des images en face avant. Afin de réduire la distorsion optique induite par le passage de la lumière à travers les dioptres cylindriques du tube interne, l'espace entre le tube en verre et les hublots plans est rempli d'eau [58]. On parle alors de boîte de correction d'indice. L'eau remplissant la VB est en circulation : elle provient de la boucle de thermalisation à une température d'environ 90°C, et permet également d'isoler thermiquement la VB afin de prévenir la recondensation de la vapeur. Afin d'évaluer la déformation résiduelle des images enregistrées, une procédure de calibration a été mise en place. Pour ce faire, l'image d'une mire de calibration – positionnée dans le tube en verre – est prise, une fois ConBo en eau, avec la caméra. Les dimensions de la mire étant connues, la déformation de l'image enregistrée peut être évaluée afin de corriger les images issues des essais.

Malgré tout le soin apporté à la calibration, cette métrologie optique permet uniquement la visualisation des régimes d'écoulement, sans donner accès à une mesure directe tridimensionnelle du taux de vide. Elle ne fournit qu'une projection du taux de vide dans le plan de l'image. Pour certains régimes, le caractère tridimensionnel des interfaces séparant les deux phases peut rendre cette mesure très incertaine (voir Fig. 2.6). Or, une évaluation précise de la fraction volumique de vapeur – aussi appelée taux de vide α_{vap} – est indispensable à la réalisation de cartes d'écoulement [81, 75].

Du fait de l'importante puissance requise pour faire bouillir le débit d'eau, il existe peu, voire pas, de dispositifs semblables à ConBo dans la littérature. Il faut cependant noter que, pour limiter les contraintes expérimentales et faciliter l'instrumentation, les conditions de fonctionnement de ConBo diffèrent de celles des récepteurs GDV sur trois points. Sa pression de fonctionnement est de 1,2 bar, alors que les récepteurs opèrent entre 10 et 70 bar. La gamme de Reynolds explorable se limite à $Re \leq 10\,000$, alors que les Re peuvent être bien plus élevés dans les récepteurs industriels. Enfin, l'inducteur répartit le flux de chaleur de manière homogène sur la surface extérieure de la SE, tandis que, du fait de la concentration solaire, le flux thermique

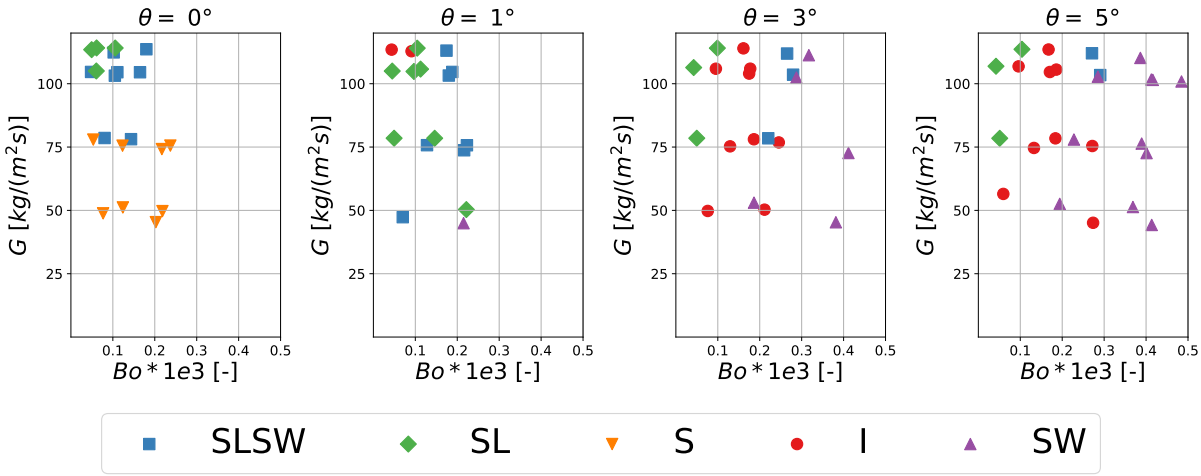

FIGURE 2.7 – Carte expérimentale préliminaire des régimes d'écoulement observés dans la section d'essai (TS) de CONBO, en fonction du débit massique G et du Boiling number Bo. Les symboles représentent les différents régimes identifiés visuellement : S (stratifié), SW (stratifié à vagues), I (intermittent), SL (poche), SLSW (poche–stratifié à vagues). Chaque carte correspond à une inclinaison Θ différente de la TS.

est inhomogène à la surface d'un RS. Malgré ces différences, CONBO constitue un dispositif de référence pour l'étude des écoulements bouillants eau-vapeur en macroconduite horizontale.

2.3.2 Résultats préliminaires

La mise en service de l'installation est très récente, et des campagnes expérimentales étendues doivent encore être réalisées. On présente cependant quelques résultats préliminaires issus de CONBO dans cette section.

Les premières campagnes de mesures montrent que les régimes stratifié (S), stratifié à vagues (SW), intermittent (I), de poche (SL) et mixte poche–stratifié à vagues (SLSW) apparaissent dans la TS de CONBO. De plus, l'apparition de ces régimes est fortement corrélée à l'inclinaison Θ de la TS.

Sur la Fig. 2.7, ces régimes sont représentés dans le plan (G, Bo), où Bo désigne le *Boiling number*, défini comme le rapport entre le flux de chaleur imposé en paroi q et le flux thermique associé à la vaporisation du fluide. Le dénominateur est modifié dans notre cas pour tenir compte du sous-refroidissement à l'entrée dans nos expériences :

$$Bo = \frac{q}{G\,\Delta h_{lv}} \qquad \longrightarrow \qquad Bo = \frac{q}{G\,(h_{\text{sat}} - h_{\text{in}} + \Delta h_{lv})} \tag{2.1}$$

où q est le flux de chaleur en paroi [W/m^2], G le débit massique [kg·s^{-1}·m^{-2}], Δh_{lv} l'enthalpie de vaporisation de l'eau [J/kg], et h_{sat} (resp. h_{in}) représente l'enthalpie à la saturation (resp. à l'entrée de la TS).

On observe qu'à inclinaison nulle, pour des débits faibles, un régime stratifié est présent. Lorsque le débit augmente, deux régimes apparaissent selon la valeur du Boiling number : SL et SLSW. Pour des valeurs de Θ positives, traduisant un écoulement ascendant dans la TS, le régime S disparaît, tandis que les régimes I et SW apparaissent.

Des expérimentations complémentaires restent nécessaires pour caractériser finement les transitions de régimes. De plus, une attention particulière sera portée à l'évaluation de l'efficacité des transferts thermiques en paroi pour chacun de ces régimes.

2.4 Sélection d'articles en lien avec cet axe de recherche

Solar Energy 287 (2025) 113215

Contents lists available at ScienceDirect

Solar Energy

journal homepage: www.elsevier.com/locate/solener

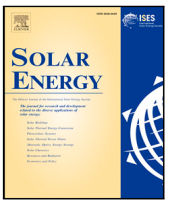

Numerical investigation of tilt angle effect on a Direct Steam Generation solar receiver

Israël Aguilera-Cortes *, Adrien Toutant, Samuel Mer

PROMES Laboratory, CNRS - Université de Perpignan Via Domitia, Perpignan, France

ARTICLE INFO

Keywords:
Direct Steam Generation
CFD modeling
Conjugate heat transfer
Boiling flow

ABSTRACT

Direct steam generation (DSG), which is currently gaining renewed interest in concentrated solar power technologies, offers several advantages, such as reducing the number of components in the plant and lowering operating costs by replacing conventional heat transfer fluids — usually synthetic oils or molten salts — with water. However, it also introduces certain complexities due to the two-phase flow in the receiver. In horizontal receivers, gravity tends to separate the two phases, generating a stratified flow regime. In this regime, steam transfers heat less efficiently, causing the upper part of the receiver to overheat and creating significant temperature gradients within the receiver. These gradients can lead to fatigue and reduce the lifespan of components. Therefore, predicting flow regimes is crucial for the design and operation of solar power plants. In pursuit of this objective, we are developing a 3D transient modeling tool using the NEPTUNE_CFD and Syrthes software to account for the two-phase flow dynamic and coupled heat transfers within the receiver. Simulations, based on a 67 m long receiver module from the eLLO plant, study the influence of the receiver's inclination and the distribution of concentrated solar flux on the receiver's performance. The results show that flux distribution mainly affects the temperature distribution in the solid but does not impact steam production. Flow regimes are strongly influenced by the receiver's inclination. Downward configurations promote steam production at the cost of greater temperature gradients.

1. Introduction

Concentrated Solar Power (CSP) is an emerging technology that is positioning itself as a viable alternative to conventional energy generation technologies [1]. The fundamental principle of this technology lies in concentrating solar radiation at a focal point (as in tower or Dish Stirling plants) or along a focal line (as in parabolic trough or Fresnel plants). This focused concentration of electromagnetic radiation enables the working fluid to reach high temperatures up to 560 °C for molten salts. Inside the receiver, the heat transfer fluid (HTF) is responsible for absorbing the radiation energy concentrated by the mirrors. This energy now held in the HTF can be used for different purposes, such as the production of electricity, the salt-water desalinization or the production of steam for industrial processes. When the HTF is water, steam is generated directly in the receiver, leading to the so-called Direct Steam Generation (DSG) technology. In this process, pressurized subcooled water is injected into the receiver, where it first heats up to the saturation temperature and then evaporates, creating a mixed flow of water and steam. The steam produced can be either used in a steam turbine to produce electricity or directly in steam driven industrial processes (*e.g.*: paper mills, food processing, oil extraction...). The DSG technology presents several significant advantages:

- **Simplicity and efficiency:** Eliminating the heat transfer fluid simplifies the system and reduces the number of heat exchangers (preheater, boiler, and superheater). This increases the overall efficiency of the plant [2] due to the reduction in the number of components.
- **Cost reduction:** Eliminating the working fluid reduces acquisition, maintenance, and operational costs, making the plant more cost-effective in the long term [3].
- **Reduced environmental impact:** Simplifying the design and reducing the number of components decreases the associated carbon footprint. It also reduces plant waste, enhancing social acceptance.

The process of generating steam directly in the receiver involves the coexistence of both liquid and steam phases during evaporation. Due to differences in densities and buoyancy forces, the steam phase tends to move upward toward the top of the receiver. The presence of these two phases in a horizontal receiver generates various flow patterns, which depend on the system's operational parameters, such as mass flow rate, heat flux, or tilt. Studying these flow patterns is crucial, as

* Corresponding author.
E-mail address: israel.aguilera-cortes@cnrs.fr (I. Aguilera-Cortes).

https://doi.org/10.1016/j.solener.2024.113215
Received 25 October 2024; Received in revised form 6 December 2024; Accepted 18 December 2024

Nomenclature

Abbreviations

CG	Continuous gas
CL	Continuous liquid
CSP	Concentrated solar power
DG	Dispersed gas
DISS	Direct solar steam
DSG	Direct steam generation
HTF	Heat transfer fluid
LFC	Linear fresnel concentrator
PTC	Parabolic-trough collector
RANS	Reynolds-averaged Navier–Stokes equations
RMS	Root mean square
SIMPLE	Semi-implicit method for pressure linked equations

Greek symbols

α	Void fraction [-]
δ	Kronecker symbol [-]
κ	Interface curvature [m^{-1}]
λ	Wall conductivity [W m^{-1} K^{-1}]
μ	Dynamic viscosity [kg m^1 s^{-1}]
ρ	Density [kg m^{-3}]
σ	Surface tension [N m^{-1}]
τ	Characteristic time [s]
Θ	Circumferential angle [°]
θ	Tilt angle [°]
ϵ	Turbulent kinetic energy dissipation [m^2 s^{-3}]

Roman symbols

$\ddot{x}$	Dynamic steam quality [-]
$\dot{m}$	Mass flow rate [kg s^{-1}]
$\dot{x}$	Steam quality [-]
c_p	Thermal capacity [J K^{-1} kg^{-1}]
D	Diameter [m]
E^{int}	Interfacial thermal transfer [W m^{-3}]
G	Mass flux [kg m^{-2} s^{-1}]
g	Gravity [m s^{-2}]
H	Enthalpy [J kg^{-1}]
h	Heat transfer coefficient [W m^{-2} K^{-1}]
I	Momentum transfer [N m^{-3}]
L	Length [m]
P	Pressure [Pa]
Q	Conductive flow [W m^{-2}]
Re	Reynolds number [-]
St	Stanton number [-]
T	Temperature [K]
u	Velocity [m s^{-1}]

Subscripts

b	Bubble
crl	Critical
c	Convective
d	Detachment
e	Evaporation
i, j	Spacial direction
in, out	Inlet, outlet
l, s, v	Liquid, solid, vapor
lat	Latent
p, k	Phase p, k
q	Quenching
sat	Saturation
w	Wall

Subscripts

AM	Added mass
D	Drag
F	Friction
int	Interface
L	Lift
nuc	Nucleation
P	Penalty force
T	Turbulent

the heat transfer coefficient between the receiver tube and the fluid varies significantly with the flow pattern [4–6]. Numerous flow regime maps have been developed for two-phase flow in horizontal pipes, with and without phase change. Baker [7] proposed a map for flow in small-diameter pipes using various fluids adiabatic flow data. In its representation, the flow pattern depends on the mass flow rates of each phases, ponderated by non-dimensional parameters taking into account physical properties of the fluids (density, viscosity, surface tension). Mandhane et al. [8] studied two-phase flow in small-diameter pipe adiabatic air–water flows and constructed a map based on gas and liquid surface velocities. This type of map is now the most widely used. Taitel and Dukler [4] developed a theoretical and mechanistic flow regime map, which remains widely used today. However, the flow regime maps available in the literature are not fully adapted to the current operating conditions of modern plants. Specifically, the work by [4,7,8] focuses on horizontal air–water flows without accounting for heat and mass transfer. In a DSG receiver, the vapor mass flow rate is null at the inlet and grows wih the streamwise direction owing to boiling. The previously introduced maps do not account for this phenomenon and require the *a priori* knowledge of the *gas* mass flow rates. Horizontal boiling flow maps do exist in the literature, one can refer to the work of [5,6], however, those maps are limited to small-diameter tubes (where confinement plays a dominant role) and refrigerants (which have a much lower latent heat compared to water).

The modeling and simulation of direct steam generation (DSG) have extensively employed two principal approaches: the homogeneous equilibrium model (HEM) and the two-fluid model (TFM), each offering distinct advantages and limitations. HEM, which assumes thermal and mechanical equilibrium between phases, has been successfully applied in scenarios with homogeneous flow conditions, such as the recirculation operation mode, where its simplicity and low computational cost make it highly effective. Notable examples include its use in thermohydraulic studies of parabolic collectors integrated with thermal energy storage systems, as demonstrated in the DISS project, and its implementation in simplified modeling tools such as TRNSYS [2], RELAP5 HEM [9] or in-house codes made by several institutions such as University of New South Wales [10], DLR [11,12] or PSA [13,14]. However, HEM lacks precision in representing complex or transient flows.

Conversely, TFM offers a significant advancement by independently modeling mass, momentum, and energy conservation equations for each phase [15], enabling a more accurate representation of phenomena such as bifurcated flow patterns and thermohydraulic instabilities. This approach has been employed in advanced simulations using tools such as NEPTUNE CFD, which incorporates interfacial interaction models to enhance the prediction of behavior at the evaporation endpoint

and superheating sections. These capabilities are particularly valuable for addressing challenges related to solar radiation transients and flow pattern transitions, which are critical in DSG applications. Similarly, SYRTHES complements this approach by focusing on transient heat transfer between fluids and solids, facilitating the design and evaluation of thermal energy storage systems in DSG receivers.

Thermal stress in linear solar concentrators is also a significant area of research due to how concentrated radiation affects the receiver. In linear Fresnel concentrators (LFC), only about half of the receiver is exposed to concentrated radiation. In Direct Steam Generation (DSG) systems, thermal stress becomes even more critical for two main reasons. Firstly, higher operating pressures require thicker tube walls, which intensify temperature gradients within the tube [16,17]. On the other hand, the stratification of the two phases increase these gradients because the steam at the top of the receiver evacuates the heat inefficiently compare to the water at the bottom. As a result, uneven heat transfer within the tube increases thermal load, causing thermal bending that may damage the absorber tube.

It is evident that the flow regimes in the receiver are a crucial point when designing a power plant. The topography of the solar field must also be taken into account, as the phase distribution changes with the slope of the receiver. The effect of tilt has been previously studied experimentally at the DISS experimental facility at the Plataforma Solar de Almería [18,19], showing that inclination of the absorber pipe reduced the stratified region. However such experimental studies have their limitations [20,21], as temperature sensors measure point temperature while a temperature field is required to precisely assess the thermal gradient generating the thermal stress. Numerical simulations appears to be an interesting tool to study these phenomena. Previous numerical studies focusing on horizontal receivers operating with DSG technology are reported in the literature. Those are mainly dedicated to PTC and non-Fresnel receivers [22,23]. However, these have been carried out using stationary numerical method, while the nature of the flow pattern inside the receivers is deeply transient.

This study aims to investigate the influence of the tilt angle on a receiver with a similar geometry of a real commercial plant (eLLO). Both positive and negative tilt angles are considered, as well as the influence of boundary conditions and the application of homogeneous and non-homogeneous heat flux on the external surface of the receiver. The study approach involves performing Computational Fluid Dynamics (CFD) simulations considering conjugated heat transfer in the solid domain of the receiver. The software used for these simulations are NEPTUNE_CFD and SYRTHES, which were both developed by a french consortium of industrial nuclear energy actors, led by EDF. The numerical methods involved in those two solvers are fully transient and will allow the evaluation of temporal fluctuations of the parameters of interest.

The paper is organized as follows. Section 2 presents the case study of the eLLO power plant. In Section 3 the different equations and hypotheses of the numerical method used are detailed. A validation by comparison with various cases of the literature is subsequently presented in Section 4 along with a mesh sensitivity analysis. Section 5 presents the simulated calculation configurations and the simulation procedure. The results obtained are presented and analyzed in Section 6. Finally, Section 7 summarizes the main findings and draw some prospects for this work.

2. Case study: eLLO plant

The eLLO plant, a 9 MW Fresnel-type facility located in Cerdanya in southern France, uses DSG technology. It is the first and only commercial plant of its kind in the world that produces and injects electricity into the grid. The power plant includes a large thermal storage system consisting of 9 Ruth accumulators, each one with a capacity of 120 m^3, connected in parallel [25]. It enables an electrical production delayed from the solar resource. Such construction is in accordance with the findings of [26] who observed that Fresnel concentrators are generally preferred for DSG electricity production. Table 1 presents the main features of the power plant. One particular feature of this plant is that it is built on sloped terrain that was not previously leveled, resulting in receivers inclined both in the direction of the flow and perpendicularly (Fig. 1). The tilt angle of the receiver tubes in the solar field ranges from −5° to 5°. [27] modeled the solar field thanks to ray tracing allowing to determine the concentrated solar flux received by the heliostat field (see Fig. 2). This flux distribution will be considered in the simulations to assess the non-homogeneity effect on the temperature field in the receiver.

Table 1
Solar field and power block specifications of the eLLO power plant. Available at [24].

Solar field	
Field aperture area [m^2]	153 000
Mirror width in line [m]	14
Number of lines	27
Mirror line length [m]	340
Power block	
Cycle capacity [MW]	9
Operating pressure [bar]	70
Cooling type	Dry

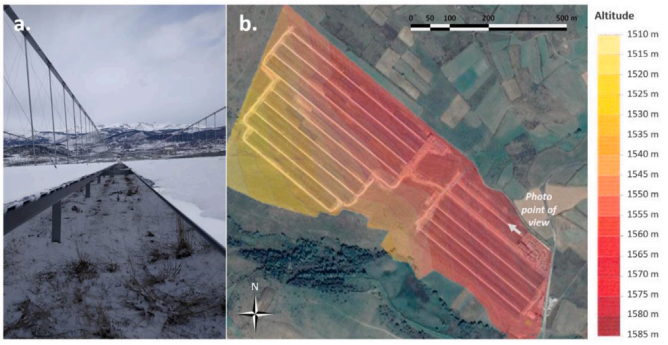

Fig. 1. Photo of eLLO's solar lines; b. topography of the site [27].

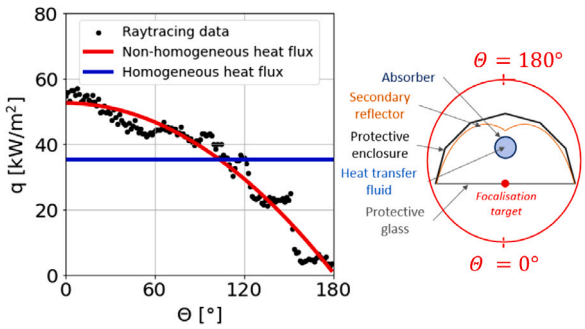

Fig. 2. Incident concentrated heat flux on the receivers of the eLLO power plant. The black points materialize the ray tracing simulations of [27] while the red curve represent a second degree polynomial fit (see Eq. (27)) of them. (For interpretation of the references to color in this figure legend, the reader is referred to the web version of this article.)

3. Numerical method

The numerical fluid dynamics simulations were conducted using version 7.0.2 of NEPTUNE_CFD. This software has been developed over several decades by French specialists in nuclear energy (EDF, CEA, IRSN and Framatome) and is among the most advanced tools for the numerical simulation of two-phase flows using the n-fluid approach. This approach is an extension of the two-fluid model by [28] to multiple

phases. It is a multiphase flow solver built upon the open-source software Code_Saturne.

NEPTUNE_CFD utilizes the Euler-Euler two-fluid model [29]. The governing equations within the software are discretized using a finite volume method with co-located variables. This technique solves the conservation equations of mass, momentum, and energy for each phase under a single pressure assumption. A second-order linear upwind scheme updates the volume fraction of each phase. The velocity field is computed using the SIMPLE algorithm [30]. To maintain the conservation of mass and energy, an iterative coupling method is applied to these equations [31]. The "alpha-pressure-energy cycle" algorithm used in Neptune CFD for solving flow is a pressure-based solver at first order in time. This means that the algorithm does not directly solve the Euler equations in their conservative form, but instead aims to achieve conservativity iteratively. This iterative approach allows for the coupling of velocity, pressure, and enthalpy to ensure consistency and guarantee an implicit resolution. This discretization scheme offers greater numerical robustness, efficiently manages fluid properties, and accurately models phase transitions. A coupled NEPTUNE_CFD/SYRTHES simulation was conducted to investigate the solid domain of the receiver. At each time step, SYRTHES calculates the temperature based on the heat flux applied to the outer surface of the tube. This temperature is then transmitted to NEPTUNE_CFD to compute the heat flux at the fluid–solid interface. This coupling method has been previously studied and validated in various applications where the accurate calculation of temperature within a solid domain is critically important [32–34]

3.1. Primary equations of the multi-regime Euler–Euler approach

For each cell, volume fractions α_k must satisfy the condition:

$$\sum_k \alpha_k = 1 \tag{1}$$

where $k \in [l, v]$ is the phase index.

The conservation of mass for the field k is expressed as:

$$\frac{\partial}{\partial t}\left(\alpha_k \rho_k\right) + \frac{\partial}{\partial x_i}\left(\alpha_k \rho_k u_{k,i}\right) = \sum_{p \neq k} \Gamma^c_{(p\to k)} + \Gamma^{nuc}_{(w,k)} \tag{2}$$

with $u_{k,i}$ the velocity component in the x_i direction, $\sum \Gamma^c_{(p\to k)}$ the mass transfer term at the interface from phase p to k given by Eq. (3), $\Gamma^{nuc}_{(w,k)}$ the mass term from wall-induced boiling to phase k.

$$\Gamma^c_{(p\to k)} = -\frac{\Pi'_{(p\to k)} + \Pi'_{(k\to p)}}{H^\sigma_{(p\to k)} - H^\sigma_{(k\to p)}} \tag{3}$$

with $\Pi'_{(p\to k)}$ the interfacial heat transfer independent of the mass transfer (calculated by the wall boiling model detailed in Section 3.2) and $H^\sigma_{(p\to k)}$ the enthalpy jump at the interface linked to the mass transfer.

The conservation of momentum for the field k is expressed :

$$\begin{aligned}\frac{\partial}{\partial t}(\alpha_k \rho_k \mathbf{u}_k) + \nabla \cdot (\alpha_k \rho_k \mathbf{u}_k \mathbf{u}_k) = -\alpha_k \nabla(P) + \alpha_k \rho_k \mathbf{g} \\ + \nabla \cdot \left(\alpha_k \left(\mu_k \mathbf{S}_k + \frac{S^T_k}{3}\mathbf{I}\right)\right) + \sum_{p\neq k} \mathbf{I}_{p\to k} + \alpha_k \mathbf{S}_c\end{aligned} \tag{4}$$

$\mathbf{I}_{p\to k}$ represents the momentum transfer term from phase p to k. The viscous stress $\mathbf{S}_k$ is given by Eq. (5).

$$\mathbf{S}_k = \frac{\partial \mathbf{u}_k}{\partial x_j} + \frac{\partial \mathbf{u}_k}{\partial x_i} - \frac{2}{3}\frac{\partial \mathbf{u}_k}{\partial x_i}\delta_{ij} \tag{5}$$

The momentum transfer at the interface depend on the flow topology. Originally, the method was developed for dispersed gaz liquid flow. In this case, the momentum transfer term reduces to the sum of a drag $\mathbf{M}^D_k$ [35], an added mass $\mathbf{M}^{AM}_k$ [36], a lift $\mathbf{M}^L_k$ [37,38] and a turbulent dispersion forces $\mathbf{M}^T_k$ [39] as depicted on Eq. (6).

$$\sum_{p\neq k} \mathbf{I}_{p\to k} = \mathbf{M}^D_k + \mathbf{M}^{AM}_k + \mathbf{M}^L_k + \mathbf{M}^T_k \tag{6}$$

Since fifteen years, a strong modeling effort [40–43] has been devoted to develop new closure law able to simulate cases involving multiple flow regimes. The main ingredients of such models consist of a detection algorithm, able to detect the interface type in the calculation domain, and specific closures, adapted to each flow regimes. For a detailed analysis of those models the reader is referred to the work of [44]. In our approach, bubbles smaller than the grid size, are considered as a dispersed gas phase (DG). For those structures Eq. (6) is considered. Larger bubbles and free surface flows, considered as continuous gas phase (CG), are modeled differently to enforce the normal velocity continuity at the interface and allow the latter to deform. To do so, one must consider a friction force $\mathbf{M}^F_k$ [40], a penalty force $\mathbf{M}^P_k$ [40] and a capillary force $\mathbf{M}^\sigma_k$ [45] as depicted on Eq. (7).

$$\sum_{p\neq k} \mathbf{I}_{p\to k} = \mathbf{M}^F_k + \mathbf{M}^P_k + \mathbf{M}^\sigma_k \tag{7}$$

The energy conservation is solved for the total enthalpy which leads to the formulation given by Eq. (8).

$$\begin{aligned}\frac{\partial}{\partial t}(\alpha_k \rho_k H_k) + \nabla \cdot (\alpha_k \rho_k H_k \mathbf{u}_k) = -\nabla \cdot (\alpha_k \mathbf{Q}_k) \\ + \alpha_k \frac{\partial P}{\partial t} + \alpha_k \rho_k \mathbf{g} \cdot \mathbf{u}_k + E^{int}_{p\to k}\end{aligned} \tag{8}$$

where $\mathbf{Q}_k = -\lambda_k \nabla T_k$, with λ_k as the thermal conductivity of phase k containing both molecular and turbulent contributions. P is the mean pressure and H_k is the total enthalpy of phase k, defined Eq. (9) and $E^{int}_{p\to k}$ the energy transfer term at the interface given by Eq. (10).

$$H_k = e_k + \frac{1}{2}u_k^2 + \frac{P}{\rho_k} \tag{9}$$

$$E^{int}_{p\to k} = \Gamma_{p\to k} H^\sigma_{p\to k} + \Pi'_{p\to k} \tag{10}$$

$\Gamma_{p\to k} H^\sigma_{p\to k}$ depends on mass transfer whereas $\Pi'_{p\to k}$ does not depend on the latter.

3.2. Wall boiling model

In the absence of wall boiling model dedicated to horizontal configuration at intermediate pressure levels in the literature, we used state of the art model implemented in the solver [46]. The model consists of two steps: the condition for boiling incipience and the heat flux calculation.

Hsu criterion is implemented to define the onset of boiling at the wall. It indicates that a bubble will grow in a vapor cavity if the liquid temperature, at the extremity of this cavity, is at least equal to the saturation temperature within the bubble [47]. Vapor is created inside a cavity if the radius is larger than the activation radius defined by:

$$r_{cl} = \frac{\lambda_s T_{crl}}{2\varphi_{wall}} \tag{11}$$

where T_{crl} is defined as the limit temperature below which there is no sustained boiling.

$$T_{crl} = \frac{8\sigma T_{sat}\varphi_{wall}}{H_{lat}\rho_{sat}\lambda_s}^{1/2} \tag{12}$$

Well-documented experimental study of [48] confirms the previous hypotheses. The boiling heat flux is splitted into three different terms: a single-phase flow convective heat flux q_c unaffected by the presence of bubbles, a quenching heat flux q_q and a vaporization heat flux q_e. Liquid convective heat transfer is written as:

$$q_c = A_c h_{\log}(T_w - T_l) \tag{13}$$

with T_w as the wall temperature and $h_{\log}$ the heat exchange coefficient. The heat flux due to quenching is given by:

$$q_q = A_b t_q f \frac{2\lambda_l (T_w - T_i)}{\sqrt{\pi a_l t_q}} \tag{14}$$

where A_b is the wall fraction occupied by bubble nucleation and $A_c = 1 - A_c$, f is the bubble detachment frequency, t_q is the quenching time and a_l is the liquid thermal diffusivity.

The bubble detachment diameter (d_d) is given by the correlation from [49]. The latter is valid for subcooled liquid but has been extended to saturated liquid. The bubble detachment diameter is given by:

$$d_d = 2.42 \times 10^{-5} P^{-0.709} \frac{a}{\sqrt{b\varphi}} \tag{15}$$

where P is the pressure and a, b and φ are parameters respectively given by Eqs. (16), (17), (19).

$$a = \frac{\left(T_w - T_{sat}\right)\lambda_s}{2\rho_v \ell \sqrt{\pi a_s}} \tag{16}$$

where λ_s and a_s denote the wall conductivity and thermal diffusivity, ρ_v denotes the vapor density and ℓ is the latent heat of vaporization.

$$b = \begin{cases} \frac{T_{sat} - T_l}{2(1-\rho_v/\rho_l)} & \text{if } St < 0.0065 \\ \frac{1}{2(1-\rho_v/\rho_l)} \frac{q_c + q_q + q_e}{0.0065 \rho_l C_{pl} |\mathbf{u}_l|} & \text{otherwise} \end{cases} \tag{17}$$

where $\|\mathbf{U_l}\|$ is the norm of the liquid velocity and St is the Stanton number which is defined by:

$$\mathrm{St} = \frac{q_c + q_q + q_e}{\rho_l C_{pl} \|\mathbf{U_l}\| \left(T_{sat} - T_i\right)} \tag{18}$$

$$\varphi = \max\left(1, \left(\frac{\|\mathbf{V}\|}{V_0}\right)^{0.47}\right), \text{ with } V_0 = 0.61\,\mathrm{m \cdot s^{-1}} \tag{19}$$

The quenching time and the bubble detachment frequency are modeled as proposed by [50]:

$$t_q = 1/f \tag{20}$$

$$f = \sqrt{\frac{4\, g\, |\rho_v - \rho_l|}{3 \rho_l d_d}} \tag{21}$$

The third heat flux density q_e used to model evaporation is given by:

$$q_e = f \frac{\pi d_d^3}{6} \rho_v \ell n \tag{22}$$

3.3. Turbulence modeling

The turbulence model chosen is the $R_{ij} - \varepsilon$ SSG model. Unlike the initial models proposed for single-phase flows ($k-\varepsilon$) for [51], the $R_{ij}-\varepsilon$ model is a second-order RANS model proposed by [52], in which each component of Reynolds stress tensor R_{ij} is solved as:

$$\frac{\partial R_{ij}}{\partial t} + v_k \frac{\partial R_{ij}}{\partial x_k} = -R_{ik}\frac{\partial \bar{u}_j}{\partial x_k} - R_{jk}\frac{\partial \bar{u}_i}{\partial x_k} + \\ - \Pi_{ij} + \frac{2}{3}\varepsilon\delta_{ij} + \mathcal{G}_{ij} \tag{23}$$

where $P_{ij} = -R_{ik}\frac{\partial \bar{v}_j}{\partial x_k} - R_{jk}\frac{\partial \bar{v_i}}{\partial x_k}$ is the shear stress production term, Π_{ij} is the pressure-strain term, ε represents the scalar dissipation rate and $\mathcal{G}$ represents the gravity term. Similarly, advection/diffusion equation is solved for the dissipation ε:

$$\rho\frac{\partial \varepsilon}{\partial t} + \nabla\cdot(\rho\mathbf{u}\varepsilon - \mu\nabla\varepsilon) = d_\varepsilon + C_{\varepsilon_1}\frac{\varepsilon}{k}\left(\mathcal{P} + \mathcal{G}_\varepsilon\right) \\ - \rho C_{\varepsilon_2}\frac{\varepsilon^2}{k} + \varepsilon\nabla\cdot(\rho\underline{u}) \tag{24}$$

where d_ε is the turbulent diffusion term, $\mathcal{P}$ is the shear stress production term and $\mathcal{G}_\varepsilon$ represents the gravity term for ε given by Eq. (25)

$$\mathcal{G}_\varepsilon = \max\left(0, \frac{1}{2}G_{kk}\right) \tag{25}$$

This turbulence model has been selected based on previous studies that have demonstrated the ability of this model to handle two-phase flows, where flow regime varies along the length [34].

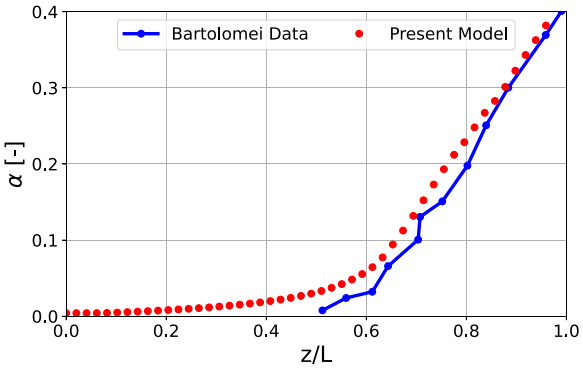

Fig. 3. Void fraction variation in the axial direction for the vertical boiling case of [53]. Comparison of our numerical results to the experimental data.

4. Model validation and mesh sensitivity analysis

4.1. Vertical boiling flow of Bartolomei

Our modeling approach has been validated using the experimental data obtained by [53]. The experiments were conducted with water in a vertical tube, of 15.4 mm inner diameter and 2 m length. The operating pressure is 45 bar, the mass flow rate is $G = 900\ \mathrm{kg \cdot m^{-2} \cdot s^{-1}}$, and a uniform heat flux $\dot{q} = 570\,\mathrm{kW \cdot m^2}$ is applied to the wall. Void fraction was determined by g-radiography. Signals were continuously recorded as the radiography unit was smoothly moved along the channel and provided void fraction measurements at any cross-section.

These data were chosen for validation because the experiments were conducted with water at high pressure, making them suitable for validating the present approach, especially the boiling model. The numerical results obtained for this case are confronted to the experimental data in Fig. 3. We observe a close match between the two evolutions, attesting the ability of our approach to model boiling flows.

4.2. DSG receiver of Pal & Kumar

Additionally, the approach is also confronted to horizontal boiling flow for which a stratified regime was numerically observed. DSG solar receiver simulations from [22] were selected as they consider the same physics. The selected case corresponds to a horizontal receiver with an inner diameter of 50 mm, an outer diameter of 70 mm, and a length of 12 m. The operating pressure is 30 bar, the mass flux is $G = 152\ \mathrm{kg \cdot m^{-2} \cdot s^{-1}}$, and a uniform heat flux of $\dot{q} = 15.74\,\mathrm{kW \cdot m^{-2}}$ is applied on the outer surface of the receiver. In their model, the authors consider the conjugated heat transfer between the receiver tube and the two phase flow inside. Fig. 4 shows the averaged void fraction along the length. A close match is observed between the two approaches as the discrepancies remains below 5%. Fig. 5 shows the comparison of the outer wall temperature profiles obtained with the two approaches for different streamwise positions. One can observe that our approach agrees well with the reference data. However, slight differences in wall bottom temperature are systematically observed. This might be due to water properties differences between the two softwares. The pressure drop along the domain was also assessed, in our simulations we calculated $\Delta P = 243.58$ Pa, while *Pal and Kumar* obtained $\Delta P_{\mathrm{Kumar}} = 221.85$ Pa. It represents a difference of 8.21%.

This comparison confirms the ability of our approach to model the horizontal boiling flows that occur in DSG solar receivers. Before describing our computational configuration, a detailed a mesh convergence study is presented.

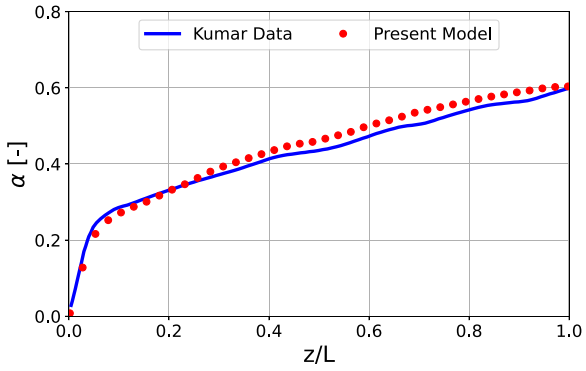

Fig. 4. Comparison of void fraction variation in the axial direction from numerical data recorded by [22].

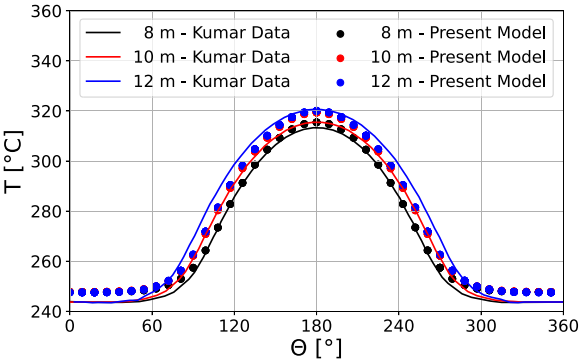

Fig. 5. Comparison of outer wall temperature from numerical data recorded by [22].

Table 2
Total number of cells per mesh. The cell number is given in thousands.

Streamwise	Elements per diameter			
asp. ratio	20	30	40	50
2	720	2321.4	5745.6	1154.4
4	360	1160.4	2872.8	5772
6	240	774	1915.2	3848
8	180	579.9	1436.4	2886

Table 3
Pressure drop for each case in Pa.

Streamwise	Elements per diameter			
asp. ratio	20	30	40	50
2	438.2	432.9	436.9	434.3
4	432.7	431.3	432.0	431.5
6	423.3	430.6	428.6	428.1
8	432.5	427.7	427.5	425.3

4.3. Mesh sensitivity analysis

To perform this mesh convergence study, both the number of cells per diameter and the aspect ratio of elements in the longitudinal direction are varied. The simulated case correspond to a 12 m long receiver operating at a pressure of 70 bar and with a mass flow rate $G = 304\ \mathrm{kg \cdot m^{-2} \cdot s^{-1}}$. The external homogeneous heat flux applied is $\dot{q} = 15.74\ \mathrm{kW \cdot m^{-2}}$. The different meshes employed are detailed in Table 2 with: the number of element per diameter, the aspect ratio in the streamwise direction and the resulting number of elements. A total of 16 simulations were performed. The pressure drop calculated for each mesh is presented in Table 3, indicating a maximum variation of 12 Pa between the different cases which is less than 3% variation. A second convergence indicator consists in calculating the root mean square (RMS) of the void fraction at the receiver outlet that was calculated for each case using Eq. (26). The results are shown in Fig. 6.

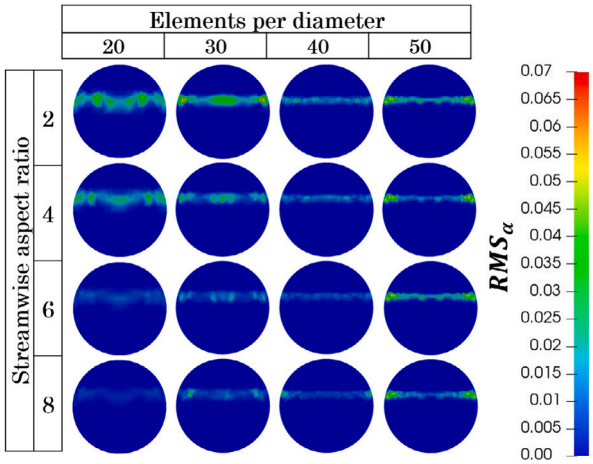

Fig. 6. Results for the mesh sensitivity analysis.

$$RMS_\alpha = \sqrt{\frac{1}{N}\sum_{i=1}^{N}(\alpha_i - \bar{\alpha})^2} \tag{26}$$

For this case, the two phase flow regime is stratified wavy. For such flow, the RMS_α is non-zero in cells crossed by the interface. The value of the indicator is directly linked to the ability of the mesh to capture the wave propagation on the interface. On Fig. 6, one can observe that, for meshes with less than 40 meshes per diameter, the contour of RMS_α gets blurry, meaning the resolution is not sufficient to properly capture the interface oscillation. This is in accordance with the work of [34]. A similar tendency is observed for meshes with high aspect ratio, the waves are poorly captured leading to a degradation of the subsequent temporal analyses. A fair trade-off between precision and mesh number — *ie* calculation cost — seems to be found for 40 meshes per diameter and an aspect ratio of 4. This mesh will then be used for the following simulations. Regarding the meshing in the solid part of the receiver, we have opted for 5 elements in the thickness of the tube, as previously done in similar studies by [22,34].

5. Numerical configurations and simulations procedure

5.1. Numerical set-up

In this study, we consider a 67 m long receiver, matching the dimensions of one of the modules of the eLLO power-plant. The inner diameter is 77.9 mm while the outer is 88.9 mm. The receiver is made of stainless steel whose thermophysical properties are detailed in Table 4. In the simulations, both uniform and non-uniform heat fluxes were applied to the outer surface of the receiver. The non-uniform heat flux was determined through Ray-Tracing simulations (see Fig. 2). Montanet et al. [27] concluded that the total concentrated incoming power does not vary by more than 1.4% with the tilt angle. For the sake of simplicity, it has been assumed in the following that concentrated incoming power remains the same whatever the tilt angle. Furthermore it does not depend on the streamwise direction. The simulation results were fitted with a second degree polynomial with respect to the circumferential coordinate ($0 < \Theta < 360$), to obtain Eq. (27). For the uniform heat flux case, the energy received from the non-uniform flux was integrated and divided by the surface area, yielding an equivalent uniform energy profile, depicted in Eq. (28).

$$\dot{q} = -0.0016\,\Theta^2 + 0.5734\,\Theta + 1.0311 \quad [\mathrm{kW \cdot m^{-2}}] \tag{27}$$

Table 4
Receiver material specifications [22].

Parameters	Value
Inner diameter	77.9 mm
Outer diameter	88.9 mm
Length	67 m
Density	8030 kg/m^3
Specific heat	503 J/kg K
Thermal conductivity	20 W/m K

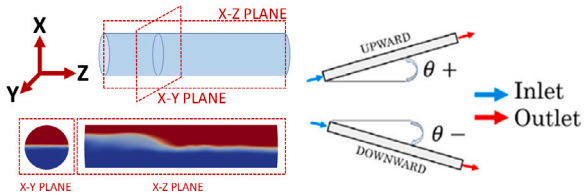

Fig. 7. Criteria for results and tilt.

$$\dot{q}_{\text{uniform}} = \frac{1}{360}\int_0^{360} \dot{q}(\Theta)\, d\Theta = 35.3 \quad [\text{kW}\cdot\text{m}^{-2}] \tag{28}$$

The boundary conditions considered for the case are as follows:

- **Inlet:** A constant mass flow of pure saturated liquid is imposed. Two mass flow were tested : $G = 300\ \text{kg}\cdot\text{m}^{-2}\cdot\text{s}^{-1}$ and $G = 600\ \text{kg}\cdot\text{m}^{-2}\cdot\text{s}^{-1}$.
- **Outlet:** A pressure condition is applied at the outlet and set at $P_{out} = 70$ bar which corresponds to the nominal operating pressure of the plant.
- **Inner wall:** No-slip walls are considered on the inner surface of the receiver, where the coupling between NEPTUNE_CFD and SYRTHES takes place.
- **Outer wall:** The previously mentioned uniform and non-uniform heat fluxes are applied.

The receiver tilt angle θ (see. Fig. 7) is adjusted throughout a volumetric force which allows to modify gravity as $g_x = -g\cos\theta$ and $g_z = -g\sin\theta$.

The working fluid is water. Its liquid and vapor physical properties are obtained from the CATHARE library integrated into the NEPTUNE_CFD code [54]. A detailed two-dimensional schematic model with boundary conditions is shown in Fig. 8. The geometry and meshing were generated using SALOME 9.6.0 software. Hexahedral elements were used for the fluid part, and tetrahedral elements for the receiver part, the latter being compatible with SYRTHES. The mesh was structured, oriented to keep the faces of the fluid part elements parallel to the interface position, thus minimizing numerical diffusion at the interface.

5.2. Simulation procedure

In this three-dimensional study of transient conjugate heat transfer, a total of 28 different simulations are conducted taking in account the whole domain without any symmetry plane. These simulations are performed to investigate the effects of mass flow rate, receiver tilt angle, and applied heat flux. Key aspects such as variation in void fraction, steam quality, steam outlet velocity, dynamic steam quality, and temperature distribution within the receiver are analyzed. Detailed analysis of the results is performed using the Paraview data postprocessing tool. The results are presented both as time-averaged values and in terms of temporal variability. A specific methodology has been followed to carry out the simulations, with the aim of optimizing computational resources, due to the number of simulated cases and

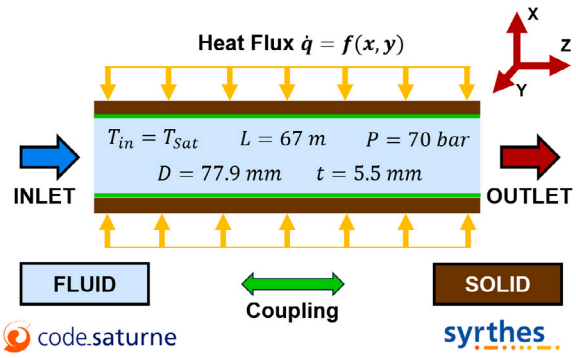

Fig. 8. 2D schematic diagram of the computational case.

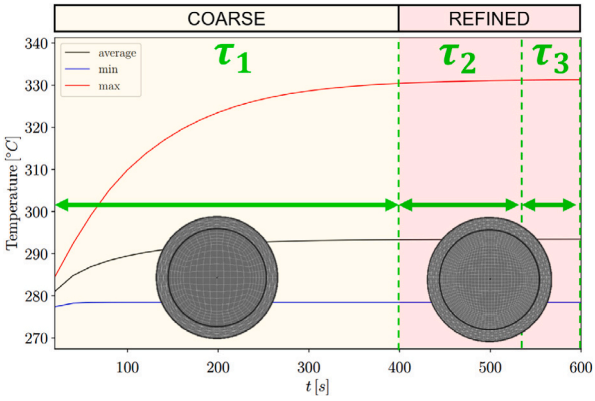

Fig. 9. Methodology followed in the simulation.

the size of the simulated domain. For this purpose, the simulation has been divided into three stages, which are chained one after the other by means of the option of resuming the simulation with a different mesh, available in the Neptune software. A first τ_1 time simulation is performed, starting from the receiver completely filled with liquid, on a coarse mesh. It allows to reach the desired quasi-steady state rapidly. Subsequently, the simulation is stopped and a time τ_2 is resumed with a refined mesh corresponding to the one selected in Section 4.3. This second stage aims to generate more accurate results, especially in the regions of the liquid-gas interface. Finally, the simulation is resumed again at time τ_3 where all the results are saved for further post-processing. Fig. 9 schematizes the methodology followed.

With respect to the temporal resolution of the simulation, an adaptive time-stepping approach has been employed. This methodology is particularly advantageous in simulations involving phase change at the interface, as the vapor phase generated can induce parasitic velocities. Ensuring an appropriate time step is crucial for maintaining the numerical stability of the simulation. To this end, the adaptative time step method ensures that the simulation time step never exceed the convective and diffusive stability timestep calculated for both phases.

6. Results and discussion

6.1. Tilt angle effect on void fraction, steam quality and flow pattern

Fig. 10 presents the evolution of the void fraction along the receiver length for various tilt angles, two different mass flow rate, $G = 300\ \text{kg}\cdot\text{m}^{-2}\cdot\text{s}^{-1}$ on Fig. 10(a) and $G = 600\ \text{kg}\cdot\text{m}^{-2}\cdot\text{s}^{-1}$ on Fig. 10(b), and a homogeneous heat flux distribution. It is evident that, whatever the tilt angle, the shape of the void fraction evolution slightly depends on the mass flow rate. Indeed, profiles are similar for both cases. However, for the smaller mass flow rate the void fraction is higher all along the

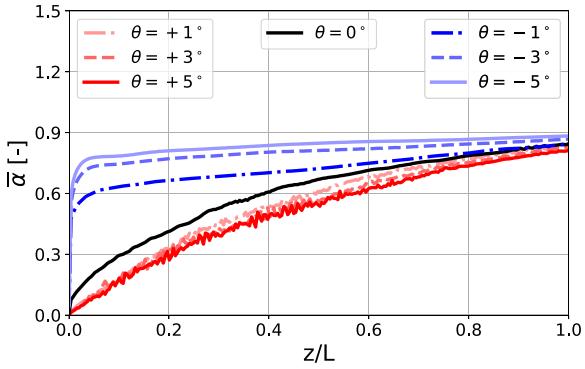

(a) G = 300 kg/(m²s)

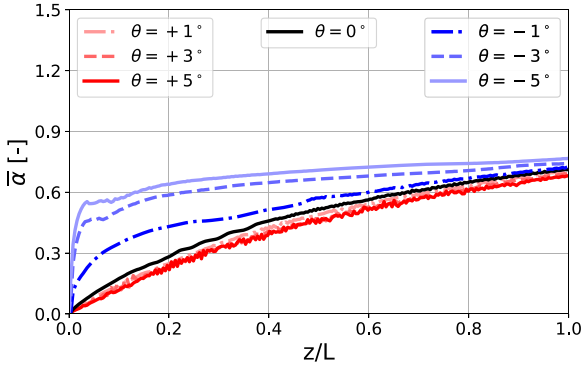

(b) G = 600 kg/(m²s)

Fig. 10. Void fraction versus dimensionless axial position.

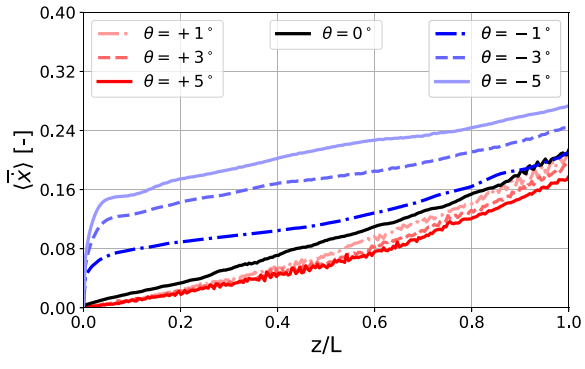

(a) G = 300 kg/(m²s)

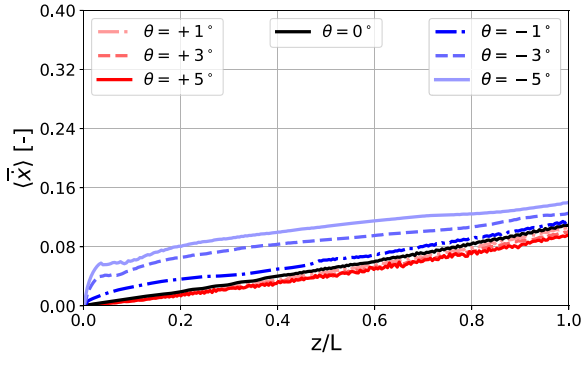

(b) G = 600 kg/(m²s)

Fig. 11. Steam quality versus dimensionless axial position.

receiver. At the outlet ($z/L = 1$), for the horizontal case, the void fraction reaches $\alpha_v = 0.85$ for the lower mass flow rate while it barely reaches $\alpha_v = 0.75$ for the higher one. This can be easily explained by an energy balance on the fluid flow. Furthermore, by comparison with the non-homogeneous flux case we observed the resulting void fraction evolution does not dependent on the applied heat flux distribution, owing to the redistribution effect of the solid wall, as depicted in Fig. 16. Regarding the influence of the tilt, Fig. 10 shows that for negative tilt angles, the steam travels towards the receiver inlet due to buoyancy effect, resulting in a rapid increase in void fraction at the inlet of the receiver. For positive angles, the volumetric fraction values tend to be lower, as the buoyancy force in this case acts in the streamwise direction and tends to evacuate the steam towards the outlet. For upward configurations, the evolution of α_v is noisier, reflecting the presence of a stratified wavy regime. In contrast, for descending configurations, the void fraction evolution flow is much more stable indicating a stably stratified regime.

Regarding steam quality, it has been computed according to Eq. (29):

$$\langle \bar{x} \rangle = \frac{\langle \overline{\alpha \rho_v} \rangle}{\langle \overline{\alpha \rho_v} \rangle + \langle \overline{(1-\alpha)\rho_l} \rangle} \tag{29}$$

where ρ_l and ρ_v correspond respectively to liquid and steam densities. As there is no significant variation of the properties along the receiver length, similar trends to those observed for void fractions are obtained in Fig. 11. It can be generally concluded that negative tilt angles favor steam production. Indeed, in such cases, the buoyancy effects tend to increase the residence time of the steam in the receiver, leading to a rise in overall steam production.

To visualize the flow patterns inside the receiver, the temporal fluctuation of the void fraction has been computed using Eq. (26). As discussed before, Fig. 12 shows that for negative tilt angles, owing to a stably stratified regime, no temporal oscillations of the void fraction are observed. Whereas for positive tilt angles, a stratified-wavy regime is observed. This flow pattern arises when void fractions are below $\alpha = 0.5$ and steam phase velocities are high, and tend to trigger shear instabilities forming waves (as observed experimentally in [6]). The occurrence of larger oscillations in the flow pattern has been observed previously by Odeh [55]. He reported that tilting the receiver caused the flow pattern to transition to intermittent flow which is undesirable in plant operation due to the large massflow and pressure fluctuations associated to this flow pattern. Fig. 13 shows that the streamwise steam velocity is higher for positive tilt angles. For $x/L = 0.2$, whatever the mass flow rate, it is clear that the streamwise velocity is roughly twice faster for $\theta = 5°$ than for $\theta = -5°$. Finally, it is apparent that for all the simulated cases, no intermittent flow pattern — where the receiver cross section is sometimes filled with liquid water — is observed. From an operational standpoint, this outcome is favorable, as such a flow pattern complicates the operation of the solar plant.

6.2. Tilt angle effect on the streamwise steam velocity and dynamic quality

Fig. 12 shows different contour plot in the XZ planes after a geometrical adjustment required to display the entire domain for such a high aspect ratio geometry. In the center plot, the region occupied by the liquid phase is shaded in black and color map indicates the magnitude of the streamwise component of the steam velocity. It can be noted that for negative tilt angles the appearance of negative velocity indicating the presence of steam recirculation towards the inlet. Such recirculation is observed, whatever the mass flows and the heat flux distribution, for all negative tilt angle simulations. The latter is driven by the buoyancy force acting on the vapor phase. This backward circulation results in a region with axial velocity close to zero for negative tilt angles. The opposite effect is also observed for positive tilt angles, the buoyancy force aids evacuating the steam towards the outlet, resulting in steam acceleration and higher outlet velocities. Fig. 12 depicts that for a mass

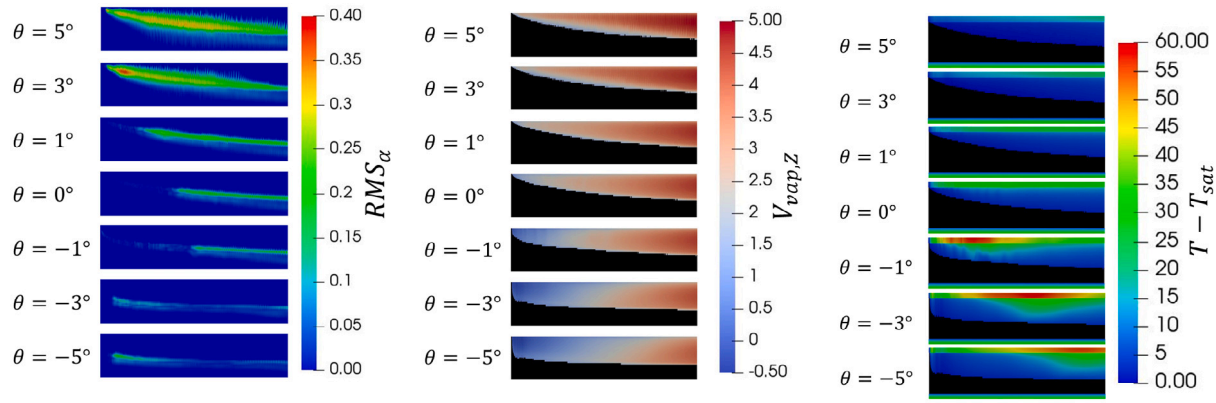

Fig. 12. XZ planes of RMS of void fraction (left), time averaged steam velocity (center) and time averaged steam and tube temperature (right) for non-homogeneous heat flux and $G = 600\ \mathrm{kg \cdot m^{-2} \cdot s^{-1}}$.

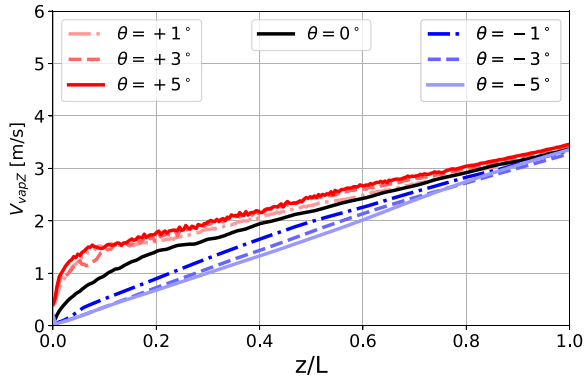

(a) G = 300 kg/(m²s)

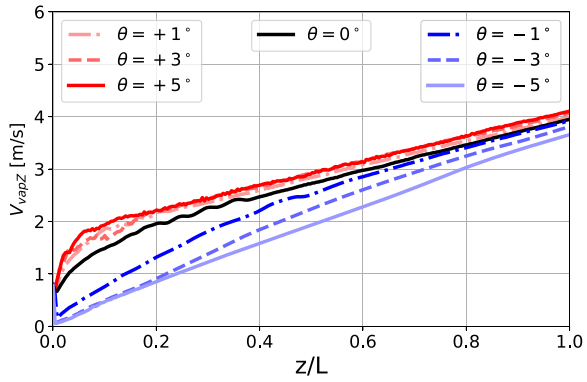

(b) G = 600 kg/(m²s)

Fig. 13. Steam streamwise velocity versus dimensionless axial position for a non homogeneous heat flux distribution.

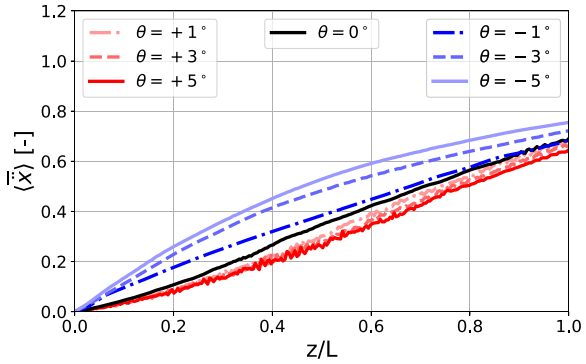

(a) G = 300 kg/(m²s)

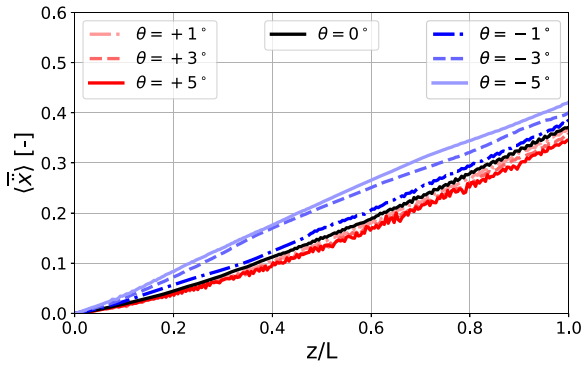

(b) G = 600 kg/(m²s)

Fig. 14. Dynamic quality versus dimensionless axial position.

flow of $G = 600\ \mathrm{kg \cdot m^{-2} \cdot s^{-1}}$, the steam velocity at the outlet locally reaches up to $v_v = 5$ m/s.

The cross section averaged streamwise steam velocity evolution along the receiver is depicted in Fig. 13. For negative tilt angles, the steam velocities near the inlet are lower than the imposed inlet velocities of the case, respectively $v_{in} = 0.41\ \mathrm{m \cdot s^{-1}}$ for $G = 300\ \mathrm{kg \cdot m^{-2} \cdot s^{-1}}$ and $v_{in} = 0.82\ \mathrm{m \cdot s^{-1}}$ for $G = 600\ \mathrm{kg \cdot m^{-2} \cdot s^{-1}}$. This is directly related to the recirculation observed on Fig. 12 and provides an indication of its influence. For a positive tilt, two regions can be distinguish on the average velocity curve. A first region in which the vapor accelerates rapidly following a logarithmic law, which stabilizes around $z/L = 0.1$ (resp. $z/L = 0.2$) for $G = 300\ \mathrm{kg \cdot m^{-2} \cdot s^{-1}}$ (resp. $G = 600\ \mathrm{kg \cdot m^{-2} \cdot s^{-1}}$). In the second region, the flow linearly accelerates until the receiver outlet.

A similar trend is observed for the dynamic steam quality — calculated with Eq. (30) (where v_l and v_v correspond respectively to liquid and steam velocities) and shown in Fig. 14 — where values are higher for negative tilt angles than for positive ones.

$$\langle \bar{\dot{x}} \rangle = \frac{\langle \overline{\alpha \rho_v v_v} \rangle}{\langle \overline{\alpha \rho_v v_v} \rangle + \langle \overline{(1-\alpha)\rho_l v_l} \rangle} \tag{30}$$

6.3. Tilt angle effect on steam and solid temperature

The right part of Fig. 12 shows temperature excess ($T - T_{sat}$) contours of in the XZ-plane (see Fig. 7) of both the vapor and the solid phase for

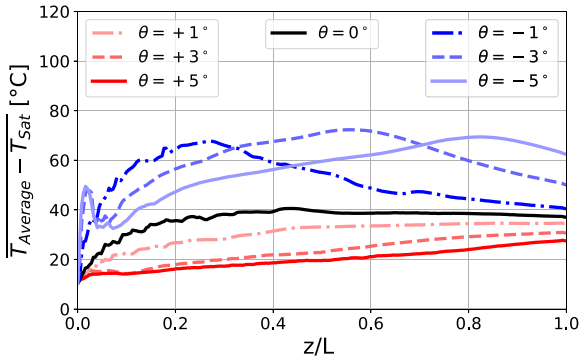

(a) Homogeneous heat flux.

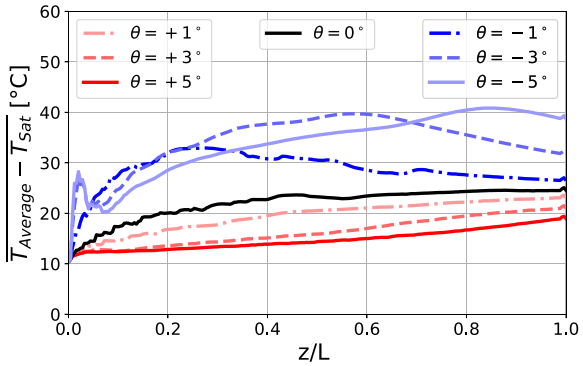

(b) Non-Homogeneous heat flux.

Fig. 15. Average cross section tube temperature versus dimensionless axial position for $G = 600$ kg/(m^{2}s).

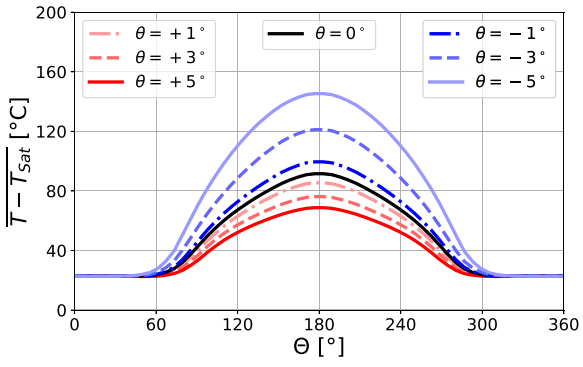

(a) Homogeneous heat flux.

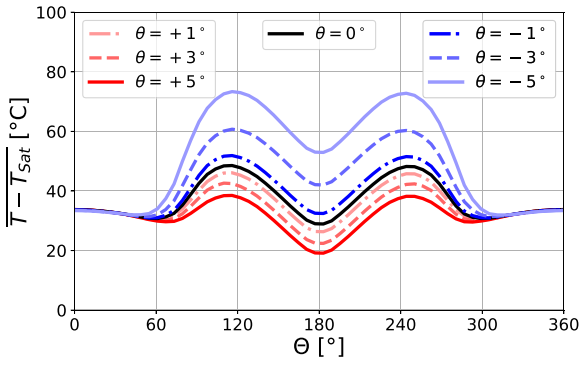

(b) Non-Homogeneous heat flux.

Fig. 16. Outer wall tube temperature versus circumferential position for $G = 600$ kg/(m^{2}s).

a non homogeneous flux distribution and $G = 600\ \mathrm{kg \cdot m^{-2} \cdot s^{-1}}$. For positive tilt angles, the temperature excess in the steam phase remains always below 10 K highlighting a relative homogeneity. In the receiver, no hot spot is visible and the temperature excess does not exceed 40 K. Both quantities linearly increase in the streamwise direction. Whereas, for negative tilt angles, both the steam and receiver temperature highlight strong non-homogeneous spatial variation. Analysis reveals that the maximum peak temperature location of both the steam and the receiver, appear at a streamwise upper location depending on the tilt angle. Decreasing the tilt angle results in the hot spot moving closer to the inlet. Such displacement of the hot spot can also be seen in Fig. 15 which displays the cross section averaged of the temperature excess in the receiver with respect to the length, for $G = 600\ \mathrm{kg \cdot m^{-2} \cdot s^{-1}}$ and both heat flux distributions. The trends are similar for both flux distribution but the peak temperature reach systematically higher values for the homogeneous distribution, for example for $\theta = -5°$ it reaches 70 K for the homogeneous distribution against 40 K for the non-homogeneous one. In the case of stratified flow, the upper portion of the receiver is exclusively exposed to vapor. When a homogeneous flux distribution is applied, the heat flux in the upper region is excessively high to be effectively dissipated by the vapor flow, resulting in an increase in the temperature of the solid. Additionally, for positive and zero tilt angles the temperature excess evolution is monotonous with respect to the length. The more negative the tilt angles the smaller the temperature excess.

Finally, Fig. 16 compares the external receiver temperature distribution at the outlet ($x/L = 1$) for both flux distributions. It is observable that for the homogeneous one, the temperature excess maximum appears at the top of the receiver — owing to both the thermal boundary condition and the low heat transfer coefficient of the vapor phase in contact with the upper part of the receiver. It becomes clear on Fig. 16(b) that the temperature distribution is strongly affected by the heat flux distribution. For the non-homogeneous flux, the temperature excess peak is no longer at the top but shifts by about 60° — owing to the coupling between the Θ distribution of the heat flux and the ability of the flow to efficiently evacuate the heat. For both flux distribution, the tilt angle effects on the temperature excess is similar. For downward flows, the temperature excess increases with the tilt while it decreases for upward flows. Fig. 17 shows, for $G = 600\ \mathrm{kg \cdot m^{-2} \cdot s^{-1}}$ and the non-homogeneous flux distribution, temperature excess contour at four different streamwise position and for all tilt angles. The temperature profile obtained are consistent with the analysis proposed for Figs. 15(b) and 16(b).

7. Summary and concluding remarks

In this study, we evaluated the tilt angle and the concentrated solar heat flux distribution effects on flow regimes and temperature distribution in a DSG solar receiver. To this end, a non-stationary three-dimensional model taking into account conjugate heat transfer has been set up coupling NEPTUNE_CFD and SYRTHES software. The approach has been validated by comparison to relevant cases from the literature. A mesh convergence analysis allowed to identify a mesh yielding a satisfactory trade-off between precision and calculation cost. Simulations reproduce a 67 m long module of the eLLO power plant. Two mass flow rates, $G = 300\ \mathrm{kg \cdot m^{-2} \cdot s^{-1}}$ and $G = 600\ \mathrm{kg \cdot m^{-2} \cdot s^{-1}}$, eleven tilt angles, ranging from −5° to 5° and two different flux distributions were simulated. The main findings are summarized below.

1. **Heat flux distribution effect:** Homogeneous heat flux leads to higher section averaged receiver temperature than the non-homogeneous distribution. The maximum moves towards the inlet for angles close to horizontal and towards the outlet for more negative angles, indicating significant temperature gradients. In a cross section, the homogeneous heat flux generates a single receiver temperature maximum at the top of the receiver

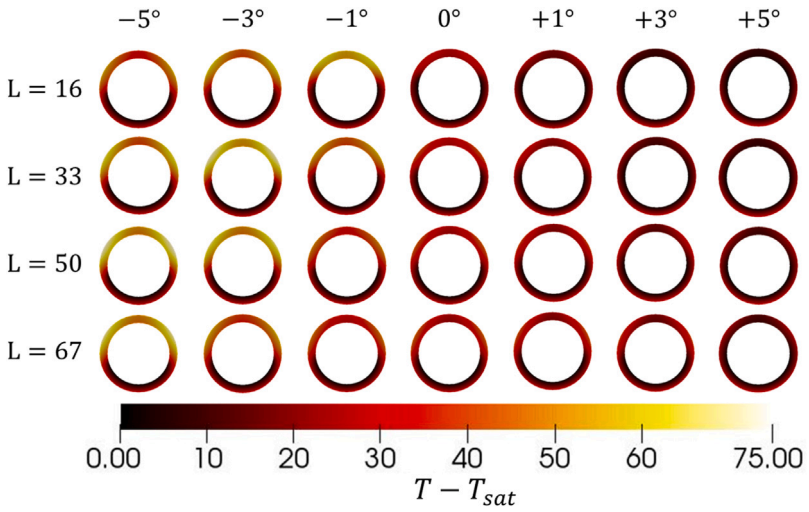

Fig. 17. Results for fluid and solid part for non-homogeneous heat flux and $G = 600$ kg/(m^{2}s).

while a non-uniform distribution leads to two maxima shifted by 60° from the top. The boundary condition strongly influences the temperature distribution in the receiver, but does not affect the total amount of steam produced. This conclusion can be useful when pre-dimensioning a solar receiver, since it states that the exact flux distribution is not required to pre-dimension the line length to reach the targeted steam quality at the receiver's outlet.

2. **Mass Flow Rate effect:** The void fraction increases with a decrease of the mass flow rate due to longer fluid residence time in the receiver. For lower mass flow, the receiver temperature maximum is reached closer to the inlet and has a higher magnitude.
3. **Tilt angle effect on flow patterns:** Tilt angle significantly influences phase distribution in the receiver. Negative angles increase void fraction near the inlet due to buoyancy-driven recirculation, while positive angles reduce it by aiding steam evacuation. Positive tilts enhance steam evacuation and outlet velocities, promoting shear instabilities and stratified-wavy flow. In contrast, negative tilts lead to stably stratified flow with steam recirculating toward the inlet, reducing steam streamwise velocity. Steam quality trends follow these patterns, with higher dynamic steam quality at negative angles, but increasing near the outlet for positive tilts at lower mass flow rates. Our results highlight that although the amount of steam produced is slightly higher for negative tilt angles, the receiver temperature reached levels that might compromise its integrity. Such tilts configuration must thus be avoided. Furthermore, although a slight positive tilt promotes a stratified wavy flow, it significantly decreases the receivers's temperature in operation which might increase the receiver lifespan.
4. **Design and Operational Implications:** These findings are critical for optimizing solar plant receivers. Avoiding intermittent flow patterns is vital for stable operation, as constant fluid contact with the receiver's surface is necessary to prevent operational complications. Simulations highlight that downward flows promote steam production but generate stronger temperature gradient in the receiver which may generate stronger thermal stress and fatigue.

The present study investigates the influence of tilt angle and boundary conditions on the nominal operating parameters of the eLLO solar plant, as summarized in the previous conclusions. Although pressure is a variable that directly affects the thermophysical properties of the fluid, the results indicate that flow regimes are primarily influenced by gravitational effects for such horizontal flow configuration.

Future improvements to this work should include a broader exploration of operating parameters and transient phenomena, such as the effect of cloud transients on the dynamics of steam generation within the receiver. These conclusions underscore the importance of considering mass flow rate, tilt angle, and heat flux distribution when designing and operating solar receiver systems to optimize thermal performance and enhance durability. Future efforts will focus on developing an experimental database for horizontal and slightly tilted boiling flow applicable to this technology.

CRediT authorship contribution statement

Israël Aguilera-Cortes: Writing – original draft, Validation, Software, Project administration, Methodology, Funding acquisition, Formal analysis, Data curation, Conceptualization. **Adrien Toutant:** Writing – review & editing, Visualization, Supervision, Conceptualization. **Samuel Mer:** Writing – review & editing, Visualization, Supervision, Project administration, Funding acquisition, Conceptualization.

Declaration of competing interest

The authors declare that they have no known competing financial interests or personal relationships that could have appeared to influence the work reported in this paper.

Acknowledgments

This work was funded by the European Union as part of the TOPCSP project (HORIZON MSCA Doctoral Network, Project number 101072537). This project was provided with computer and storage resources by GENCI at IDRIS thanks to the grant 2023-A0152B14649 on the CSL partition of the supercomputer Jean Zay. Finally, the authors would like to thank Florent Lecat (eLLO), Nicolas Merigoux (EDF), Hervé Neau (IMFT) and Maxime Pigou (IMFT) for their technical support.

References

[1] H.M. Müller-Steinhagen, F. Trieb, Concentrating solar power, — A review of the technology, 2004, URL https://api.semanticscholar.org/CorpusID:106949393.

[2] M. Biencinto, L. González, L. Valenzuela, A quasi-dynamic simulation model for direct steam generation in parabolic troughs using TRNSYS, Appl. Energy 161 (2016) 133–142, http://dx.doi.org/10.1016/j.apenergy.2015.10.001, URL https://linkinghub.elsevier.com/retrieve/pii/S0306261915012283.

[3] A. Fernández-García, E. Zarza, L. Valenzuela, M. Pérez, Parabolic-trough solar collectors and their applications, Renew. Sustain. Energy Rev. 14 (7) (2010) 1695–1721, http://dx.doi.org/10.1016/j.rser.2010.03.012, URL https://linkinghub.elsevier.com/retrieve/pii/S1364032110000675.
[4] Y. Taitel, A.E. Dukler, A model for predicting flow regime transitions in horizontal and near horizontal gas–liquid flow, AIChE J. 22 (1) (1976) 47–55, http://dx.doi.org/10.1002/aic.690220105, URL https://aiche.onlinelibrary.wiley.com/doi/10.1002/aic.690220105.
[5] N. Kattan, J.R. Thome, D. Favrat, Flow boiling in horizontal tubes: Part 1—Development of a diabatic two-phase flow pattern map, J. Heat Transfer 120 (1) (1998) 140–147, http://dx.doi.org/10.1115/1.2830037, URL https://asmedigitalcollection.asme.org/heattransfer/article/120/1/140/383031/Flow-Boiling-in-Horizontal-Tubes-Part-1Development.
[6] L. Wojtan, T. Ursenbacher, J.R. Thome, Investigation of flow boiling in horizontal tubes: Part II—Development of a new heat transfer model for stratified-wavy, dryout and mist flow regimes, Int. J. Heat Mass Transfer 48 (14) (2005) 2970–2985, http://dx.doi.org/10.1016/j.ijheatmasstransfer.2004.12.013, URL https://linkinghub.elsevier.com/retrieve/pii/S001793100500027X.
[7] O. Baker, Design of pipelines for the simultaneous flow of oil and gas, in: SPE Annual Technical Conference and Exhibition?, SPE, 1953, pp. SPE–323.
[8] J.M. Mandhane, G.A. Gregory, K. Aziz, A flow pattern map for gas—liquid flow in horizontal pipes, Int. J. Multiph. Flow 1 (4) (1974) 537–553, http://dx.doi.org/10.1016/0301-9322(74)90006-8, URL https://linkinghub.elsevier.com/retrieve/pii/0301932274900068.
[9] R. Cundapí, S.L. Moya, L. Valenzuela, Approaches to modelling a solar field for direct generation of industrial steam, Renew. Energy 103 (2017) 666–681, http://dx.doi.org/10.1016/j.renene.2016.10.081, URL https://linkinghub.elsevier.com/retrieve/pii/S0960148116309582.
[10] S.D. Odeh, Direct Steam Generation Collectors for Solar Electric Generation Systems (Ph.D. thesis), UNSW Sydney, 1999.
[11] M. Eck, W. Steinmann, Dynamic behavior of the direct solar steam generation in parabolic trough collectors: A simulation study, in: Proc, of 10th Solar PACES Int. Symp. on Solar Thermal Concentrating Technologies, 2000, pp. 101–106.
[12] W.-D. Steinmann, Dynamik Solarer Dampferzeuger (Ph.D. thesis), Universität Stuttgart, 2001.
[13] R. Silva, M. Pérez, A. Fernández-Garcia, Modeling and Co-simulation of a parabolic trough solar plant for industrial process heat, Appl. Energy 106 (2013) 287–300.
[14] L. Valenzuela, D. Hernández-Lobón, E. Zarza, M. Pérez, Pressure losses in small-sized parabolic-trough solar fields for industrial process heat, in: ISES Solar World Congress. Kassel, Germany, 2011.
[15] M. Ishii, K. Mishima, Two-fluid model and hydrodynamic constitutive relations, Nucl. Eng. Des. 82 (2–3) (1984) 107–126, http://dx.doi.org/10.1016/0029-5493(84)90207-3, URL https://linkinghub.elsevier.com/retrieve/pii/0029549384902073.
[16] M.I. Roldán, L. Valenzuela, E. Zarza, Thermal analysis of solar receiver pipes with superheated steam, Appl. Energy 103 (2013) 73–84, http://dx.doi.org/10.1016/j.apenergy.2012.10.021, URL https://linkinghub.elsevier.com/retrieve/pii/S0306261912007271.
[17] J.J. Serrano-Aguilera, L. Valenzuela, L. Parras, Thermal 3D model for direct solar steam generation under superheated conditions, Appl. Energy 132 (2014) 370–382, http://dx.doi.org/10.1016/j.apenergy.2014.07.035, URL https://linkinghub.elsevier.com/retrieve/pii/S030626191400717X.
[18] E. Zarza, L. Valenzuela, J. Leo'n, H.-D. Weyers, M. Eickhoff, M. Eck, K. Hennecke, The DISS project: Direct steam generation in parabolic trough systems. Operation and maintenance experience and update on project status, J. Sol. Energy Eng. 124 (2) (2002) 126–133, http://dx.doi.org/10.1115/1.1467645, URL https://asmedigitalcollection.asme.org/solarenergyengineering/article/124/2/126/461459/The-DISS-Project-Direct-Steam-Generation-in.
[19] E. Zarza, L. Valenzuela, J. León, K. Hennecke, M. Eck, H.-D. Weyers, M. Eickhoff, Direct steam generation in parabolic troughs: Final results and conclusions of the DISS project, Energy 29 (5–6) (2004) 635–644, http://dx.doi.org/10.1016/S0360-5442(03)00172-5, URL https://linkinghub.elsevier.com/retrieve/pii/S0360544203001725.
[20] M. Eck, W.-D. Steinmann, J. Rheinländer, Maximum temperature difference in horizontal and tilted absorber pipes with direct steam generation, Energy 29 (5–6) (2004) 665–676, http://dx.doi.org/10.1016/S0360-5442(03)00175-0, URL https://linkinghub.elsevier.com/retrieve/pii/S0360544203001750.
[21] O.E. Itabiyi, THE effect of tilt angle and mass flow rate on the performance of a parabolic trough solar concentrator via experimentation, Adv. Phys. Theor. Appl. (2024) http://dx.doi.org/10.7176/APTA/88-01, URL https://iiste.org/Journals/index.php/APTA/article/view/62130.
[22] R.K. Pal, R.K. K, Thermo-hydrodynamic modeling of flow boiling through the horizontal tube using Eulerian two-fluid modeling approach, Int. J. Heat Mass Transfer 168 (2021) 120794, http://dx.doi.org/10.1016/j.ijheatmasstransfer.2020.120794, URL https://linkinghub.elsevier.com/retrieve/pii/S0017931020337327.
[23] R.K. Pal, R.K. K, Two-fluid modeling of direct steam generation in the receiver of parabolic trough solar collector with non-uniform heat flux, Energy 226 (2021) 120308, http://dx.doi.org/10.1016/j.energy.2021.120308, URL https://linkinghub.elsevier.com/retrieve/pii/S0360544221005570.
[24] eLLO solar thermal project CSP project, URL https://solarpaces.nrel.gov/project/ello-solar-thermal-project.
[25] M. Ploquin, S. Mer, A. Toutant, F. Roget, CFD investigation of level fluctuations in steam accumulators as thermal storage: A direct steam generation application, Sol. Energy 245 (2022) 11–18, http://dx.doi.org/10.1016/j.solener.2022.08.048, URL https://linkinghub.elsevier.com/retrieve/pii/S0038092X22005977.
[26] J. Muñoz-Antón, R. Abbas, J. Martínez-Val, M. Montes, Going further with Fresnel receiver: New design window for direct steam generation, Energy Procedia 49 (2014) 184–192, http://dx.doi.org/10.1016/j.egypro.2014.03.020, URL https://linkinghub.elsevier.com/retrieve/pii/S1876610214004743.
[27] E. Montanet, S. Rodat, Q. Falcoz, F. Roget, Influence of topography on the optical performances of a Fresnel linear asymmetrical concentrator array: The case of the eLLO solar power plant, Energy 274 (2023) 127310, http://dx.doi.org/10.1016/j.energy.2023.127310, URL https://linkinghub.elsevier.com/retrieve/pii/S0360544223007041.
[28] T. Hibiki, M. Ishii, One-dimensional drift-flux model and constitutive equations for relative motion between phases in various two-phase flow regimes, Int. J. Heat Mass Transfer 46 (25) (2003) 4935–4948, http://dx.doi.org/10.1016/S0017-9310(03)00322-3, URL https://linkinghub.elsevier.com/retrieve/pii/S0017931003003223.
[29] M. Ishii, T. Hibiki, Connection to other statistical averages, in: Thermo-Fluid Dynamics of Two-Phase Flow, Springer New York, New York, NY, 2011, pp. 119–128, http://dx.doi.org/10.1007/978-1-4419-7985-8_6, URL https://link.springer.com/10.1007/978-1-4419-7985-8_6.
[30] S.V. Patankar, D.B. Spalding, A calculation procedure for heat, mass and momentum transfer in three-dimensional parabolic flows, Int. J. Heat Mass Transfer 15 (10) (1972) 1787–1806, http://dx.doi.org/10.1016/0017-9310(72)90054-3, URL https://linkinghub.elsevier.com/retrieve/pii/0017931072900543.
[31] S. Mimouni, M. Boucker, J. Laviéville, A. Guelfi, D. Bestion, Modelling and computation of cavitation and boiling bubbly flows with the NEPTUNE_CFD code, Nucl. Eng. Des. 238 (3) (2008) 680–692, http://dx.doi.org/10.1016/j.nucengdes.2007.02.052, URL https://linkinghub.elsevier.com/retrieve/pii/S0029549307003494.
[32] J.P. Mañes, V.H. Sánchez Espinoza, S. Chiva Vicent, M. Böttcher, R. Stieglitz, Validation of NEPTUNE-CFD two-phase flow models using experimental data, Sci. Technol. Nucl. Install. 2014 (2014) 1–19, http://dx.doi.org/10.1155/2014/185950, URL http://www.hindawi.com/journals/stni/2014/185950/.
[33] N. Mérigoux, J. Laviéville, S. Mimouni, M. Guingo, C. Baudry, S. Bellet, Verification, validation and application of NEPTUNE_CFD to two-phase pressurized thermal shocks, Nucl. Eng. Des. 312 (2017) 74–85, http://dx.doi.org/10.1016/j.nucengdes.2016.06.041, URL https://linkinghub.elsevier.com/retrieve/pii/S0029549316302023.
[34] E. Butaye, A. Toutant, S. Mer, Euler–Euler multi-scale simulations of internal boiling flow with conjugated heat transfer, Appl. Mech. 4 (1) (2023) 191–209, http://dx.doi.org/10.3390/applmech4010011, URL https://www.mdpi.com/2673-3161/4/1/11.
[35] M. Ishii, N. Zuber, Drag coefficient and relative velocity in bubbly, droplet or particulate flows, AIChE J. 25 (5) (1979) 843–855, http://dx.doi.org/10.1002/aic.690250513, URL https://aiche.onlinelibrary.wiley.com/doi/10.1002/aic.690250513.
[36] N. Zuber, On the dispersed two-phase flow in the laminar flow regime, Chem. Eng. Sci. 19 (11) (1964) 897–917, http://dx.doi.org/10.1016/0009-2509(64)85067-3, URL https://linkinghub.elsevier.com/retrieve/pii/0009250964850673.
[37] A. Tomiyama, H. Tamai, I. Zun, S. Hosokawa, Transverse migration of single bubbles in simple shear flows, Chem. Eng. Sci. 57 (11) (2002) 1849–1858, http://dx.doi.org/10.1016/S0009-2509(02)00085-4, URL https://linkinghub.elsevier.com/retrieve/pii/S0009250902000854.
[38] R.M. Wellek, A.K. Agrawal, A.H.P. Skelland, Shape of liquid drops moving in liquid media, AIChE J. 12 (5) (1966) 854–862, http://dx.doi.org/10.1002/aic.690120506, URL https://aiche.onlinelibrary.wiley.com/doi/10.1002/aic.690120506.
[39] M. Lance, M.L. De Bertodano, Phase distribution phenomena and wall effects in bubbly two-phase flows, Multiph. Sci. Technol. 8 (1–4) (1994) 69–123, http://dx.doi.org/10.1615/MultScienTechn.v8.i1-4.30, URL http://www.dl.begellhouse.com/journals/5af8c23d50e0a883,2d2fda127764a47f,1e6b5eaa78073157.html.
[40] P. Coste, A large interface model for two-phase CFD, Nucl. Eng. Des. 255 (2013) 38–50, http://dx.doi.org/10.1016/j.nucengdes.2012.10.008, URL https://linkinghub.elsevier.com/retrieve/pii/S0029549312005213.
[41] R. Denèfle, S. Mimouni, J.-P. Caltagirone, S. Vincent, Multifield hybrid approach for two-phase flow modeling — Part 1: Adiabatic flows, Comput. & Fluids 113 (2015) 106–111, http://dx.doi.org/10.1016/j.compfluid.2014.07.018.
[42] N. Merigoux, J. Lavieville, S. Mimouni, M. Guingo, C. Baudry, A generalized large interface to dispersed bubbly flow approach to model two-phase flows in nuclear power plant, in: CFD4NRS-6, Cambridge, MA - USA, Paper 11-1, 2016, pp. 1–20.
[43] S. Fleau, Multifield Approach and Interface Locating Method for Two-Phase Flows in Nuclear Power Plant (Ph.D. thesis), Univ. Paris Est Marne-La-Vallée, France, 2017.

[44] S. Mer, O. Praud, H. Neau, N. Merigoux, J. Magnaudet, V. Roig, The emptying of a bottle as a test case for assessing interfacial momentum exchange models for Euler–Euler simulations of multi-scale gas-liquid flows, Int. J. Multiph. Flow 106 (2018) 109–124, http://dx.doi.org/10.1016/j.ijmultiphaseflow.2018.05.002, URL https://linkinghub.elsevier.com/retrieve/pii/S0301932218301472.

[45] J.U. Brackbill, D.B. Kothe, C. Zemach, A continuum method for modeling surface tension, J. Comput. Phys. 100 (2) (1992) 335–354, http://dx.doi.org/10.1016/0021-9991(92)90240-Y, URL https://linkinghub.elsevier.com/retrieve/pii/002199919290240Y.

[46] N. Kurul, M.Z. Podowski, Multidimensional effects in forced convection subcooled boiling, in: Proceeding of International Heat Transfer Conference 9, Begellhouse, Jerusalem, Israel, 1990, pp. 21–26, http://dx.doi.org/10.1615/IHTC9.40, URL http://ihtcdigitallibrary.com/conferences/6ec9fdc764f29109,3b6668e93c4d03e5,1968e4d71e4e45b1.html.

[47] Y.Y. Hsu, On the size range of active nucleation cavities on a heating surface, J. Heat Transfer 84 (3) (1962) 207–213, http://dx.doi.org/10.1115/1.3684339, URL https://asmedigitalcollection.asme.org/heattransfer/article/84/3/207/430157/On-the-Size-Range-of-Active-Nucleation-Cavities-on.

[48] R. Hino, T. Ueda, Studies on heat transfer and flow characteristics in subcooled flow boiling—Part 1. Boiling characteristics, Int. J. Multiph. Flow 11 (3) (1985) 269–281, http://dx.doi.org/10.1016/0301-9322(85)90058-8, URL https://linkinghub.elsevier.com/retrieve/pii/0301932285900588.

[49] H.C. Ünal, Maximum bubble diameter, maximum bubble-growth time and bubble-growth rate during the subcooled nucleate flow boiling of water up to 17.7 MN/m2, Int. J. Heat Mass Transfer 19 (6) (1976) 643–649, http://dx.doi.org/10.1016/0017-9310(76)90047-8, URL https://linkinghub.elsevier.com/retrieve/pii/0017931076900478.

[50] R. Cole, A photographic study of pool boiling in the region of the critical heat flux, AIChE J. 6 (4) (1960) 533–538, http://dx.doi.org/10.1002/aic.690060405, URL https://aiche.onlinelibrary.wiley.com/doi/10.1002/aic.690060405.

[51] B.E. Launder, D.B. Spalding, The numerical computation of turbulent flows, Comput. Methods Appl. Mech. Engrg. 3 (2) (1974) 269–289, http://dx.doi.org/10.1016/0045-7825(74)90029-2, URL https://linkinghub.elsevier.com/retrieve/pii/0045782574900292.

[52] C.G. Speziale, S. Sarkar, T.B. Gatski, Modelling the pressure–strain correlation of turbulence: An invariant dynamical systems approach, J. Fluid Mech. 227 (1991) 245–272, http://dx.doi.org/10.1017/S0022112091000101, URL https://www.cambridge.org/core/product/identifier/S0022112091000101/type/journal_article.

[53] G.G. Bartolomei, V.G. Brantov, Y.S. Molochnikov, Y.V. Kharitonov, V.A. Solodkii, G.N. Batashova, V.N. Mikhailov, An experimental investigation of true volumetric vapor content with subcooled boiling in tubes, Therm. Eng. 29 (3) (1982) 132–135.

[54] P. Emonot, A. Souyri, J. Gandrille, F. Barré, CATHARE-3: A new system code for thermal-hydraulics in the context of the NEPTUNE project, Nucl. Eng. Des. (2011) S0029549311004018, http://dx.doi.org/10.1016/j.nucengdes.2011.04.049, URL https://linkinghub.elsevier.com/retrieve/pii/S0029549311004018.

[55] S.D. Odeh, M. Behnia, G.L. Morrison, Hydrodynamic analysis of direct steam generation solar collectors, J. Sol. Energy Eng. 122 (1) (2000) 14–22.

Chapitre 3

Lits fluidisés comme fluide caloporteur dans les technologies solaires à concentration (CST)

Sommaire

Préambule

Cette thématique de recherche est portée au laboratoire PROMES depuis une trentaine d'années par G. Flamant. À la suite de mon recrutement, je suis venu renforcer cette thématique, notamment en encadrant la thèse expérimentale de R. Gueguen aux côtés de F. Bataille. Les résultats présentés dans ce chapitre sont issus de ces travaux. Dans le cadre des projets ANR PRME SiCSun et européen P2P, des simulations thermohydrauliques – utilisant les outils décrits dans la section 2.2 – de récepteurs et d'échangeurs de chaleur à lit fluidisé seront initiées d'ici fin 2025.

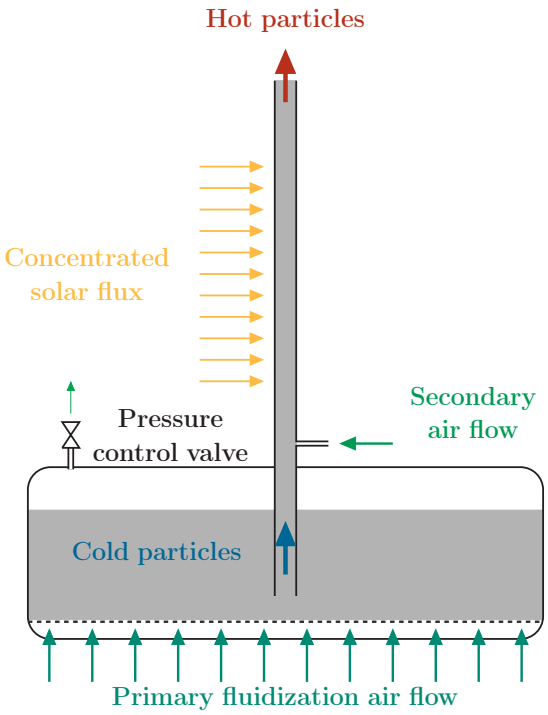

FIGURE 3.1 – Représentation schématique d'un récepteur solaire à lit fluidisé en circulation ascendante.

3.1 Contexte

Afin d'augmenter la température de sortie du récepteur – et donc le rendement de conversion – des prochaines générations de centrales à tour, nous développons au laboratoire un récepteur solaire à lit fluidisé en circulation ascendante.

Dans ce procédé, schématisé pour un récepteur monotube sur la Fig. 3.1, le tube récepteur est plongé dans un lit fluidisé nourrice. Une vanne permet de pressuriser le ciel gazeux de ce dernier, de telle sorte qu'au fur et à mesure que la pression augmente, les particules montent dans le tube puis s'écoulent à son sommet. Le rayonnement solaire chauffe la paroi extérieure du tube, et, par convection avec les parois, les particules se réchauffent durant leur ascension.

Du fait du fort rapport d'aspect du tube (H/D) et de la densité des particules, l'écoulement gaz-particules résultant est instable. Ainsi, un débit d'air – dit secondaire – est injecté à la base du tube afin de stabiliser et de contrôler le débit de particules ainsi que le régime d'écoulement. L'écoulement de particules est donc forcé par l'action conjointe d'un gradient de pression et d'un débit d'air, donnant lieu à un écoulement dense de particules.

Dans le cadre de la thèse de R. Gueguen, nous nous sommes attachés à caractériser les régimes d'écoulement apparaissant dans le récepteur ainsi que les transitions entre ces régimes. En effet, chaque régime est associé à un niveau d'agitation et à une concentration en particules qui impactent directement l'efficacité des transferts thermiques, et donc les performances du récepteur. Pour ce faire, nous avons d'abord caractérisé l'hydrodynamique du lit à température ambiante, puis évalué l'effet des transferts thermiques couplés sur ces régimes.

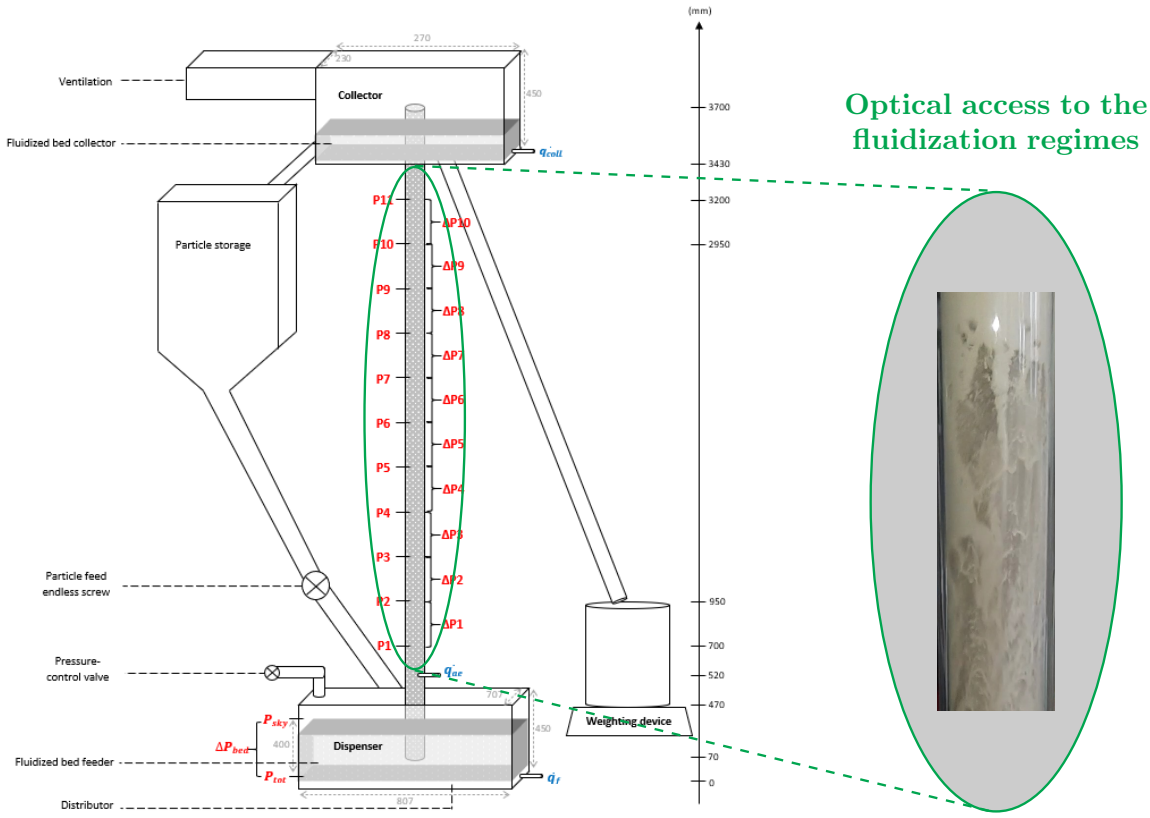

FIGURE 3.2 – Représentation schématique du banc expérimental RALF et de ses dimensions. Il permet l'étude, à température ambiante, des régimes d'écoulement gaz-particules apparaissant dans les récepteurs solaires à lit fluidisé en circulation ascendante.

3.2 Etude de l'hydrodynamique à température ambiante

3.2.1 Description du banc RALF et de son instrumentation

Le banc expérimental RALF, schématisé sur la Fig. 3.2, est conçu pour l'étude, à température ambiante, du comportement d'une suspension gaz-particules dans un récepteur solaire à circulation ascendante. Le dispositif est principalement composé d'un lit fluidisé nourrice (aussi appelé *dispenser*), d'un tube vertical en verre transparent (représentant le récepteur) et d'un collecteur.

Le dispenser est un réservoir parallélépipédique ($0{,}707 \times 0{,}807 \times 0{,}45\,\mathrm{m}^3$) dans lequel les particules d'olivine sont fluidisées à l'aide d'un débit d'air dont la vitesse équivaut à $\sim 2\,U_{mf}$. Ce débit traverse un distributeur métallique poreux assurant une répartition homogène de l'air et maintenant un régime de bullage établi. Un tube en verre ($D_{in} = 45\,\mathrm{mm}$, $H = 3{,}63\,\mathrm{m}$) est immergé dans le dispenser et relie ce dernier au collecteur situé en partie haute.

L'écoulement des particules est piloté par la pression totale dans le dispenser (P_{tot}), qui dépend de la pression du ciel gazeux (P_{sky}) et de la composante hydrostatique du lit (ΔP_{disp}). La pression dans le ciel gazeux est contrôlée par une vanne de fuite, tandis qu'une vanne rotative assure l'alimentation en particules du dispenser (débit maximal : $2150\,\mathrm{kg{\cdot}h^{-1}}$).

L'aération secondaire, injectée à 52 cm au-dessus du distributeur poreux, stabilise la suspen-

sion gaz-particules et permet d'ajuster le régime de fluidisation. La hauteur de cette injection secondaire est prise comme référence pour la suite.

Le tube est équipé de 11 prises de pression régulièrement espacées tous les 25 cm, la première étant située à 18 cm au-dessus de l'aération secondaire. Deux types de capteurs y sont connectés : (i) des capteurs de pression relative (réponse rapide : 5 ms, précision : 3 mbar), permettant une analyse dynamique ; (ii) des capteurs de pression différentielle (réponse lente : 270 ms, précision : 0,05 mbar), permettant une mesure précise de la fraction volumique de particules.

Des capteurs similaires sont placés dans le dispenser pour mesurer P_{tot} et ΔP_{disp}.

3.2.2 Analyses des résultats

L'essentiel des résultats issus de cette étude est détaillé dans la publication introduite en page 49 de ce chapitre. Quelques résultats principaux sont cependant présentés dans cette section.

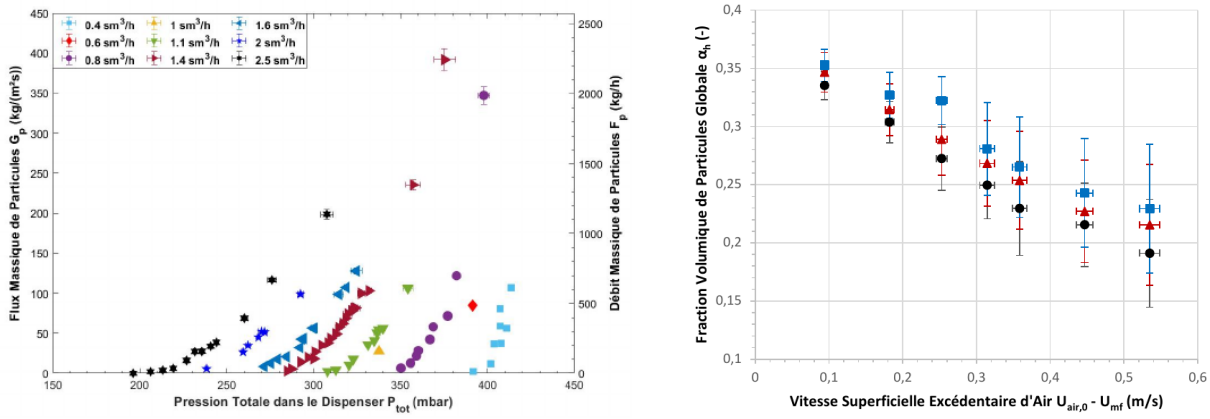

(a) (b)

FIGURE 3.3 – (a) Flux massique de particules en fonction de la pression totale dans le dispenser. Chaque couple marqueur/couleur correspond à un débit d'aération donné, précisé dans la légende. (b) Fraction volumique globale de particule dans le tube en fonction de la vitesse superficielle excédentaire d'air à l'aération. La fraction volumique globale est calculée comme la moyenne des fractions volumiques locales sur toute la hauteur du tube. Le débit d'aération q_{ae} est défini comme le produit de la section de la buse d'aération S_{ae} et de la vitesse d'air à l'aération $U_{\text{air},0}$. Chaque couleur correspond à un débit massique surfacique de particules G_p : • $G_p = 0$, $H_{\text{lit}} = 2\,\text{m}$; ▲ $G_p = 50\,\text{kg}\cdot\text{m}^{-2}\cdot\text{s}^{-1}$; ■ $G_p = 100\,\text{kg}\cdot\text{m}^{-2}\cdot\text{s}^{-1}$.

Les campagnes expérimentales menées ont permis d'identifier l'influence des deux paramètres de contrôle que sont la pression totale dans le dispenser et le débit d'aération. La pressurisation du dispenser permet de faire monter les particules dans le tube récepteur. Passée une pression seuil – qui dépend du débit d'aération secondaire, comme le montre la Fig. 3.3a – le débit massique de particules augmente avec cette pression. Cependant, il est à noter qu'un écoulement stable dans le récepteur est impossible en l'absence d'aération secondaire. La Fig. 3.3b montre également que, circulation ou non, la fraction volumique de particules dépend fortement du débit d'aération. En effet, comme on pouvait s'y attendre, plus la vitesse de l'air augmente, plus la fraction volumique de particules diminue.

L'analyse dynamique des signaux de pression et de leurs fluctuations a permis l'identification

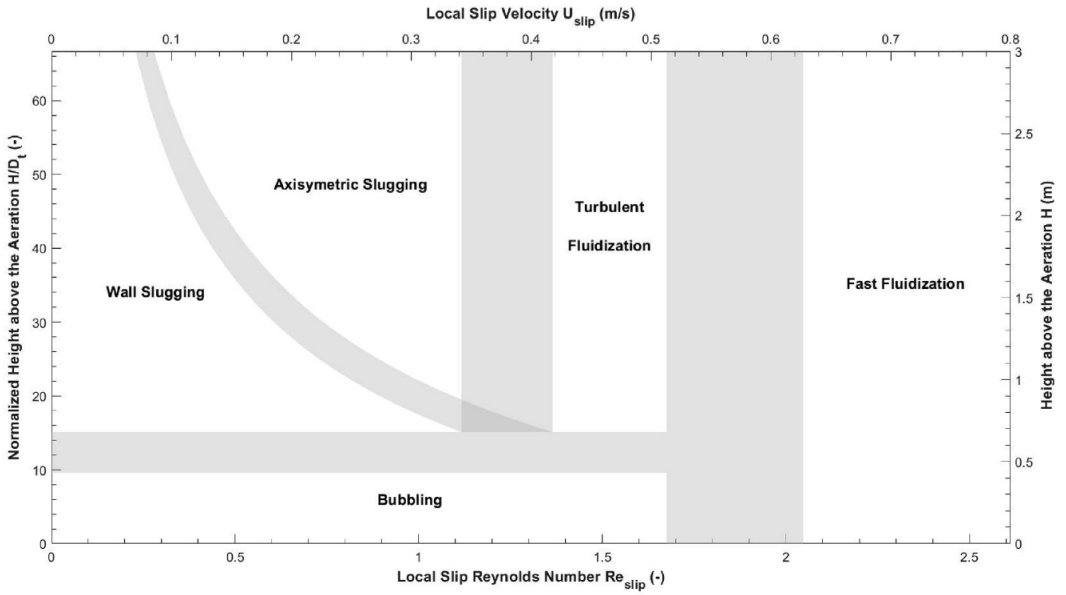

FIGURE 3.4 – Diagramme simplifié des régimes de fluidisation, représenté en termes de nombres adimensionnels. Les zones de transition entre les régimes sont identifiées par des aires grisées. Ce diagramme a été établi sur la base de 1167 points expérimentaux collectés lors de 170 essais différents.

des régimes d'écoulement pour les 170 expériences réalisées. Ceux-ci sont représentés sur la Fig. 3.4 en fonction de la hauteur et du nombre de Reynolds de glissement – relié au débit d'air secondaire. Les transitions de régimes sont principalement pilotées par la vitesse de glissement. Le régime de bullage, qui peut apparaître en partie basse du tube, disparaît au-delà d'un $Re_{\text{slip}} \sim 1{,}7$. En deçà de ce seuil, deux ou trois régimes cohabitent généralement sur la hauteur du tube. Au-delà, le régime de *fast fluidization* colonise l'ensemble du tube. Chaque régime se caractérise par une concentration en particules et un niveau d'agitation propres. Ces deux propriétés ont un impact direct sur les capacités de transfert thermique de la suspension, point capital pour la conception d'un récepteur solaire performant. Grâce au dispositif RALFI, nous avons ainsi investigué les capacités d'échange thermique associées à chacun des régimes.

3.3 Caractérisation d'un récepteur solaire à lit fluidisé en fonctionnement réel

3.3.1 Le banc RALFI et son instrumentation

Le banc expérimental RALFI est une évolution de RALF, conçu pour étudier le comportement d'une suspension gaz-particules en conditions thermiques représentatives d'un récepteur solaire. Contrairement à RALF, qui fonctionne à température ambiante, 1 m du tube récepteur de RALFI est chauffé par irradiation solaire concentrée, au foyer du grand four solaire d'Odeillo.

Le dispositif repose sur un tube en Inconel 601, de diamètre interne 48 mm, plongé dans un lit fluidisé d'olivine et irradié sur une hauteur de 1 m. Pour maximiser l'absorption du rayonnement,

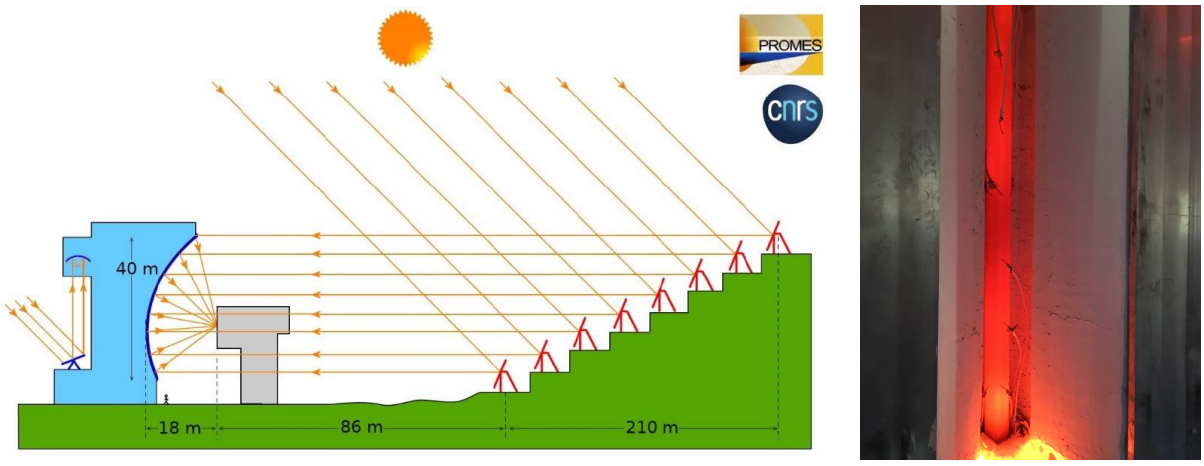

(a) (b)

FIGURE 3.5 – (a) Schéma de principe du four solaire d'Odeillo montrant la technique de concentration du rayonnement solaire. Le dispositif RALFI est positionné à son foyer durant les campagnes expérimentales. (b) Tube récepteur chauffé dans sa cavité après une expérience.

le tube récepteur est peint avec une peinture haute température (Pyromark). Une cavité isolante, revêtue d'oxyde de magnésium réfléchissant, limite les pertes thermiques par rayonnement (voir Fig. 3.5b). Comme dans RALF, l'écoulement des particules est contrôlé par la pression imposée dans le dispenser et stabilisé par une injection d'air secondaire. Un réservoir monté sur balance permet de mesurer le débit massique des particules sortantes. RALFI est donc représentatif d'un récepteur solaire industriel, et son instrumentation, décrite ci-après, permet l'étude approfondie de ses performances thermiques.

L'instrumentation de RALFI se distingue de celle de RALF par la mesure détaillée des effets thermiques sur le tube et les particules. Comme sur RALF, onze prises de pression sont réparties dans le système : deux dans le dispenser pour mesurer la pression totale et la composante hydrodynamique du lit, et neuf le long du tube pour suivre la fraction volumique des particules et identifier le régime d'écoulement à l'aide de capteurs de pression relative et différentielle. En complément, 59 thermocouples (type K) sont installés pour surveiller la température du mélange diphasique et du récepteur. Trois thermocouples mesurent la température moyenne des particules dans le dispenser, tandis que 24 sont répartis dans le tube pour suivre la température locale du lit fluidisé. De plus, 32 thermocouples sont soudés sur la paroi externe du récepteur afin d'analyser la distribution thermique sous irradiation solaire. Trois sections du tube – en entrée, au milieu et en sortie de la zone irradiée – sont finement instrumentées pour permettre une cartographie détaillée des transferts thermiques dans cette zone.

Enfin, l'expérience est placée au foyer du grand four solaire de 1 MW du CNRS à Odeillo. Comme le montre la Fig. 3.5a, l'irradiation solaire est concentrée par un double système de réflexion : d'abord via un champ d'héliostats (miroirs plans), puis par une parabole focalisante. Afin d'assurer une distribution homogène du flux solaire sur le tube récepteur, le suivi des héliostats a été ajusté et calibré. Les flux obtenus varient entre un facteur de concentration de 220 et 600 selon la configuration, avec des inhomogénéités plus marquées pour les flux les plus élevés. Une distribution spécifique a été testée pour analyser la sensibilité du système à de fortes

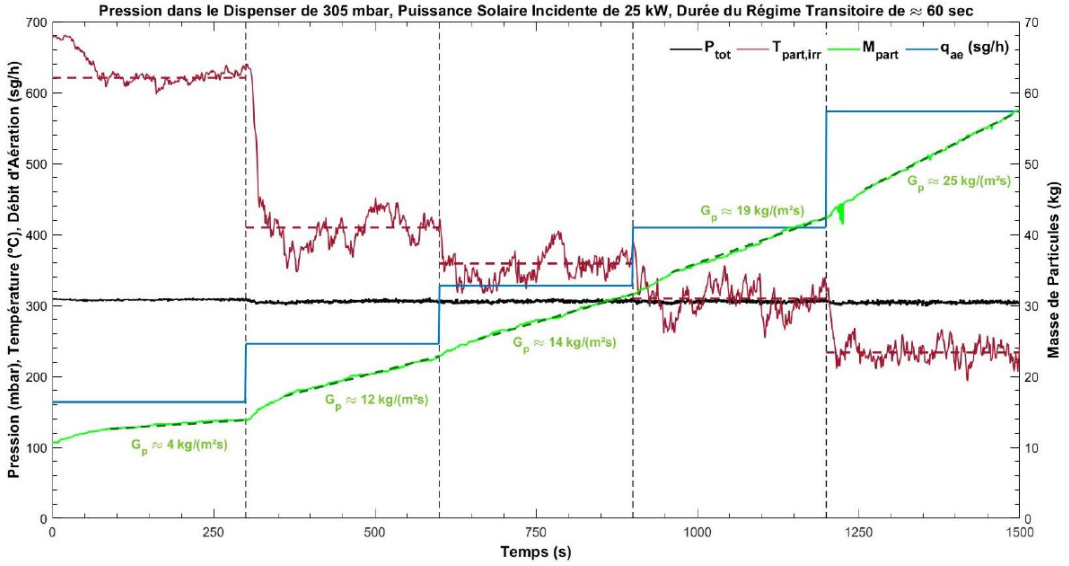

FIGURE 3.6 – Réponse dynamique du récepteur à une variation du débit d'aération (en bleu), pour une pression totale dans le dispenser (en noir) et une puissance solaire incidente constantes. L'évolution de la masse de particules et de la température moyenne dans la zone irradiée est représentée respectivement en vert et en rouge.

variations de flux le long du tube. Pour ce cas particulier, la stratégie de pointage est telle que le facteur de concentration varie de 255 à 830 sur la hauteur du tube.

3.3.2 Fonctionnement dynamique d'un récepteur solaire sous irradiation

Afin d'évaluer la pilotabilité d'un récepteur solaire reposant sur cette technologie, la réponse dynamique du système a été étudiée face à des variations de ses paramètres de contrôle, à savoir : la puissance solaire incidente, la pression totale dans le dispenser et le débit d'aération. Le premier paramètre n'a pas été exploré dynamiquement pour des raisons de sécurité. En effet ceci aurait requis la modification brusque de la stratégie de pointage des héliostats ce qui peut entrainer l'apparition de point chaud sur le récepteur. Nous présentons ici les enseignements issus de la réponse dynamique du récepteur à des variations de débit d'aération et de pression totale dans le dispenser.

L'effet de la variation de pression a été étudié avec un débit d'aération constant et une puissance solaire incidente donnée. Une fermeture partielle de la vanne entraîne une augmentation de la pression totale, ce qui modifie le flux massique des particules et leur température. L'augmentation de pression accroît le débit de particules, entraînant une hausse de la puissance absorbée et une baisse de leur température. Une variation modérée de pression (+10 %) induit de fortes variations du flux massique (+90 %) et de la température (−54 %). La durée du régime transitoire, définie comme le temps nécessaire pour atteindre 95 % de la variation totale de pression, est d'environ 70 s. Ces résultats suggèrent que la pression peut constituer un levier efficace pour le contrôle d'un récepteur solaire. Cependant, l'amplitude importante des variations induites pourrait compliquer la pilotabilité du système.

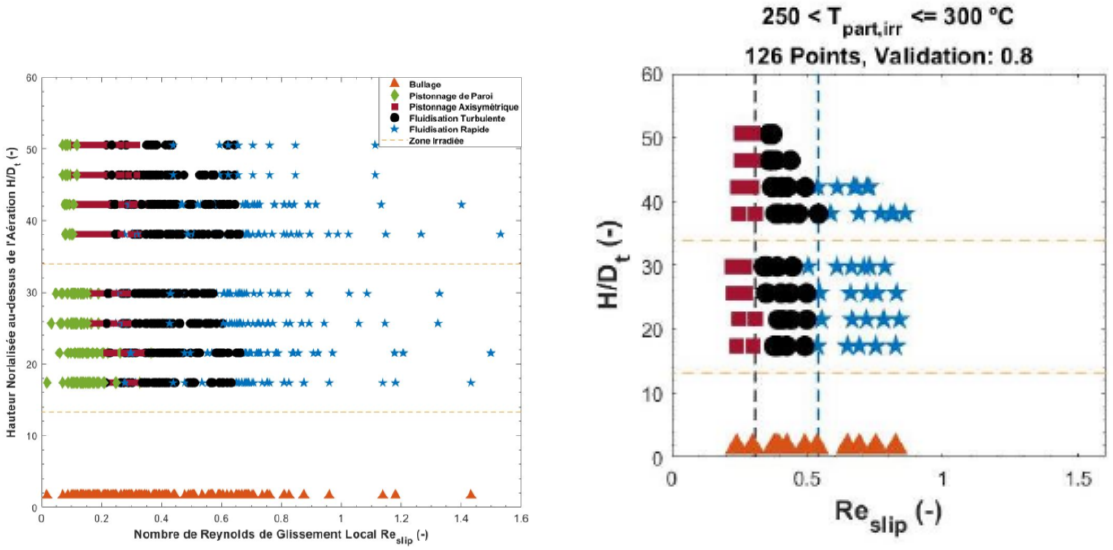

(a) (b)

FIGURE 3.7 – Représentation des régimes de fluidisation identifiés sur les 187 essais effectués sous irradiation solaire. Les régimes sont déterminés par post-traitement des signaux de pression dynamique recueillis le long de la hauteur du tube. Les tirets jaunes délimitent la zone irradiée. Les régimes sont représentés par les marqueurs suivants : ▲ bullage, ♦ pistonnage de paroi, ■ pistonnage axisymétrique, ● fluidisation turbulente, ★ fluidisation rapide. (a) Représentation de l'ensemble des essais dans le plan $(Re_{\text{slip}}, H/D_t)$; (c) Représentation conditionnelle en fonction de la température des particules dans la zone irradiée, $T_{\text{part,irr}}$. Sont représentés uniquement les essais pour lesquels $250°\text{C} < T_{\text{part,irr}} \leq 300°\text{C}$.

La Fig. 3.6 montre la réponse dynamique du système à une variation du débit d'aération, pour une pression constante de 305 mbar et une puissance solaire incidente de 25 kW. L'essai débute en régime stationnaire, puis, à $t = 300$ s, le débit d'aération est progressivement augmenté. Chaque augmentation réduit la fraction volumique de particules, ce qui dilue la suspension et accroît soit la hauteur du lit fluidisé, soit le débit massique en circulation. À puissance solaire incidente constante, cela induit une baisse de la température du lit dans la zone irradiée.

Toutefois, nos travaux ont également montré qu'à q_{ae} et G_p fixés, une diminution de $T_{\text{part,irr}}$ entraîne une augmentation de la fraction volumique. Ces deux mécanismes, aux effets opposés, induisent des oscillations transitoires avant stabilisation. Ce phénomène d'autorégulation dure environ 60 s par séquence. La Fig. 3.6 montre qu'une augmentation de 33 % du débit d'aération entraîne une hausse de 16 % du flux massique et une baisse de 12 % de la température. Ainsi, le débit d'aération apparaît comme un levier efficace pour ajuster finement le débit de solide en circulation.

Pour plus de détails sur cette analyse dynamique, le lecteur est invité à consulter la publication fournie page 63 de ce chapitre.

3.3.3 Régime de fluidisation et performances thermiques

Les régimes de fluidisation sont représentés sur un diagramme dans le plan $(Re_{\text{slip}}, H/D_t)$, similaire à celui réalisé à température ambiante sur la Fig. 3.7a. Toutefois, une superposition des régimes rend difficile l'identification des transitions, car, contrairement aux essais à température ambiante, Re_{slip} dépend ici de deux paramètres : le débit d'aération et la température de fonctionnement. En effet, la densité et la viscosité de l'air varient fortement entre 150°C et 700°C, ce qui nécessiterait une représentation en trois dimensions pour observer l'impact de la température sur l'hydrodynamique de la suspension de particules.

Pour mieux comprendre cet impact tout en conservant une représentation 2D, les points expérimentaux ont été regroupés par gammes de température de 50°C, de 150°C à 700°C. Un diagramme des régimes a été tracé pour chaque gamme dans le plan $(Re_{\text{slip}}, H/D_t)$. Pour ce faire, la température $T_{\text{part,irr}}$ est définie comme la température moyenne des particules au centre du tube récepteur, à mi-hauteur de la zone irradiée. Cette définition permet d'établir une température de référence s'affranchissant de la variation de température avec la hauteur – celle-ci peut atteindre 300 à 400°C pour certains essais. Une illustration des régimes de fluidisation, pour la plage 250°C $< T_{\text{part,irr}} \leq$ 300°C, est représentée sur la Fig. 3.7b. Cela permet de regrouper les points par régimes de fluidisation et de limiter les superpositions. Les autres représentations testées n'ont pas permis d'améliorer l'interprétation.

Comme à température ambiante, les régimes de bullage, de pistonnage, de fluidisation turbulente et de fluidisation rapide sont observés, chacun étant associé à une fraction volumique et à un niveau d'agitation distincts. Ces régimes correspondent à des gammes de Reynolds de glissement et de hauteur relative spécifiques. Les points sur les diagrammes sont conditionnés par la température moyenne des particules dans la zone irradiée, ce qui permet d'analyser l'impact combiné de la température et des propriétés de l'air (notamment la viscosité) sur les transitions entre régimes.

Une analyse détaillée des régimes et de leurs transitions est proposée dans [31]. Par souci de concision, nous nous limiterons ici à mettre en avant deux comportements remarquables. Premièrement, l'analyse de l'ensemble des cartes conditionnées en température montre que les valeurs de Re_{slip} pour lesquelles apparaissent les régimes de fluidisation turbulente et rapide décroissent toutes deux avec la température. Ces valeurs limites sont nettement inférieures à celles établies à température ambiante. Deuxièmement, le domaine de Re_{slip} dans lequel subsiste le régime de fluidisation turbulente se réduit fortement avec l'augmentation de la température.

Enfin, l'efficacité des transferts thermiques associés aux différents essais a été évaluée sur la base du calcul du coefficient d'échange thermique global $h_{\text{paroi,part}}$ et du coefficient de transfert thermique adimensionnel $H_{\text{paroi,part}}$ (correspondant à un nombre de *Stanton*), dont les expressions sont détaillées ci-dessous :

$$h_{\text{paroi,part}} = \frac{\phi_{\text{part}}}{S_{\text{ech}}\,\Delta T_{\text{paroi,part}}} = \frac{G_p\,S_t\,C_{p,\text{part}}\,\Delta T_{\text{part}}}{S_{\text{ech}}\,\Delta T_{\text{paroi,part}}} \tag{3.1}$$

$$H_{\text{paroi,part}} = \frac{h_{\text{paroi,part}}\,S_{\text{ech}}}{G_p\,S_t\,C_{p,\text{part}}} = \frac{\Delta T_{\text{part}}}{\Delta T_{\text{paroi,part}}} \tag{3.2}$$

où ϕ_{part} est la puissance absorbée par les particules, S_{ech} la demi-surface interne du tube, et $\Delta T_{\text{paroi,part}}$ l'écart de température entre la paroi et les particules, calculé comme un ΔT_{LM}

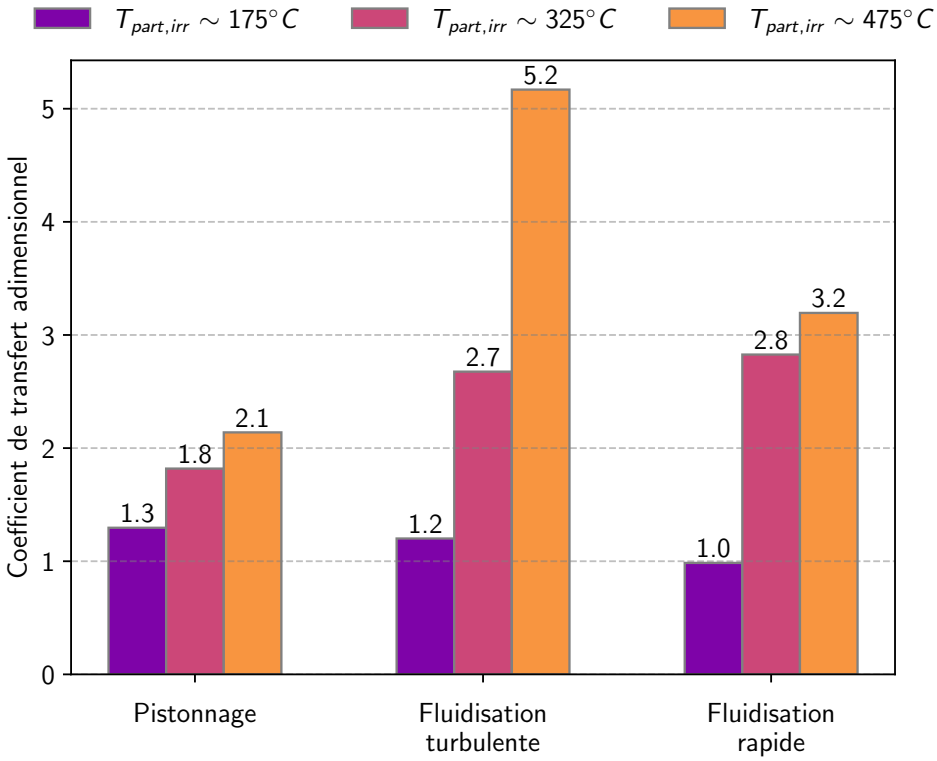

FIGURE 3.8 – Coefficient de transfert thermique adimensionnel $H_{\text{paroi,part}}$ en fonction des régimes d'écoulement et du niveau de température des particules dans la zone irradiée.

(moyenne logarithmique). La puissance thermique absorbée par les particules est évaluée comme le produit du débit massique surfacique G_p, de la section transverse du tube S_t, de la capacité thermique massique des particules $C_{p,\text{part}}$, et de l'élévation de température dans la zone irradiée $\Delta T_{\text{part}} = T^{\text{out}}_{\text{part}} - T_{\text{disp}}$.

RALFI étant pilotée en flux thermique imposé à la paroi externe du récepteur, et non en température, la température de paroi diminue lorsque G_p augmente. Cela complique notablement l'analyse des variations de $h_{\text{paroi,part}}$ en fonction de G_p pour différentes configurations de chauffe. Si le débit de particules est faible, la chaleur est mal évacuée, la paroi chauffe et les pertes vers l'ambiance augmentent. La puissance effectivement absorbée par les particules est alors réduite, de même que le coefficient d'échange thermique. On retiendra néanmoins que, dans la majorité des expériences, le coefficient d'échange global se situe entre 800 et 1200 $\text{W} \cdot \text{m}^{-2} \cdot \text{K}^{-1}$ pour des particules d'olivine de 70 μm de diamètre moyen. Afin de s'affranchir de la dépendance au débit G_p, le coefficient de transfert thermique adimensionnel $H_{\text{paroi,part}}$ a été calculé pour chaque essai. Ce coefficient, à un facteur de surface près (tenant compte de l'irradiation partielle du tube), est analogue à un nombre de Stanton (St). Il caractérise l'efficacité de l'échange de chaleur entre le lit fluidisé et la paroi, et permet d'évaluer l'importance relative de la convection par rapport à d'autres mécanismes de transfert (notamment le rayonnement). Grâce à la base de données expérimentale constituée, ce coefficient a été évalué pour les différents régimes de fluidisation et à divers niveaux de température. La Fig. 3.8 montre tout d'abord qu'indépendamment du régime de fluidisation, $H_{\text{paroi,part}}$ augmente avec la température. Cette tendance pourrait être

associée à une augmentation des transferts radiatifs entre la paroi et le lit à mesure que la température s'élève. De plus, il apparait que le régime de fluidisation turbulente favorise les échanges thermiques les plus efficaces à haute température. En effet, quels que soient le régime et le niveau de température, les coefficients $H_{\text{paroi,part}}$ plafonnent généralement autour de 3, alors que le régime de fluidisation turbulente atteint 5,2 lorsque $T_{\text{part,irr}} \sim 475°\text{C}$.

Ce régime de fluidisation est donc à privilégier pour évacuer efficacement la chaleur d'un récepteur solaire en fonctionnement.

3.4 Sélection d'articles en lien avec cet axe de recherche

Chemical Engineering Science 267 (2023) 118360

Contents lists available at ScienceDirect

Chemical Engineering Science

journal homepage: www.elsevier.com/locate/ces

Fluidization regimes of dense suspensions of Geldart group A fluidized particles in a high aspect ratio column

Ronny Gueguen [a], Guillaume Sahuquet [a], Samuel Mer [b], Adrien Toutant [b], Françoise Bataille [b], Gilles Flamant [a,*]

[a] Processes, Materials and Solar Energy Laboratory, PROMES-CNRS, 7 Rue du Four Solaire, 66120 Font-Romeu, France
[b] Processes, Materials and Solar Energy Laboratory, PROMES-CNRS, University of Perpignan (UPVD), Tecnosud, Rambla de la Thermodynamique, 66100 Perpignan, France

HIGHLIGHTS

- Particle-driven receiver involves fluidization in tubes with high aspect ratio.
- Fluidization regimes result from both overpressure and secondary air flow.
- The local slip velocity governs the fluidization regimes and their transitions.
- Regime transitions differ from the one previously observed in risers.

GRAPHICAL ABSTRACT

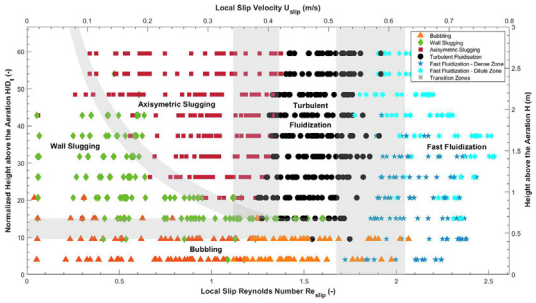

ARTICLE INFO

Article history:
Received 29 July 2022
Received in revised form 28 October 2022
Accepted 25 November 2022
Available online 28 November 2022

Keywords:
Tubular particle solar receiver
Particle-driven CSP
Fluidization regimes
Particle circulation
Fluidization diagram
Slip velocity

ABSTRACT

Fluidization regimes were studied in numerous papers with applications in risers in which gas velocity is the main driving force. The situation is different when a tube is immersed in a fluidized bed vessel in which a pressure is imposed to move the particle upward. The particle-in-tube solar receiver concept is based on this latter operation mode with the aim to heat particles at high temperature with concentrated solar energy. This study identifies the fluidization regimes in a pressure-driven system that includes a secondary aeration to control the air velocity in the tube. Bubbling, slugging, turbulent and fast fluidization regimes are determined thanks to temporal pressure signal processing methods and a regime map is plotted. The transition velocities are significantly lower than in classical risers. The local slip velocity is defined as the governing parameter of the flow structure and the variation of the local particle volume fraction is discussed.

1. Introduction

1.1. Particles as heat transfer medium

Concentrated solar technology can produce clean and dispatchable power and thus contribute solving the global climate change issue. Indeed, solar thermal energy offers the possibility to produce electricity on demand from an unlimited resource when coupled with a heat storage. In concentrated solar power plants, in particular for solar power towers, the solar radiation is focused thanks to a heliostat field toward a receiver located at the top of a tower, in which a heat transfer fluid is circulating. This heat transfer fluid can be stored and then used in the energy conversion process, or directly brought into a heat exchanger to heat a working fluid that powers a turbine.

Several heat transfer fluids are used in commercial concentrated solar plants depending on the desired temperatures and

* Corresponding author.
E-mail address: Gilles.Flamant@promes.cnrs.fr (G. Flamant).

https://doi.org/10.1016/j.ces.2022.118360
0009-2509/

Nomenclature

d_X	Diameter corresponding to the X % value on the cumulated particle size distribution (μm)
d_{SV}	Sauter diameter of the powder sample (μm)
d_V	Volume diameter of the powder sample (μm)
D_t	Internal diameter of the tube (m)
G_p	Particle mass flux ($kg.m^{-2}.s^{-1}$)
h_s	Transition height from bubbles to established slugs (m)
H_{bed}	Height of the suspension in the tube (m)
H_t	Height of the tube (m)
$\dot{m}_p$	Particle mass flow rate ($kg.s^{-1}$)
P_i	Relative pressure in the tube at the level of the i^{th} pressure socket (mbar)
P_{sky}	Freeboard pressure in the dispenser (mbar)
P_{tot}	Total relative pressure in the dispenser (mbar)
q_{ae}	Aeration flow rate ($m^3.h^{-1}$)
Re_{slip}	Particular Reynolds number relative to the slip velocity (–)
S_t	Internal section of the tube (m^2)
U_{air}	Superficial air velocity in the tube ($m.s^{-1}$)
U_k	Fast fluidization velocity ($m.s^{-1}$)
U_{mb}	Minimum bubbling velocity ($m.s^{-1}$)
U_{mf}	Minimum fluidization velocity ($m.s^{-1}$)
U_{slip}	Slip velocity between the air and the particle ($m.s^{-1}$)
U_t	Turbulent fluidization velocity ($m.s^{-1}$)
α_h	Overall particle volume fraction in the tube (–)
α_i	Local particle volume fraction in the tube (–)
α_{bulk}	Particle volume fraction of the fixed bed (–)
ΔH	Distance between two pressure sockets (m)
ΔP_{acc}	Pressure drop due to the particles acceleration (mbar)
ΔP_{bed}	Pressure drop through the fluidized bed in the dispenser (mbar)
ΔP_i	Differential pressure in the tube between two pressure sockets (mbar)
μ_{air}	Dynamic viscosity of the air ($kg.m^{-1}.s^{-1}$)
ρ_p	Bulk density of the particle sample ($kg.m^{-3}$)

the concentration technology (Benoit et al., 2016). In solar towers, the most commonly used heat transfer fluid is molten salt. The molten salt operation temperatures range between 220 and 565 °C to avoid solidification and decomposition, respectively. The lower limit involves a constant energy consumption to maintain the salt temperature above the melting point, while the upper limit is a security constraint linked to the nitrate salt decomposition (Zhang et al., 2017).

In order to increase the global efficiency of the power plant, several high-efficiency thermodynamic cycles are under development, such as combined or supercritical cycles (Dunham and Iverson, 2014). These cycles need high working temperature, above 650 °C, which thus requires the change of the heat transfer fluid. One of the possible options consists in using solid particles because they are suitable for operating as both heat transfer and storage media. This option eliminates high-pressure constraints, enables high working temperatures (of 1000 °C and even more) and leads to low-cost thermal energy storage (Jacob et al., 2016).

Three main technologies of solar receiver using particles are under development. In the falling particle and the centrifugal receivers, designed respectively by the Sandia National Laboratory (USA) and the German Aerospace Center (Germany), the particles are directly irradiated by the concentrated solar flux (Ho et al., 2017; Wu et al., 2014). The PROMES laboratory of the National Center for Scientific Research (CNRS, France) develops since 2010 with partners a concept of solar receiver based on the circulation of fluidized particles (Flamant et al., 2010). In this concept, named "particle-in-tube receiver" or "Upward Bubbling Fluidized Bed", the particles are fluidized in a vessel fluidized bed called "the dispenser". The vertical irradiated tubes are immersed in the fluidized bed, and an upward forced circulation is set up by controlling the overpressure in the dispenser. The particles are thus indirectly heated by the tube's walls, which is similar to the molten salt receiver technology. A secondary air flow rate called "aeration" is injected at the bottom of the tubes to stabilize the particle flow. Several experimental and numerical studies have been carried out with the particle-in-tube solar receiver under the European projects CSP2 and Next-CSP (https://cordis.europa.eu/project/id/282932; Next-CSP, 2020). Particles that belong to the group A of the Geldart's classification have been selected (Geldart, 1973). Outlet particles temperatures and wall-to-particles heat transfer coefficients above respectively 700 °C and 1000 W/m^2K have been determined experimentally and numerically, largely proving the interest of the concept (Flamant et al., 2013; Benoit et al., 2015; Perez-Lopez et al., 2016; Boissiere et al., 2015; Le Gal et al., 2019; Ansart et al., 2017; Benoit et al., 2018; Kong et al., 2017; Sabatier et al., 2020; Deng et al., 2021). However, in such a gas-particle flow, several fluidization regimes can occur in the receiver tubes depending on the operating conditions. The regimes result in various particle volume fraction and particle mixing, thus various heat transfer rates (Kunii and Levenspiel, 1991). Therefore, it is necessary to establish a link between the operating conditions and the fluidization regimes in order to improve the performance of the solar receiver. Nonetheless, the suspension behavior was not thoroughly analyzed in the earlier cited studies because of their insufficient number of pressure probes.

1.2. Fluidization regimes in classical columns

In classical fluidization columns, the air injection at the bottom of the column enables the particles fluidization. Several fluidization regimes occur depending on the air velocity, the column geometry and the particles properties (Kunii and Levenspiel, 1991).

The minimum fluidization velocity is the gas velocity that delimitates the transition between the fixed bed and the fluidized bed, where the particles acquire the properties of a quasi-fluid (Kunii and Levenspiel, 1991). Increasing the gas velocity for group A particles of the Geldart's classification results in a dense and homogenous fluidized bed, without any bubble until the minimum bubbling velocity, at which the first bubble erupts at the bed surface (Abrahamsen and Geldart, 1980). Bubbles are then coalescing with the height until they reach a maximum bubble size (Geldart, 1973). Either at higher gas velocity or if the bubble size reaches approximately 60 % of the column diameter, bubbles are merging into slugs (Kong et al., 2017). The consequence of the slugging regime – large and slow bubbles – is the decrease of both the mean particle volume fraction and the particle mixing. In wall-heating conditions, it is associated with a decrease of the wall-to-fluidized bed heat transfer coefficient (Deng et al., 2021).

Increasing the gas velocity results in the appearance of the turbulent fluidization when the bubble coalescence becomes compensated by their scission (Yerushalmi and Cankurt, 1979). Disordered

gas structures – vortices – appear in the bed, resulting in a less defined upper surface of the fluidized bed. In this regime, the gas-particle suspension is still relatively dense and the particle mixing is vigorous, thus leading to a high heat transfer rate (Bi et al., 2000).

The fast fluidization regime occurs when the gas velocity reaches the particle terminal velocity (Grace et al., 2020). In this regime, the particles are entrained outside of the column as clusters (Grace et al., 2020). The commonly used Circulating Fluidized Bed – involving risers – are generally working in the fast fluidization regime that results in strong particle mixing but low mean particle volume fraction.

Fluidization regimes in risers have been widely studied in the literature, and several attempts to establish regimes diagrams have been published (Yerushalmi and Cankurt, 1979; Grace et al., 2020; Rabinovich and Kalman, 2011; Geldart and Chap, 1986; Bi and Grace, 1995). Nonetheless, the establishment of the particle circulation differs in the fluidized particle-in-tube solar receiver concept studied in this paper. Actually, in the latter, the upward flow of the gas-particle suspension is the result of the combination of both the air velocity and the overpressure in the dispenser, while in risers, it is commonly generated by applying a high gas velocity at the bottom of the tube (Hafizur Rahman et al., 2020; Breault et al., 2020). Moreover, riser diameters are larger than solar receiver tubes and their tube aspect ratios are smaller (typically around 10) (Stefanova et al., 2011). The original characteristics of fluidized particle-in-tube solar receiver concept offer the opportunity to maintain a dense suspension, i.e. a relatively high particle volume fraction, and consequently to reach a high wall-to-bed heat transfer rate.

1.3. Objectives

In the previous cited studies about the fluidized particle-in-tube receiver (Flamant et al., 2013; Benoit et al., 2015; Perez-Lopez et al., 2016; Boissiere et al., 2015; Le Gal et al., 2019; Ansart et al., 2017; Benoit et al., 2018; Kong et al., 2017; Sabatier et al., 2020; Deng et al., 2021), the superficial air velocities in the tube were limited to a maximum of 0.30 m/s, in order to reduce the formation of slugs. A concept of "Bubble Rupture Promoter (BRP)" within the tube has been tested, aiming to prevent slugs' formation (Deng et al., 2021). The main idea behind this solution is creating turbulent fluidization inside the space limited by the BRP, but such inserts integrated in an industrial-scale solar receiver are expected to be expensive regarding the number of tubes and their heights (Gueguen et al., 2020). This approach may be applied in the bare tubes (without insert) of the fluidized particle-in-tube concept by increasing the air velocity, to reach the conditions of the turbulent fluidization regime (Grace et al., 2020).

In a previous work, tests in specific conditions – without particle circulation, and with particle mass fluxes of 50 and 100 kg/(m^2.s) – have been precisely analyzed, proving that the fluidization regimes encountered in the tube are similar to those encountered in risers (Gueguen et al., 2021). The turbulent and fast fluidization regimes have been observed thanks to the increase of the air velocity up to 0.54 m/s. Furthermore, it shown that the identification of the regimes is possible using a non-intrusive method, i.e. by analyzing the pressure evolution with different signal processing methods. More extensive data are presented in this paper.

The present research is an original experimental contribution to the analysis of fluidization regimes inside a tube characterized by a high aspect ratio (height over diameter >70), at ambient temperature. It extends our earlier study (Gueguen et al., 2021) – where classical fluidization regimes have been observed – in establishing a precise fluidization regime diagram while specifying their transitions velocities. The experimental set-up is first presented (particles used, description of the cold rig and presentation of the pressure signals processing methods), followed by the evolution of the particle flow characteristics – particle flow rate, particle volume fraction and fluidization regime – as functions of the operating parameters. It then leads to the establishment of a fluidization regimes diagram accounting for all test results. Finally, a discussion on the regime's detection criteria is proposed.

2. Experimental set-up

2.1. Particles

Olivine particles have been selected as heat transfer medium in the framework of the Next CSP European project because they offer attractive thermomechanical, health and cost characteristics (Next-CSP, 2020; Kang et al., 2019). The fluidization properties of the olivine particles are presented in Table 1. They have been experimentally measured and more detailed in (Gueguen et al., 2021).

The various diameters that characterize the particle size distribution have been determined by laser diffraction, using a Malvern Mastersizer 3000 granulometer. The Sauter mean diameter d_{SV} is estimated at 61 μm, slightly lower than the median diameter d_{50} because of fine particles in the sample (Geldart, 1986; Dodds and Baluais, 1993). Combined with the bulk density ρ_p of the powders, it confirms that it belongs to the group A of the Geldart classification (Geldart, 1973).

The particle volume fraction for the packed bed, α_{bulk}, was estimated at 0.48 by weighing a known particle volume. The minimum velocities of the various fluidization regimes have been experimentally measured in a 0.09 m I.D. (Internal Diameter) fluidization column, using the classic pressure drop versus the air velocity method. The minimum fluidization velocity, U_{mf}, was determined at the intersection of the curves relative to the fixed and fluidized beds, at decreasing air velocity (Kunii and Levenspiel, 1991). The minimum bubbling velocity, U_{mb}, was noticed when the first bubble erupts at the bed surface. It was identified in the pressure drop versus air velocity evolution by a brusque decrease (Abrahamsen and Geldart, 1980). Experimental values of U_{mf} and U_{mb} are in good agreement with the correlations generally used for group A particles (Grace et al., 2020; Wu and Baeyens, 1991).

At higher air velocities, the turbulent fluidization regime (U_t) is related to the maximum of the pressure fluctuations (Bi et al., 2000). In the scientific literature, it may be reported as the chocking velocity. But as discussed in (Bi et al., 1993), several chocking velocities have been introduced with different definitions. To avoid any confusion, the limit of the turbulent fluidization regime is named U_t in the present paper. The fast fluidization regime is noticed when the particles are entrained outside of the column. The bed is emptying, and it is identified by a permanent decrease of the pressure drop. The corresponding velocity is the particle terminal velocity, named U_k. The latter is characterized by a strong decrease of the pressure drop in a column without particle circulation (Bi et al., 2000; Rabinovich and Kalman, 2011).

2.2. Cold mock-Up description

A schematic description of the one-tube mock-up and its instrumentation is presented in Fig. 1. The olivine particles are fluidized in a 0.57 m^2 vessel, called the "dispenser", thanks to a constant air flow rate of 16.5 sm^3/h through a sintered porous bronze plate distributor. It corresponds to a superficial air velocity of 0.97 cm/s, i.e. 1.7 times the minimum bubbling velocity of the particles. A glass tube of 3.63 m total height and 45 mm internal diameter (D_t) –

Table 1
Thermal, physical and fluidization properties of the olivine sample.

Thermal and Physical Properties							Fluidization Threshold Air Velocities			
d_{10}(μm)	d_{50}(μm)	d_{90}(μm)	d_{SV}(μm)	d_V(μm)	ρ_p(kg/m^3)	α_{bulk}	Minimum of Fluidization, U_{mf} (cm/s)	Minimum of Bubbling, U_{mb} (cm/s)	Incipient Turbulent Fluidization, U_t (m/s)	Incipient Fast Fluidization, U_k (m/s)
39	70	124	61	81	3300	0.48	0.42	0.57	0.40	0.49

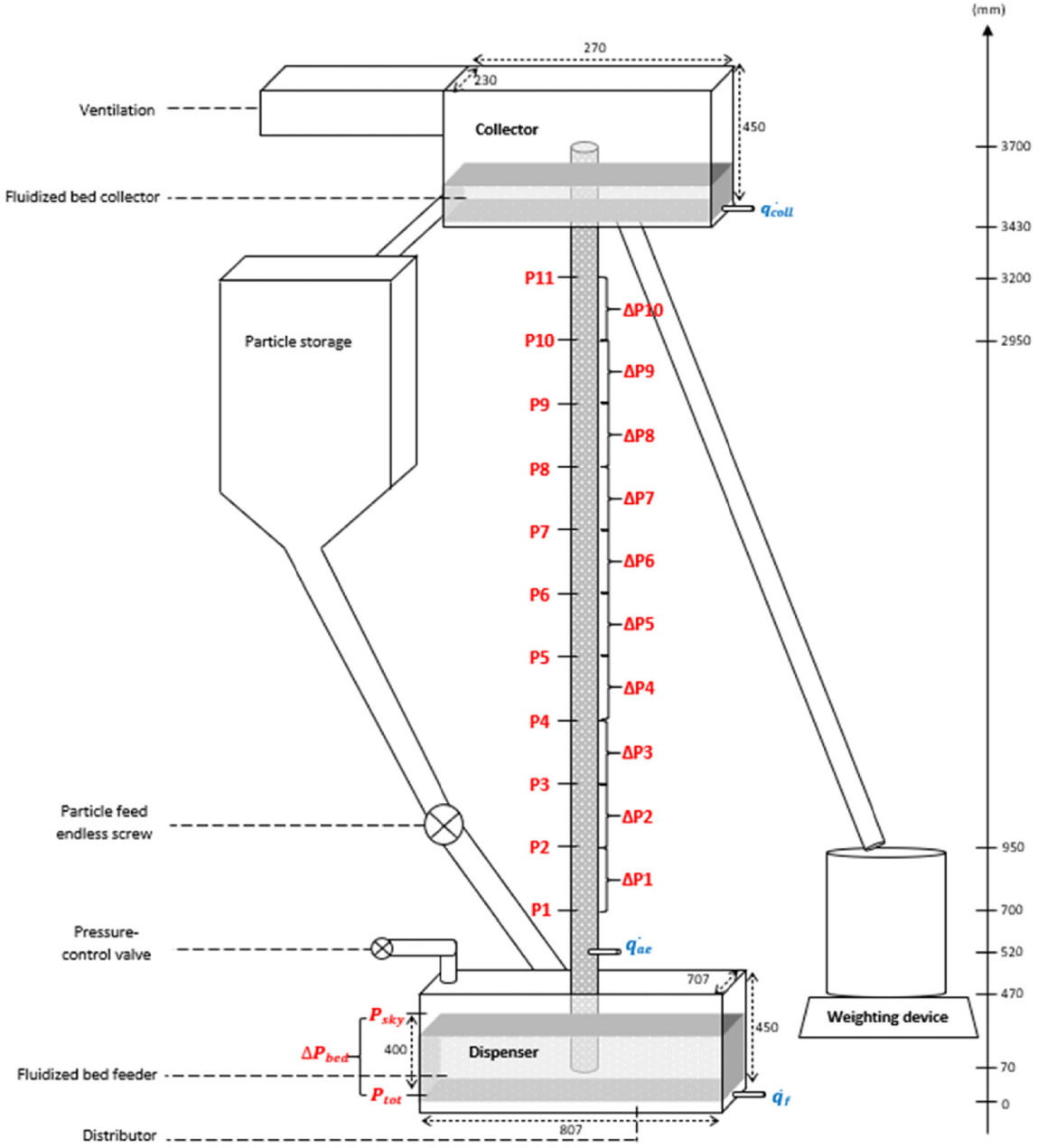

Fig. 1. Schematic description of the mock-up and its instrumentation (Gueguen et al., 2021).

i.e. an internal section S_t of 1.6 × 10^{-3} m^2 – is plunged in the fluidized bed up to 7 cm above the distributor. The upper part of the tube ends in a collector at atmospheric pressure in which particles are also fluidized. A secondary airflow, called "aeration", is injected at 0.45 m above the tube inlet at an airflow rate $\dot{q}_{ae}$ through a 1.5 mm I.D. nozzle to stabilize the suspension (Boissiere et al., 2015). The aeration is also used to control the fluidization regimes. The position of the nozzle is considered as the reference height for the rest of the study.

A leak valve is implemented at the top of the dispenser to control the freeboard pressure, P_{sky}. Closing the valve results in an increase of the pressure, leading to the gas-particle suspension flowing upward in the tube. The difference between the pressure in the dispenser, $P_{tot} = P_{sky} + \Delta P_{bed}$, and the atmospheric pressure,

is the driving force of the system, with ΔP_{bed} the pressure drop through the fluidized bed.

When the suspension reaches the collector, the particles flow outside of the tube in a tank placed on a weighing scale. The data are recorded at a frequency of 1 Hz with a precision of 0.01 kg, and the particle mass flow rate $\dot{m}_p$ is calculated by linear regression of the particles flowing in the tank. As a particle flow leads to a decrease of the amount of particles in the dispenser (controlled by the pressure drop ΔP_{bed}), the dispenser is fed from a storage tank thanks to a rotary valve to keep the pressure in the dispenser approximately constant during a test.

Eleven pressure sockets are implemented along the tube height each 0.25 m, the first one being located at 0.18 m above the aeration injector. They are connected to relative and differential pressure sensors as illustrated in Fig. 1, themselves connected to an acquisition system. The relative sensors (Siemens brand, model 7MF1641) having a small response time (5 ms) and an accuracy of 3 mbar, they are used for the analysis of flow dynamics with an acquisition frequency of 20 Hz. The differential sensors (Rosemont brand, model 2051C) have a long response time but high accuracy (0.05 mbar error), hence they are used to measure the particle volume fraction with high precision, with an acquisition frequency of 4 Hz. In order to prevent any particle entering inside the sensors, the sockets are equipped with sintered porous plates.

The data are recorded with acquisitions systems (National Instruments USB-6218 and Graphtec Midi Logger GL840) that fit the experimental requirements, connected to the Labview software. The pressure signals are analyzed thanks to several methods presented in the following section.

2.3. Identification and characteristics of the fluidization regimes

Several methods have been developed in the literature to identify and characterize the fluidization regimes, for example using acoustic measurement (Li et al., 2011), or thanks to pressure signal analyses (Stefanova et al., 2020; Chen et al., 2015; Vaidheeswaran et al., 2022; van der Schaaf et al., 2002; Johnsson et al., 2000; Fan et al., 1983). The latter are often used since it is a non-invasive method that enables relevant results even at elevated temperature. Then, as explained in the Introduction section, an earlier work shown that identifying the fluidization regimes in this concept of receiver is possible by using and combining temporal pressure signals processing methods (Gueguen et al., 2021). Firstly, the coherence analysis was used, in the frequency domain (van der Schaaf et al., 2002). The shape of the spectra, and both the frequencies and the magnitudes of the dominant peaks are characteristics of the regimes. Secondly, the cross-correlation function between two pressure signals was calculated, in the time domain (Johnsson et al., 2000). Here, both the shape of the function and the value of the maximum are relevant, the latter being related to the upward velocity of the perturbation (bubble, slug, cluster) (Fan et al., 1983). Thirdly, the relative pressure fluctuations and the shape of the particle fraction versus height trends were also pertinent indicators of the fluidization regime (Gueguen et al., 2021). The observed fluidization regimes and their characteristics are summarized below.

Classically, the acquisition times are of the order of the hour for pressure signals analyses in fluidized beds. Actually, most of the studies in the scientific literature is related to works without particle circulation, or in closed loops. The signals can be hence recorded at high acquisition frequencies to divide them into a high number of groups and to average the associated spectra for smoothing the data (van der Schaaf et al., 2002; Johnsson et al., 2000). In the present study, the acquisition time is limited during experiments in the particle circulation mode due to the capacity of the storage tank, because the system works in open loop. A high acquisition frequency would just lead to considerable noise in the spectra. The identification of the fluidization regimes is nonetheless possible by combining the different analysis methods, with pressure measurements recorded at 10 Hz for 205 s, to divide the signals in 4 groups of 1024 points each (Gueguen et al., 2021).

The exploding bubbling regime in the dispenser and the single bubbling regime identified at the bottom of the tube present the same characteristics. At low air velocities, but above the minimum bubbling velocity, these regimes are characterized by small bubbles at relatively high frequencies, with several peaks in the distributions at frequencies larger than 1 Hz and with very low magnitudes (van der Schaaf et al., 2002). As bubbles cause small pressure fluctuations, they are not detectable with the cross-correlation. The bubbles are coalescing with the tube height, until they are impacted by the walls and merge into slugs (Kong et al., 2017). The established slugging regime is axisymmetric, where the slugs are slow. On the spectra, slugs are characterized by a shift of the peak's distributions to the low frequencies, below 1 Hz. The associated pressure fluctuation magnitudes are still low but higher than for the bubbling regime. The latter increases with the increase of the air velocity. The cross-correlation function presents a maximum that enables calculating the upward slug velocity, which is in good agreement with the two-phase flow theory (Fan et al., 1983). Before the establishment of the axisymmetric slugging regime, bubbles are progressively merging into intermediate wall slugs, as shown by (Sabatier et al., 2020), where the bubbles are flowing along the tube walls. There is a coexistence of bubbles and slugs in this regime, and the spectra present the characteristics of both regimes.

At air velocities higher than U_t, the coalescence is compensated by the scission of the bubbles. It results in a transition to the turbulent fluidization regime with tube height (Bi et al., 2000). The latter is characterized in the spectra by peak distributions below 1 Hz associated with high magnitudes. Velocities are measurable with the cross-correlation function, and are higher than the upward slug velocities calculated with the two-phase theory.

The last regime identified is the fast fluidization, for air velocities higher than U_k. It corresponds to the entrainment of the particles in the fluidization column that induces a separation of the bed into a dense zone and a more dilute zone (Grace et al., 2020). At the bottom of the column, the relatively dense zone is associated to strong pressure fluctuations, and the particle fraction is lower than in the previous regimes. This regime is characterized in the spectra by low frequency peak distributions and very high magnitudes, higher than measured in the previous regimes. Along the tube height, a more dilute zone follows this bottom zone, where the particles are entrained outside of the tube. This entrainment is due to the formation of particles clusters (Grace et al., 2020). These clusters are identifiable both in the spectra with peaks around 0.6 Hz and in the cross-correlation analysis, where the associated upward velocities are much higher than predicted by the two-phase theory for slugs. In the dilute zone, the particle fraction evolution with the height exhibits a curved trend, instead of an approximately linear trend in the other regimes. The peak distributions in the spectra are similar in both dense and dilute zones, but the magnitudes are lower in the dilute one.

3. Results and discussions

The control parameters of the experimental setup are the relative pressure in the dispenser, P_{tot}, and the aeration flow rate, $\dot{q_{ae}}$. They vary respectively in the ranges 90 – 430 mbar and 0 – 2.5 sm^3/h during all the experiments. The air flow rate range

corresponds to a superficial air velocity in the tube – at the height of the aeration – between 0.01 and 0.54 m/s. Depending on these control parameters, the height of the suspension in the tube – ranging from 0 to H_t – and the particle mass flow rate – ranging from 0 to 392 kg/m^{2}s – are managed. The measured characteristics of the fluidized system are the particle volume fraction and the fluidization regime. The evolutions of the latter are presented in the following section.

3.1. Macroscopic quantities

3.1.1. Height of the suspension

Even if the glass tube enables the visualization of the suspension, it is not always obvious to precisely identify the upper limit of the fluidized bed (without particle circulation), noted H_{bed}, due to the fluctuations of the bed surface. Consequently, the relative pressure profile measured along the tube height is used for a better accuracy. Fig. 2 presents three examples of pressure profile without circulation (circles and triangles), and with particle circulation (squares), each with an aeration flow rate of 0.8 sm^3/h. The pressure decreases linearly, and the height of the suspension is identified at the intersection between the linear regression and the ordinate. With circulation, the relative pressure is necessarily null at the end of the tube, i.e. $H_t = 3.18$ m above the aeration. Based on the experimental data, the method results in a measured height of 3.06 ± 0.13 m, in agreement with the real value of H_t accounting for the measurement uncertainty.

Fig. 3 shows the evolution of the bed height versus the pressure in the dispenser, P_{tot}, without particle circulation, for several values of the aeration flow rate. The bed reaches the level of the injection for a total pressure in the dispenser of approximately 55 – 60 mbar. The trends are then linear for all the tested aeration flow rates (0 – 1.6 sm^3/h). It proves that the hydrostatic pressure of the suspension only contributes to the total pressure drop without particle circulation and that the pressure drop due to wall friction is negligible as explained in (Geldart and Chap, 1986). Furthermore, the particle volume fraction seems to be independent of the bed height, H_{bed}. This point will be discussed in a following section.

3.1.2. Particle mass flow rate

When the suspension reaches the upper tip of the tube, the particles are circulating. The particle mass flux G_p is the particle mass flow rate normalized by the internal tube section, $G_p = \dot{m}_p/S_t$. It varies as a function of both the pressure in the dispenser and the aeration flow rate, as illustrated in Fig. 4. Each point in the Figure corresponds to the mean value over the acquisition period, and the uncertainty bars are calculated as the sum of the measurement uncertainty and the standard deviation of the signal. The latter is relatively low because steady state is reached during the tests, in terms of both pressure and particle mass flow rate variations. As expected, increasing the pressure in the dispenser for a given aeration flow rate or vice versa leads to an increase of the particle mass flux.

At low aeration flow rate, the trends in Fig. 4 are nearly linear, as it was previously observed for relatively low air velocities (Boissiere et al., 2015; Le Gal et al., 2019). Actually, at low values of $\dot{q_{ae}}$, the suspension is dense because the void structures are relatively small and ordered. Then, increasing the pressure leads to the increase of the suspension height without particle circulation. Since the height of the tube is already reached, it corresponds to a linear increase of the particle flow rate. However, an increase of the aeration flow rate results in more disordered void structures that are characteristic of the turbulent and fast fluidization regimes. Then, at low G_p, the particle flow rate is due to the strong fluctuations of the bed surface (in the turbulent fluidization regime), or to the entrainment of particles clusters (in the fast fluidization regimes). Even if the mean suspension has not reached the tube height yet, a slight particle flow is observed. This is the reason why there is no data at these $\dot{q_{ae}}$ values in Fig. 3. When the particle mass flux increases, the trends become more linear because the mean H_{bed} value approaches H_t.

3.1.3. Particle volume fraction

The particle volume fraction α is the ratio of the volume occupied by the particles over the total volume of the gas-particle suspension. According to (Geldart and Chap, 1986), the pressure drop between two pressure probes can be discomposed in three terms.

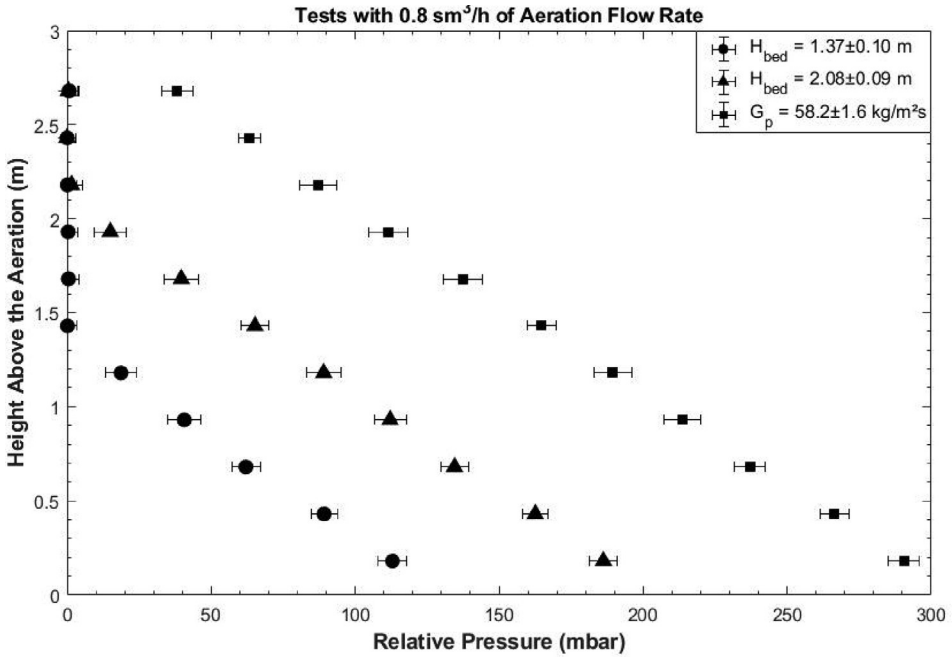

Fig. 2. Typical evolutions of the relative pressure with respect to the height in the tube. Circles and triangles. Without particle circulation, squares. With particle circulation.

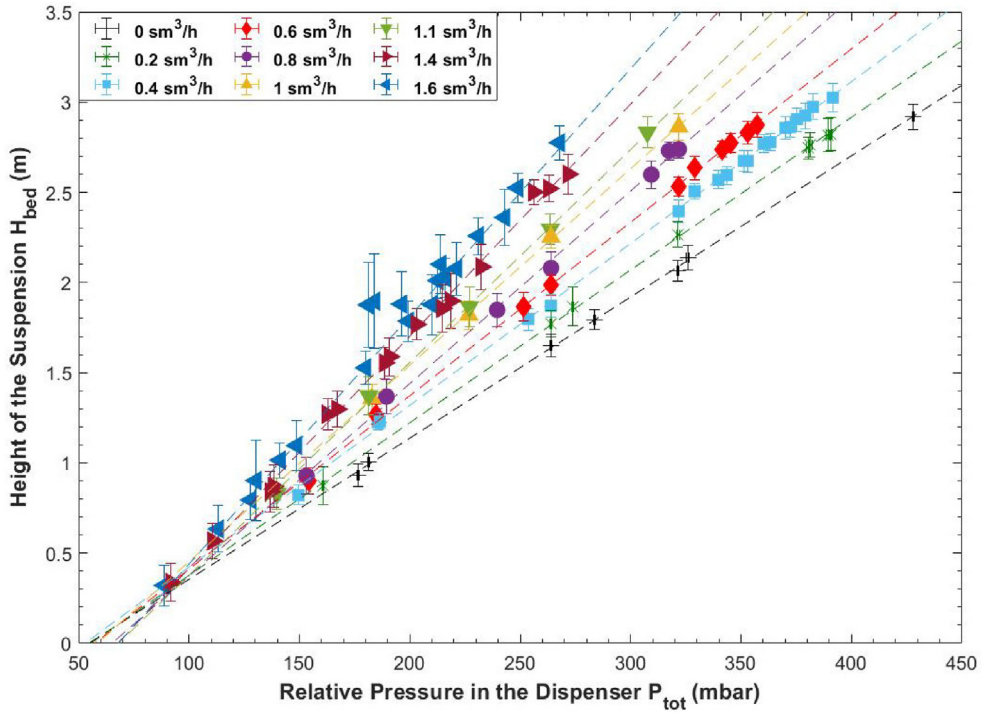

Fig. 3. Evolution of the suspension height versus the pressure in the dispenser for various aeration flow rates. Each symbol corresponds to a given aeration flow rate.

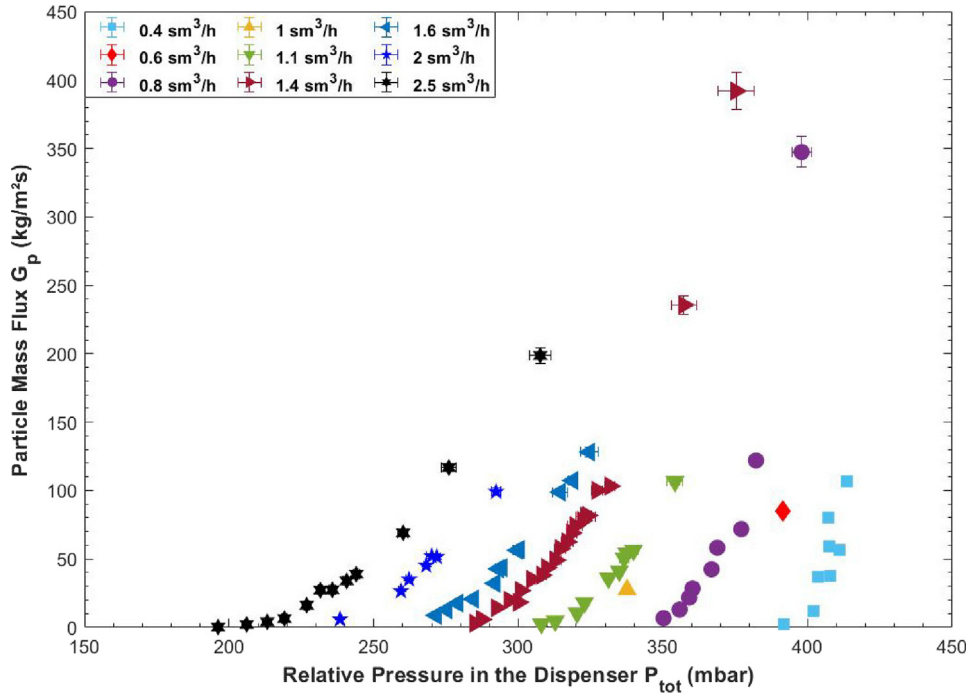

Fig. 4. Evolution of the particle mass flux versus the pressure in the dispenser for various aeration flow rates. Each symbol corresponds to a given aeration flow rate.

A term due to the effective weight of the suspension, a term due to the energy used to accelerate the particle until their upward velocity – proportional to the particle flow rate – and a term due to the friction against the tube walls (Zhang et al., 2017). During all the experiments, the total pressure losses due to particle acceleration and friction represent less than 3 % of the measured pressure drops and are thus neglected. Hence, the local particle volume fraction, noted α_i, can be calculated with Equation (1), with $\bar{\Delta P_i}$ the mean value of the ith differential pressure signal and ΔH the distance between two pressure sockets, i.e. 0.25 m. The associated uncertainty is low due to the low measurement error of the differential pressure sensors, i.e. 0.05 mbar.

$$\alpha_i = \frac{\bar{\Delta P_i}}{\left(\rho_p - \rho_{air}\right) g \Delta H} \tag{1}$$

The evolution of α_i with respect to the height is strongly correlated with the fluidization regime as shown in (Gueguen et al., 2021). A question arising is whether the acquisition time is large enough for the calculation of the particle volume fraction to be representative of the test. To provide an answer a test of one hour has been recorded, without particle circulation and for an aeration flow rate of 0.8 sm^3/h. Fig. 5 plots the evolution of the calculated value of α_i at 1.56 m above the aeration injection as a function of time taken to compute the average value of the differential pressure signal. The horizontal dashed lines represent the value of α_i calculated over all the acquisition duration in black, and the associated uncertainty in red. A minimum acquisition time of around 200 s is needed to converge toward the final value, which is of the order of magnitude of the time needed for the dynamic analysis.

To study the influence of the experimental parameters on the particle volume fraction, an overall value over the bed height is calculated for each test, $\alpha_h = \sum_{i=1}^{N} \alpha_i$. Fig. 6 shows the evolution of the overall particle volume fraction as a function of the suspension height, without circulation. In the Figure, the error bars on α_h and H_{bed} correspond to the pressure and suspension height fluctuations respectively. First, the overall particle fraction is slightly dependent of H_{bed} but decreases with the aeration flow rate. Second, the error bars are stronger for aeration flow rates of 1.4 and 1.6 sm^3/h because such aeration corresponds to the turbulent fluidization regime that is characterized by strong pressure fluctuations.

Fig. 7 presents the evolution of α_h with the particle mass flux G_p, for various aeration flow rates. The increase of the particle volume fraction with the particle mass flow rate, for a given aeration, is due to the acceleration term in the pressure drop balance, $\Delta P_{acc} = G_p/(\rho_p \alpha)$ (Zhang et al., 2017). It means that considering a constant energy given in the system (i.e. the pressure in the dispenser and the aeration flow rate), a part of this energy is consumed to accelerate the particles until their upward velocity. Compared to a case at lower particle velocity – i.e. at lower particle mass flow rate – for a same aeration flow rate, the fraction of total energy used to separate the particle's aggregates decreases at high particle velocity, hence the bed porosity reduces.

Furthermore, one can observe a strong dependency of α_h with the aeration flow rate either for a given particle mass flux or the height of the suspension, as shown in (Gueguen et al., 2021). Actually, the increase of the air velocity is due to the increase of the air flow rate and thus of the air quantity in the tube, which logically results in a quasi-linear decrease of the volume occupied by the particles.

3.2. Fluidization regimes

3.2.1. Diagram of the fluidization regimes

The signal processing described in the previous section have been applied to the 177 tests of the experimental campaign that cover a large range of operating parameters. Fig. 8 presents a diagram of the fluidization regimes identified during this experimental campaign, where 1167 points are plotted, with and without particle circulation. The regimes are identified in the Figure by markers and colors, and plotted in terms of tube height. The height within the tube is normalized with respect to the distance from the aeration nozzle and the internal tube diameter to compare the diagram with the data of previous works on fluidization regimes. Furthermore, according to the scientific literature on circulating fluidized beds, the slip velocity U_{slip} is responsible of the transition between regimes (Rabinovich and Kalman, 2011). The latter is the difference between the interstitial air velocity and the particle velocity (Eq. (2)). It is calculated locally by taking into account of the increase of the local superficial air velocity with height due to the absolute pressure decrease. Actually, considering air as an ideal gas, Equation (3) calculates the superficial air velocity at a given height in the tube, with respect to the superficial air velocity and the pressure at the height of the aeration injection (identified by the subscript $h = 0$). Finally, the points in the diagram are plotted versus the slip velocity expressed as a dimensionless quantity, the local particle Reynolds number (Eq. (4)).

The representation selected for the diagram allows gathering the points in zones corresponding to the same fluidization regime, confirming that the slip velocity is the pertinent parameter that governs the regime transitions. In Fig. 8, the limits between the fluidization regimes are also plotted. The transitions between the different regime zones are discussed in the following paragraphs.

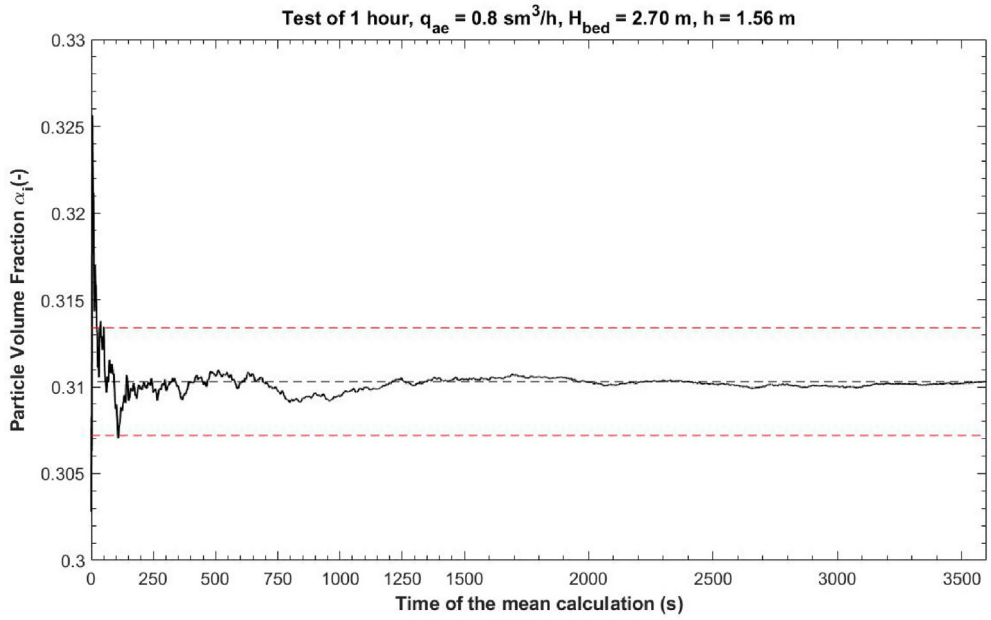

Fig. 5. Evolution of the local particle volume fraction versus the time taken to compute the average differential pressure.

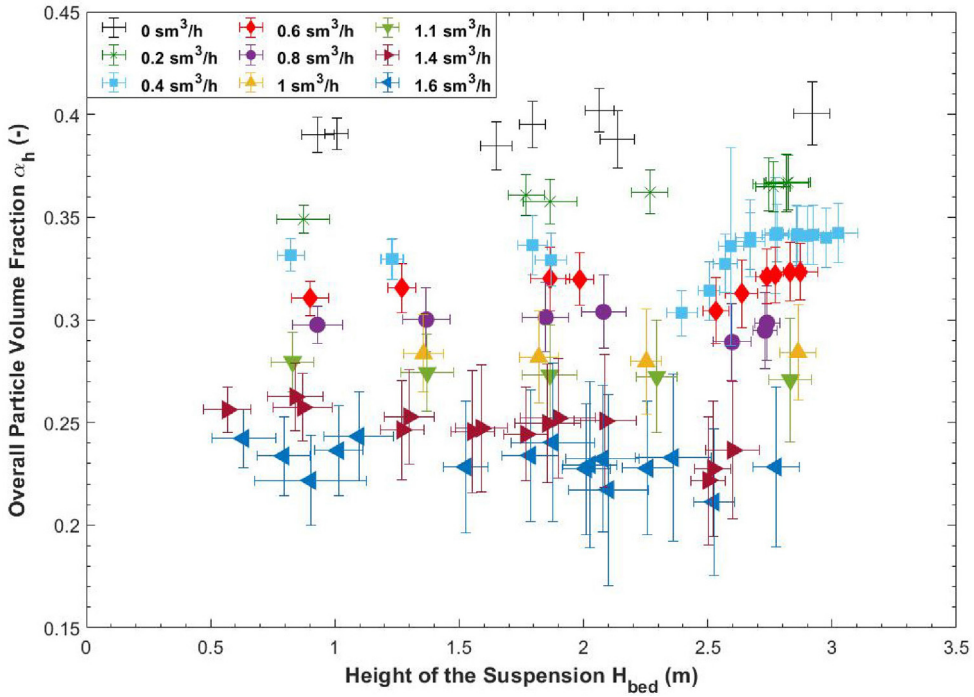

Fig. 6. Evolution of the overall particle volume fraction versus the suspension height for various aeration flow rates. Each symbol corresponds to a given aeration flow rate.

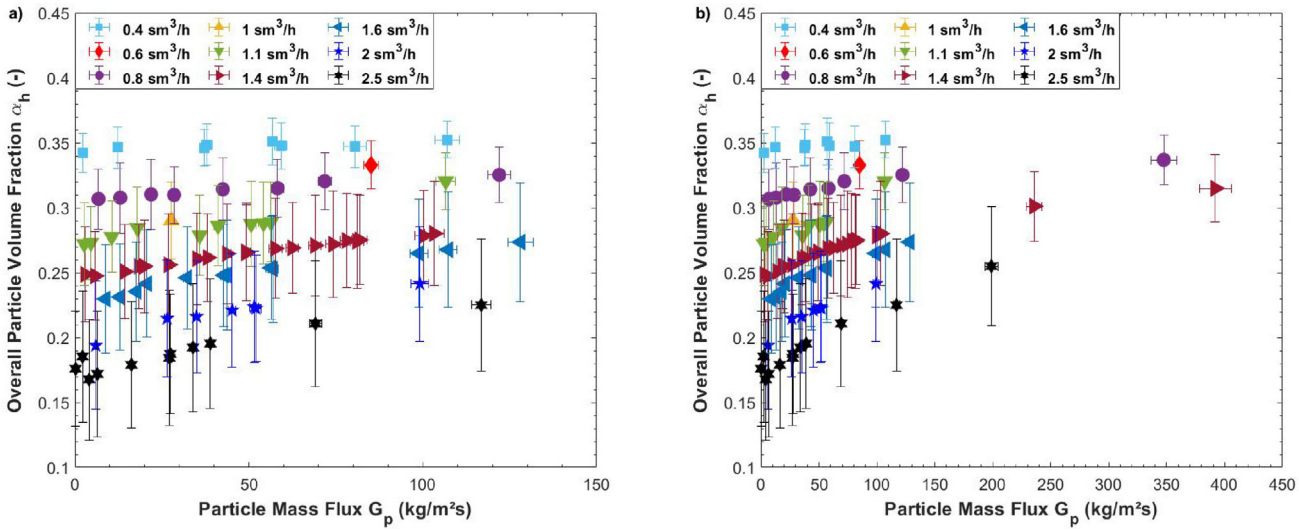

Fig. 7. Evolution of the overall particle volume fraction versus the particle mass flux for various aeration flow rates. Each symbol corresponds to a given aeration flow rate. Fig. 7a is a zoom up to a particle mass flux of 150 kg/(m^{2}s), where a major part of the experimental results is obtained, while the x-axis of Fig. 7b is scaled up to 450 kg/(m^{2}s).

$$U_{slip,i} = \frac{U_{air,i}}{1-\alpha_i} - \frac{G_p}{\rho_p \alpha_i} \tag{2}$$

$$U_{air,i} = \frac{U_{air,h=0} P_{h=0}}{P_i} \tag{3}$$

$$Re_{slip} = \frac{\rho_{air} U_{slip} d_{SV}}{\mu_{air}} \tag{4}$$

Compared to the previous experimental works on the fluidized particle-in-tube receiver concept (Flamant et al., 2013; Benoit et al., 2015; Perez-Lopez et al., 2016; Boissiere et al., 2015; Le Gal et al., 2019; Ansart et al., 2017; Benoit et al., 2018; Kong et al., 2017; Sabatier et al., 2020; Deng et al., 2021), this diagram highlights the turbulent and fast fluidization regimes at high slip velocities. Along the tube height, the turbulent fluidization zone (black circles in the Figure) is preceded by a bubbling zone until approximately dimensionless height of 10 above the aeration, where the bubbles are splitting instead of coalescing, as previously observed (Gueguen et al., 2021). Actually, according to (Grace et al., 2020), the transition velocity from bubbling to turbulent regimes for fine particles can be predicted by assuming the existence of a maximum stable bubble size. Trailing bubbles split in the turbulent wake of leading bubbles. A leading bubble of maximum stable size induces the break of a trailing bubble into small voids by interaction with its turbulent wake. Consequently, when bubble splitting becomes dominant, the massive breakdown of bubbles transforms the flow from bubbling to turbulent fluidization. To simplify the

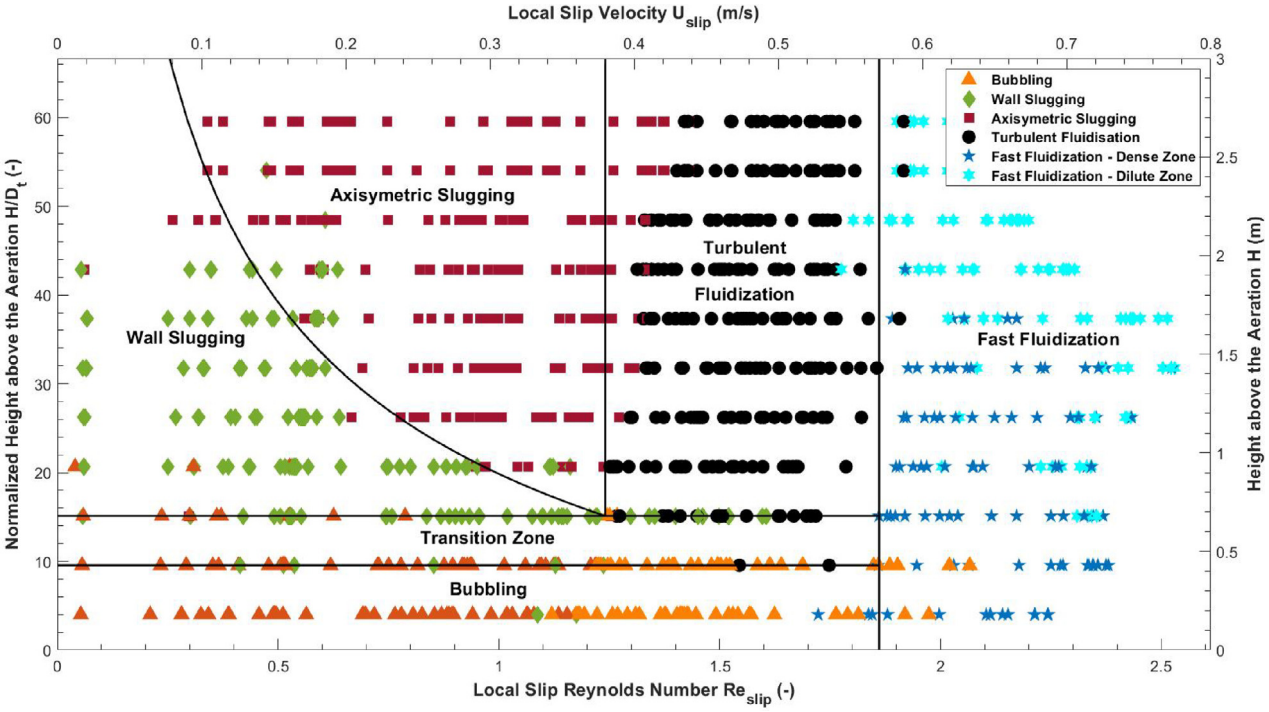

Fig. 8. Diagram of the fluidization regimes encountered in the tube and their transitions with the height as a function of the experimental parameters expressed in terms of dimensionless quantities.

diagram, vertical limits are considered and calculated to maximize the number of points corresponding to the regimes in the associated zones. The limits of regimes are obtained with 233 points identified as in turbulent fluidization regime in the related zone among a total of 269 points, and 200 points identified as fast fluidization regime over 209 points in their corresponding zone. The velocity limits for U_t and U_k are 0.38 and 0.57 m/s respectively, i.e. particle Reynolds numbers of 1.24 and 1.86 respectively. Moreover, it seems that the turbulent fluidization occurs when the wall slugging zone disappears (in green in the Figure). This finding is in good agreement with the interpretation that the bubble's coalescence becomes negligible compared to their scission at the onset of the turbulent fluidization regime, as proposed by (Bi et al., 2000). Limit of the wall slugging zone is discussed below.

The points identified as in bubbling regime below the turbulent and fast fluidization zones slightly differ from those related to the classical single bubbling regime (they are represented in the Figure with triangles lighter than those corresponding to the classical bubbling). Actually, their spectra present the classical peak distribution above 1 Hz but also some peak distributions below 1 Hz, even if the latter have very low magnitudes, too low to be considered as indicators of turbulent or fast fluidization. This may be due to the retroaction of strong fluctuations occurring at higher locations in the tube but also to the influence of the aeration injection. Indeed, given the air flow rates injected through the small diameter injection, between 0 and 2.5 sm^3/h, the corresponding horizontal air velocity ranges between 0 and 480 m/s ($0 \leq Re \leq 38\,200$). According to (Wang et al., 2015), the length of the penetration jet is increasing with the increase of $\dot{q_{ae}}$, with approximately $2D_t$ for an aeration flow rate of 2.5 sm^3/h. Furthermore, penetration jets are associated to various upward angles that decrease with the increase of the air flow rate. For an aeration of 2.5 sm^3/h, this angle θ is estimated at 10°. A simple calculation allows to estimate the height of the corresponding jet in the vertical main tube, $D_t/\sin\theta$, of 0.26 m, i.e. above the first pressure sensor. As a conclusion, strong perturbations are induced in the aeration nozzle zone that results in a dissipation height spreading until the firsts pressure sensors. Numerical simulations are under progress to study this phenomenon and complete this interpretation.

There is a slight zone between the second and the third pressure sockets, i.e. between approximately 10 and 15 of dimensionless heights above the aeration, where all three bubbling, wall slugging and turbulent fluidization regimes are identified depending on the operation conditions. This zone is named "Transition Zone" to take into account the identification uncertainties. Then, below this transition zone 97 points are identified as in bubbling regime over 102 points.

As explained above in the paper, in a bubbling/slugging operation conditions, the bubbles are progressively merging into slugs (Sabatier et al., 2020). In the diagram, at approximately a dimensionless height of 10 above the aeration, bubbles start to coalesce into an intermediate wall-slugging zone. The wall-slugging zone appears to be thinner and thinner with the increase of the slip velocity. This observation differs with previous published works, where the wall slugging to the axisymmetric slugging transition was identified at a constant height (Kong et al., 2017; Sabatier et al., 2020; Deng et al., 2021). Regarding the bubbles coalescence, the reference study (Mori and Wen, 1975) proposed an empirical correlation for the evolution of the bubble diameter with height for group B particles as a function of the air velocity. Considering the diameter at which the bubbles are coalescing into slugs, i.e. around 60 % of the tube diameter (Geldart, 1986), the equation can be reworked in order to determine the height of the slug transition, here noted h_s, as a function of the slip velocity to take into account the particle circulation. The general trend is given by Equation (5), with the coefficients A, B and C determined for group B particles in the initial empirical correlation (Mori and Wen, 1975). To determine these coefficients in the case of group A particles, we assume the following. Since the minimum bubbling velocity is defined as the air velocity at which the first bubble is erupting at the bed surface (Abrahamsen and Geldart, 1980), the transition height for the coalescence of the same bubble into a slug

at this velocity can be mathematically considered at the infinite. In Equation (5), it happens when the term in the logarithm becomes null. Then, considering $U_{slip} = U_{mb}$, it gives $C = BU_{mb}^{0.4}$. Furthermore, a given point of the correlation can be identified at the beginning of the turbulent fluidization regime, i.e. at $U_{slip} = 0.38$ m/s and a height of approximately 0.7 m (i.e. respectively at $Re_{slip} = 1.24$ and $H/D_t = 15$), fixing the A coefficient as a function of B. Several values of the B coefficient have been numerically tested, and it has been determined by maximizing both the ratio of the points identified as wall slugs over the total points in the wall slugging zone (below the transition), and the ratio of the points identified as axisymmetric slugs over the total points in the axisymmetric slugging zone (above the transition). The best fit has been established for the following coefficients: $A = 227.168$, $B = 1.15$ and $C = 0.1456$. A total of 126 points have been identified as in wall-slugging regime among 157 points in the associated zone, and 216 points have been identified as in axisymmetric slugging regime among 229 points in the corresponding zone.

It comes, height of the slug transition,

$$h_s = -A \ln\left(B - \frac{C}{U_{slip}^{0.4}}\right) \tag{5}$$

With $A = 227.168$, $B = 1.15$ and $C = 0.1456$.

Finally, combining all the limits presented above, it gives 872 points well-identified in their corresponding fluidization regime zones over a total of 966 points, i.e. a validation of the transition limits of 90.26 %.

For the sake of clarity, Fig. 9 illustrates the diagram of the fluidization regimes without any experimental points but only with the transitions between the fluidization regimes, considering a relative uncertainty of 10 %. Actually, the relative uncertainties due to measurement related to the local slip velocities are between 5 and 7 %. Then, four transition zones appear in the simplified diagram of Fig. 9 (in gray), delimiting the regimes zones of bubbling, wall slugging, axisymmetric slugging, turbulent fluidization, and fast fluidization.

Obtaining a complete diagram of the fluidization regimes is one of the major issues in the fluidization domain. As the regime transitions depend on the particle properties, some authors have established diagrams in terms of Archimedes' number to compare the various Geldart groups of particles (Geldart, 1973), as Bi & Grace (Grace et al., 2020; Rabinovich and Kalman, 2011; Geldart and Chap, 1986; Bi and Grace, 1995) and more recently Rabinovitch and Kalman (Rabinovich and Kalman, 2011). In these diagrams, the air velocity and the tube geometry are gathered in the Reynolds' number. Nevertheless, these widely used diagrams are related to circulating fluidized beds inside risers. Consequently, the limits of the turbulent and fast fluidization regimes differ significantly with our experimental values that are much lower than the established correlations, even considering the large uncertainties associated with correlations (around 30 %) (Ellis et al., 2004). The results indicate turbulent and fast fluidization transition velocities from 1.3 to 2.4 times lower than literature correlations. Two main explanations arise. First, the correlations are based the Sauter diameter, while the powder used in this study is characterized by a rather large particle size distribution with a non-negligible amount of fine particles that can modify the fluidization properties. Second, the pressure is a control parameter of our system. Actually, pressurizing the system rises the particle energy level. As a result, the energy share – associated to the air phase – required to induce the regime transition is lower than the one observed in risers. Consequently, a general criterion or correlation cannot gather the two kinds of concept – risers and pressure-driven fluidized particle-in-tube – for the moment.

3.2.2. Discussion on the detection criteria

Fig. 10 presents the measured local solid volume fraction, α_i, in terms of the local slip Reynolds number $Re_{slip,i}$, calculated at the same height, over all the tests. The experimental points and their associated regimes are the same that in Fig. 8. They gather in a linear trend, independently of the aeration and the particle mass flow rates, with and without particle circulation. The limits of the fluidization regimes are identified in the Figure with the transition

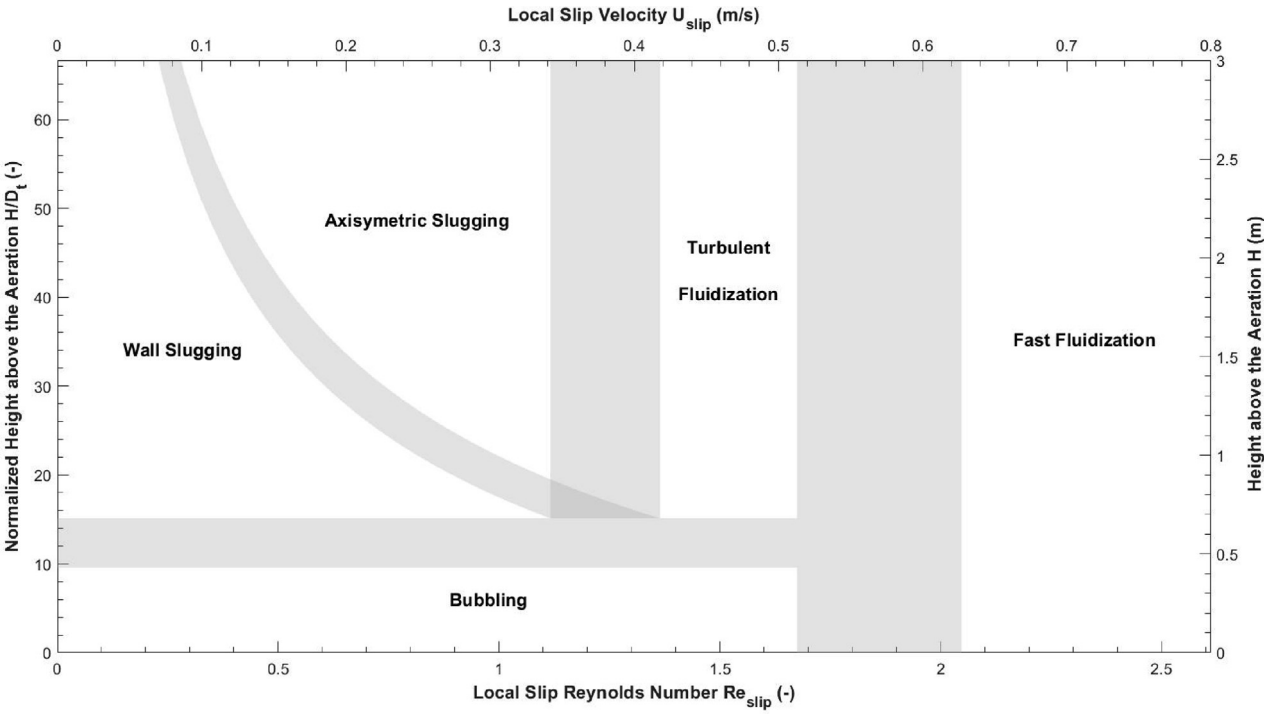

Fig. 9. Simplified diagram of the fluidization regimes with transition zones established with a trust interval of 90 %.

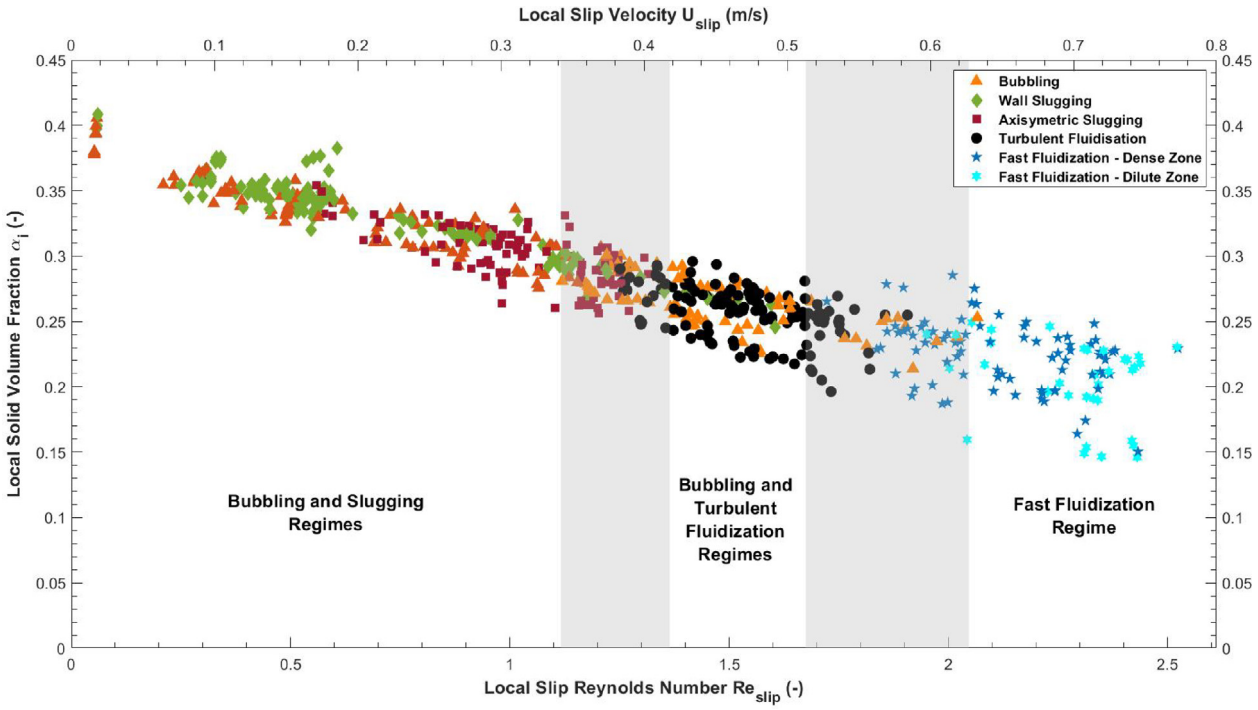

Fig. 10. Evolution of the local particle volume fraction with the local slip Reynolds number.

zones of Fig. 8. Values of the particle volume fraction can thus be associated to these regimes as presented in Table 2. The range of the particle volume fraction corresponding to the turbulent fluidization regime, i.e. between 0.21 and 0.29, is in good agreement with the two-phase theory that predicts a value of 0.275 (Grace et al., 2020).

Then, simple calculation of the particle volume fraction at a given height and local slip velocity allow identifying the fluidization regimes. This simple method prevents heavy dynamic analyses of the pressure signals.

Since the local slip velocity is the governing parameters of the fluidization regimes, it is relevant to discuss the evolution of the local relative pressure fluctuations – i.e. the ratio of the standard deviation of a differential pressure signal by its mean value – versus the local slip Reynolds number. The results indicate that the local relative pressure fluctuations increase with this number. Accounting for the decrease of the local volume fraction with the local slip Reynolds number (Fig. 10), Fig. 11 represents the relationship between the pressure fluctuation and the particle volume fraction. Interestingly, the two parameters are correlated, and the trend is a negative exponential curve. In addition, Fig. 11 shows that the bubbling regime exhibits a different trend than the others fluidization regimes.

Table 2
Ranges of local slip Reynolds numbers and particle volume fractions associated to the fluidization regimes configurations.

Fluidization Regimes	Dimensionless Transition Height, H/D_t	Local Particle Volume Fraction, α_i	Local Slip Reynolds Number, Re_{slip}
Bubbling and Slugging	10 – 15	0.26 – 0.41	0 – 1.12
Bubbling and Turbulent Fluidization	10 – 15	0.21 – 0.29	1.37 – 1.67
Fast Fluidization (Dense and Dilute Zones)	Varying	0.14 – 0.27	2.05 – 2.53

4. Conclusions

The behavior of upward gas-particle fluidized beds has been studied in a tube with a large aspect ratio at ambient temperature, for application as heat transfer fluid in a tubular particle solar receiver. The selected particles are Geldart group A olivine, the superficial air velocity ranges between 0.01 and 0.54 m/s, and the particle mass flux varies from 0 to 390 kg/(m^2.s).

Experimental results show that the particle volume fraction α varies slightly with the height of the suspension without particle circulation. With particle circulation, it increases with the particle mass flux due to supplementary pressure drop terms. Moreover, at a given height or particle flow rate, α decreases strongly and quasi linearly with the superficial air velocity.

The fluidization regimes are driving the particle mixing and thus the heat transfer between the tube walls and the particles. Bubbling, slugging (wall and axisymmetric), turbulent fluidization and fast fluidization regimes have been identified in the tube depending on the experimental conditions using pressure signals processing methods.

A complete diagram of the fluidization regimes has been established by considering the height in the tube versus the local slip velocity, ranging from 0.01 to 0.78 m/s. It proves that, even for a pressure-assisted system, the slip velocity is the pertinent parameter that governs the flow structure. It is shown that at low slip velocities, bubbles are present at the bottom of the tube and coalesce with the height into axisymmetric slugs when the bubble size (D_b) is comparable to the tube diameter (D_t), with $D_b/D_t > 0.6$. The intermediate zone between bubbles and axisymmetric slugs is a coalescence zone, where wall slugs are present. This zone shrinks with the increase in the slip velocity, as it can be verified by applying a simple coalescence correlation. At higher slip velocity, the interaction of the maximum bubble size wake with the following bubbles results in the splitting of the latter in small voids. In other words, the split of the bubbles exceeds the coalescence, leading to the turbulent fluidization regime. At higher velocity, bubbles disappear and the gas solid flow structure is dominated by particle

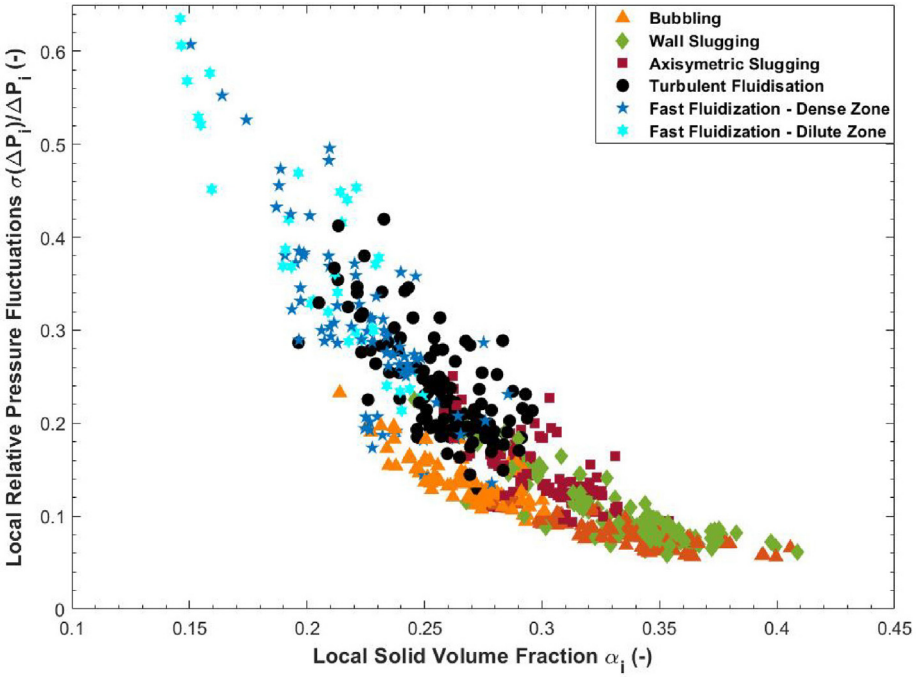

Fig. 11. Evolution of the local relative pressure fluctuations with the local particle volume fraction.

aggregates, the clusters, representative of the fast fluidization regime.

The following observations arise from the analysis of the pressure signal processing. Starting with the bubbling and slugging regime zone at low velocity and increasing the slip velocity leads to a decrease of the dominant frequency and an increase of the associated magnitude in the power spectra. Both the relative pressure fluctuations and the velocity measured with the cross-correlation method increase, while the local particle volume fraction decreases. Furthermore, increasing the slip velocity leads both to a decrease of the local particle volume fraction and an increase of the local relative pressure fluctuations, these two parameters being strongly correlated. The main shortcomings of the regimes' identification method based on the analysis of temporal pressure signals are its weak precision and inability to measure the special distribution of the detected structures. It was selected since it is applicable at high temperature under on-sun operation, which is the targeted application.

According to the literature data related to risers, the turbulent fluidization regime is the best compromise in terms of heat transfer because it is associated with a strong particle mixing and a rather dense suspension, hence it should be preferred in wall-heating conditions of tubes. The limits of the turbulent fluidization regime have been measured for a local slip velocity between 0.42 and 0.51 m/s, corresponding to particle Reynolds number of 1.37 and 1.67. Furthermore, it appears that the particle volume fraction (α) decreases linearly with the slip velocity. The corresponding limits for the turbulent fluidization regime are 0.29 – 0.21. Finally, the knowledge of the particle volume fraction at a known height – thanks to pressure drop measurement may be sufficient to identify the fluidization regimes in the tube, if the acquisition time is sufficient.

Considering concentrating solar thermal applications, the question of influence of temperature on the fluidization regimes and their transitions is a key issue. Experiments under concentrated solar power using a refractory alloy receiver tube are in progress to answer this question and measure the associated wall-to-bed heat transfer coefficients.

CRediT authorship contribution statement

Ronny Gueguen: Investigation, Methodology, Data curation, Writing – original draft, Writing – review & editing. **Guillaume Sahuquet:** Investigation, Methodology, Data curation, Writing – original draft, Writing – review & editing. **Samuel Mer:** Validation, Data curation, Writing - review & editing. **Adrien Toutant:** Validation, Data Curation, Visualization, Writing – review & editing. **Françoise Bataille:** Validation, Data Curation, Visualization, Writing – review & editing. **Gilles Flamant:** Investigation, Methodology, Data curation, Writing – original draft, Writing – review & editing, Supervision, Project administration, Funding acquisition.

Data availability

Data will be made available on request.

Declaration of Competing Interest

The authors declare that they have no known competing financial interests or personal relationships that could have appeared to influence the work reported in this paper.

Acknowledgements

The characterization of the olivine sample was conducted with the help of the Material Characterization Platform – Surfaces and Interfaces Analyses of the PROMES (CNRS) laboratory.

Funding

This work was funded by the French "Investments for the future" ("*Investissements d'Avenir*") program managed by the National Agency for Research (ANR) under contract ANR-10-

LABX-22-01 (labex SOLSTICE). Additional funding was awarded by the European Union's Horizon 2020 research and innovation program under Grant Agreement 727762, Next-CSP project. Additional funding was obtained by the Occitanie French region for the cold mock-up installation.

References

Abrahamsen, A.R., Geldart, D., 1980. Behaviour of Gas-Fluidized Beds of Fine Powders Part I. Homogeneous Expansion. Powder Technol. 26, 35–46. https://doi.org/10.1016/0032-5910(80)85005-4.

Ansart, R., Garcia-Triñanes, P., Boissière, B., Benoit, H., Seville, J.P.K., Simonin, O., 2017. Dense gas-particle suspension upward flow used as heat transfer fluid in solar receiver: PEPT experiments and 3D numerical simulations. Powder Technol. 307, 25–36. https://doi.org/10.1016/j.powtec.2016.11.006.

Benoit, H., Perez Lopez, I., Gauthier, D., Sans, J.L., Flamant, G., 2015. On-sun demonstration of a 750 °C heat transfer fluid for concentrating solar systems: Dense particle suspension in tube. Solar Energy 118, 622–633. https://doi.org/10.1016/j.solener.2015.06.007.

Benoit, H., Spreafico, L., Gauthier, D., Flamant, G., 2016. Review of heat transfer fluids in tube-receivers used in concentrating solar thermal systems: Properties and heat transfer coefficients. Renewable Sustainable Energy Rev. 55, 298–315. https://doi.org/10.1016/j.rser.2015.10.059.

Benoit, H., Ansart, R., Neau, H., Garcia Triñanes, P., Flamant, G., Simonin, O., 2018. 3D numerical simulation of upflow bubbling fluidized bed in opaque tube under high flux solar heating. Am. Inst. Chem. Eng. J. 64. https://doi.org/10.1002/aic.16218.

Bi, H.T., Grace, J.R., Zhu, J.X., 1993. Types of Chocking in Vertical Pneumatic Systems. Int. J. Multiph. Flow 19, 1077–1092. https://doi.org/10.1016/0301-9322(93)90079-A.

Bi, H.T., Grace, J.R., 1995. Flow regime diagrams for gas-solid fluidization and upward transport. Int. J. Multiph. Flow 21, 1229–1236. https://doi.org/10.1016/0301-9322(95)00037-X.

Bi, H.T., Ellis, N., Abba, I.A., Grace, J.R., 2000. A state-of-the-art review of gas-solid turbulent fluidization. Chem. Eng. Sci. 55, 4789–4825. https://doi.org/10.1016/S0009-2509(00)00107-X.

Boissiere, B., Ansart, R., Gauthier, D., Flamant, G., Hemati, M., 2015. Experimental Hydrodynamic Study of Gas-Particle Dense Suspension Upward Flow for Application as New Heat Transfer and Storage Fluid. Can. J. Chem. Eng. 93 (2), 317–330.

Breault, R.W., Weber, J., Shadle, L.J., 2020. The development of a generalized riser flow regime map based upon higher moment and chaotic statistics using electrical capacitance volume tomography (ECVT). Power Technol. 365, 12–27. https://doi.org/10.1016/j.powtec.2019.03.036.

Chen, Y., Lim, C.J., Grace, J.R., Zhang, J., Zhao, Y., Zheng, C., 2015. Characterization of pressure fluctuations from a gas-solid fluidized bed by structure density function analysis. Chem. Eng. Sci. 129, 156–167. https://doi.org/10.1016/j.ces.2015.02.009.

Deng, Y., Sabatier, F., Dewil, R., Flamant, G., Le Gal, A., Gueguen, R., Baeyens, J., Li, S., Ansart, R., 2021. Dense upflow fluidized bed (DUFB) solar receivers of high aspect ratio: Different fluidization modes through inserting bubble rupture promoters. Chem. Eng. J. 418,. https://doi.org/10.1016/j.cej.2021.129376 129376.

Dodds, J., Baluais, G., 1993. Particle size characterization. Sci. Géol. 46, 79–104. https://doi.org/10.3406/sgeol.1993.1898.

Dunham, M.T., Iverson, B.D., 2014. High-efficiency thermodynamic power cycles for concentrated solar power systems. Renew. Sustain. Energy Rev. 30, 758–770. https://doi.org/10.1016/j.rser.2013.11.010.

Ellis, N., Bi, H.T., Lim, C.J., Grace, J.R., 2004. Hydrodynamics of turbulent fluidized beds of different diameters. Powder Technol. 141, 124–136. https://doi.org/10.1016/j.powtec.2004.03.001.

Fan, L.T., Ho, T.C., Walawender, W.P., 1983. Measurements of the Rise Velocities of Bubbles, Slugs and Pressure Waves in a Gas-Solid Fluidized Bed Using Pressure Fluctuation Signals. American Inst. Chem. Eng. J. 29, 33–39. https://doi.org/10.1002/aic.690290105.

CSP2 (2015). Dense suspensions of solid particles as a new heat transfer fluid for CSP. https://cordis.europa.eu/project/id/282932 (accessed on 6 May 2022).

G. Flamant, H. Hemati, Dispositif Collecteur D'énergie Solaire (Device for Collecting Solar Energy), French Patent FR 1058565, 20 October 2010; PCT extension WO2012052661, 26 April 2012.

Flamant, G., Gauthier, D., Benoit, H., Sans, J.L., Garcia, R., Boissière, B., Ansart, R., Hemati, M., 2013. Dense suspension of solid particles as a new heat transfer fluid for concentrated solar thermal plants: On-sun proof of concept. Chem. Eng. Sci. 102, 567–576. https://doi.org/10.1016/j.ces.2013.08.051.

Geldart, D., 1973. Types of Gas Fluidization. Powder Technol. 7, 285–292. https://doi.org/10.1016/0032-5910(73)80037-3.

Geldart, D., 1986. Chap.2: Single particles, Fixed and Quiescent Beds. In Gas Fluidization Technology, pp. 11–32.

Geldart, D., 1986. Chap.4: Hydrodynamics of Bubbling Fluidized Beds. In Gas Fluidization Technology, pp. 53–96.

Geldart, D., 1986. Chap. 6: Particle Entrainment and Carryover. In Gas Fluidization Technology, 123–154.

Grace, J.R., Bi, X., Ellis, N., 2020. Chap. 4: Gas Fluidization Flow Regimes. In Essential of Fluidization Technology, 55–74.

Grace, J.R., Bi, X., Ellis, N., 2020. Chap. 9: Turbulent Fluidization. In Essential of Fluidization Technology, 163–180.

Gueguen, R., Grange, B., Bataille, F., Mer, S., Flamant, G., 2020. Shaping High Efficiency, High Temperature Cavity Tubular Solar Receivers. Energies 13, 4803. 10.3390.en13184803.

Gueguen, R., Sahuquet, G., Mer, S., Toutant, A., Bataille, F., Flamant, G., 2021. Gas-Solid Flow in a Fluidized-Particle Tubular Solar Receiver: Off-Sun Experimental Flow Regimes Characterization. Energies 14, 7392. https://doi.org/10.3390/en14217392.

Hafizur Rahman, M., Bi, X.T., Grace, J.R., Jim Lim, C., 2020. Comparison of techniques for measuring CFB solids circulation rates at low and high temperatures. Powder Technol. 360, 43–54. https://doi.org/10.1016/j.powtec.2019.10.033.

Ho, C.K., Christian, J., Yellowhair, J., Jeter, S., Golob, M., Nguyen, C., Repole, K., Abdel-Khalik, S., Siegel, N., Al-Ansary, H., El-Leathy, A., Gobereit, B., 2017. Highlights of the high-temperature falling particle receiver project: 2012–2016. AIP Conference Proceeding 1850,. https://doi.org/10.1063/1.4984370 030027.

Jacob, R., Belusko, M., Ines Fernandez, A., Cabeza, L.F., Saman, W., Bruno, F., 2016. Embodied energy and cost of high temperature thermal energy storage systems for use with concentrated solar power plants. Appl. Energy 180, 586–597. https://doi.org/10.1016/j.apenergy.2016.08.027.

Johnsson, F., Zijerveld, R.C., Schouten, J.C., van den Bleek, C.M., Leckner, B., 2000. Characterization of fluidization regimes by time-series analysis of pressure fluctuations. Int. J. Multiph. Flow 26, 663–715. https://doi.org/10.1016/S0301-9322(99)00028-2.

Kang, Q., Flamant, G., Dewil, R., Baeyens, J., Zhang, H.L., Deng, Y., 2019. Particles in a circulation loop for solar energy capture and storage. Particuology 43, 149–156. https://doi.org/10.1016/j.partic.2018.01.009.

Kong, W., Tan, T., Baeyens, J., Flamant, G., Zhang, H., 2017. Bubbling and slugging of Geldart group A powders in small diameters columns. Ind. Eng. Chem. Res. 56, 4136–4144. https://doi.org/10.1021/acs.iecr.6b04798.

Kunii, D., Levenspiel, O., 1991. Chap 3: Fluidization and Mapping of Regimes. In Fluidization Eng., 61–94

Le Gal, A., Grange, B., Tessonneaud, M., Perez, A., Escape, C., Sans, J.L., Flamant, G., 2019. Thermal analysis of fluidized particle flows in a finned tube solar receiver. Sol. Energy 191, 19–33.

Li, Y.-Q., Grace, J.R., Gopaluni, R.B., Bi, H., Lim, C.J., Ellis, N., 2011. Characterization of gas-solid fluidization: A comparative study of acoustic and pressure signals. Powder Technol. 214 (2), 200–210.

Mori, S., Wen, Y., 1975. Estimation of Bubble Diameter in Gaseous Fluidized Beds. Am. Inst. Chem. Eng. J. 21, 109–115. https://doi.org/10.1002/aic.690210114.

Next-CSP, 2020. High Temperature Concentrated Solar Thermal Power Plant with Particle Receiver and Direct Thermal Storage. https://cordis.europa.eu/project/id/727762 (accessed on 10 March 2022).

Perez-Lopez, I., Benoit, H., Gauthier, D., Sans, J.L., Guillot, E., Mazza, G., Flamant, G., 2016. On-sun operation of a 150 kW_{th} pilot solar receiver using dense particle suspension as heat transfer fluid. Sol. Energy 137, 463–476. https://doi.org/10.1016/j.solener.2016.08.034.

Rabinovich, E., Kalman, H., 2011. Flow regime diagram for vertical pneumatic conveying and fluidized bed systems. Powder Technol. 207, 119–133. https://doi.org/10.1016/j.powtec.2010.10.017.

Sabatier, F., Ansart, R., Zhang, H., Baeyens, J., Simonin, O., 2020. Experiments support simulations by NEPTUNE CFD Code in a Upflow Bubbling Fluidized Bed reactor. Chem. Eng. J. 385,. https://doi.org/10.1016/j.cej.2019.123568 123568.

Stefanova, A., Bi, H.T., Lim, J.C., Grace, J.R., 2011. Local hydrodynamics and heat transfer in fluidized beds of different diameter. Powder Technol. 212, 57–63. https://doi.org/10.1016/j.powtec.2011.04.026.

Stefanova, A., Bi, H.T., Lim, C.J., Grace, J.R., 2020. A probabilistic heat transfer model for turbulent fluidized beds. Powder Technol. 365, 163–171. https://doi.org/10.1016/j.powtec.2019.01.066.

Vaidheeswaran, A., Li, C., Ashfaq, H., Wu, X., Rowan, S., Rogers, W.A., 2022. Validation experiments on bubbling fluidization of Group B glass particles. Exp. Comput. Multiphase Flow 4, 264–273. https://doi.org/10.1007/s42757-021-0108-4.

van der Schaaf, J., Schouten, J.C., Johnsson, F., van den Bleek, C.M., 2002. Non-intrusive determination of bubble and slug length scales in fluidized beds by decomposition of the power spectral density of pressure time series. Int. J. Multiph. Flow 28 (5), 865–880.

Wang, S., Yang, Q., Shao, B., Zhao, J., Liu, L., Liu, Y., 2015. Numerical Simulation of Horizontal Jet Penetration Using Filtered Fluid Model in Gas-Solid Fluidized Bed. Powder Technol. 276, 1–9. https://doi.org/10.1016/j.powtec.2015.02.009.

Wu, W., Amsbeck, L., Buck, R., Uhlig, R., Ritz-Paal, R., 2014. Proof of concept test of a centrifugal particle receiver. Energy Proc. 49, 560–568. https://doi.org/10.1016/j.egypro.2014.03.060.

Wu, S.Y., Baeyens, J., 1991. Effect of operating temperature on minimum fluidization velocity. Powder Technol. 67, 217–220. https://doi.org/10.1016/0032-5910(91)80158-F.

Yerushalmi, J., Cankurt, N.T., 1979. Further studies of the regimes of fluidization. Powder Technol. 24, 187–205. https://doi.org/10.1016/0032-5910(79)87036-9.

Zhang, H., Kong, W., Tan, T., Baeyens, J., 2017. High-efficiency concentrated solar power plants need appropriate materials for high-temperature heat capture, conveying and storage. Energy 139, 52–64. https://doi.org/10.1016/j.energy.2017.07.129.

Zhang, H., Kong, W., Tan, T., Flamant, G., Baeyens, J., 2017. Experiments support an improved model for particle transport in fluidized beds. Sci. Rep. 7, 10178. https://doi.org/10.1038/s41598-017-10597-3.

Solar Energy 265 (2023) 112118

Contents lists available at ScienceDirect

Solar Energy

journal homepage: www.elsevier.com/locate/solener

Heat transfer in a fluidized bed tubular solar receiver. On-sun experimental investigation

Ronny Gueguen [a], Guillaume Sahuquet [a], Michael Tessoneaud [a], Jean-Louis Sans [a], Emmanuel Guillot [a], Alex Le Gal [a], Roger Garcia [a], Samuel Mer [b], Adrien Toutant [b], Françoise Bataille [b], Gilles Flamant [a,*]

[a] Processes, Materials and Solar Energy Laboratory, PROMES-CNRS, 7 Rue du Four Solaire, 66120 Font-Romeu, France
[b] Processes, Materials and Solar Energy Laboratory, PROMES-CNRS, University of Perpignan (UPVD), Tecnosud, Rambla de la Thermodynamique, 66100 Perpignan, France

ARTICLE INFO

Keywords:
Tubular particle solar receiver
Particle-driven CSP
Geldart group A fluidized particles
Upward particle circulation
Heat transfer coefficient

ABSTRACT

Using particles as heat transfer fluid in a solar receiver is an attractive way to increase the global efficiency of solar power plants. In the case of the particle-in-tube solar receiver concept, the fluidized particles circulate vertically in tubes thanks to a controlled pressure gradient and an additional air injection. Experiments are conducted with olivine particles in a one-tube mock-up at the 1 MW CNRS solar furnace (France). The tube of high aspect ratio (more than 3 m height over 48 mm internal diameter) is irradiated along a 1-m height with several solar flux configurations that correspond to realistic operation conditions of a solar thermal power plant. The novelties of this paper lie in extending the operating parameters compared to earlier studies and in linking the fluidization regimes to wall heat transfer. Slugging, turbulent fluidization and fast fluidization regimes are detected within the receiver tube. It is shown that the system can tolerate high solar flux densities, up to 800 kW/m^2. The system proves to be highly controllable and flexible with respect to particle mass flux variation and transient operations. Particle temperature increase ranges from 100 to 650 °C depending on the particle mass flux. Maximum thermal efficiency and particle outlet temperature of respectively ~ 60 % and 680 °C are obtained, proving that this technology can be combined with highly efficient thermodynamic cycles. Global wall-to-particle heat transfer coefficient varies strongly with particle mass flux. It reaches a quasi-plateau above 15 kg/(m^2s) with a mean value of 1000 ± 200 W/(m^2K) and peaks data up to 1500 W/(m^2K). A dimensionless heat transfer index is derived to account for the effects of the particle mass flux on the experimental results. It highlights that both increasing the temperature and working in the turbulent fluidization regime result in the increase of the heat transfer between the tube walls and the particles.

1. Introduction

Concentrated solar power (CSP) plants produce electricity from direct solar irradiation. They offer the key advantage of being able to store the energy directly in the form of heat, in order to align electricity production and consumption. Current commercial power tower CSP plants use molten salt as heat transfer fluid (HTF) to absorb solar energy and store thermal energy, and a Rankine thermodynamic cycle to produce electricity. Increasing the overall efficiency of the power plants and reducing production cost are the shared objectives of the CSP community. The main option for the increase in efficiency of power tower is the integration of a high efficiency conversion cycle that operates at high temperature (>650 °C) while maintaining the main advantages of molten salt (both HTF and storage medium). An attractive solution for fulfilling the previous conditions is to use solid particles [18,34]. It offers the possibility to reach high solar receiver outlet temperatures – higher than 565 °C, which is the current limit with molten salt [11,50]. Temperature higher than 650 °C enables taking advantage of high efficiency thermodynamic cycles based on supercritical fluids (i.e. with water or CO_2) and reducing the total cost of the system [15]. In addition, unlike molten salt, particles do not freeze at low temperatures. Thus, it is no longer necessary to maintain a threshold temperature in the pipes – via electrical resistances – as in the case of molten salt. Consequently, the particle solution removes of the tracking electrical consumption. In addition, oxide particles are chemically stable, have a low toxicity, and

* Corresponding author.
E-mail address: Gilles.Flamant@promes.cnrs.fr (G. Flamant).

https://doi.org/10.1016/j.solener.2023.112118
Received 27 February 2023; Received in revised form 12 September 2023; Accepted 12 October 2023

Nomenclature

Abbreviations

CSP	Concentrated Solar Power
DNI	Direct Normal Irradiation
HTF	Heat Transfer Fluid
I.D.	Internal diameter

Arabic letters

$C_{p,part}$	Particle heat capacity (kJ/(kgK))
d_{sv}	Powder Sauter diameter (μm)
D_t	Tube internal diameter (m)
e_t	Tube thickness (mm)
g	Standard gravity (m/s^2)
G_p	Particle mass flux (kg/(m^{2}s))
H_t	Tube height (m)
$h_{wall,part}$	Wall-to-particle heat transfer coefficient (W/(m^{2}K))
$H_{wall,part}$	Dimensionless wall-to-particle heat transfer index (Ø)
$\dot{m}_p$	Particle mass flow rate (kg/s)
P_{tot}	Relative pressure in the dispenser (mbar)
$\dot{q_{ae}}$	Aeration flow rate (sm^3/h)
S_t	Internal tube section (m^2)
T_{disp}	Particle temperature in the dispenser (°C)
$T_{part,irr}$	Mean particle temperature in the irradiated zone of the tube (°C)
T_{part}^{out}	Particle temperature at the outlet of the irradiated zone of the tube (°C)
$T_{wall,int}$	Internal tube temperature (°C)
$T_{wall,ext}$	External tube temperature (°C)
U_{air}	Superficial air velocity (m/s)

Greek letters

α	Particle volume fraction (Ø)
α_{irr}	Mean particle volume fraction in the irradiated zone of the tube (Ø)
ΔT_{part}	Particle temperature increase in the solar receiver (°C)
$\Delta T_{wall,part}$	Logarithmic mean difference between the walls and particles temperatures (°C)
η_{th}	Thermal efficiency of the receiver (Ø)
ρ_{air}	Air density (kg/m^3)
ρ_{part}	Particle density (kg/m^3)
ϕ_{abs}	Absorbed power by the particles (kW)
φ_{sol}	Incident concentrated solar flux density (kW/m^2)
ϕ_{sol}	Incident concentrated solar power (kW)

low cost. The particle concept can be applied to medium power CSP plants [5].

Three main types of solar receiver using particles are currently being developed. First, the falling particle receiver, designed by Sandia National Laboratory – USA [31,32]. As suggested by its name, the particles are falling as a curtain and are directly irradiated by the concentrated solar flux. It enables working with high concentrated solar flux density (≥700 kW/m^2) associated to high efficiencies and temperatures, respectively around 6 70 % and 700 °C. However, several drawbacks appear as the loss of particles through the cavity aperture and the difficulty to control the particle flow rate, which is imposed by gravity. Second, the centrifugal receiver, designed by the German Aerospace Center – Germany [16,48]. The system is similar to a cement mixer (but working in the centrifugal mode), where the particle flow rate is controlled by the rotational speed of the receiver. The speed is adjusted depending on the incident solar flux. As for the falling particle receiver, the particles are directly irradiated. High receiver outlet temperatures (around 900 °C) have been obtained at lab-scale, which makes it a promising system. However, the receiver size is limited by the necessity to create a stable particle layer at the cylinder wall that limits its thermal power around few MW$_{th}$. Finally, the "particle-in-tube receiver", studied in this paper, developed by PROMES – CNRS laboratory in collaboration with European partners [12,42,17,19]. In this system, the particles are fluidized in a vessel, and circulate upward in vertical metallic irradiated tubes. The flow is imposed by both a pressure gradient and a secondary air injection. Particles are then indirectly heated by the hot internal surface of the tube. The air injection at the bottom of the receiver tubes stabilizes the particle mass flow and enables controlling the fluidization regimes of the suspension. Moreover, changing the injection air flow rate results in gradual variation of the particle mass flux in the tube. The main limitations associated with this concept are the energy used to fluidize the particles and the control of the fluidization regimes that considerably affect the wall-to-particles heat transfer and thus the thermal efficiency of the system [36,44]. Moreover, contrarily to the previously discussed concepts, the indirect heating of particles makes metal tube maximum operation temperature the main limiting factor. Nevertheless, the tubular receiver design is similar to commercial power tower receivers. It can therefore benefit from previous studies, especially concerning the design of a cavity-type receivers, aiming at limiting the thermal losses [20,26].

Table 1
Comparison between the on-sun experimental studies about the particle-in-tube concept of solar receiver.

Reference	[17]	[7]	[43]	[38]	*Present Study*
Particles	Silicon Carbide (SiC)	SiC	SiC	Olivine	Olivine
Particles Diameter (μm)	63.9	63.9	63.9	61	61
Internal Tube Diameter (mm)	36	36	29.7	46	48
Tube Height (m)	1	1	2.27	2.5	2.8
Irradiated Height (m)	0.5	0.5	1	1	1
Superficial Air Velocity (m/s)	0.011 – 0.109	0.021 – 0.042	0.09	0.03 – 0.11	0.025 – 0.469
Particle Mass Flux (kg/(m^{2}s))	7.4 – 24.6	10.2 – 45.1	17 – 44	20 – 110	0 – 93
Comments	One bare tube, proof of concept	One bare tube, extended parameters ranges	16 bare tubes inside a cavity	One finned tube	One bare tube

Since the 2010's, the particle-in-tube concept of solar receiver, also called "Upward Bubbling Fluidized Bed (UBFB)", has been studied in various configurations, gathered in Table 1. First, silicon carbide particles were used, mainly because of their thermal properties. After the proof of concept [17], experiments at ambient temperature were performed to understand the behavior of the gas-particle suspension [10], followed by simulations and on-sun experiments [7,6] with a 0.5 m irradiated tube. Then, a 150 kW$_{th}$ cavity solar receiver composed of 16 tubes, 1 m-height irradiated, has been built in the framework of the

Table 2
Properties of the olivine sample.

Sauter diameter d_{sv}	Bulk density ρ_{part}	Heat capacity $C_{p,part}$	Minimum Fluidization Velocity U_{mf}	Minimum Bubbling Velocity U_{mb}
61 μm	3300 kg/m^3	1 kJ/(kgK) if $T <$ 400 °C Eq.(1) if $T \geq$ 400 °C	0.42 cm/s	0.57 cm/s

CSP2 European project [43]. All these studies showed that this concept of solar receiver can operate with medium solar flux density on the tube walls – up to approximately 400 – 500 kW/m^2 – and led to particle temperatures increase (i.e. difference between the outlet and the inlet of the receiver) of approximately 500 °C. Then, cost and health properties of the particles have been taken into account in the framework of the Next CSP European project that led to the choice of olivine particles as solid material [35]. On-sun experiments have been performed with a single 1-m irradiated long finned tube. A global wall-to-particle heat transfer coefficient of roughly 1200 ± 400 W/(m^{2}K) was measured [38]. This result represents an intensification of the heat transfer compared to the previously cited studies. The main parameter responsible of this increase is the use of fins inside the tube that increases the transfer area. The particles size and physical properties have also a significant impact on the convective transfer. No experimental results with 1 m irradiated long bare tube have been reported. The other operating condition that influences the heat transfer is the fluidization regime. Previous works at ambient temperature identified the fluidization regimes in 3 m long tube [29,28]. They extended the ranges of the particle mass flux and the superficial air velocity compared to previous studies, determined the existence of several fluidization regimes within the tube and their transitions. The turbulent fluidization regime is theoretically associated to the best heat transfer rate [9,24], and it is thus the expected optimal regime for a fluidized particle solar receiver. Nevertheless, the effect of temperature on the regimes transitions velocities is not well known, justifying additional experimental campaign. More generally, the understanding of the suspension behavior at high temperature is necessary to define a control strategy of the solar receiver.

In this context, this paper aims at measuring and characterizing the thermal performances of a single particle-in-tube solar receiver tube using olivine particles as HTF over a large range of the operating

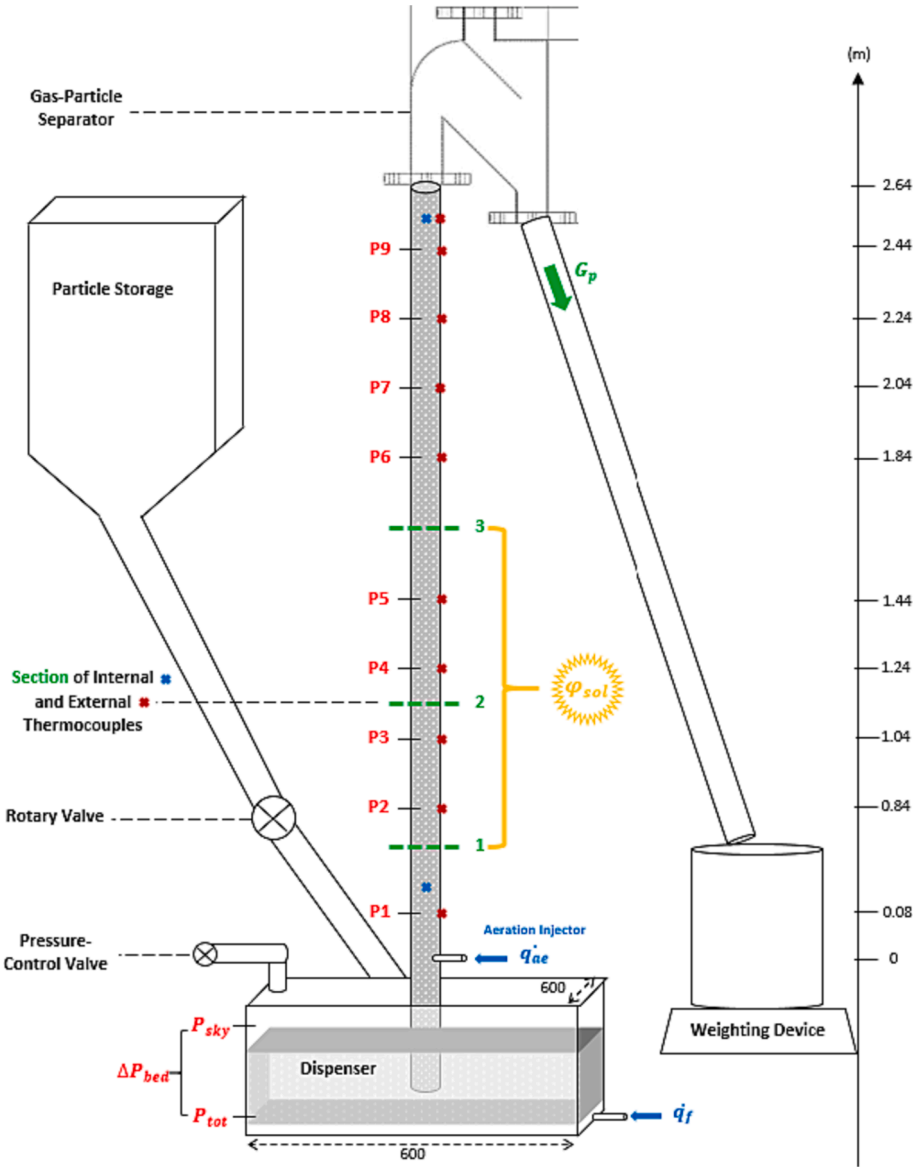

Fig. 1. Schematic representation of the receiver tube.

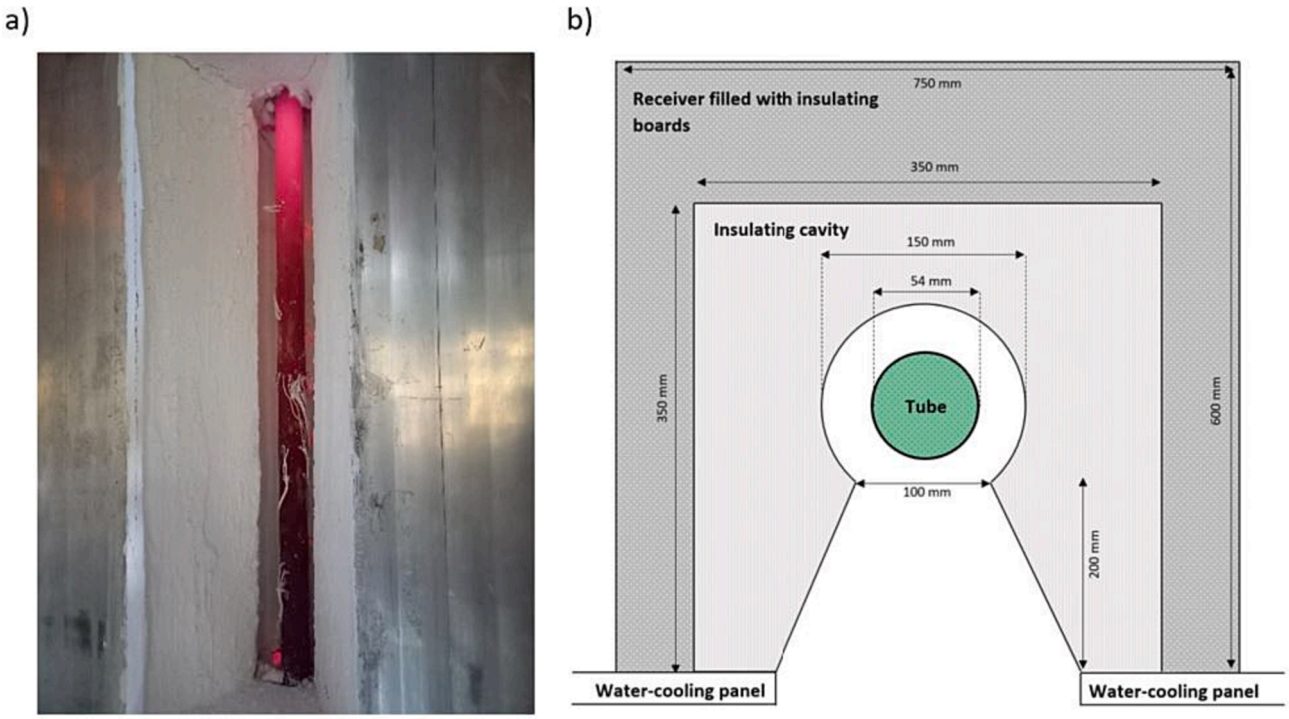

Fig. 2. a) picture of the receiver tube inside its cavity after an on-sun experiment, and b) schematic representation of the tube inside the cavity.

parameters. The behavior of such a solar receiver is first presented in terms of response to control parameters and transient regime. Then, the thermal performances are described. Finally, the wall-to-particle heat transfer coefficients are determined and correlated with the fluidization regimes.

2. Experimental Set-Up

2.1. Particles

Properties of olivine particles used are presented in Table 2. More details can be found in [29]. Both the Sauter diameter d_{sv} and the density ρ_{part} confirm that they belong to the group A of the Geldart classification [23]. Consequently, fluidization of such particles occurs at low air velocities. The heat capacity, $C_{p,part}$, is given by Equation (1) (with T the temperature in degree Celsius). For particle temperature below 400 °C, the heat capacity is fixed to 1 kJ/(kgK) [35,38].

The storage capacity of the suspension can be estimated by calculating the apparent volume heat capacity, given by $\alpha\rho_{part}C_{p,part}$. Assuming an average particle volume fraction α of 0.48 (measured for the fixed bed), this yields an apparent volume heat capacity of around 1.6 MJ/(m^{3}K). This value is in the same order of magnitude than the one of commonly used liquid HTFs [8]. While the storage capacity obtained is twice higher for molten salt, the price per ton of olivine is almost ten times lower (about $100-$150/ton [8,35]).

$$C_{p,part}(T) = 9.70{*}10^{-8}T^3 - 2.62{*}10^{-4}T^2 + 0.73T + 806 \quad (1)$$

2.2. Set-Up description

The experimental setup is illustrated in Fig. 1. The olivine particles are fluidized in a "dispenser" vessel – at the bottom of the mock-up – of squared section of 0.36 m^2, with an air flow rate of 10.6 sm^3/h. It corresponds to a fluidization velocity of 0.97 cm/s, i.e. 1.7 times the minimum bubbling velocity U_{mb}. This air flow passes through a sintered porous bronze plate distributor that enables a homogeneous freely bubbling fluidization regime inside the dispenser.

The receiver is composed of a single Inconel 601® tube of internal diameter (I.D.) $D_t = 48$ mm and thickness $e_t = 3$ mm. The bottom tip of the tube is plunged inside the dispenser fluidized bed. Increasing the pressure in the dispenser, thanks to a leak valve, results in an upward fluidized particle flow in the tube. The latter is driven by the pressure difference between the overpressure imposed in the dispenser P_{tot} and the atmospheric pressure at the top of the tube. The particles are indirectly heated thanks to concentrated solar radiation over a 1-m high zone, identified in yellow in the figure. The tube is painted with an absorbing black paint Pyromark® [1,33] to maximize the solar absorption. Furthermore, the tube is placed inside an insulating cavity with an aperture of 0.1-m width and 1-m height to reduce the thermal losses. The insulating material is painted with highly reflective white magnesium oxide. Fig. 2a shows a picture of the receiver tube inside its cavity after an experiment. A water-cooled panel is placed in front of the cavity that is filled with insulating boards – Insulfrax® insulating material [41], as shown in Fig. 2b.

A secondary air flow rate $\dot{q_{ae}}$, called "aeration", is injected at the bottom of the tube, 50 cm above the porous distributor in the dispenser, through a nozzle of 1.5 mm I.D.. It enables to both stabilize the gas-particle suspension [10] and control the fluidization regimes within the tube [29,28]. The aeration injection height is chosen as the reference height in this study, leading to a tube height $H_t = 2.80$ m. When the height of the suspension reaches this limit, the particles flow outside of the receiver in a tank placed on a weighing scale (see Fig. 1).

2.3. Instrumentation

Eleven pressure probes are implemented in the system (in red in Fig. 1). Two are placed in the dispenser, to measure both the total pressure P_{tot} and the pressure drop through the fluidized bed. The latter is directly related to the mass of particles and allows to keep it approximately constant during a test. Particles feed the dispenser from the storage tank thanks to a vane motor to maintain stationary conditions. Moreover, nine pressure probes are implemented along the tube, regularly spaced. The heights of the probes are detailed in Appendix A. They are connected to differential and relative pressure sensors, to

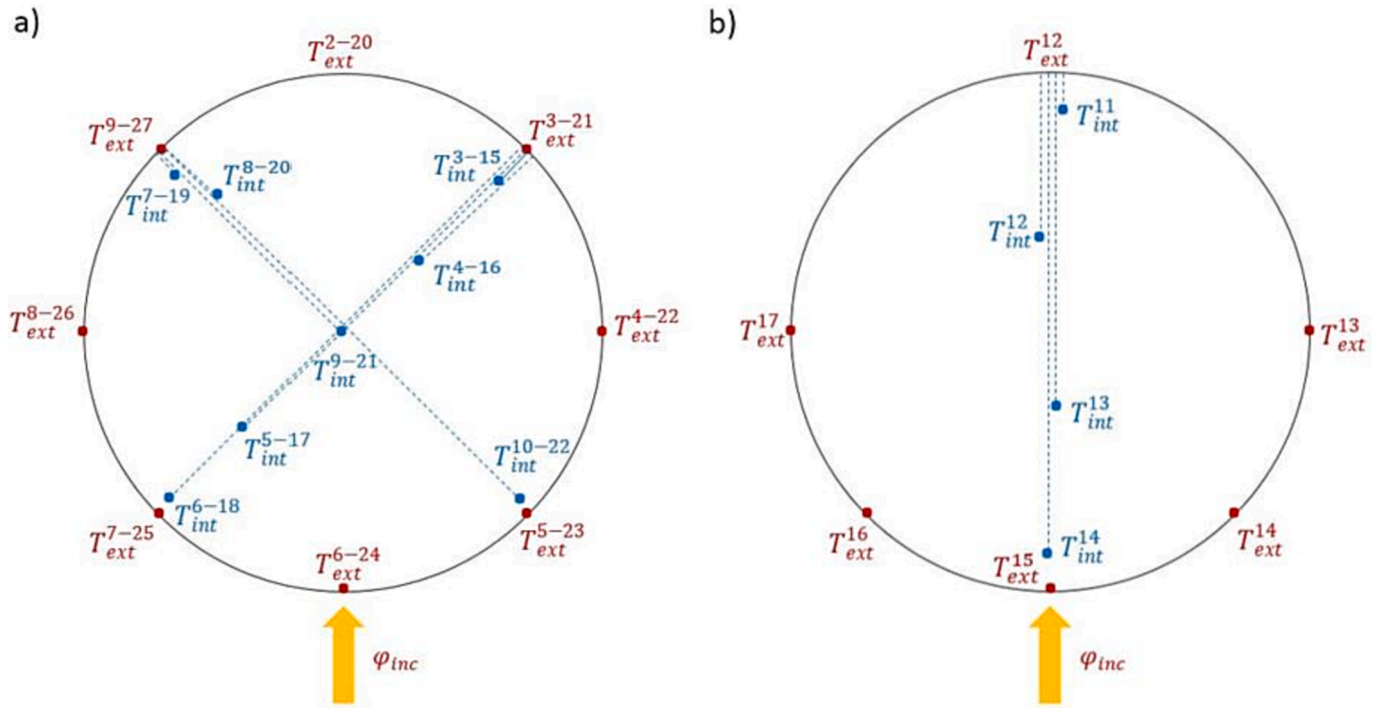

Fig. 3. a) Sections 1 and 3 of thermocouples, at 0.6 and 1.6 m above the aeration respectively that delimitates the irradiated zone, and b) Section 2 of thermocouples at 1.1 m above the aeration at the middle of the irradiated zone.

respectively measure the particle volume fraction and identify the fluidization regime using various signal processing methods that are detailed in [29].

Furthermore, the system is instrumented with 59 K-type thermocouples. In a gas-particle fluidized bed, the thermocouple (TC) arrays can modify the gas-particle flow since the diameter of the TC is approximately 25 times the particles one. Nevertheless, this disturbance influences mainly the flow downstream and, consequently, the TC

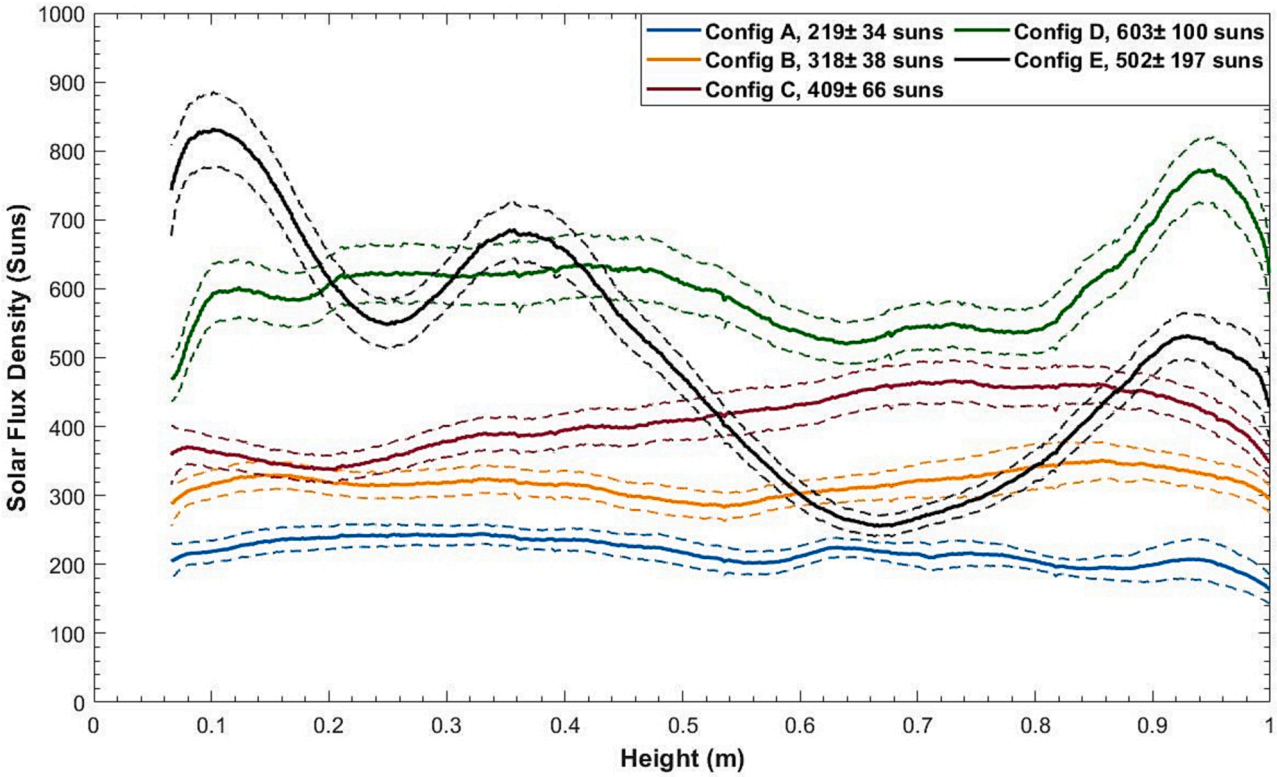

Fig. 4. Measured solar flux distributions used for the experimental campaign. The mean values range between 200 and 600 suns, while local value is measured up to 830 suns.

measurement is a little affected. Another source of uncertainty can be the imperfect contact between the particles and the TC. This issue is not considered as significant since, in fluidized beds, the gas and the solid phase are at the same temperature thanks to the efficient particle mixing and the large surface area of small size powders. Consequently, the temperature measured by the thermocouples is the temperature of both the air and the particles [25]. Moreover, the small particle size favors the contact with any immersed surface. Three thermocouples are dedicated to the measurement of the mean particle temperature in the dispenser, T_{disp}. In the receiver tube, 24 thermocouples indicate the local particle temperature and 32 thermocouples are welded on the outside walls to measure the external tube temperatures. All of them are represented in blue and red respectively in both Fig. 1 and Fig. 3. Three cross sections of the tube are fully instrumented as represented in Fig. 3a-b. They are located at the entrance, the middle and at the end of the irradiated zone of the tube, as identified with green dashed lines on Fig. 1.

The precise positions of the pressure probes and thermocouples in the receiver tube are detailed in Appendix A.

2.4. Concentrated solar flux

The experimental set-up is placed at the focus of the 1 MW solar furnace of CNRS (Odeillo, France). The sun light is reflected twice before reaching the receiver: the first reflection is performed by the heliostats field while the second is performed by the parabola [30,47]. A schematic representation of the working principle is given in Supplementary Information SI-1. To achieve the solar flux distributions, the tracking setpoint of the heliostats were modified to widen the focus of the parabola and illuminate the receiver tube with the best solar irradiation homogeneity. The chosen method consists in acquiring images of a previously calibrated diffusing surface. This method therefore comprises two steps: calibration and image acquisition. To carry out the calibration, a calorimeter is positioned at the location of the solar receiver. One or more heliostats are used to achieve the selected flux densities. Then, an alumina coated (deposited by plasma) aluminum bar is placed inside the cavity of the receiver, at the position of the cavity aperture, and water-cooled. A camera placed in front of the receiver – at a distance of 18 m – provides images of the bar illuminated by the heliostats. These images enable establishing a grayscale-flux correspondence. The next step consists in activating the heliostats in tracking position according to the solar flux density they provide as well as their geometrical distributions (shape at the focus). Five heliostats configurations have been obtained that correspond to maps of the solar flux density distribution at the cavity aperture. Then, a mean value of the flux density is calculated at each height over the larger, and an associated uncertainty is calculated as the sum of the measurement error and of the standard deviation of the measured values. The five distributions are presented in Fig. 4. As the total solar flux density depends on the direct normal irradiation (DNI), the distributions are presented in the figure in terms of concentration ratios, i.e. expressed in suns. The dashed lines are representative of the uncertainties. For each configuration, a mean value can be calculated that varies between 220 and 600 suns. It is associated to an uncertainty calculated as the sum of the calculation error and of the standard deviation of the distribution, then representative of the homogeneity over the height. These values are indicated in the legend of the figure.

Fig. 4 indicates that although the A and B distributions are relatively constant over the height, the C and D distributions – at higher mean solar flux – are less homogenous. Actually, it is difficult to obtain homogeneous high flux configurations over 1-meter height with the solar furnace because such a solar facility is usually designed to obtain a very high concentration ratio (up to 10,000) on small areas [3]. A solar tower is more adapted to deliver this type of distribution for a scaled-up receiver [5,46]. The E distribution (in black in the figure) has been

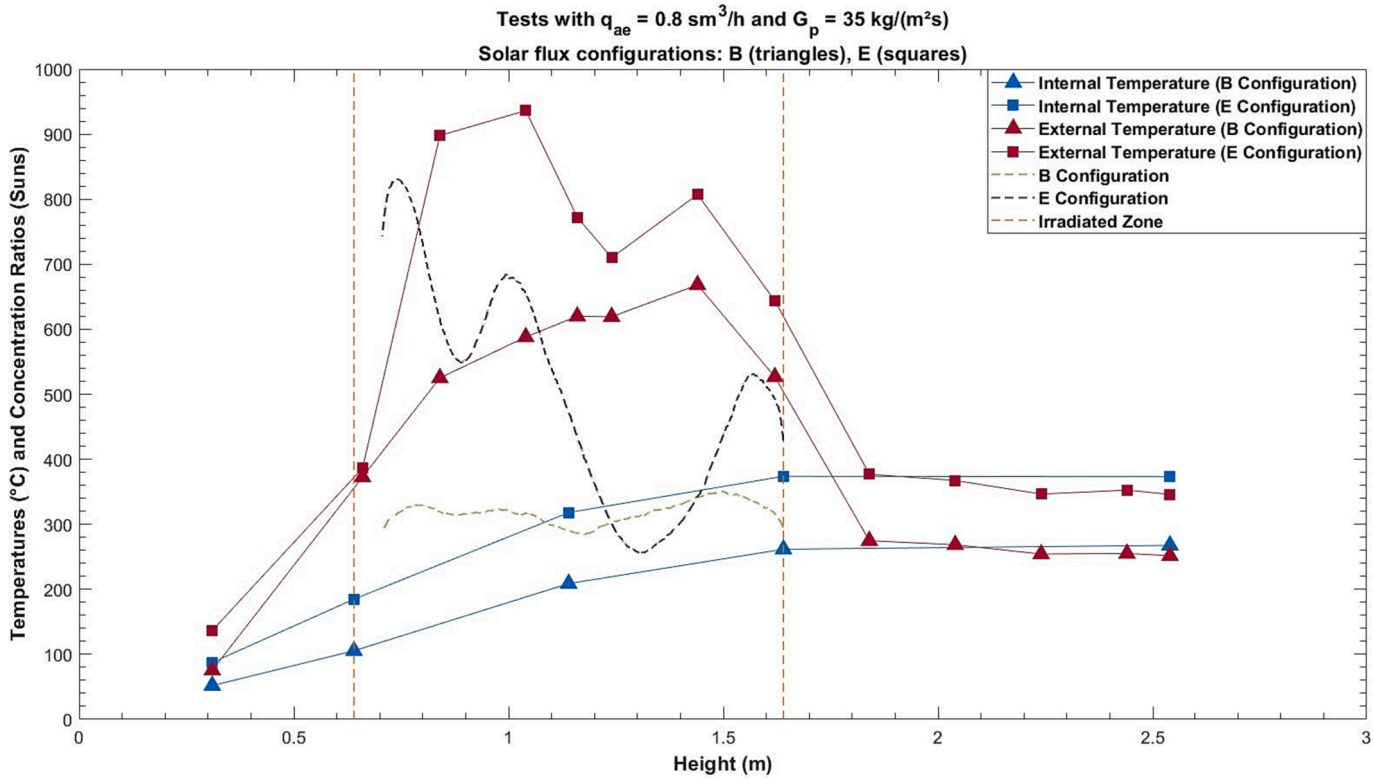

Fig. 5. Temperature distributions with respect to the height: front wall (red) and particle (blue) temperatures, for the B and E solar flux configurations (triangles and squares respectively). The associated flux distributions are respectively in green (B) and black (E). The aeration flow rate and the particle mass flux are identical for both cases and respectively equal to 0.8 sm^3/h and 35 $kg/(m^2s)$. (For interpretation of the references to color in this figure legend, the reader is referred to the web version of this article.)

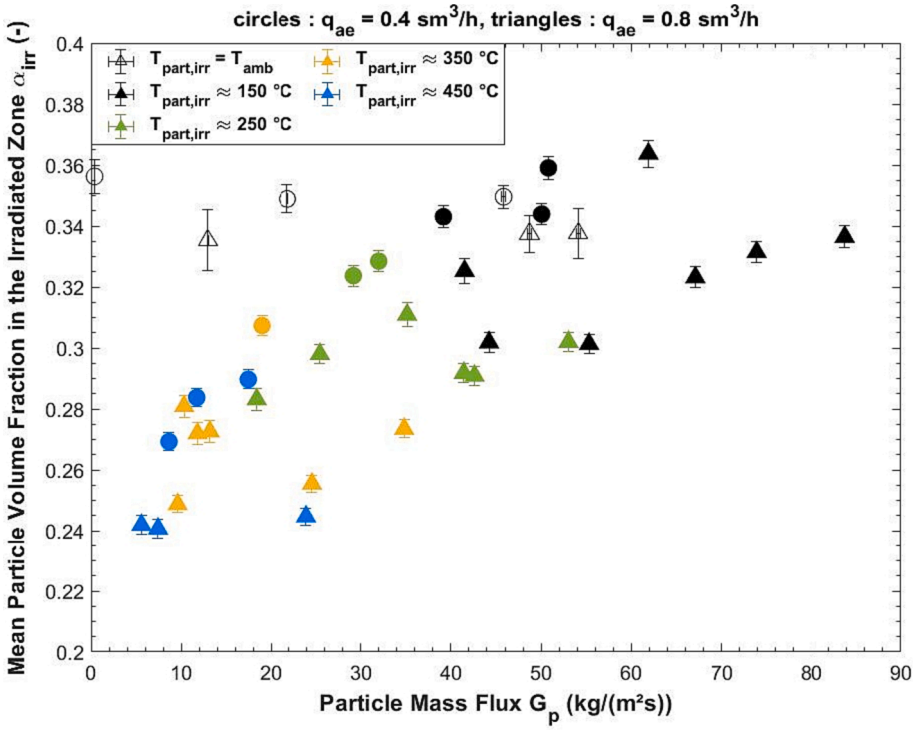

Fig. 6. Evolution of the mean particle volume fraction in the irradiated zone as a function of the particle mass flux, for aeration flow rates of 0.4 (circles) and 0.8 (triangles) sm^3/h, and for various particle temperatures.

selected to test the sensitivity of the system to strong flux density differences along the height, with similar total incident power than the D distribution. The maximum is at 830 suns at the bottom of the receiver, and the minimum, at 255 suns.

3. Results

A total of 187 tests have been performed in stationary conditions in terms of particle mass flux, pressure and temperature, using a large range of experimental parameters. The associated results are presented in this section.

3.1. Control of the solar power plant

3.1.1. Operating parameters

The experimental setup can be controlled thanks to three parameters:

- The total relative pressure in the dispenser, P_{tot}, which imposes the driven pressure gradient. It ranges from 145 to 380 mbar in the reported experiment.
- The aeration flow rate, $\dot{q_{ae}}$, which enables finely tuning the particle mass flow rate and the fluidization regimes. The later ranges from 0.1 to 2.5 sm^3/h in the reported experiment, which corresponds to superficial air velocity in the tube between 0.025 and 0.469 m/s.
- The incoming concentrated solar flux density that imposes the thermal load of the receiver. According to the solar flux density distributions presented above and the variations of the DNI during the experiments – between 750 and 1030 W/m^2 – the net incident solar power on the receiver ϕ_{sol} varies between 19 and 56 kW.

By adjusting the previous parameters, the operating point of the receiver can be prescribed. The first operating characteristic is the particle mass flow rate, $\dot{m}_p$. Experimentally, it is calculated by linear regression of the particle mass flowing on the weighing scale over time. The uncertainty associated with this measurement is due to both the regression error and the accuracy of the scale (0.01 kg for data recorded at 10 Hz). In the field of fluidization, the particle mass flux G_p is more classically used. It corresponds to the particle mass flow rate normalized by the internal section of the tube. It varies between 0 and 93 $kg/(m^2s)$ during the experimental campaign, that corresponds to a particle mass flow rate of 0.17 kg/s, or 613 kg/h. An example of the evolution of the particle mass flux with respect to the total pressure in the dispenser and for various aeration flow rates and incident solar flux densities is given in Supplementary Information SI-2. Increasing the solar flux leads to a decrease of the total pressure required to reach a given particle mass flux. This behavior is mostly due to the temperature increase, which results in a decrease of the particle volume fraction, α. The same trend is observed when increasing the aeration flow rate, as observed at ambient temperature in [28]. This point is discussed in the next section.

The second important characteristic of the solar receiver is the particle temperature. To characterize the suspension temperature from a global point of view, an average temperature is calculated over the irradiated zone, $T_{part,irr}$. According to the results, this average is very similar to the value of the particle temperature at the middle of the irradiated zone. Then, to facilitate the calculations, only the latter is considered. The average temperature is calculated by Equation (2), and the positions of T_{int}^{12} and T_{int}^{13} are presented in Fig. 3b (the two sensors are located 1.1 m above the aeration, at radial positions of respectively $D_t/3$ and $2D_t/3$).

$$T_{part,irr} = \frac{T_{int}^{12} + T_{int}^{13}}{2} \tag{2}$$

Fig. 5 presents the particle and front wall temperatures distributions along the tube height for two similar tests done with 0.8 sm^3/h of aeration flow rate and 35 $kg/(m^2s)$ of particle mass flux, for the B and E solar flux density configurations, identified respectively with the triangles and squares. In the irradiated zone, delimited in the figure by the vertical dashed lines, the wall temperatures profiles (red) follow the shapes of the solar flux distributions (green and black respectively for the B and E configurations), while the particle temperatures (blue)

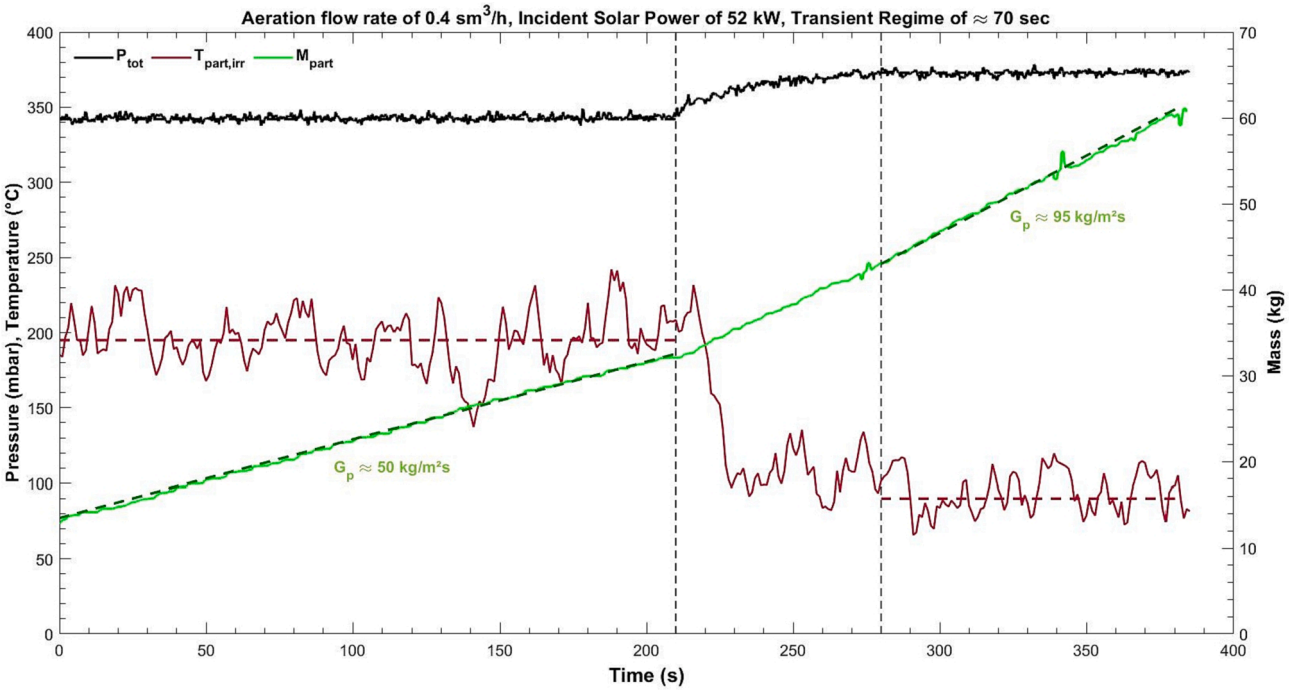

Fig. 7. Time evolutions of the particle temperature inside the irradiated zone (red), the particle mass flux (green) after an increase of the pressure in the dispenser (black) and for a constant aeration flow rate. (For interpretation of the references to color in this figure legend, the reader is referred to the web version of this article.)

increase with the height due to the internal mixing. In these examples, although the particles are at ambient temperature in the dispenser – around 20 °C – they are already heated at their entrance in the irradiated zone. This is related to the reflux of the particles at the tube walls, previously highlighted by [7], and to conduction in the tube walls.

3.1.2. Particle volume fraction

Since the HTF is composed of air and particles, a change of the operating parameters may lead to a change of the effective density, which depends on the particle volume fraction, α. A special concern is thus dedicated to the evolution of this quantity. The particle volume fraction is the fraction occupied by the particles in a given control volume, calculated with Equation (3). It is measured thanks to the differential pressure ΔP between two successive pressure probes, spaced by Δh along the tube height. Neglecting the pressure drop terms related to the acceleration and friction of the particles, α is directly due to the relative weight of the suspension [22,50].

For the sake of clarity, an average volume fraction is calculated inside the irradiated zone, α_{irr}, i.e. between the pressure probes $P2$ and $P5$ (cf. Fig. 1).

$$\alpha = \frac{\Delta P}{(\rho_{part} - \rho_{air}) g \Delta h} \tag{3}$$

Fig. 6 represents the evolution of α_{irr} as a function of the particle mass flux G_p, for two aeration flow rates: 0.4 (circles) and 0.8 (triangles) sm^3/h. The marker colors are representative of the mean particle temperature $T_{part,irr}$. Previous works [29,28] have shown that at ambient temperature, α decreases quasi-linearly with the aeration flow rate and slightly depends on the particle mass flux, as observed here by the empty markers on the figure. However, for a given aeration flow rate, the trend is significantly different when the system is irradiated. For example, at ambient temperature and 0.8 sm^3/h of $\dot{q_{ae}}$, the particle volume fraction slightly varied between 0.31 and 0.33 for a particle mass flux ranging from 0 to 90 $kg/(m^2s)$. With particles temperature between 150 and 450 °C and the same aeration flow rate, α_{irr} ranges here from 0.24 to 0.33 in the same range of particle mass flux. This Figure also highlights that the particle volume fraction decreases with the temperature. A more detailed evolution of α_{irr} as a function of the superficial air velocity and the particle temperature is presented in Supplementary Information SI-3.

3.1.3. Transient regime

A change of one of the control parameter, for example a change of DNI induced by cloud passing, involves a transient response of the system. The management of such event is of paramount importance to optimize control, operation security, and performances of future large-scale particle receiver. In the following section, the effect of different parameters on the transient response of the system is discussed.

Fig. 7 presents the transient response of the system to a variation of the dispenser pressure, for a constant aeration flow rate of 0.4 sm^3/h and an incident solar power of 52 kW (using the D solar flux configuration). The test starts with stationary conditions in terms of the particle temperature in the irradiated zone $T_{part,irr}$ (in red) and of the particle mass flux G_p (linear regression of the particle mass M_{part} in green). At $t = 210$ s, the dispenser pressure increases by closing the leak valve. As a results, the pressure P_{tot} (in black) rises from 340 to 375 mbar. The transient duration, defined as the time required for the pressure to reach 95 % of the pressure variation, is equal to 70 s. The latter is identified on the figure by the vertical dashed lines.

Without particle circulation, an increase of the pressure in the dispenser induces a rise of the suspension height. When the suspension flows, the height cannot be adjusted, thus the dispenser pressure increase results in an increase of the particle mass flow rate. The latter is identified in Fig. 7 by a slope change in the mass weighted by the scale (green curve). For on-sun operation, the particle mass flux increase results in a decrease of the particle temperature. For this test, a slight change of pressure – a 10 % increase in this example – led to a 90 % relative increase of the particle mass flux (from 50 to 95 $kg/(m^2s)$) and to a 54 % relative decrease of the particle temperature (from 195 to 90 °C). From a process control point of view, the power plant operator could thus use a pressure based control in case of “strong variation”

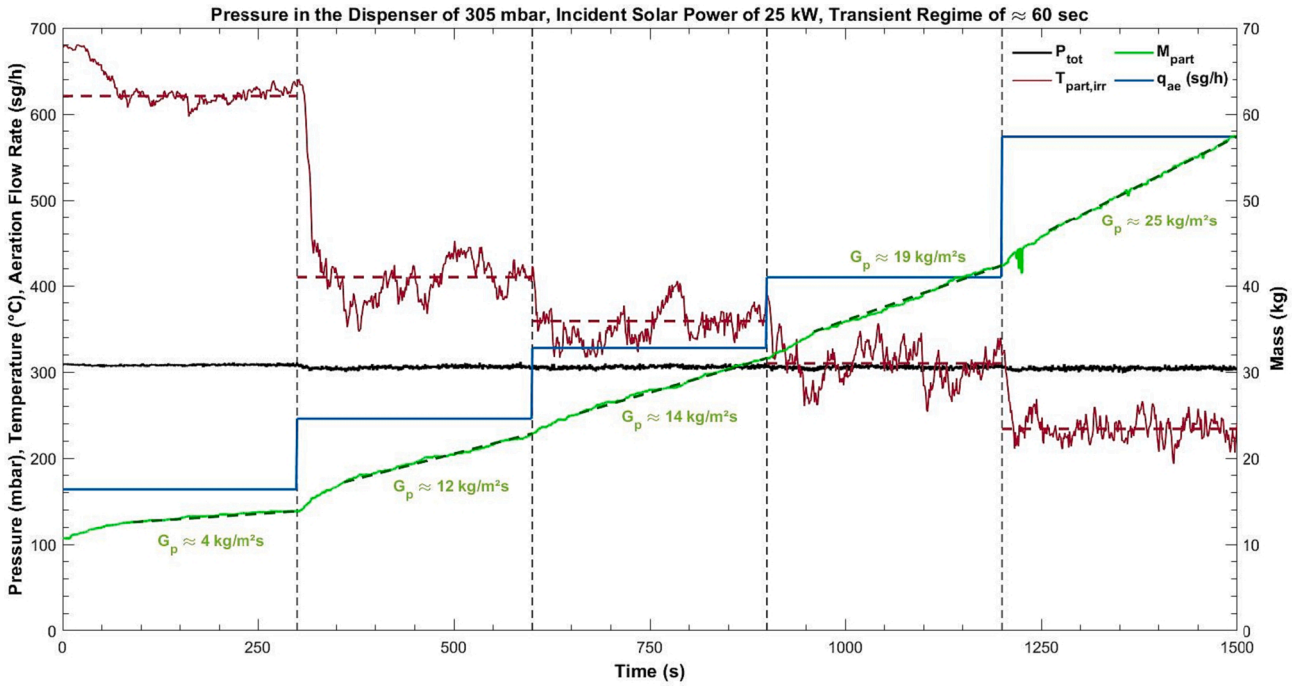

Fig. 8. Temporal evolutions of the particle temperature inside the irradiated zone (red), the particle mass flux (green) after an increase of the aeration flow rate (blue) and for a constant pressure in the dispenser (black). (For interpretation of the references to color in this figure legend, the reader is referred to the web version of this article.)

events.

Fig. 8 shows the response of the system to an aeration flow rate variation, with a constant pressure in the dispenser of 305 mbar, and a constant incident solar power of 25 kW (the B solar flux configuration). The initial steady state corresponds to a particle temperature in the irradiated zone $T_{part,irr}$ (in red), a particle mass flux G_p (in green) and an aeration flow rate (blue), expressed in sg/h instead of sm^3/h to fit with the scale of the figure. At $t = 300$ s, the aeration flow rate increases from 0.16 to 0.24 sm^3/h. Successive aeration mass flow rate changes are presented on the figure. The starting time of each transient is illustrated by a vertical dashed line. The air flow rate rise induces a dilution of the suspension, i.e. a decrease of the particle volume fraction α. As a first approximation, the particle volume fraction over the tube height is proportional to P_{tot} (the pressure drop over the height of the tube) according to Eq.(3). As the driving pressure of the flow (i.e. P_{tot}) remains constant during the test, a reduction of α results in an increase of the particle mass flux to respect the pressure balance. As in Fig. 7, the mass flow rise is characterized by an increase of the slope of the particle mass variation after each increase of $\dot{q_{ae}}$. Assuming a constant incident solar power, the mass flux rise induces a decrease of the temperature. As discussed before (Section 3.1.2), for a given aeration flow rate and particle mass flux, when $T_{part,irr}$ decreases, the particle volume fraction increases. This sequence highlights a self-regulation behavior of the system that oscillates around its new equilibrium before stabilizing. In Fig. 8, five successive steady states induced by five successive increases of the aeration flow rate are illustrated. For each sequence, the self-regulation duration lasts approximately 60 s and can be summarized as follows.

$$\dot{q_{ae}}\nearrow \Rightarrow \alpha_{irr}\searrow \Rightarrow G_p\nearrow \Rightarrow T_{part,irr}\searrow \Rightarrow \alpha_{irr}\nearrow$$

Between the first and the second sequence, a very strong decrease of the particle temperature occurs due to a very low initial particle mass flux. Between the second and the third sequence, the aeration flow rate increases from 0.24 to 0.32 sm^3/h, i.e. a relative increase of 33 %. This strong variation of the control parameter results in small relative variations of the particle temperature and mass flux, respectively of 12 % (from 410 to 360 °C) and 16 % (from 12 to 14 kg/(m^2s)). To summarize, from a process control point of view, the power plant operator could thus use an aeration flow-based control to finely adjust the operating conditions.

Table 3
Response of the system from an increase of the pressure in the dispenser and of the aeration flow rate.

Increase of the operating parameter		Consequences		
		Particle mass flux Increase	Particle mass flux Increase	Duration of the transient regime
Pressure	10 % From 340 to 375 mbar	90 % From 50 to 95 kg/(m^2s)	54 % From 195 to 90 °C	70 s
Aeration flow rate	33 % From 0.24 to 0.32 sm^3/h	16 % From 12 to 14 kg/(m^2s)	12 % From 410 to 360 °C	60 s

The responses of the system to an increase of the pressure and the aeration flow rate are summarized in Table 3.

3.2. Thermal performances of the receiver

3.2.1. Absorbed power

The particle temperature increase in the solar receiver is given by $\Delta T_{part} = T_{part}^{out} - T_{disp}$. The particle outlet temperature, T_{part}^{out}, is given in Equation (4). It is calculated as the average of the particle temperature measured within the tube at the outlet of the irradiated zone, at radial positions of $D_t/3$, $D_t/2$ and $2D_t/3$ (cf. Fig. 3a). However, the particle inlet temperature is not measured at the inlet of the irradiated zone, because the particles are already heated due mainly to the reflux at the tube walls [7]. To account for these effects on the measurements and describe the real increase due to the solar irradiation, the temperature in the dispenser T_{disp} is used. During the experimental campaign, the

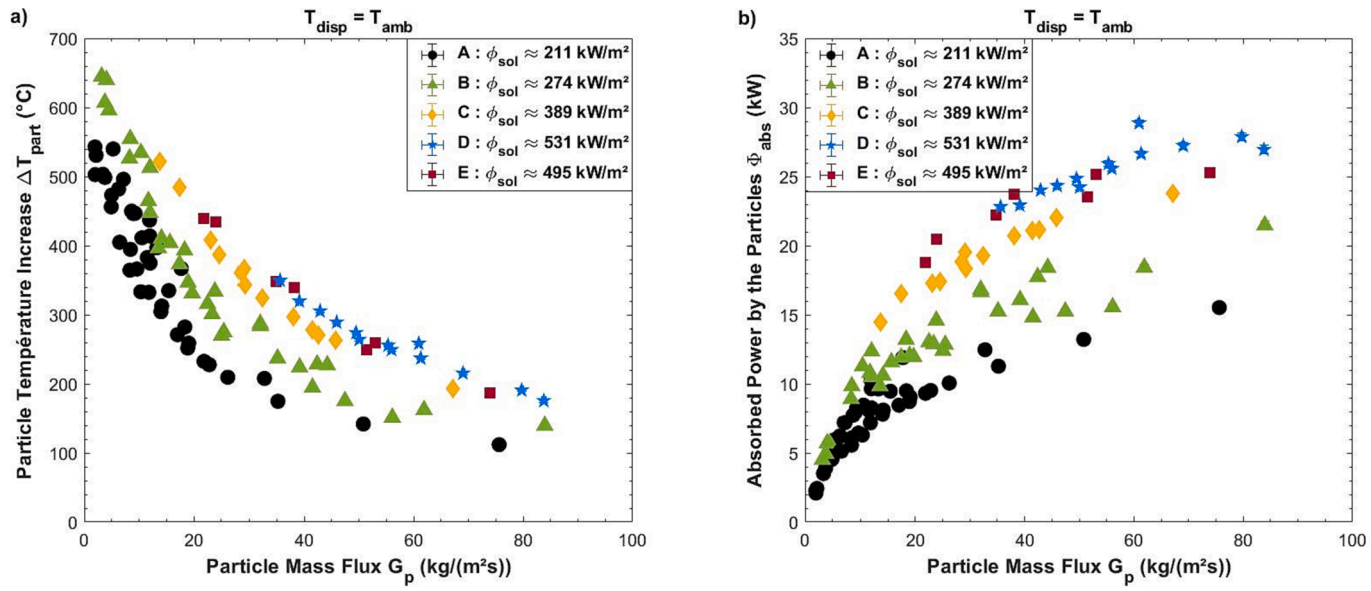

Fig. 9. Evolutions of a) the increase of the particle temperature, and b) the absorbed power by the particles, as a function of the particle mass flux and for various incident solar flux densities.

temperature increase ΔT_{part} ranges between 105 and 645 °C, as shown in Fig. 9a as a function of the particle mass flux.

Fig. 9b shows the evolution of the absorbed power by the particles ϕ_{abs}, calculated by Equation (5) with respect to the particle mass flux. In this Equation, $C_{p,part}$ is calculated as a function of the mean particle temperature in the irradiated zone, $T_{part,irr}$ (cf. Equations (1)–(2)). Since, the particles belong to the class A of the Geldart classification [23], the air velocities needed to fluidize them (and vary the fluidization regimes) are low. Consequently, the absorbed power by the air represents less than two percent of the power absorbed by the particles. This quantity is thus negligible in the power balance [43].

In Fig. 9a-b, the various markers and colors are representative of the incident concentrated solar flux density, i.e. the product of the concentration ratio and the DNI. For all the tests, the dispenser is at ambient temperature, ~25 °C. The bars amplitudes indicate the measurement and calculations errors of the particle mass flux and of the particle temperatures.

$$T_{part}^{out} = \frac{T_{int}^{16} + T_{int}^{17} + T_{int}^{21}}{3} \tag{4}$$

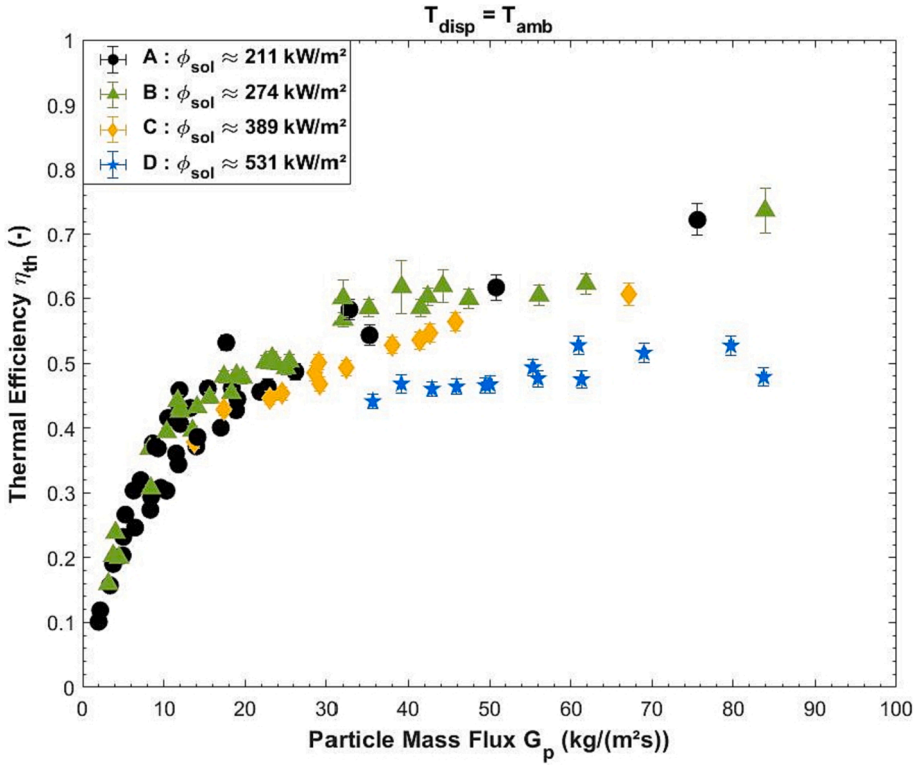

Fig. 10. Evolution of the thermal receiver efficiency as a function of the particle mass flux and for various incident solar flux densities.

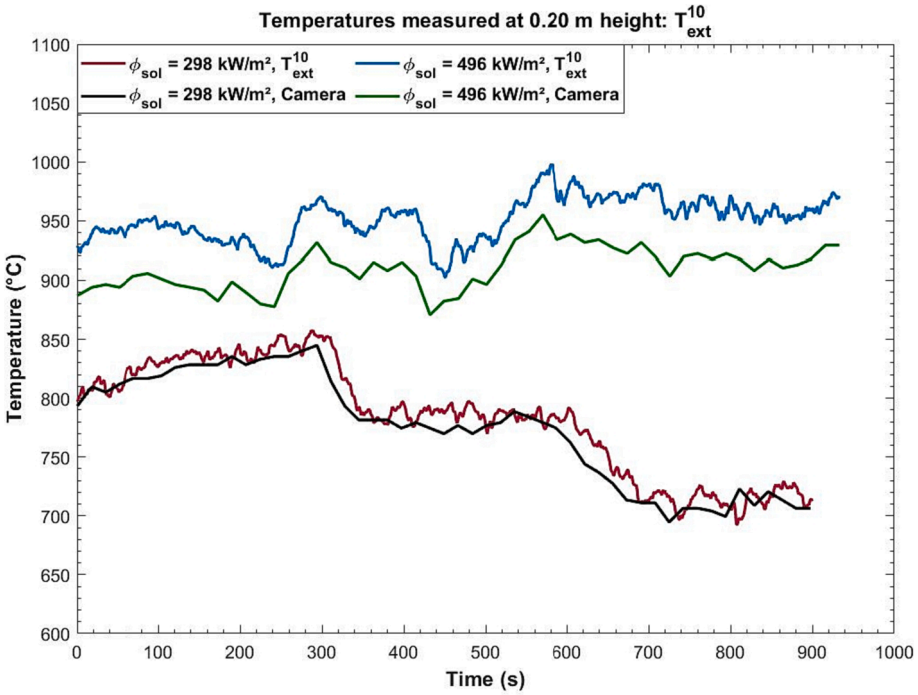

Fig. 11. Comparisons of the temperatures measured by the thermocouple T_{ext}^{10} and the infrared camera, at 0.84 m height, for two solar flux configurations.

$$\phi_{abs} = \dot{m}_p C_{p,part}\left(T_{part}^{out} - T_{disp}\right) \quad (5)$$

Figrrrure 9a-b illustrates that, for a given solar power, increasing the particle mass flux leads to an increase of the absorbed power by the particles and a decrease of the particle temperature. This is directly related to the particle mean residence time in the irradiated part of the tube. For example, for a particle mass flux of 2 kg/(m^{2}s), the mean residence time is approximately 400 s and corresponds to a temperature increase of 530 °C, while for a particle mass flux of 93 kg/(m^{2}s), it drops to respectively 7.5 s and 105 °C. Furthermore, for a given G_p, increasing the solar power leads to an increase of the wall and particles temperature, and finally of the absorbed power.

Despite very high peak in terms of concentration ratio for the E solar flux configuration (above 800 suns) the maximum tube wall temperature remains below 1000 °C. Compared to the D configuration, the particle temperature increase is very similar but the wall temperature distribution is very different (cf. Section 2.4). It means that from the particle temperature increase view point, only the total energy received on the aperture of the cavity matters. Since the E configuration is a limiting case that results in very high wall temperature gradient and heterogeneity, is not taken into account anymore in the following result analysis.

3.2.2. Thermal efficiency

The thermal efficiency of the receiver, η_{th}, represents the ratio of the absorbed power over the incident solar power, as presented in Equation (6). Fig. 10 presents the variation of η_{th} with respect to the particle mass flux. The trend is logically similar to the one presented for the absorbed power. Increasing the particle mass flux leads to an asymptotic increase of the receiver thermal efficiency which seems to converges for mass flux above 30 – 40 kg/(m^{2}s). This finding agrees with the data of [38] with one finned tube. However, the efficiencies obtained in this latter work were slightly higher (of approximately 5 % for all the solar configurations tested) due to the higher exchange surface between the hot tube and the particles. Considering the small increase in efficiency, the addition of fins within the tube of the particle-in-tube solar receiver seems to be not worthy. Furthermore, the efficiency was much higher (between 0.85 and 90 for particle mass flux around 40 kg/(m^{2}s)) in the earlier study with 16 bare tubes tanks to the cavity effect [43].

$$\eta_{th} = \frac{\phi_{abs}}{\phi_{sol}} \quad (6)$$

Fig. 9 and Fig. 10 presented above highlight the need of combining high particle mass flux and high incident solar power to obtain both high particle outlet temperature and high thermal efficiency. Results are obtained with particle inlet temperature at the ambient. Additional experiments have been performed with preheated particles in the dispenser, with temperature ranging from 100 to 300 °C. The results are presented in Supplementary Information SI-4. For given particle mass flux and incident solar flux, preheating the particles leads, as expected, to higher particle outlet temperature. Nevertheless, as the temperature increases, the thermal losses – mostly radiative – increase too, which leads to a decrease of the absorbed power and thus to the thermal efficiency.

3.3. Heat transfer

3.3.1. Global heat transfer coefficient

To characterize the heat transfer between the internal walls of the tube and the particles over all the irradiated zone height, a global wall-to-particles heat transfer coefficient, $h_{wall,part}$, is calculated with Equation (7) [7,38]. The latter is similar to the classical formulation of convective exchange in a heat exchanger. Since $h_{wall,part}$ aims to quantify the way the concentrated heat power is transferred to the particle in the irradiated part of the tube, the considered exchange area is half of the internal cylinder surface, $S_{exch} = \pi D_t H_{irr}/2$.

To consider the variations of the wall to particle temperature difference over the tube height, a logarithmic mean value is considered between the inlet and the outlet of the irradiated zone, $\Delta T_{wall,part}$ (Equation (8)). The associated uncertainties are detailed in Appendix B.

$$h_{wall,part} = \frac{\phi_{abs}}{S_{exch}\Delta T_{wall,part}} \quad (7)$$

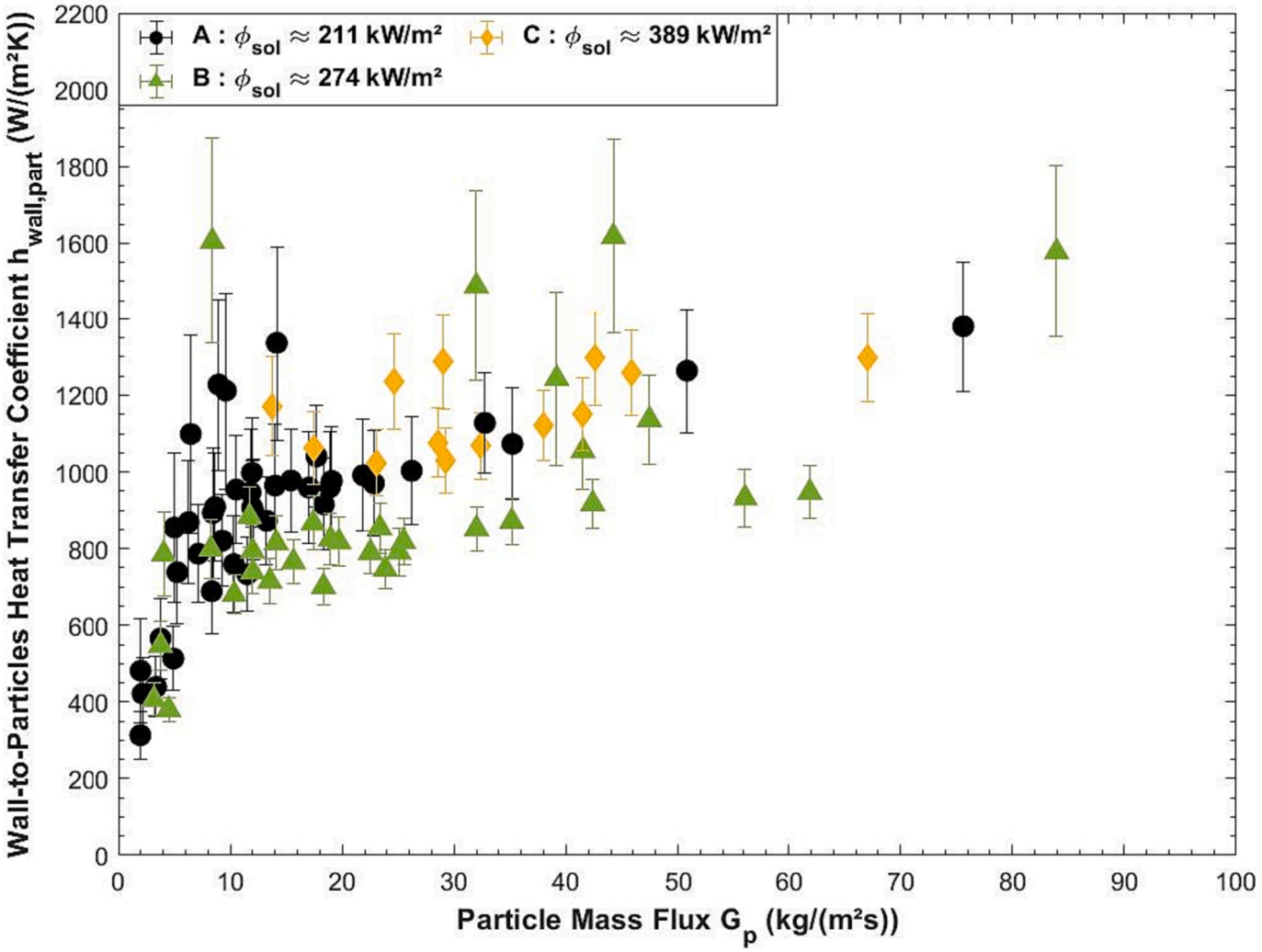

Fig. 12. Evolution of the wall-to-particles heat transfer coefficient as a function of the particle mass flux and for various incident solar flux densities.

$$\Delta T_{wall,part} = \frac{\left(T^{in}_{wall,int} - T^{in}_{part}\right) - \left(T^{out}_{wall,int} - T^{out}_{part}\right)}{\ln\left(\frac{T^{in}_{wall,int} - T^{in}_{part}}{T^{out}_{wall,int} - T^{out}_{part}}\right)} \tag{8}$$

For this calculation, the particle inlet temperature considered is not anymore the dispenser temperature but an average of the recorded temperature at the inlet of the irradiated zone, T^{in}_{part} (Equation (9)). The internal wall temperatures, $T^{in}_{wall,int}$ and $T^{out}_{wall,int}$, are estimated based on the measurement performed on the external walls and considering the heat conduction trough the tube (Equation (10)). In the equation, the mean solar flux density φ_{sol} is given by the solar flux distributions, $\alpha_{pyro} = 0.85$ is the absorptivity of the Pyromark® paint in the solar wavelengths ("Alloy Wire International, Inconel 601," 2020; [33], and $\lambda_{inconel}$ is the thermal conductivity of the Inconel® material ("Alloy Wire International, Inconel 601," 2020). The latest is given by Equation (11) with T the temperature in °C. Finally, the external wall temperatures, $T^{in}_{wall,ext}$ and $T^{out}_{wall,ext}$, are measured by the welded thermocouples (cf. Section 2.3).

$$T^{in}_{part} = \frac{T^{4}_{int} + T^{5}_{int} + T^{9}_{int}}{3} \tag{9}$$

$$T^{in,out}_{wall,int} = T^{in,out}_{wall,ext} - \frac{e_t}{\lambda_{inconel}} \alpha_{pyro} \varphi_{sol} \tag{10}$$

$$\lambda_{inconel} = 0,0169{*}T + 10,95 \tag{11}$$

However, previous experiments have highlighted the difficulty to measure precisely the temperatures with externally welded thermocouples [38]. For on-sun experiment, when the welded thermocouple is exposed to high concentrated solar flux, its temperature may be higher than the tube walls due to the thermal resistance between the weld and the surface. Consequently, the temperature must be corrected. A second measurement were performed using an infrared camera placed in front of the receiver (at 18 m of the focus of the parabola) to estimate the measurement error due to the thermal resistance. A comparison of the two measurement results, at the location of the thermocouple T^{10}_{ext} (0.84 m above the aeration injection), is presented in Fig. 11 for two solar flux configurations. The temperature is post-processed from the camera image using an emissivity of 0.85. For relatively low solar flux density, the temperature given by the two measurement agrees very well. However, for high solar flux density, the temperature given by the thermocouple (blue) is overestimated compared to the temperature given by the camera (green) by approximately 50 °C.

Then, experiments were performed with the infrared camera to compare the temperatures given by the thermocouples at various height of the tube. Nevertheless, it is experimentally difficult to extract significant trend of the temperature difference versus the solar flux because several parameters can affect the temperature given by the camera. First, the emissivity of the tube can vary along the tube height. Second,

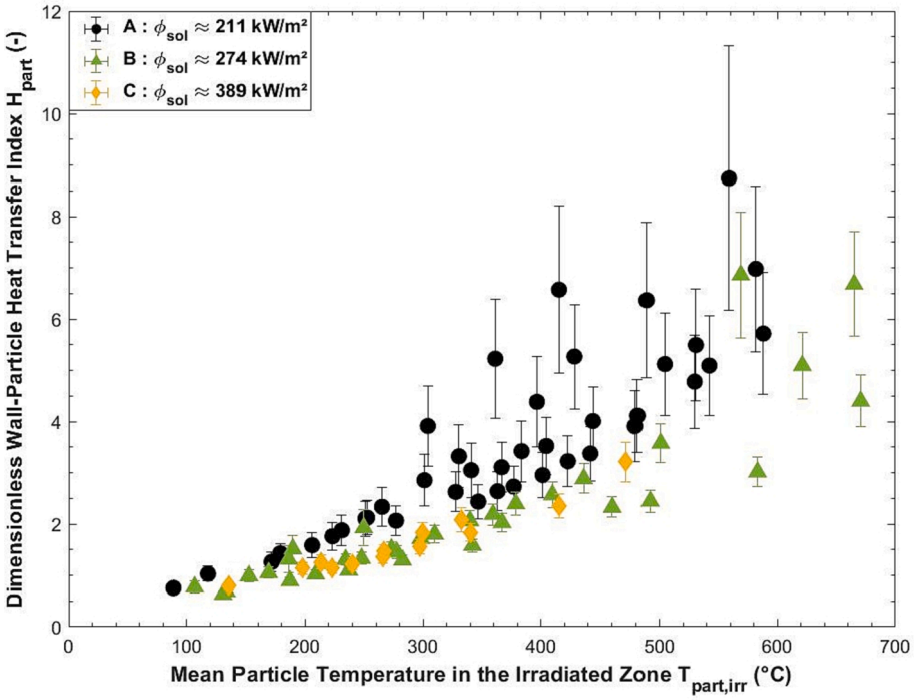

Fig. 13. Evolution of the dimensionless wall-to-particle heat transfer index as a function of the mean particle temperature in the irradiated zone, and for various incident solar flux densities.

the resolution of the camera limits the spatial accuracy of the measurement at 1 pix/cm. Third, the external welded thermocouples have white ceramic sheaths (as shown in Fig. 2a) that may be recorded by the camera and result in wrong local data. As the temperatures measured by the thermocouples are always higher than the temperatures measured by the IR camera and the difference varies with the solar flux density, we chose to decrease the measured data by a mean value of 25 °C. It is associated to a constant uncertainty of 25 °C.

Fig. 12 presents the evolution of the global wall-to-particles heat transfer coefficient as a function of the particle mass flux, for three incident solar flux densities. Due to the strong heterogeneities of the D and E solar distributions, they are not presented in the figure.

According to Equation (7), $h_{wall,part}$ varies similarly to the absorbed power by the particles. Since the extracted power by the particles increases with the particle mass flux as does $h_{wall,part}$. A plateau is reached when the increase in the temperature difference between the wall and the fluidized bed compensates the previous trend. The calculated values are consistent with previous studies. For examples, [38] obtained mean heat transfer coefficients of 1200 ± 400 W/(m^{2}K) with a finned tube, for particle mass flux higher than 40 kg/(m^{2}s) and solar flux density of 236 kW/m^2. Logically, this value is higher than the one obtained in the present study in similar operating conditions (for homogeneous solar flux configurations A et B) since fins enhance heat exchange area. Furthermore, with silicon carbide particles and one bare tube, [7] measured mean coefficients of 800–900 W/(m^{2}K) for particle mass flux in the range 30–40 kg/(m^{2}s) and solar flux density of 387 kW/m^2. The operation conditions correspond to the C solar flux configuration, for which the measured values of $h_{wall,part}$ are slightly higher in the present study. The main difference between the two experiments is the irradiated length of the tube, that was 0.5 m for [7].

As a conclusion, according to Fig. 12, the global wall-to-particle heat transfer coefficient varies mainly with the particle mass flux. It reaches a quasi-plateau above 15 kg/(m^{2}s) with a mean value of 1000 ± 200 W/(m^{2}K) and some peaks data up to 1500 W/(m^{2}K). However, it is difficult to extract the influence of the particle temperature and of the fluidization regime from this global heat transfer coefficient. An alternative approach is discussed in the next section.

3.3.2. Discussion about the heat transfer

In an ideal solar receiver, the temperature of the absorber wall is equal to the temperature of the HTF. It corresponds to an infinite heat transfer coefficient between the wall and the HTF. Consequently, the value of the heat transfer coefficient is required to design a solar receiver and to estimate the wall-to-HTF temperature difference, the thermal gradient along and around the tube, the associated thermal stresses and, finally, the lifetime of the component. The main objective being to reach the highest outlet temperature of the HTF with the smallest temperature difference between the irradiated wall and the HTF. From this concern, the heat transfer coefficient is a global quantitative data that does not traduce qualitatively the internal temperature distribution inside the tube from the internal wall to the core of the HTF flow. This data is unknown for fluidized particle flowing in a solar-irradiated tube. Consequently, the following section is an attempt to analyze the quality of the heat transfer as a function of the fluidized particle flow characteristics with the objective to reach high outlet temperature with reduced thermal gradient at the wall-to-particle interface.

A dimensionless quantity, $H_{wall,part}$, is defined in Equation (12). It represents the ratio of the particle temperature increase over the average temperature difference between the internal walls and the particles. For example, if both the particle temperature increase (ΔT_{part}) and the temperature difference between the walls and the particles ($\Delta T_{wall,part}$) are high, it means that the heat is not correctly extracted from the hot tube. Conversely, high values of $H_{wall,part}$ correspond to high temperature increases of the particle with reduced temperature differences between the internal walls and the particle flow. It means that this dimensionless number is an effective indicator of the heat transfer quality.

$$H_{wall,part} = \frac{h_{wall,part} S_{exch}}{G_p S_t C_{p,part}} = \frac{\Delta T_{part}}{\Delta T_{wall,part}} \tag{12}$$

Fig. 13 shows the evolution of the dimensionless index $H_{wall,part}$ as a function of the mean particle temperature in the irradiated zone. It increases with the particle temperature in agreement with [7], despite the

Table 4
Comparisons of the dimensionless heat transfer index for various fluidization regimes, at given mean particle temperature, for aeration flow rate between 0.24 and 0.81 sm^3/h and particle mass flux between 4.4 and 23.1 $kg/(m^2s)$.

Mean Particle Temperature $T_{part,irr}$	Fluidization Regime	Dimensionless Heat Transfer Index H_{part}
343 ± 4 °C	Slugging	1.58 ± 0.13
	Fast Fluidization	1.84 ± 0.18
	Turbulent Fluidization	2.93 ± 0.49
404 ± 7 °C	Slugging	2.57 ± 0.25
	Fast Fluidization	3.35 ± 0.63
	Turbulent Fluidization	4.38 ± 0.88

associated low particle mass flux. Actually, the heat transfer in a fluidized bed is the sum of convective, conductive and radiative components [25]. All of these terms increase with the temperature in classical fluidized beds. Above 500 °C, the radiative component predominates the heat transfer. Furthermore, the highest dimensionless heat transfer indices are obtained for the lowest flux configuration. Two explanations arise. First, at high solar flux, the wall-to-particles temperature difference increases. Second, the lowest flux distribution is the most homogeneous.

The temperature has also an influence on the particle flow. Actually, as discussed in [13], the effect of temperature on fluidized Group A particles flow is related to both macro-scale change of gas properties (density and viscosity) and micro-scale changes. At micro-scale, Geldart's Group A particles are subjected to clustering contrarily to Group B as shown in [39]. Clustering is due to inter-particle forces that are important for small particles (Group A). Nevertheless, in fluidized beds the particle volume fraction decreases (the bed porosity increases) with temperature as shown in [21,27] due to weaker attraction forces. This tendency dominates until the sintering effect becomes significant and results in particles agglomeration. This phenomenon was extensively studied, in particular, in fluidized bed combustion since ashes are subjected to agglomeration [4,40]. In dense granular flows studied for CSP applications [2,37], the increase of the coefficient of interparticle static sliding friction leads to a decrease of the particle steady-state mass flow rate. Since the sintering temperature of olivine is approximately 1450 °C no agglomeration was observed in our fluidized bed experiments.

A detailed analysis of the link between heat transfer and fluidization regimes is out of the scope of this paper, it can be found in [27]. However, some preliminary results can be accessed. Since the dimensionless heat transfer index, $H_{wall,part}$, depends on the particle temperature, it has been fixed at approximately 340 and 400 °C, and the result analysis has been done for tests with aeration flow rates and particle mass fluxes varying respectively in the ranges 0.24 – 0.81 sm^3/h, and 4.4 – 23.1 $kg/(m^2s)$. The fluidization regimes have been identified, and results are presented in Table 4. At a given particle temperature, the slugging regime is associated with the lowest heat transfer coefficient. This is mostly due to the large air structures (slugs) that decrease the particle mixing and slow down the particle flow [14,45]. Conversely, as expected, the turbulent fluidization regime is associated to the best heat transfer. Actually, in this regime, the scission of the air structures is predominant compared to their coalescence, that results in vortices and a strong particle mixing [9,49]. The intermediate regime in terms of heat

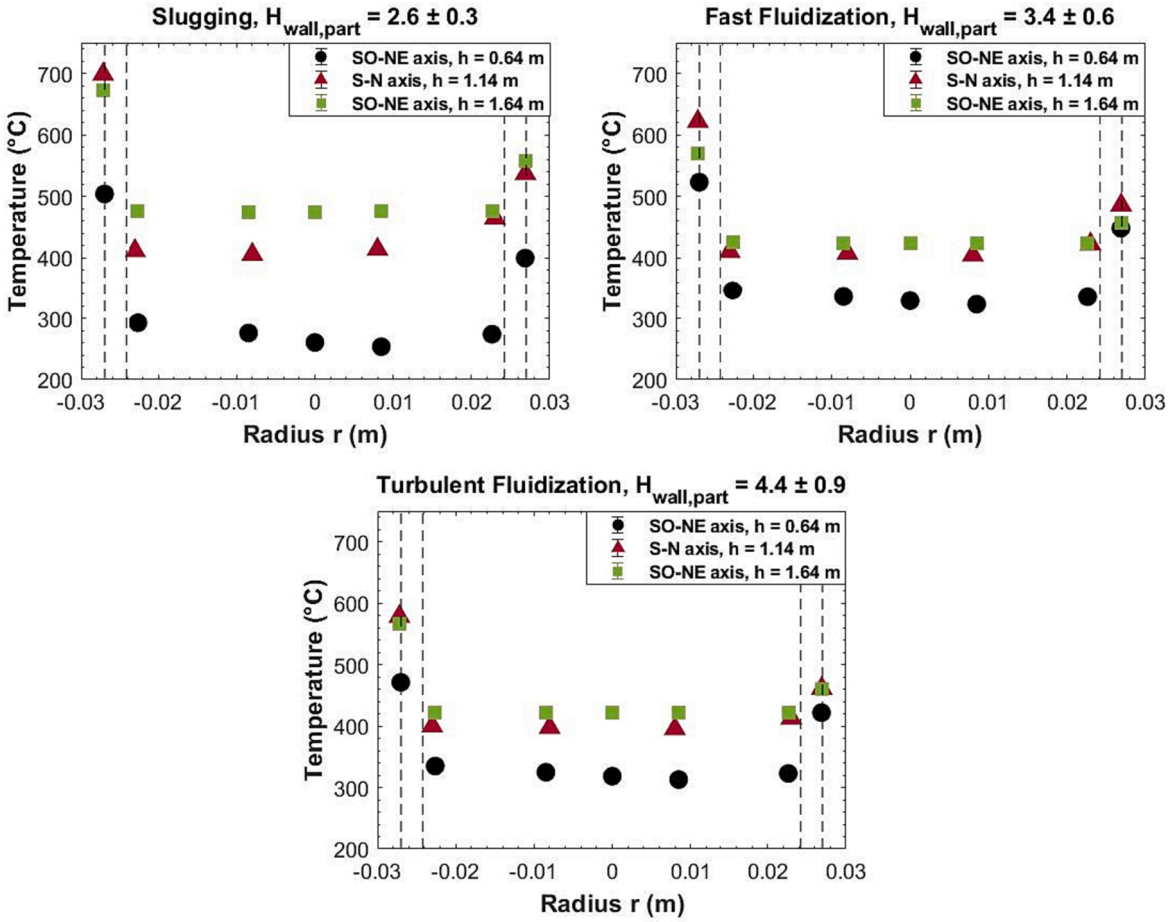

Fig. 14. Evolutions of the temperature with the radius of the tube, at various heights and for various fluidization regimes, for mean particle temperature in the middle of the irradiated zone fixed at approximately 400 °C, and at ambient temperature (around 25 °C) in the dispenser.

Table A1
Heights of the pressure probes implemented on the receiver tube.

N°	$P1$	$P2$	$P3$	$P4$	$P5$	$P6$	$P7$	$P8$	$P9$
Height $z(m)$	0.08	0.84	1.04	1.24	1.44	1.84	2.04	2.24	2.44

Table A2
Positions of the internal and external thermocouples implemented on the receiver tube.

	$x(m)$	$y(m)$	$z(m)$		$x(m)$	$y(m)$	$z(m)$		$x(m)$	$y(m)$	$z(m)$
T_{int}^{1}	0	0	0,31	T_{int}^{20}	−0,015	0,015	1,64	T_{ext}^{15}	0,016	−0,022	1,16
T_{int}^{2}	−0,023	0	0,31	T_{int}^{21}	0	0	1,64	T_{ext}^{16}	0,001	−0,027	1,16
T_{int}^{3}	0,016	0,016	0,64	T_{int}^{22}	0,016	−0,016	1,64	T_{ext}^{17}	−0,020	−0,018	1,16
T_{int}^{4}	0,006	0,006	0,64	T_{int}^{23}	0	0	2,54	T_{ext}^{18}	−0,013	0,024	1,24
T_{int}^{5}	−0,006	−0,006	0,64	T_{int}^{24}	−0,023	0	2,54	T_{ext}^{19}	0	−0,027	1,44
T_{int}^{6}	−0,016	−0,016	0,64	T_{ext}^{1}	0	−0,027	0,31	T_{ext}^{20}	0,001	0,027	1,61
T_{int}^{7}	−0,016	0,016	0,64	T_{ext}^{2}	0	0,027	0,66	T_{ext}^{21}	0,018	0,020	1,61
T_{int}^{8}	−0,015	0,015	0,64	T_{ext}^{3}	0,019	0,019	0,66	T_{ext}^{22}	0,027	0,004	1,61
T_{int}^{9}	0	0	0,64	T_{ext}^{4}	0,027	0	0,66	T_{ext}^{23}	0,021	−0,017	1,61
T_{int}^{10}	0,016	−0,016	0,64	T_{ext}^{5}	0,019	−0,019	0,66	T_{ext}^{24}	0,004	−0,027	1,61
T_{int}^{11}	0	0,023	1,14	T_{ext}^{6}	−0,002	−0,027	0,66	T_{ext}^{25}	−0,016	−0,022	1,62
T_{int}^{12}	0	0,008	1,14	T_{ext}^{7}	−0,017	−0,021	0,66	T_{ext}^{26}	−0,027	−0,001	1,62
T_{int}^{13}	0	−0,008	1,14	T_{ext}^{8}	−0,027	0	0,66	T_{ext}^{27}	−0,020	0,018	1,62
T_{int}^{14}	0	−0,023	1,14	T_{ext}^{9}	−0,021	0,017	0,66	T_{ext}^{28}	0	−0,027	1,84
T_{int}^{15}	0,016	0,016	1,639	T_{ext}^{10}	0	−0,027	0,84	T_{ext}^{29}	0	−0,027	2,04
T_{int}^{16}	0,006	0,006	1,639	T_{ext}^{11}	0,001	−0,027	1,0394	T_{ext}^{30}	0	−0,027	2,24
T_{int}^{17}	−0,006	−0,006	1,639	T_{ext}^{12}	−0,018	0,020	1,16234	T_{ext}^{31}	0	−0,027	2,4366
T_{int}^{18}	−0,016	−0,016	1,64	T_{ext}^{13}	0,025	0,010	1,15934	T_{ext}^{32}	0	−0,027	2,5366
T_{int}^{19}	−0,016	0,016	1,64	T_{ext}^{14}	0,025	0,009	1,16				

transfer is the fast fluidization, in which there is a phase inversion. There is a relatively dense zone at the bottom of the suspension followed by a dilute zone where clusters or particles are ejected upward [24]. Although the latter regime might be a good compromise for the heat transfer, it is more difficult to control the suspension from a practical point of view, and it needs high air velocities – i.e. high air flow rates – which is finally associated to high power consumption to compressed the air in the case of a commercial-scale power plant. Finally, the best compromise in terms of both heat transfer and energy consumption is the turbulent fluidization regime.

To confirm the previous conclusion, Fig. 14 presents the radial temperatures distribution associated to the three tests presented in Table 4 for particle temperatures of approximately 400 °C, i.e. for three fluidization regimes. In the figures, each color corresponds to a specific height where such profiles can be measured, namely, the three well instrumented sections at the bottom, middle and top of the irradiated zone (cf. Fig. 3). The negative x-axis values correspond to the irradiated face of the tube, and the vertical dashed lines represent the tube thickness. First, the particle temperature inside the tube is very homogenous, whatever the fluidization regime, which highlight the good mixing inherent to fluidized bed. Second, for an increase of the particle temperature nearly equivalent for the three tests, $\Delta T_{part} \approx 400$ °C, the temperature difference between the wall and the particles is the lowest in the turbulent fluidization case. This is coherent with the dimensionless heat transfer index presented in Table 4. Third, due to both the cavity effect and the conduction in the tube thickness, the external temperatures at the back face are always higher than the particle temperatures inside the tube. The previous analysis confirms that the dimensionless heat transfer index is a relevant indicator of the quality of the heat transfer.

4. Conclusion

The thermal performances of a gas-particle dense suspension used as heat transfer fluid in a tubular solar receiver irradiated along 1 m are assessed over a large range of the operating parameters. Olivine particles belonging to Geldart class A are selected as solid medium with mass flux up to 93 mg/(m^{2}s). Incident solar flux density configurations between 220 and 600 suns are tested, with various distribution homogeneity.

The main findings are related to the receiver thermal behavior with respect to the incident solar flux density, particle temperature increase through the receiver tube and the associated thermal efficiency, the dynamic response of the system, the experimental values of the heat transfer coefficient and the link between the heat transfer coefficient and the fluidization regimes.

Even if the recommended operation solar flux density is 400 – 500 kW/m^2, the system can hold high peak densities (from 800 suns at the bottom of the tube to 250 suns only 60 cm above).

The maximum particle temperature increase along the 1 m irradiated length reaches 650 °C for a medium incident solar power of approximately 30 kW and particle preheating to 300 °C in the dispenser. The thermal efficiency varies in the range 40 – 70 % for particle mass flux between 15 and 80 kg/(m^{2}s). The thermal efficiency can be improved using a cavity-type solar receiver.

The dynamic responses of the system are studied, showing that the control of the receiver can be pressure-based or based on the aeration flow rate, for respectively large and small variations of the particle mass flux and temperature. For example, a 10 % increase of the pressure in the dispenser results in a 90 % increase of the particle mass flux, whereas it is only 16 % for a 33 % increase of the aeration flow rate. The duration of the transient phases is relatively small for both types of control, typically 60 – 70 s.

The measured global mean heat transfer coefficient is 1000 ± 200 W/(m^{2}K) for particle mass flux above 15 kg/(m^{2}s), with peak values at 1500 W/(m^{2}K).

A dimensionless heat transfer index is derived. It enables to highlights (i) the increase of the heat transfer with the temperature, and (ii) the influence of the fluidization regime on the heat transfer intensity. The turbulent fluidization regime corresponds to the highest heat transfer index.

Declaration of Competing Interest

The authors declare that they have no known competing financial interests or personal relationships that could have appeared to influence the work reported in this paper.

Acknowledgements

The characterization of the olivine sample was conducted with the help of the Material Characterization Platform – Surfaces and Interfaces Analyses of the PROMES (CNRS) laboratory. Special thanks to Regis Rodriguez for his help with the Labview acquisition software.

Funding.

This work was funded by the French "Investments for the future" ("*Investissements d'Avenir*") program managed by the National Agency for Research (ANR) under contract ANR-10-LABX-22-01 (Labex SOLSTICE).

Appendix A. Instrumentation of the Set-Up

Tables A1 and A2 list respectively the position of the pressure probes and of the thermocouples in the main tube, in Cartesian coordinates, where the origin {0 0 0} is the center of the tube at the height of the aeration injection.

Appendix B. Uncertainties on the heat transfer coefficient

The uncertainty on the heat transfer coefficient, $\delta h_{wall,part}$, is given by Equation (13). In this equation, $\delta(\Delta T_{wall,part})$ is the uncertainty of the logarithmic mean of the temperatures differences between the internal wall and the particles. It is determined by Equations (14)–(16) by using the method of the differentials. To simplify the reading of the equations, $\Delta T^{in,out} = T^{in,out}_{wall,int} - T^{in,out}_{part}$, and thus the associated uncertainties $\delta(\Delta T^{in,out}) = \delta T^{in,out}_{paroi,int} + \delta T^{in,out}_{part}$.

$$\frac{\delta h_{wall,part}}{h_{wall,part}} = \frac{\delta \phi_{abs}}{\phi_{abs}} + \frac{\delta S_{exch}}{S_{exch}} + \frac{\delta(\Delta T_{wall,part})}{\Delta T_{wall,part}} \tag{13}$$

$$\delta(\Delta T_{wall,part}) = \left|\frac{\partial(\Delta T_{wall,part})}{\partial(\Delta T^{in})}\right| \delta(\Delta T^{in}) + \left|\frac{\partial(\Delta T_{wall,part})}{\partial(\Delta T^{out})}\right| \delta(\Delta T^{out}) \tag{14}$$

$$\frac{\partial(\Delta T_{wall,part})}{\partial(\Delta T^{in})} = \frac{\ln\left(\frac{\Delta T^{in}}{\Delta T^{out}}\right) - \frac{\Delta T^{in} - \Delta T^{out}}{\Delta T^{in}}}{\left(\ln\left(\frac{\Delta T^{in}}{\Delta T^{out}}\right)\right)^2} \tag{15}$$

$$\frac{\partial(\Delta T_{wall,part})}{\partial(\Delta T^{out})} = \frac{-\ln\left(\frac{\Delta T^{in}}{\Delta T^{out}}\right) + \frac{\Delta T^{in} - \Delta T^{out}}{\Delta T^{out}}}{\left(\ln\left(\frac{\Delta T^{in}}{\Delta T^{out}}\right)\right)^2} \tag{16}$$

Appendix C. Supplementary data

Supplementary data to this article can be found online at https://doi.org/10.1016/j.solener.2023.112118.

References

[1] Alloy Wire International, Inconel 601 [WWW Document], 2020. URL www.alloywire.fr/products/inconel-601 (accessed 9.11.20).
[2] M.V. Bagepalli, S.Y. Jeong, J.D. Brooks, Z.M. Zhang, D. Ranjan, P.G. Loutzenhiser, Experimental characterization of extreme temperature granular flows for solar thermal energy transport and storage, Sol. Energy Mater. Sol. Cells 248 (2022), 112020, https://doi.org/10.1016/j.solmat.2022.112020.
[3] M. Balat-Pichelin, J.-L. Sans, E. Bêche, L. Charpentier, A. Ferrière, S. Chomette, Emissivity at high temperature of Ni-based superalloys for the design of solar receivers for future tower power plants, Sol. Energy Mater. Sol. Cells 227 (2021), 111066, https://doi.org/10.1016/j.solmat.2021.111066.
[4] M. Bartels, W. Lin, J. Nijenhuis, F. Kapteijn, J.R. van Ommen, Agglomeration in fluidized beds at high temperatures: Mechanisms, detection and prevention, Prog. Energy Combust. Sci. 34 (2008) 633–666, https://doi.org/10.1016/j.pecs.2008.04.002.
[5] O. Behar, B. Grange, G. Flamant, Design and performance of a modular combined cycle solar power plant using the fluidized particle solar receiver technology, Energ. Conver. Manage. 220 (2020), 113108, https://doi.org/10.1016/j.enconman.2020.113108.
[6] H. Benoit, R. Ansart, H. Neau, P. Garcia Triñanes, G. Flamant, O. Simonin, Three-dimensional numerical simulation of upflow bubbling fluidized bed in opaque tube under high flux solar heating, AIChE J 64 (2018) 3857–3867, https://doi.org/10.1002/aic.16218.
[7] H. Benoit, I. Pérez López, D. Gauthier, J.-L. Sans, G. Flamant, On-sun demonstration of a 750 °C heat transfer fluid for concentrating solar systems: Dense particle suspension in tube, Sol. Energy 118 (2015) 622–633, https://doi.org/10.1016/j.solener.2015.06.007.
[8] H. Benoit, L. Spreafico, D. Gauthier, G. Flamant, Review of heat transfer fluids in tube-receivers used in concentrating solar thermal systems: Properties and heat transfer coefficients, Renew. Sustain. Energy Rev. 55 (2016) 298–315, https://doi.org/10.1016/j.rser.2015.10.059.
[9] H.T. Bi, N. Ellis, I.A. Abba, J.R. Grace, A state-of-the-art review of gas–solid turbulent fluidization, Chem. Eng. Sci. 55 (2000) 4789–4825, https://doi.org/10.1016/S0009-2509(00)00107-X.
[10] B. Boissiere, R. Ansart, D. Gauthier, G. Flamant, M. Hemati, Experimental hydrodynamic study of gas-particle dense suspension upward flow for application as new heat transfer and storage fluid, Can. J. Chem. Eng. 93 (2015) 317–330, https://doi.org/10.1002/cjce.22087.
[11] M. Castro-Quijada, D. Faundez, R. Rojas, A. Videla, Improving the working fluid based on a NaNO3-KNO3-NaCl-KCl molten salt mixture for concentrating solar power energy storage, Sol. Energy 231 (2022) 464–472, https://doi.org/10.1016/j.solener.2021.11.058.
[12] CSP2 Project: Dense Suspensions of Solid Particles as a New Heat Transfer Fluid for CSP [WWW Document], 2015. URL https://cordis.europa.eu/project/id/282932 (accessed 12.12.22).

[13] H. Cui, P. Sauriol, J. Chaouki, High temperature fluidized bed reactor: measurements, hydrodynamics and simulation, Chem. Eng. Sci. 58 (2003) 1071–1077, https://doi.org/10.1016/S0009-2509(02)00649-8.
[14] Y. Deng, F. Sabatier, R. Dewil, G. Flamant, A. Le Gal, R. Gueguen, J. Baeyens, S. Li, R. Ansart, Dense upflow fluidized bed (DUFB) solar receivers of high aspect ratio: Different fluidization modes through inserting bubble rupture promoters, Chem. Eng. J. 418 (2021), 129376, https://doi.org/10.1016/j.cej.2021.129376.
[15] M.T. Dunham, B.D. Iverson, High-efficiency thermodynamic power cycles for concentrated solar power systems, Renew. Sustain. Energy Rev. 30 (2014) 758–770, https://doi.org/10.1016/j.rser.2013.11.010.
[16] M. Ebert, L. Amsbeck, J. Rheinländer, B. Schlögl-Knothe, S. Schmitz, M. Sibum, R. Uhlig, R. Buck, Operational experience of a centrifugal particle receiver prototype, in: Presented at the SOLARPACES 2018: International Conference on Concentrating Solar Power and Chemical Energy Systems, 2019, p. 030018, https://doi.org/10.1063/1.5117530.
[17] G. Flamant, D. Gauthier, H. Benoit, J.-L. Sans, R. Garcia, B. Boissière, R. Ansart, M. Hemati, Dense suspension of solid particles as a new heat transfer fluid for concentrated solar thermal plants: On-sun proof of concept, Chem. Eng. Sci. 102 (2013) 567–576, https://doi.org/10.1016/j.ces.2013.08.051.
[18] G. Flamant, B. Grange, J. Wheeldon, F. Siros, B. Valentin, F. Bataille, H. Zhang, Y. Deng, J. Baeyens, Opportunities and challenges in using particle circulation loops for concentrated solar power applications, Prog. Energy Combust. Sci. 94 (2023), 101056, https://doi.org/10.1016/j.pecs.2022.101056.
[19] G. Flamant, M. Hemati, Dispositif Collecteur D'energie Solaire. (2010), 1058565.
[20] R. Flesch, H. Stadler, R. Uhlig, R. Pitz-Paal, Numerical analysis of the influence of inclination angle and wind on the heat losses of cavity receivers for solar thermal power towers, Sol. Energy 110 (2014) 427–437, https://doi.org/10.1016/j.solener.2014.09.045.
[21] B. Formisani, R. Girimonte, L. Mancuso, Analysis of the fluidization process of particle beds at high temperature, Chem. Eng. Sci. 53 (1998) 951–961, https://doi.org/10.1016/S0009-2509(97)00370-9.
[22] D. Geldart, Chap. 6: Particle Entrainment and Carryover, in: Gas Fluidization Technology. John Wiley & Sons Ltd.: Chichester, U.K., 1986. pp. 123–154.
[23] D. Geldart, Types of gas fluidization, Powder Technol. 7 (1973) 285–292, https://doi.org/10.1016/0032-5910(73)80037-3.
[24] J.R. Grace, X. Bi, N. Ellis, Chap. 9: Turbulent Fluidization, in: Essential of Fluidization Technology. John Wiley & Sons Ltd.: Chichester, U.K., 2020a. pp. 163–180.
[25] J.R. Grace, X. Bi, N. Ellis Chap. 14: Heat and Mass Transfer, in: Essential of Fluidization Technology. John Wiley & Sons Ltd.: Chichester, U.K., 2020b. pp. 291–332.
[26] R. Gueguen, B. Grange, F. Bataille, S. Mer, G. Flamant, Shaping High Efficiency, High Temperature Cavity Tubular Solar Central Receivers, Energies 13 (2020) 4803, https://doi.org/10.3390/en13184803.
[27] R. Gueguen, S. Mer, A. Toutant, F. Bataille, G. Flamant, Effect of temperature on the hydrodynamics of a fluidized bed circulating in a long tube for a solar energy harvesting application, Chem. Eng. Sci. (2023), 119218, https://doi.org/10.1016/j.ces.2023.119218.
[28] R. Gueguen, G. Sahuquet, S. Mer, A. Toutant, F. Bataille, G. Flamant, Fluidization Regimes of Dense Suspensions of Geldart Group A Fluidized Particles in a High Aspect Ratio Column, Chem. Eng. Sci. (2022), 118360, https://doi.org/10.1016/j.ces.2022.118360.
[29] R. Gueguen, G. Sahuquet, S. Mer, A. Toutant, F. Bataille, G. Flamant, Gas-Solid Flow in a Fluidized-Particle Tubular Solar Receiver: Off-Sun Experimental Flow Regimes Characterization, Energies 14 (2021) 7392, https://doi.org/10.3390/en14217392.
[30] E. Guillot, R. Rodriguez, N. Boullet, J.-L. Sans, ARGOS: Solar furnaces flat heliostats tracking error estimation with a direct camera-based vision system. Presented at the SolarPACES 2017: International Conference on Concentrating Solar Power and Chemical Energy Systems, Santiago, Chile, p. 200001. 2018. 10.1063/1.5067202.
[31] C.K. Ho, A review of high-temperature particle receivers for concentrating solar power, Appl. Therm. Eng. 109 (2016) 958–969, https://doi.org/10.1016/j.applthermaleng.2016.04.103.
[32] Ho, C.K., Christian, J., Yellowhair, J., Jeter, S., Golob, M., Nguyen, C., Repole, K., Abdel-Khalik, S., Siegel, N., Al-Ansary, H., El-Leathy, A., Gobereit, B., 2017. Highlights of the high-temperature falling particle receiver project: 2012 - 2016. Presented at the SOLARPACES 2016: International Conference on Concentrating Solar Power and Chemical Energy Systems, Abu Dhabi, United Arab Emirates, p. 030027. 10.1063/1.4984370.
[33] C.K. Ho, A.R. Mahoney, A. Ambrosini, M. Bencomo, A. Hall, T.N. Lambert, Characterization of Pyromark 2500 Paint for High-Temperature Solar Receivers, J. Sol. Energy Eng. 136 (2014), 014502, https://doi.org/10.1115/1.4024031.
[34] K. Jiang, X. Du, Q. Zhang, Y. Kong, C. Xu, X. Ju, Review on gas-solid fluidized bed particle solar receivers applied in concentrated solar applications: Materials, configurations and methodologies, Renew. Sustain. Energy Rev. 150 (2021), 111479, https://doi.org/10.1016/j.rser.2021.111479.
[35] Q. Kang, G. Flamant, R. Dewil, J. Baeyens, H.L. Zhang, Y.M. Deng, Particles in a circulation loop for solar energy capture and storage, Particuology 43 (2019) 149–156, https://doi.org/10.1016/j.partic.2018.01.009.
[36] D. Kunii, O. Levenspiel, Chap. 3: Fluidization and Mapping of Regimes, in: Fluidization Engineering, Elsevier, 1991, pp. 61–94, https://doi.org/10.1016/B978-0-08-050664-7.50009-3.
[37] Laubscher, H.F., Albrecht, K.J., Ho, C.K., 2020. High-Temperature Particle Flow Testing in Parallel Plates for Particle-to-Supercritical CO2 Heat Exchanger Applications, in: ASME 2020 14th International Conference on Energy Sustainability. Presented at the ASME 2020 14th International Conference on Energy Sustainability, American Society of Mechanical Engineers, Virtual, Online, p. V001T02A011. 10.1115/ES2020-1664.
[38] A. Le Gal, B. Grange, M. Tessonneaud, A. Perez, C. Escape, J.-L. Sans, G. Flamant, Thermal analysis of fluidized particle flows in a finned tube solar receiver, Sol. Energy 191 (2019) 19–33, https://doi.org/10.1016/j.solener.2019.08.062.
[39] B. Leckner, Regimes of large-scale fluidized beds for solid fuel conversion, Powder Technol. 308 (2017) 362–367, https://doi.org/10.1016/j.powtec.2016.11.070.
[40] S. Leimbach, J. Lukas, S. Kolb, L. Yang, T. Plankenbühler, M. Sega, J. Harting, J. Karl, Early Detection of Agglomeration in Fluidized Beds by Means of Frequency Analysis of Pressure Fluctuations, Energy Fuels 36 (2022) 4924–4932, https://doi.org/10.1021/acs.energyfuels.1c04356.
[41] MCI Technologies, Properties of Insulfrax [WWW Document], 2020. URL https://www.mci-tech.com/produits/nappes-et-feutres-ht/insulfrax (accessed 9.11.20).
[42] Next-CSP Project: High Temperature Concentrated Solar Thermal Plant with Particle Receiver and Direct Thermal Storage [WWW Document], 2020. URL https://cordis.europa.eu/project/id/727762 (accessed 12.12.22).
[43] I. Perez Lopez, H. Benoit, D. Gauthier, J.L. Sans, E. Guillot, G. Mazza, G. Flamant, On-sun operation of a 150 kWth pilot solar receiver using dense particle suspension as heat transfer fluid, Sol. Energy 137 (2016) 463–476, https://doi.org/10.1016/j.solener.2016.08.034.
[44] E. Rabinovich, H. Kalman, Flow regime diagram for vertical pneumatic conveying and fluidized bed systems, Powder Technol. 207 (2011) 119–133, https://doi.org/10.1016/j.powtec.2010.10.017.
[45] A. Reyes Urrutia, H. Benoit, M. Zambon, D. Gauthier, G. Flamant, G. Mazza, Simulation of the behavior of a dense SiC particle suspension as an energy transporting vector using computational fluid dynamics (CFD), Chem. Eng. Res. Des. 106 (2016) 141–154, https://doi.org/10.1016/j.cherd.2015.12.008.
[46] A. Salomé, F. Chhel, G. Flamant, A. Ferrière, F. Thiery, Control of the flux distribution on a solar tower receiver using an optimized aiming point strategy: Application to THEMIS solar tower, Sol. Energy 94 (2013) 352–366, https://doi.org/10.1016/j.solener.2013.02.025.
[47] F. Trombe, A. Le Phat Vinh, Thousand kW solar furnace, built by the National Center of Scientific Research, in Odeillo (France), Sol. Energy 15 (1973) 57–61, https://doi.org/10.1016/0038-092X(73)90006-6.
[48] W. Wu, L. Amsbeck, R. Buck, R. Uhlig, R. Ritz-Paal, Proof of Concept Test of a Centrifugal Particle Receiver, Energy Procedia 49 (2014) 560–568, https://doi.org/10.1016/j.egypro.2014.03.060.
[49] J. Yerushalmi, N.T. Cankurt, Further studies of the regimes of fluidization, Powder Technol. 24 (1979) 187–205, https://doi.org/10.1016/0032-5910(79)87036-9.
[50] H. Zhang, W. Kong, T. Tan, F. Gilles, J. Baeyens, Experiments support an improved model for particle transport in fluidized beds, Sci. Rep. 7 (2017) 10178, https://doi.org/10.1038/s41598-017-10597-3.

Chapitre 4

Modélisation résolue d'écoulements fluide-particules

Sommaire

Préambule

Cette thématique de recherche a été initiée par A. Toutant un an avant mon arrivée au laboratoire PROMES, avec le lancement de la thèse de S. Hamidi. Dès mon arrivée (en 2019), j'ai été intégré à cette thématique pour co-encadrer la thèse de S. Hamidi (avec A. Toutant et F. Bataille), puis celle d'E. Butaye (en 2021). Ces deux thèses ont été soutenues en 2024 et se poursuivent actuellement à travers celle d'A. Labat. Les stages de R. Quintana, G. Ologaray, F. Hertrich et A. Kundu sont également venus renforcer cet axe de recherche. L'objectif est de développer un outil numérique permettant l'étude fine des mécanismes de transfert de chaleur et de quantité de mouvement dans les lits fluidisés. Pour ce faire, une approche originale de type Front-Tracking/DEM est déployée dans le code open source TRIO_CFD*, et fait l'objet de développements spécifiques.*

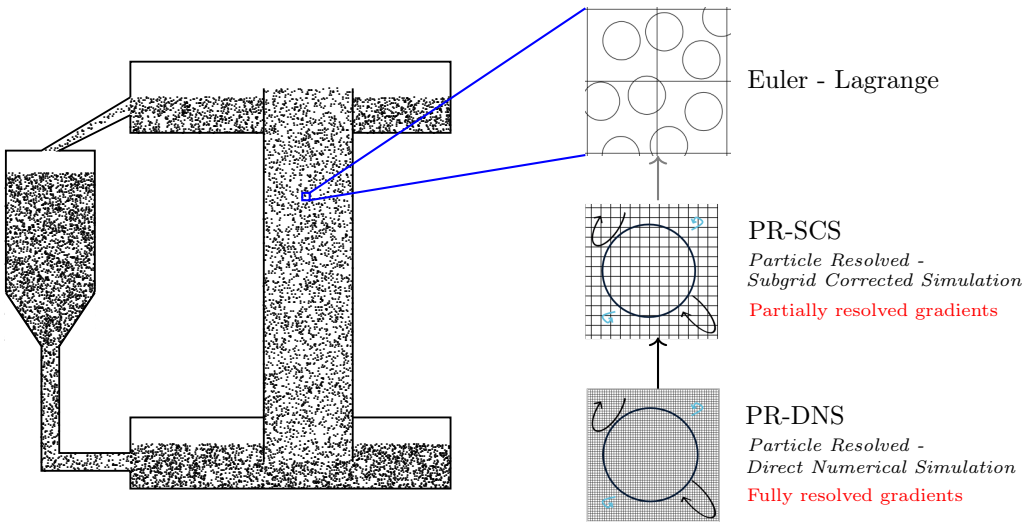

FIGURE 4.1 – Représentation schématique des différentes échelles de résolution utilisées dans la littérature pour la simulation des écoulements fluide-particules.

4.1 Contexte

La simulation numérique des écoulements fluide-particules constitue un défi majeur en raison des phénomènes multi-échelles qu'elle implique. Dans les tubes récepteurs, les structures les plus grandes – de l'ordre du mètre – sont fortement influencées par des interactions locales fluide-particule et particule-particule, dont les échelles caractéristiques sont de l'ordre du micron [37]. On distingue généralement trois échelles principales :

- ▷ l'échelle **microscopique**, associée aux interactions locales entre particules et avec le fluide ;
- ▷ l'échelle **mésoscopique**, correspondant aux effets de sillage et aux interactions collectives ;
- ▷ l'échelle **macroscopique**, représentant les mouvements globaux du lit ou du fluide.

Ces échelles interagissent et conditionnent les régimes de fluidisation en fonction de la vitesse de fluidisation, de la taille des particules et du confinement géométrique. Plusieurs approches numériques, schématisées sur la Fig. 4.1, ont été développées dans la littérature pour modéliser ces écoulements.

Les simulations dites *Particle-Resolved Direct Numerical Simulation* (PR-DNS) permettent une résolution complète des interactions hydrodynamiques en capturant les gradients de vitesse et de température autour de chaque particule [8, 6]. Bien qu'extrêmement coûteuses en ressources de calcul, ces simulations sont précieuses pour les cas académiques, car elles fournissent des données de référence détaillées. On distingue les simulations PR-DNS, qui résolvent intégralement l'hydrodynamique, des approches dites *Particle-Resolved Simulation* (PRS) [76, 56, 55], dans lesquelles l'écoulement est résolu à l'échelle de la particule, mais certaines interactions fines peuvent être modélisées ou filtrées.

Pour simuler un grand nombre de particules dans des systèmes plus réalistes, la méthode *Computational Fluid Dynamics–Discrete Element Method* (CFD–DEM) est souvent utilisée [47,

86, 17, 21]. Les particules sont modélisées de manière lagrangienne, tandis que le fluide est résolu sur une grille eulérienne, selon les équations de Navier–Stokes. Les interactions fluide-particule sont modélisées à l'aide de corrélations empiriques et de différents niveaux de couplage (one-way, two-way, four-way). Cette approche permet de suivre individuellement chaque particule et de capturer les effets de fluctuations locales, tout en s'appuyant sur des modèles de fermeture dérivés notamment de simulations PRS.

À l'échelle industrielle, la méthode *Euler–Euler* est la plus utilisée. Elle considère le fluide et les particules comme deux milieux continus – les équations de conservation sont moyennées par phase – interagissant via des termes de couplage [65, 22]. Ces simulations, bien moins coûteuses que les approches PR-DNS ou CFD–DEM, nécessitent des modèles de fermeture adaptés pour reproduire correctement les phénomènes physiques. À ce titre, les simulations CFD–DEM ou PRS jouent un rôle crucial pour alimenter et affiner ces fermetures. L'approche Euler–Euler est aujourd'hui incontournable pour l'étude et l'optimisation de procédés mettant en œuvre des lits fluidisés, notamment dans les applications solaires.

La méthode développée dans ce chapitre permet de réaliser des simulations aux échelles PR-DNS et PRS. Afin de valider les algorithmes de calcul et les outils de post-traitement, des données de référence sont générées sur des cas canoniques à l'échelle PR-DNS. Lorsqu'on monte en complexité (par exemple pour simuler des lits fluidisés complets), les simulations PR-DNS deviennent inabordables, et une approche PRS, moins coûteuse bien qu'encore résolue à l'échelle des particules, est alors privilégiée.

4.2 Modélisation numérique résolue d'écoulements fluide particules

4.2.1 L'approche monofluide de Trio_CFD

Nous développons des modèles dans le code *open source* Trio_CFD pour la simulation résolue d'écoulements fluide-particules anisothermes. Ce code, massivement parallèle et écrit en `C++ orienté objet`, a été développé par le CEA pour la simulation des écoulements à bulles gaz-liquide. Il repose sur les équations monofluide de Navier–Stokes.

Pour établir les équations de conservation, on suppose : (i) un écoulement incompressible, (ii) une masse volumique et une viscosité constantes dans chacune des phases, et (iii) l'absence de transfert de masse entre le fluide et les particules. Les équations de conservation de la masse et de la quantité de mouvement s'écrivent alors :

$$\nabla \cdot \mathbf{u} = 0 \tag{4.1}$$

$$\frac{\partial (\rho \mathbf{u})}{\partial t} + \nabla \cdot (\rho \mathbf{u} \otimes \mathbf{u}) = -\nabla p + \nabla \cdot \left[\mu \left(\nabla \mathbf{u} + \nabla^T \mathbf{u}\right)\right] + \rho \mathbf{g} + \mathbf{F}_c^E \tag{4.2}$$

où $\mathbf{u}$, ρ, μ, $\mathbf{g}$ et $\mathbf{F}_c^E$ représentent respectivement le vecteur vitesse, la masse volumique, la viscosité dynamique, la gravité et le terme de forçage eulérien modélisant les collisions entre particules (voir Sec. 4.2.4.
Dans les mailles traversées par une interface, la masse volumique (Eq. 4.3) et la viscosité dynamique (Eq. 4.4) sont définies à l'aide d'une fonction indicatrice de phase, notée I, représentant

le volume occupé par la phase fluide dans la maille.

$$\rho = I\rho_f + (1-I)\rho_p \tag{4.3}$$

$$\mu = \frac{\mu_f \mu_p}{(1-I)\mu_f + I\mu_p} \tag{4.4}$$

L'équation de conservation de l'énergie (Eq. 4.5) est formulée en température, considérée ici comme un scalaire passif. Sa résolution n'influe pas sur l'équation de la quantité de mouvement (Eq. 4.2).

$$\frac{\partial\left(\rho_f c_p T\right)}{\partial t} + \nabla\cdot\left(\rho_f c_p \mathbf{u} T\right) = \nabla\cdot\left(\lambda_f \nabla T\right) \tag{4.5}$$

À ce stade, les particules sont considérées comme des puits thermiques à température constante et homogène. La température est donc résolue uniquement dans le fluide, avec une condition de Dirichlet imposée aux interfaces fluide-solide (T_p = cst). Une méthode de type *ghost-fluid* est utilisée pour l'imposer localement à l'interface (voir [30] pour le détail de la procédure).

La méthode des volumes finis est utilisée pour discrétiser les équations de conservation. Le domaine est discrétisé à l'aide d'un maillage eulérien fixe. Les nœuds de pression et de vitesse sont localisés sur une grille décalée (voir Fig. 4.2a). Les grandeurs scalaires (p, T) sont résolues au centre des volumes de contrôle, tandis que les grandeurs vectorielles ($\mathbf{u}$) sont résolues aux faces des volumes de contrôle. Un deuxième maillage, lagrangien, est introduit par la méthode de suivi d'interface.

4.2.2 Suivi d'interfaces par une approche Front-Tracking

Les interfaces fluide-solide sont localisées à l'aide d'une méthode de Front-Tracking. Chaque interface est discrétisée par des marqueurs lagrangiens (immatériels), répartis uniformément le long de la surface des particules (voir Fig. 4.2a). Pour garantir le caractère indéformable des particules solides, tous les marqueurs i d'une même particule sont transportés avec une vitesse unique $\mathbf{u_p}$ entre deux pas de temps :

$$\mathbf{x}_i^{n+1} = \mathbf{x}_i^n + \mathbf{u}_p\,\Delta t \tag{4.6}$$

où $\mathbf{x}_i$ est la position du $i^{\text{ème}}$ marqueur lagrangien, et Δt le pas de temps de la simulation.

La vitesse $\mathbf{u}_p$ de la particule est calculée comme la moyenne pondérée des vitesses des facettes qui la composent :

$$\mathbf{u}_p = \frac{1}{S_p}\sum_{\text{facettes}} S_i\,\mathbf{u}_i \tag{4.7}$$

où S_p désigne la surface totale de la particule, et S_i, $\mathbf{u}_i$ la surface et la vitesse de la facette i. En 2D, une facette correspond au segment reliant deux marqueurs lagrangiens.

Numériquement, la vitesse de chaque marqueur est interpolée bilinéairement en 2D, ou trilinéairement en 3D, depuis le maillage eulérien (voir Fig. 4.2a). La vitesse d'une facette est ensuite calculée comme la moyenne des vitesses des marqueurs qui la composent.

4.2.3 Méthode de pénalisation visqueuse

Pour garantir le caractère indéformable des particules solides, la méthode numérique doit permettre de maintenir nul le tenseur des déformations $\frac{1}{2}(\nabla\mathbf{u} + \nabla^T\mathbf{u})$ à l'intérieur de celles-ci

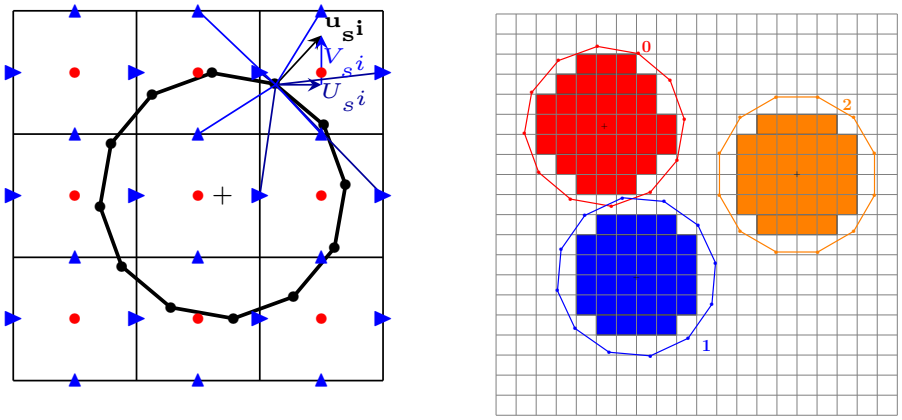

(a) (b)

FIGURE 4.2 – (a) Représentation 2D des marqueurs lagrangiens (•) sur une particule sphérique et de la méthode d'interpolation des différentes composantes de la vitesse. • : nœuds de résolution des grandeurs scalaires. ▲, ▶ : nœuds de résolution des grandeurs vectorielles. (b) Représentation 2D de la numérotation eulérienne et lagrangienne des particules dans le domaine de calcul.

[78]. Pour imposer cette contrainte, une méthode consiste à faire tendre la viscosité du fluide vers l'infini à l'intérieur des particules [72, 78].

Numériquement, nous avons observé qu'un rapport de viscosité $\mu_p/\mu_f \gtrsim 10^3$ constitue un bon compromis pour assurer la contrainte de non-déformation sans pénaliser excessivement le pas de temps des simulations [34] . Une augmentation trop importante de ce rapport pénalise doublement le calcul car d'autre part, elle tend à surestimer les frottements fluides sur la particule. En effet, lorsque μ_p/μ_f augmente, la surface effective des particules perçue par le fluide devient supérieure à leur surface réelle, ce qui peut induire une surestimation des frottements hydrodynamiques [68].

4.2.4 Modélisation des collisions entre particules et particule-paroi

La prise en compte des forces de collision est réalisée par une méthode de sphères molles [34]. Cette approche nécessite un suivi individuel des particules tout au long de la simulation, l'identification efficace des particules en contact, le calcul des forces de collision, puis leur discrétisation sur la grille eulérienne sous forme d'un terme de forçage $\mathbf{F}_c^E$ (voir Eq. 4.2).

Les forces de contact particule-particule et particule-paroi sont modélisées par un système masse-ressort sans amortissement. La force de collision dépend de l'interpénétration des particules et s'écrit :

$$\mathbf{F}_c^L = -k\,\delta_n\,\mathbf{n} \tag{4.8}$$

où δ_n est la distance d'interpénétration, k la constante de raideur du ressort, et $\mathbf{n}$ le vecteur normal au plan de collision. L'évolution de δ_n est gouvernée par l'équation :

$$m_e\ddot{\delta}_n + k\dot{\delta}_n = 0 \tag{4.9}$$

avec m_e la masse effective du système ($m_e = \frac{m_p}{2}$ pour une collision entre particules et $m_e = m_p$ pour une collision particule-paroi).

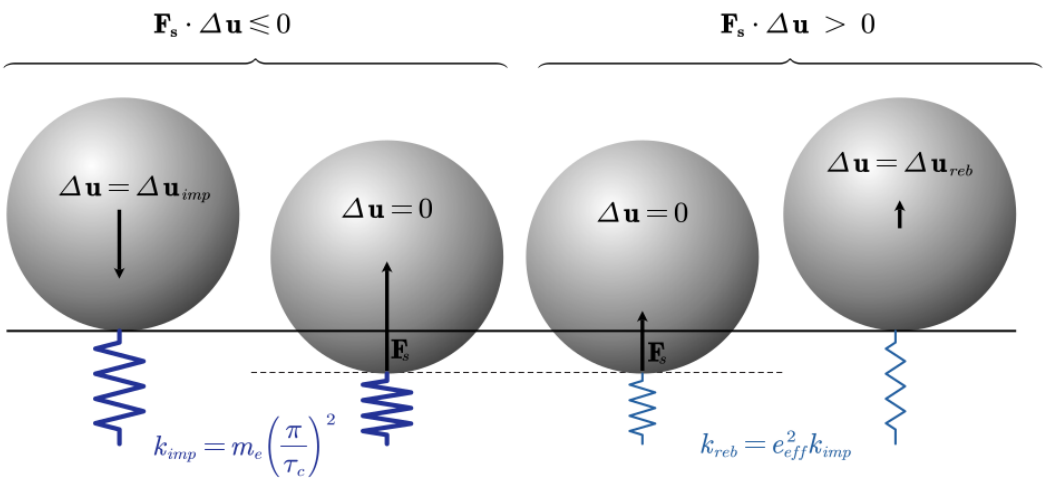

FIGURE 4.3 – Représentation schématique du modèle de sphères molles utilisé pour modéliser les collisions dans notre approche [34]. Le changement de raideur au cours de la collision permet de prendre en compte la dissipation visqueuse due au pincement du film fluide.

Le processus de collision est divisé en deux phases : l'impact (lorsque la particule décélère) et le rebond (après inversion du signe de la vitesse). Ces phases sont représentées sur la Fig. 4.3. La raideur du ressort varie selon la phase comme décrit ci-dessous :

$$k = \begin{cases} m_e \left(\frac{\pi}{\tau_c}\right)^2 & \text{durant l'impact} \\ e_{eff}^2 \, m_e \left(\frac{\pi}{\tau_c}\right)^2 & \text{durant le rebond} \end{cases} \tag{4.10}$$

où $\tau_c = 8\,\Delta t$ est le temps de collision, et $e_{eff} = e_{dry}\, e_{wet}$ est le coefficient de restitution effectif. Ce dernier représente le rapport entre la vitesse de la particule après et avant la collision. Il est calculé comme le produit d'un coefficient de restitution sec (e_{dry}), modélisant la dissipation par déformation ou vibration, et d'un coefficient de restitution humide (e_{wet}), modélisant la dissipation visqueuse. Ce dernier dépend du nombre de Stokes St selon la corrélation de Legendre [51] :

$$e_{wet} = \exp\left(-\frac{35}{St}\right) \tag{4.11}$$

La validation de ce modèle est détaillée dans [34], disponible en page 93 de ce chapitre. Ses deux paramètres principaux sont le coefficient de restitution sec e_{dry} et le temps de collision τ_c. On supposera que le coefficient de restitution est identique pour toutes les particules, indépendamment de la vitesse d'impact.

Enfin, pour tenir compte des collisions multiples, on somme les forces exercées sur une particule p :

$$\mathbf{F}_{c,p}^{L} = \sum_{q} \mathbf{F}_{c,q\to p}^{L} \tag{4.12}$$

La force lagrangienne ainsi obtenue est ensuite distribuée de manière homogène sur toutes les cellules purement solides appartenant à la particule p (cellules colorées de la Fig. 4.2b). La force

eulérienne résultante apparaît alors comme un terme de forçage dans l'équation de la quantité de mouvement (Eq. 4.2) :

$$\mathbf{F}^E_{c,p} = \frac{\mathbf{F}^L_{c,p}}{\sum_{i \text{ t.q. } \texttt{num\_compo}(i)=p} V_i} \tag{4.13}$$

4.3 Validation de la méthode : de 1 à 2134 particules

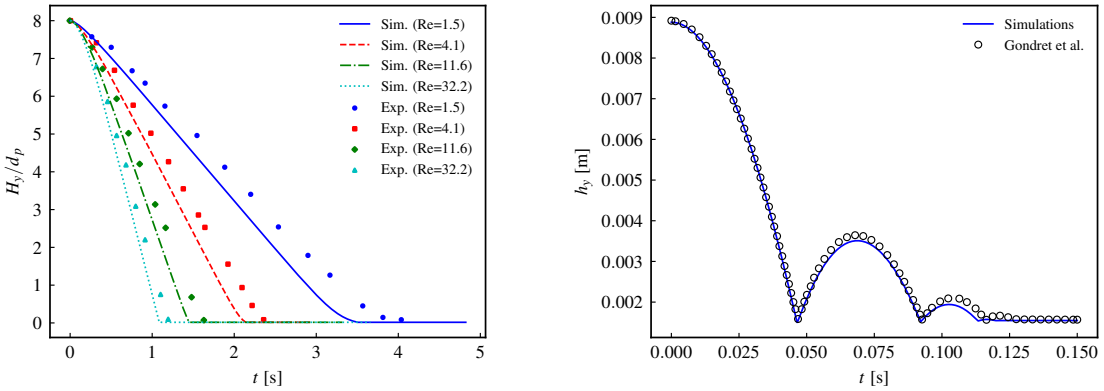

(a) (b)

FIGURE 4.4 – (a) (resp. (b)) Évolution temporelle de la position verticale dans le cas de la sédimentation dans un fluide au repos [10] (resp. du rebond sur une paroi [28]). Les traits représentent les résultats de nos simulations, tandis que les points correspondent aux données expérimentales issues de la littérature.

La méthodologie a d'abord été validée sur des cas isothermes issus de la littérature. La reproduction de cas de complexité croissante, fréquemment étudiés, a permis de valider les différents éléments numériques.

Le cas de la sédimentation d'une particule dans un fluide au repos [10] a permis de valider la méthode de pénalisation visqueuse. En effet, comme le montre la Fig. 4.4a, notre méthode est capable de reproduire correctement la dynamique de sédimentation pour différents nombres de Reynolds, et donc de capturer les efforts hydrodynamiques exercés sur la particule.

La modélisation des forces de collision a été validée à partir d'un cas de rebond sur une paroi plane [28]. Là encore, on observe un excellent accord entre notre modèle numérique et les résultats expérimentaux, comme illustré sur la Fig. 4.4b.

La méthode a ensuite été utilisée pour simuler un lit fluidisé liquide-solide comportant 2134 particules [65]. La Fig. 4.5 montre que la compacité du lit décroît avec la vitesse de fluidisation. On observe également que la surface libre du lit devient de moins en moins bien définie en raison d'éjections fréquentes et de forte amplitude de particules. Nos simulations (+) sont confrontées à la loi de fluidisation de Richardson–Zaki (- -), qui prédit la fraction volumique du lit en fonction de la vitesse de fluidisation, ainsi qu'aux simulations d'Ozel [65] (×) et aux résultats expérimentaux de Corona [14] (•). On constate un très bon accord avec ces différentes références de la littérature, ce qui renforce la validation de notre approche.

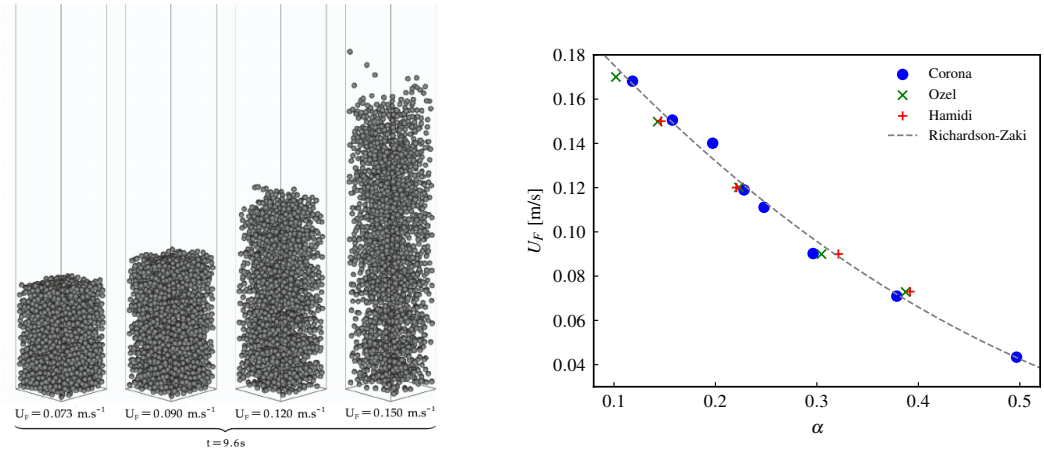

(a) (b)

FIGURE 4.5 – Simulation numérique d'un lit fluidisé liquide-solide comportant 2134 particules [65]. (a) Représentation 3D de la compaction du lit, une fois l'état statistiquement stationnaire établi, pour différentes vitesses de fluidisation. (b) Évolution de la fraction volumique de particules en fonction de la vitesse de fluidisation.

Pour de plus amples détails sur la validation de la méthode et sur ce cas de lit fluidisé isotherme, le lecteur est invité à consulter l'article [34], inclus en page 93 de ce chapitre.

4.4 Développement de l'approche PR-SCS (Particle Resolved - Subgrid Corrected Simulations)

Cette section se base sur l'article [8], paru dans *Computers & Fluids* en 2023. Par souci de concision, celui-ci n'est pas inclus dans ce document. Le lecteur intéressé pourra cependant le consulter en libre accès sur HAL (lien disponible dans la Sec. A.7).

Comme discuté en introduction de ce chapitre (voir Fig. 4.1), en PR-DNS, les gradients de vitesse et de pression sont entièrement résolus sur la grille de calcul, nécessitant plusieurs dizaines de mailles par diamètre de particule. En revanche, en PRS, avec une résolution typique d'environ 10 mailles par diamètre, ces gradients hydrodynamiques ne sont que partiellement capturés, laissant une partie des interactions fluide-solide sous-résolue. Le coût de calcul très élevé des PR-DNS en restreint l'application à des cas académiques impliquant un nombre limité de particules. Ainsi, la majorité des études numériques résolues fluide-particule dans la littérature adoptent une résolution d'une douzaine de mailles par diamètre, les plaçant dans le cadre des PRS. Dans ces configurations, les gradients de vitesse et de pression sont mal résolus, ce qui induit une erreur dans l'estimation des forces hydrodynamiques exercées par le fluide sur l'interface des particules.

Afin de mieux comprendre, quantifier et corriger la sous-résolution de ces interactions en fonction du maillage, cette section s'intéresse à la sédimentation d'une particule isolée dans un fluide au repos, en régime de Stokes. Ce cas présente l'avantage de disposer d'une solution analytique des efforts hydrodynamiques exercés sur la particule.

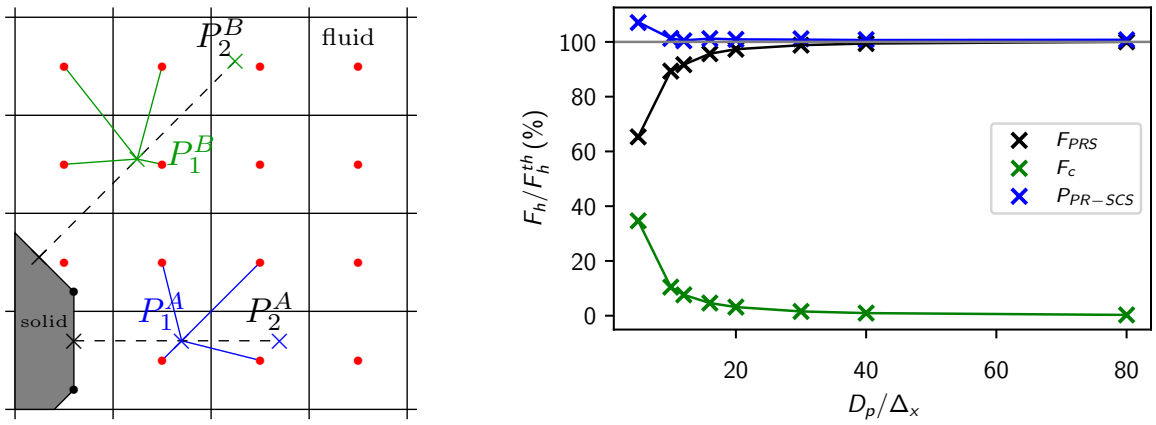

(a) (b)

FIGURE 4.6 – (a) Schéma récapitulatif de la méthode de post-traitement des efforts hydrodynamiques. (b) Effort hydrodynamique normalisé par sa valeur théorique en fonction de la résolution. — : simulation PRS, — : force de correction appliquée à la particule en fonction de la résolution, — : simulation PR-SCS.

Numériquement, une méthode originale de post-traitement a été spécifiquement développée afin de calculer les forces hydrodynamiques à la surface de la particule. Dans les cellules traversées par l'interface, les propriétés du fluide (ρ et μ) et la pression p sont, par construction, *mal posées*. Néanmoins, les forces hydrodynamiques sont classiquement évaluées en intégrant directement les grandeurs locales sur les facettes lagrangiennes. Pour améliorer la précision de ce calcul, la pression et la vitesse sont interpolées aux points P_1 et P_2 — strictement situés dans le fluide et distant respectivement de l'interface de 1 et 2 taille de maille Δ_x (voir Fig. 4.6a)—, puis extrapolées linéairement au centre des facettes lagrangiennes situées à l'interface. Plusieurs méthodes d'extrapolation existent dans la littérature [84, 11].
La méthode proposée ici repose sur une extrapolation linéaire et simplifie le calcul du tenseur des contraintes visqueuses en tirant parti du fait que, pour une particule solide, seules les dérivées radiales de la vitesse sont contributives. Cette approche permet de réduire drastiquement le coût de calcul du tenseur des contraintes, ainsi que la charge mémoire associée et la complexité algorithmique liée au calcul parallèle.

Une corrélation dépendante du maillage est ensuite introduite pour corriger numériquement les forces partiellement résolues dans le cadre PRS (voir Fig. 4.6b), donnant naissance à ce que nous appelons l'approche *Particle Resolved – Subgrid Corrected Simulations* (PR-SCS). On observe que la correction est relativement importante pour les résolutions les plus faibles, et décroît avec le raffinement du maillage. Cette correction permet de retrouver la bonne force hydrodynamique (à 1 % près) pour des résolutions supérieures à 10 mailles par diamètre. Numériquement, la correction est répartie dans le volume de la particule, à la manière du terme de forçage $\mathbf{F}_c^E$ utilisé pour modéliser les collisions (voir Eq. 4.2). Enfin, cette correction a été évaluée pour différents nombres de Reynolds et divers rapports de densité en régime de Stokes.

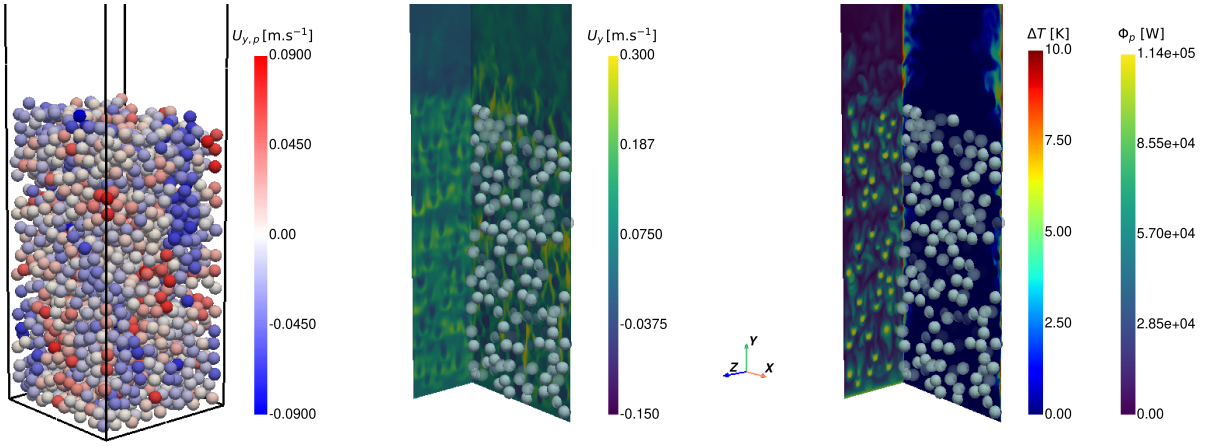

(a) (b) (c)

FIGURE 4.7 – Simulations d'un lit fluidisé liquide-solide anisotherme comportant 2134 particules, pour une vitesse de fluidisation de 0,073 m/s. (a) Vitesse verticale des particules. (b) Champ de vitesse eulérienne de la phase fluide sur deux plans orthogonaux. (c) Champ de température dans le plan médian et flux de chaleur échangé à la paroi.

4.5 Transferts thermiques en PRS

Dans cette section, nous présentons brièvement nos travaux sur la modélisation des transferts thermiques dans les approches PRS. Cette partie s'appuie sur les travaux décrits dans l'article [6], inclus en page 107 de ce manuscrit. Comme pour la partie hydrodynamique, nous commencerons par valider les méthodes et le post-traitement sur un cas mono-particule avant de passer à des simulations avec plusieurs particules.

À l'instar du calcul des efforts hydrodynamiques, une méthode a été mise en place pour calculer le flux de chaleur reçu par une particule. Une étude paramétrique sur le transfert de chaleur fluide-particule est ensuite réalisée afin d'évaluer les corrélations bien établies dans la littérature concernant une particule en sédimentation dans un fluide au repos. Un total de 77 simulations PRS ont été réalisées pour des nombres de Reynolds compris entre 1 et 32, et des nombres de Prandtl entre 0,1 et 10, avec une résolution de 20 mailles par diamètre de particule. Pour deux des trois corrélations étudiées [70, 80, 24], le flux de chaleur est prédit avec une erreur inférieure à 10%.

Pour accélérer les simulations de lits fluidisés, la méthode de détection des collisions a été optimisée grâce aux tables de Verlet. L'utilisation de ces dernières – pour réduire la zone de recherche des candidats potentiels à la collision – a permis de réduire le temps de calcul global de 20%. Un cas de lit fluidisé anisotherme de 2134 particules a ensuite été adapté à partir de la configuration d'Ozel et étudié en détail (voir Fig. 4.7). Pour ce cas, nous imposons une surchauffe de $10°C$ à la paroi par rapport à la température du fluide et des particules. Quatre vitesses de fluidisation sont considérées, associées à des fractions volumiques solides allant de 0,13 à 0,35. Trois résolutions en maillage sont testées (12, 24 et 36 mailles par diamètre de particule), afin d'analyser la sensibilité à la résolution, pour la vitesse de fluidisation la plus faible.

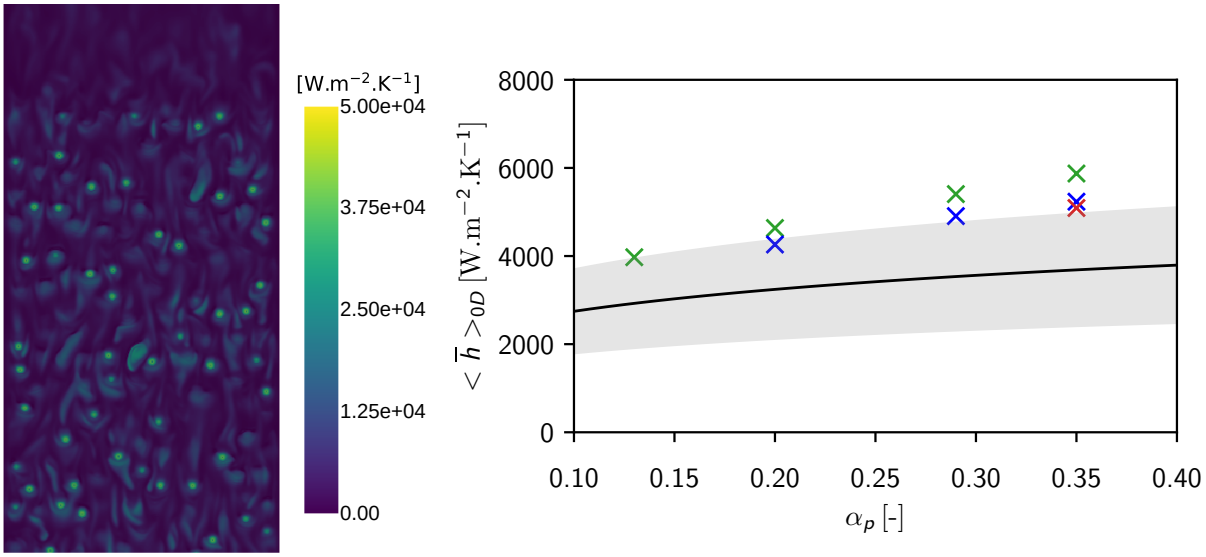

(a) (b)

FIGURE 4.8 – Coefficient de transfert de chaleur à la paroi. (a) Représentation instantanée du champ 2D pour une résolution de 24 mailles par diamètre. (b) Moyenne spatio-temporelle du coefficient d'échange à la paroi. x : $\frac{D_p}{\Delta x} = 12$, x : $\frac{D_p}{\Delta x} = 24$, x : $\frac{D_p}{\Delta x} = 36$. — : corrélation de Haid [33] et son intervalle de confiance de 34,4%.

Les résultats montrent que le comportement macroscopique du lit est bien reproduit, même avec la résolution la plus grossière, car le taux de présence des particules est correctement prédit. Cependant, des effets significatifs de la résolution du maillage sont observés sur les transferts de chaleur fluide-particules et paroi-lit (comme illustré dans la Fig. 4.8). En effet, on observe sur la figure que le transfert de chaleur décroît avec la porosité du lit, comme prédit par la corrélation d'Haid [33] :

$$Nu_p = C\, Re_p^{0,75} Pr^{0,63} (1-\alpha_l)^{1-0,75} \alpha_l^{-1}$$

Pour les résolutions les plus fines simulées, on entre dans l'intervalle de confiance de la corrélation. Enfin, les corrélations vitesse-température sont analysées en détail et montrent que le transfert de chaleur à la paroi est principalement gouverné par le flux de chaleur turbulent près de la paroi ($x^+ \sim 30$).

4.6 Sélection d'articles en lien avec cet axe de recherche

International Journal of Multiphase Flow 165 (2023) 104467

Contents lists available at ScienceDirect

International Journal of Multiphase Flow

journal homepage: www.elsevier.com/locate/ijmulflow

Assessment of a coupled VOF-Front-Tracking/DEM method for simulating fluid–particles flows

Mohamed Salim Hamidi, Adrien Toutant *, Samuel Mer, Françoise Bataille

PROMES Laboratory, CNRS - Université de Perpignan Via Domitia, Perpignan, France

ARTICLE INFO

Keywords:
Particulate flows
Fluidized bed
Front-Tracking
One-fluid method
Discrete element method
Soft sphere model

ABSTRACT

In this paper we introduce a one-fluid numerical method for the simulation of dense particle–fluid flows. The method uses a front tracking algorithm coupled to a viscous penalty method to enforce the rigidity constraint. A modified version of the collision model of Mohaghegh and Udaykumar (2019) is used to model both collisions and lubrication forces. This approach allows us to greatly reduce the amount of ad hoc numerical parameters required to perform the simulations. For validation purpose, we successfully reproduce several experimental and numerical benchmarks including the settling case of a sphere in an enclosed box performed by ten Cate et al. (2002), the bouncing motion against a planar surface performed by Gondret et al. (2002), the study of the fluid–solid fluidized bed performed by Aguilar-Corona (2008), and the particle-resolved simulations of the same case performed by Ozel et al. (2017). The method is shown to realistically reproduce the motion of a settling and a bouncing sphere in a quiescent fluid. The statistical study of the fluidized bed showed excellent agreement with the experimental data and the fluidization law: the solid volume fraction, the solid velocity variance and the anisotropy coefficient are accurately reproduced by our simulations.

1. Introduction

Fluid–particles systems are of considerable scientific and technological interest in a wide range of disciplines. They can be encountered in environmental flows as for example in sandstorms, river sediment transport or dispersal of volcanic ashes to cite just a few. In engineering, one can find them for example in pneumatic transport, pollution control or fluidized beds. The latter are ubiquitous in the chemical and energy fields because of their excellent mixing properties. Since 2010, an original concept of high temperature solar receivers using solid–gas fluidized bed as heat transfer fluid is being actively developed at the CNRS (France) (Flamant and Hemati, 2010; Flamant et al., 2013; Benoit et al., 2015; Zhang et al., 2017; Gueguen et al., 2021). Indeed, the heat transfer fluids currently used in tower power plants (*i.e.* molten salts) limit the temperature at the receiver outlet below 560 °C. In the framework of the third generation of receivers development, the trend is to increase the receiver outlet temperature in order to use high efficiency thermodynamic cycles downstream (super-critical cycle). For this purpose, the target temperature at the receiver outlet is 800 °C. Fluidized bed appears to be an excellent heat transfer fluid candidate.

The literature on the experimental studies of fluidization phenomena is extensive. Often, flat, pseudo-two-dimensional fluidized beds are used to investigate the fluidization behavior with the aid of video techniques or probe measurements because three-dimensional fluidized beds are not optically accessible (Müller et al., 2008). The main limitation of such experimental techniques is that the probes locally disturb the fluidization behavior and thereby affect the measurement itself. To address these restrictions, detailed computational models have received substantial attention over the last thirty years. With the use of computer models, one can realize non-intrusive numerical experiments to examine the flow-field. Furthermore, the use of appropriate models enables the simultaneous 'measurement' of several properties, such as the gas and particle velocities, and the porosity, which is difficult if not impossible to achieve by direct experimentation. Despite these advantages, the construction of reliable models for large-scale gas–solid systems is seriously hindered by the lack of understanding of the fundamentals of dense gas–particle flows. The prime difficulty here relies on the large separation of scales (Ge et al., 2017): the largest flow structures can be of the order of meters; yet these structures are directly influenced by the details of particles–particles and fluid–particles interactions, which take place on the scale of millimeters, or even micrometers

In this context various frameworks have been developed, i.e Two-Fluid Model (TFM), Discrete element method (DEM), Direct numerical simulations (DNS), each one of them targeting a particular level of precision or scale (see Sundaresan et al. (2018) for a comparative review of these methods). One can then use the smaller scale models to

* Corresponding author.
E-mail address: adrien.toutant@univ-perp.fr (A. Toutant).

https://doi.org/10.1016/j.ijmultiphaseflow.2023.104467
Received 18 October 2022; Received in revised form 18 March 2023; Accepted 28 March 2023
Available online 11 April 2023

develop closure laws for the larger scale models. Recently, thanks to the continuous increase in computing power, studying large particle-laden flows with finite-size particles using particle-resolved direct numerical simulations (DNS) has become possible. In the past few decades, many researchers have used particle-resolved simulations to gain a deeper understanding of the intricate physics behind flow-particle and particle–particle interactions in a variety of configurations. These simulations have been applied in a range of fields, including fluidized beds (Pan et al., 2002; Ozel et al., 2017; Esteghamatian et al., 2017; Yao et al., 2021), sedimentation (Uhlmann, 2005; Uhlmann and Doychev, 2014; Willen and Prosperetti, 2019), particles induced/interaction with turbulence (Uhlmann, 2008; Lucci et al., 2010; Wang et al., 2014; Picano et al., 2015; Fornari et al., 2016; Costa et al., 2016), and sediment patterns in channel flow (Kidanemariam and Uhlmann, 2017) among others.

Generally speaking, in the DNS approach, the governing equations for the fluid phase and the particles are implicitly coupled with each other through the no-slip condition at the particles' surfaces (2-way coupling) without the need for parametrizing the drag force between the phases. Also, long-range hydrodynamic interactions between particles are naturally captured. However, when dense flows are considered (flows with particles close enough to directly interact), additional models are required to account for short-range solid–fluid interactions (lubrication forces) and solid–solid contacts (collisions forces). The common approach to model a wet collision is to use a spring–damper system for the solid dissipation, and the lubrication theory for the viscous dissipation.

The goal of this paper is to present an extension of the Front-Tracking method of the simulation software TrioCFD (Calvin et al., 2002) to include solid–solid contact forces by means of a soft-sphere model, and to assess its capability for simulating particle–fluid flow. The resulting algorithm allows for the reduction of the number of numerical parameters required for the simulations. The Front-tracking aspect allows for a precise description of solid–fluid interfaces, which will be extremely useful when studying collisions between non-spherical particles in a future study. More specifically, we developed a method that uses Lagrangian markers to describe the solid–fluid interface. The method is developed for flows with particles of any shape. Obviously, in the tested configurations where only spherical particles are considered this method is not optimal. Indeed, we use several hundreds of Lagrangian markers to describe the surface of one sphere whereas only two parameters – the gravity center and the radius – are required. However, in the case of particles of arbitrary shape, a Lagrangian surface mesh of the solid–fluid interface become a significant asset to accurately describe the interface. To the best of the authors' knowledge, there is no combination of front-tracking approach and viscous penalty method in the literature.

We first start by presenting in Section 2 the Front-Tracking method along with the soft-sphere model used for the solid–solid contact forces. This coupled DNS–DEM technique is then validated in Section 3 through simulations of various validation cases from the literature. In Section 4, we perform simulations of fluidized bed, and present a comparison of the simulation results against numerical and experimental data obtained by Ozel et al. (2017) and Aguilar-Corona (2008). This test serves to validate the coupled DNS–DEM approach in a case with many particles simultaneously interacting. Finally, in Section 5 we draw some concluding remarks concerning this study and prospects for future work.

2. Governing equations and numerical method

The algorithm used in this work to perform direct numerical simulations of fluid–particles flow is based on the "one-fluid" formalism. In this approach, a single set of equations is used to describe the behavior of all phases present in the computational domain. The different phases are treated as a single fluid with spatially varying material properties, depending on the phase indicator function. The governing equations are given by:

$$\begin{aligned} &\nabla \cdot \mathbf{u} = 0 \\ &\frac{\partial \rho \mathbf{u}}{\partial t} + \nabla \cdot (\rho \mathbf{u}\mathbf{u}) = -\nabla p + \nabla \cdot \left(\mu \left(\nabla \mathbf{u} + \nabla^T \mathbf{u}\right)\right) + \rho \mathbf{g} + \mathbf{F_c} \end{aligned} \tag{1}$$

Where $\mathbf{u}$ is the velocity field, ρ the density field, p the pressure field. μ the dynamic viscosity field, $\mathbf{g}$ the gravitational acceleration, and $\mathbf{F_c}$ the collisional force. Both phases are considered incompressible. ρ and μ are considered constant within each phase but show an abrupt transition across the interface. The equations are identical to the equations of a single-phase flow. Therefore, the techniques developed to solve the equations for single-phase flows can readily be used. The only difference is that the solver must be adapted to handle spatially varying material properties. Here we will use a staggered grid to solve the previous equations (Fig. 1 – Right). When solving numerically Eqs. (1), it is necessary to identify which phase is present at a given location. To do this, a phase indicator function I is introduced. It is set to 1 in the solid phase, 0 in the fluid phase and is equal to the solid volume fraction $\alpha = V_{solid}/V_{cell}$ in all the cells crossed by an interface (Fig. 1). In two-phase cells, the density is defined as a mean of the fluid and the solid densities weighted by the phase indicator. Such arithmetic averaging allows to be consistent with the mass conservation principle:

$$\rho = I\rho_{solid} + (1 - I)\rho_{fluid} \tag{2}$$

The same averaging procedure cannot be used for the viscosity field, as it needs to satisfy a different kind of condition (Ritz and Caltagirone, 1999). The following subsection provides more information about this aspect.

As the particles move, the interface between the two phases is displaced. Being able to precisely locate the position of the interface is of paramount importance in the one-fluid formalism. The advection of the marker function is governed by:

$$\frac{\partial I}{\partial t} + \mathbf{u} \cdot \nabla I = 0 \tag{3}$$

Despite the apparent simplicity of the Eq. (3), the numerical integration of a discontinuous color function is one of the difficult problems in computational fluid dynamics. Over the years several methods such as the volume-of-fluid (VOF) method, The level-set method have emerged to address this problem (see Tryggvason et al. (2011) for a review on the subject). In this work we will focus on one method in particular, i.e. the Front Tracking method (Bunner and Tryggvason, 2003).

2.1. General description of the Front-Tracking method

According to this method, the boundary between the two phases is tracked by a moving surface mesh composed of connected Lagrangian marker points that are advected relatively to a fixed Eulerian mesh (Fig. 1 – Left). The flow equations are solved on the Eulerian fixed mesh. The interface velocity is calculated by first doing a tri-linear interpolation of the background velocities at each marker location (Fig. 1 – Right). The barycentric velocity of the interface $\mathring{\mathbf{u}}_m$ is then numerically calculated from:

$$\mathring{\mathbf{u}}_m = \frac{1}{\sum A_i} \sum A_i \mathring{\mathbf{u}}_i \tag{4}$$

where A_i and $\mathring{\mathbf{u}}_i$ are respectively the area, and the velocity vector associated to the ith marker of the Lagrangian mesh. The markers are then translated with the barycentric velocity:

$$\mathring{\mathbf{x}}_i^{n+1} = \mathring{\mathbf{x}}_i^{n} + \Delta t \mathring{\mathbf{u}}_m^{n+1} \tag{5}$$

Once the new positions of the markers $\mathring{\mathbf{x}}_i^{n+1}$ are known, the front is used to reconstruct the indicator function and to update the local physical properties accordingly. The difficulties usually raised by the front tracking method, related to mass conservation and the management of fragmentation and coalescence of inclusions, are absent in our

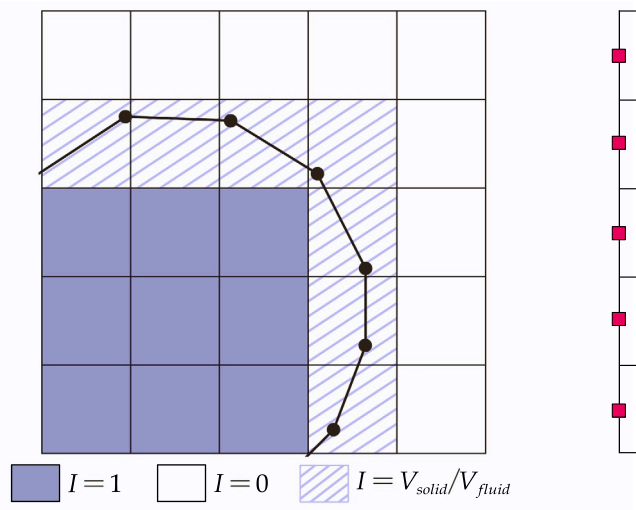

Fig. 1. (Left) Schematic illustration of the phase Indicator function and the front-tracking approach. (Right) Interpolation of the y-component of the velocity at a marker position on a 2D staggered grid: the black crosses, pink squares and green triangles indicate respectively the pressure, x-component and y-component velocity calculation points, the black dots materialize the Lagrangian marker.

situation. Indeed, as we simulate only solid–fluid flows with perfectly rigid interfaces, there is no need to utilize the expensive remeshing procedures intended to correct the degradation of the interface as it deforms over time. The special treatment intended to enforce the rigidity constraint within the solid phase is described below.

2.2. Imposing the rigid body motion

In classical Lagrangian mechanics, an object without any internal degrees of freedom is referred to as a "rigid body". Within such entity, the distance between two arbitrary points is always constant. Mathematically, for this condition to be fulfilled, it is necessary and sufficient for the velocity field inside the solid region to satisfy:

$$\mathbf{U}(\mathbf{X}) = \mathbf{U}_c + \boldsymbol{\omega} \times (\mathbf{X} - \mathbf{X}_c) \tag{6}$$

where $\mathbf{X}_c$ is the position of the center of mass, $\mathbf{U}_c$ is the velocity of the center of mass and $\boldsymbol{\omega}$ is the angular velocity of the rigid body motion. From an Eulerian point of view, this condition can be expressed as equating the strain rate to 0 (Temam and Miranville, 2005):

$$\frac{1}{2}\left(\boldsymbol{\nabla u} + \boldsymbol{\nabla}^T \boldsymbol{u}\right) = \mathbf{0} \tag{7}$$

This formulation is of great convenience with regard to the "one-fluid" equations discussed previously. It describes a localized constraint for the rigid domain that could be directly imposed over the momentum conservation equation without the need to know the velocities of the solid beforehand. Practically, it is possible to nullify the deformation tensor by imposing a high value for μ inside the solid region relative to the fluid domain. The rigid body behavior will be in that case asymptotically enforced. Such an approach is called a viscous penalty method (Ritz and Caltagirone, 1999; Caltagirone and Vincent, 2001). This strategy has the advantages to greatly simplify the coupling between the solid–fluid phases since the coupling is done implicitly and the inertia of the solid region is fully carried by the fluid solver. The velocity field inside the solid being a divergence-free field, the continuity equation is also automatically satisfied.

To impose solid body motion, a large value of the fictitious viscosity must be imposed in the solid region. This led to the existence of large viscosity ratios in the vicinity of the interface and especially in cells where the phase indicator function $I \in]0, 1[$, hereafter called diphasic flow cells. The calculation of the average viscosity in those cells is of great importance to properly reproduced the friction force applied by the fluid flow on the particle. A possible way to compute the latter is to apply an arithmetic average, as it is done for the average density. Doing so will result in a negligible contribution of the fluid viscosity to the average regardless of the solid volume fraction. If $\mu_{solid} \gg \mu_{fluid}$ then:

$$\mu = I\mu_{solid} + (1 - I)\mu_{fluid} \approx I\mu_{solid} \tag{8}$$

This will have the negative effect of making the solid appear larger than it actually is. By propagating the penalty effects to the flow near the interface, the drag forces affecting the motion of the solid is therefore overestimated. As signaled by Ritz and Caltagirone (1999), using a harmonic average would better satisfy the condition of stress continuity at the interface. However, even with this strategy, the viscosity ratio can occasionally be so high that additional treatments are required. For example, some authors proposed to reduce the radius of the particles to compensate for this effect (Vincent et al., 2014; Thiam, 2018). For the numerical investigations conducted in this paper, it was shown that utilizing a step function to apply the fluid viscosity to both the fluid cells and the two-phase cells produced the best results. It should be noted that fine-tuning the viscosity ratio is necessary before starting the simulations, as imposing low viscosity inside the particle will lead to a poorly enforced rigidity constraint. In this study a viscosity ratio between 10^3 and 10^4 is taken.

2.3. Short-range interaction modeling

In general, Non-Boundary-Fitted-Particle-Resolved (NBF-PR) methods, such as the one discussed in the previous section, are ideally suited to capture the long-range hydrodynamic interactions between the fluid and solid phases. However, they are not the best suited methods to capture the short-range interactions. The lubrication effects are under resolved, and the collisions are not taken into account intrinsically by NBF-PR methods. Additional modeling is required to take those interactions into account.

2.3.1. Lubrication modeling

As two solids are brought very close to one another, the fluid between the two surfaces is drained out of its location, generating viscous constraints. The NBF-PR methods performs a decent job of capturing the frictional forces as long as the distance between the two solids is greater than two simulation cells. In the case where the spacing becomes smaller than one cell, the viscous stress is in fact under resolved. A more realistic alternative would be to rely on a closure model based on the lubrication theory to make up for the grid's lack of

spatial resolution (Cox and Brenner, 1967; Cooley and O'Neill, 1969). In Breugem (2010), the author implemented this approach by adding an amplified Stokes drag force on the solid when the space between the solid surfaces dropped below a predetermined user-defined distance. This distance corresponds to the threshold under which the simulation method fails to solve the fluid dynamics accurately. To avoid the divergences of the analytical expression of the lubrication force, Breugem capped it starting from another user specified distance. Physically, it was justified as a means to simulate the saturation of the hydrodynamic force caused by roughness effects. As the force constantly opposes the particle's motion, it is a dissipative force by nature.

Several authors have successfully used this kind of closure procedure to model the viscous lubrication effects (Kempe and Fröhlich, 2012; ten Cate et al., 2002; Costa et al., 2015; Ardekani et al., 2016; Biegert et al., 2017; Izard et al., 2014; Brändle de Motta et al., 2013). However, this approach can be problematic in a number of ways: the lubrication model's implementation might result in a large number of ad hoc numerical parameters that must be calibrated. For instance, three separate parameters were required in Brändle de Motta et al. (2013). Additionally, the provided amplification coefficients for the lubrication force are grid dependent. Moreover, in Biegert et al. (2017) the authors showed that the dissipation may depend on the gap thickness, and more investigation is needed in that regard. Finally, for this procedure to be valid, the Stokes flow assumption must be fulfilled within the fluid film separating the two solids. This is only verified if the distance between the two interfaces is significantly smaller than the characteristic length scale of the particles (Cox and Brenner, 1967). To correctly solve for viscous dissipation in the fluid film, the mesh would need to be further refined, at the expense of computation time.

2.3.2. Collision modeling

As the surfaces of the particles come into direct contact, a collision occurs and affect the momentum of both particles. Most of the time, the trajectories are abruptly altered. According to Legendre et al. (2006), regardless of whether the collision happens in air (dry collision) or in a more viscous fluid (wet collision), the typical collision period is often several orders of magnitude shorter than the particle's viscous relaxation time. As a result, the particles perceive the collision as a discontinuity in their motions. Fully capturing the motion of the particles as they undergo collisions will require incredibly short integration time steps that would make simulating a particulate flow over an extended period of time impossible. For that reason, many authors preferred to model the collisions using a variation of the soft-sphere collision model of Cundall and Strack (1979). In the latter, the contact force applied to colliding solids is proportional to the distance separating their contact points. Glowinski et al. (1999) used a repulsive force proportional to the square of the distance separating the particles. The force that models lubrication in liquid-fluidized bed is applied from a distance beyond the particle surface to prevent any overlapping. Wan and Turek (2006) used a similar approach but the particles were allowed to overlap. Although straightforward to implement, using such force results in poor physical fidelity. Since the collision is viewed as elastic, the energy dissipation during the collision is not taken into consideration.

Based on the Hertz theory of contacts (Hertz, 1882; Johnson, 1985), other authors suggested computing a nonlinear contact force using a mass–spring–damper system (Kempe and Fröhlich, 2012).

The coefficients of the model are derived from geometrical properties and from the particle elastic characteristics. The solid dissipation can be addressed thanks to the dash-pot coefficient. This approach is well concordant with the dry collisions experiments in Stevens and Hrenya (2005). The order of the time step of the Navier–Stokes solver is larger than the collisions duration predicted by the Hertz contact theory. Due to this separation of time scales, extremely small numerical integration time steps are needed to solve the particle motion. Fortunately, it is possible to artificially stretch the collision duration to be larger than the fluid solver time step and still maintain the perceived separation of time scales (or the discontinuity) in the motion of the particles. Based on this principle, Feng et al. (2010) manually reduced the value of the spring stiffness value to obtain a satisfactory collision time. Kempe and Fröhlich (2012) suggested in their adaptive collision model (ACM) to stretch the collisions time to ten times the flow solver time step. Similarly, to the Hertz theory, a non-linear force–displacement relationship was used to model the contact force. The spring and dash-pot coefficients were computed by solving a second-order ordinary differential equation using an iterative solver. Ray et al. (2015) improved on the work of Kempe and Fröhlich by proposing an explicit formulation for the coefficients, alleviating the need for an iterative solver. In a similar fashion, Breugem (2010), Brändle de Motta et al. (2013), Izard et al. (2014), Costa et al. (2015) used the work of van der Hoef et al. (2006) to model the collision force with a damped harmonic oscillator. Which can be seen as a linearized version of the work of Kempe and Fröhlich. The spring stiffness and the damping coefficient are computed from the prescribed collision time and coefficient of restitution in a more straightforward way. A common factor among the studies mentioned above is that they were paired with a lubrication model to account for the dissipative effect of the viscous drainage. Besides that, the rebound velocity is unknown beforehand, as it can only be determined after the collision has ended.

2.3.3. Combined modeling

With the Simplified Spring Collision Method (SSCM), Mohaghegh and Udaykumar (2019) developed a different strategy that simultaneously accounts for both the dissipative effect in the solid and in the fluid gap. The collision force is modeled based on a mass–spring system with no dash-pot. Such methodology allows to reduce the number of numerical parameters introduced. The spring stiffness is chosen to satisfy the specified maximum distance of collision. This distance is the only numerical parameter of the model. No damping coefficient or lubrication model is employed in the SSCM. Instead, the spring stiffness is adjusted using the coefficient of restitution to obtain the appropriate rebound velocity. The adjustment is made during the bouncing phase, which occurs after the particle has stopped moving at the "maximum distance of collision" and has begun to rebound in the opposite direction of the impact. The SSCM differs from other models in that the rebound velocity of the particles is known before the impact even occurs. This is so because, the coefficient of restitution used to correct the spring stiffness is calculated from a well-established experimental relationship between the restitution coefficient and the Stokes number (Ruiz-Angulo and Hunt, 2010). The SSCM addresses many of the drawbacks of the precedent collision models. It allows the collision time to be stretched, enabling granular flow simulations to be run for extended times. The model's coefficients are provided explicitly, eliminating the requirement for an iterative solution. The number of numerical parameters is reduced to one (the maximum distance of collision), since no separate lubrication model is used.

In this paper we use a slightly modified version of Mohaghegh and Udaykumar (2019), as there is a quite obvious equivalence between the maximum distance of collision and the collision duration, the latter was preferred to compute the spring stiffness coefficient. We discuss the details of our modifications in the following.

Consider a collision occurring between two spherical particles p and q or between the particle p and a wall. The contact force $\mathbf{F}_c$ acting on a particle during a collision is modeled by a harmonic oscillator as:

$$\mathbf{F_c} = -k\delta_n\mathbf{n} \tag{9}$$

with k is the spring stiffness and δ_n the normal distance separating the colliding sphere surfaces given by:

$$\delta_n = \|\mathbf{x}_p - \mathbf{x}_q\| - \left(R_p + R_q\right) \tag{10}$$

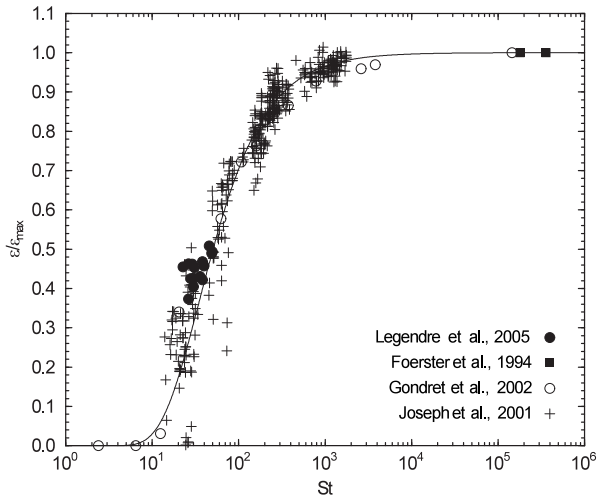

Fig. 2. Wet coefficient of restitution, as a function of the Stokes number St. The solid line is the best fit of the data points of Joseph et al. (2001), Gondret et al. (2002), Legendre et al. (2005), Foerster et al. (1994).
Source: Adapted from Legendre et al. (2006).

where $\mathbf{x}_p$ and $\mathbf{x}_q$ are the positions of the center of mass of the particles p and q, R_p and R_q are the radius of the particles. $\mathbf{n}$ is the normal vector to the plan of collision defined by:

$$\mathbf{n} = \frac{\mathbf{x}_p - \mathbf{x}_q}{\|\mathbf{x}_p - \mathbf{x}_q\|} \tag{11}$$

The differential equation describing the motion of the system is given by:

$$m_e \ddot{\delta}_n + k\delta_n = 0 \tag{12}$$

The spring stiffness k was derived by Breugem (2010) in the special case of an elastic collision:

$$k = m_e \left(\frac{\pi}{\tau_0}\right)^2 \tag{13}$$

where m_e is the effective mass and τ_0 is the prescribed collision time. For particle–particle interactions, $m_e = m_p m_q / \left(m_p + m_q\right)$ with m_p and m_q being the mass of particles p and q respectively. If the collision occurs between a particle p and a wall, then $m_e = m_p$. The stretched collision time is taken as a multiple N of the Navier–Stokes solver time step Δt:

$$\tau_0 = N\,\Delta t \tag{14}$$

Physically, collisions are inelastic, which means that some kinetic energy is dissipated during the contact. Even, in the scenario where the viscous stress is negligible, some energy is still dissipated as vibrations in the solid. The dry coefficient of restitution e_d accounts for this energy dissipation:

$$e_d = \frac{\Delta u_{reb,d}}{\Delta u_{imp,d}} \tag{15}$$

where $\Delta u_{reb,d}$ and $\Delta u_{imp,d}$ are, respectively, the rebound and impact relative velocities of the two solid surfaces colliding in the absence of fluid viscous dissipation (dry regime). The solid's dry coefficient of restitution is a physical property directly related to the material's elastic properties. The default value used in this work is $e_d = 0.97$.

In the wet regime, the energy dissipation is notably higher due to the fluid viscous dissipation. Joseph et al. (2001), Yang and Hunt (2006) have shown experimentally that the apparent or effective coefficient of restitution is strongly correlated with the Stokes number St:

$$St = \frac{2}{9}\frac{R_{eff}\,\Delta u_{imp}\rho_s}{\mu_f} \tag{16}$$

where R_{eff} is the effective radius – defined by $R_{eff} = R_p R_q / \left(R_p + R_q\right)$ in the case of two particles, and $R_{eff} = R_p$ in the case of a wall-particle collision –, Δu_{imp} is the relative velocity at the moment of impact, ρ_s the density of the particles and μ_f the dynamic viscosity of the fluid.

The relationship between the effective coefficient of restitution e and the Stokes number St can be written as the product of the constant dry coefficient of restitution and a "wet" coefficient of restitution, e_w depending on the St number. Typically e_w varies from 0 to 1:

$$e(St) = e_d\ e_w(St) = \frac{\Delta u_{reb}}{\Delta u_{imp}} \tag{17}$$

From Fig. 2, we can see the effective coefficient of restitution e is pretty much equal to the dry coefficient of restitution for $St > 1000$. This is in accordance with the fact that in this range of Stokes numbers, viscous effects are negligible. However, for lower values of St, from 10 to 1000, significant variation of e is observed. The coefficient of restitution decrease with St and the related viscous stress rise. Below the critical value St 10, no rebound is observed. Using the analogy with a dissipative mass–spring system (Legendre et al., 2005) showed that the evolution of the wet coefficient of restitution as a function of the St numbers followed the expression:

$$e_w = \exp\left(-\frac{35}{St}\right) \tag{18}$$

Similarly to Mohaghegh and Udaykumar (2019), the required rebound velocity at the end of a collision is obtained by using the $e_w(St)$ relationship (Eq. (18)) as an entry parameter of the model. The collision's effective coefficient of restitution is calculated based on the collision St number before impact and is used to adjust the spring stiffness in Eq. (9). Such procedure eliminates the requirement for a lubrication model or a dash-pot coefficient by intrinsically accounting for both energy dissipation. It is worth noticing that the pre-collision Stokes number is calculated at the time when the particles start to collide. This means that the lubrication effect has been already under-resolved, since the gap between the particles is less than a grid-cell. Hence, the Stokes number could be over-estimated. Practically speaking, the kinetic energy of the particle before and after the collision are prescribed using the effective coefficient of restitution. The difference between the two energies correspond to the dissipative effects. After translating this difference into potential energy, it can easily be shown that, to obtain the desired rebound velocity, the spring stiffness needs to be reduced by a factor of e^2 in the rebound phase (see Mohaghegh and Udaykumar (2019) for more detail about the derivation). The adjustment is made after the maximum overlap of the interfaces allowed by the spring stiffness is reached, and the particles start to go in opposite ways. The spring stiffness is treated as piece-wise function of the scalar product $\Delta\mathbf{u}\cdot\mathbf{n}$ (Eq. (19)). The change of sign of the latter is used to pinpoint the exact moment when the reduction of stiffness is done (see Fig. 3):

$$k_i = \begin{cases} k_{imp} = m_e\left(\frac{\pi}{\tau_0}\right)^2 & \text{if} \quad \Delta\mathbf{u}\cdot\mathbf{n} \leqslant 0 \\ k_{reb} = k_{imp}e^2 & \text{if} \quad \Delta\mathbf{u}\cdot\mathbf{n} > 0 \end{cases} \tag{19}$$

The collision force $\mathbf{F_c} = -k_i\delta_n\mathbf{n}$ is then applied to the purely solid cells in the simulation domain (corresponding to Indicator function strictly equal to 0). This is done at each time step until there is no overlapping between the two solids.

2.4. Numerical implementation

The Navier–Stokes equations are solved by a prediction/correction method on a staggered Cartesian grid with a Marker-And-Cell finite volume discretization (MAC) (Puckett et al., 1997). The velocity increment $\dot{\mathbf{u}}$ in the prediction step (Eq. (20)) is calculated by summing the contributions of the convection term $\mathbf{A}^n$, the diffusion term $\mathbf{D}^{n+1}$, the collisional source term $\mathbf{C}^{n+1}$, and the gravitational source term $\mathbf{g}$. The pressure is not taken into account in this step:

$$\dot{\mathbf{u}} = \frac{\mathbf{u}^* - \mathbf{u}^n}{\Delta t} = -\mathbf{A}^n + \frac{1}{\rho^n}\left(\mathbf{D}^{n+1} + \mathbf{C}^{n+1}\right) + \mathbf{g} \tag{20}$$

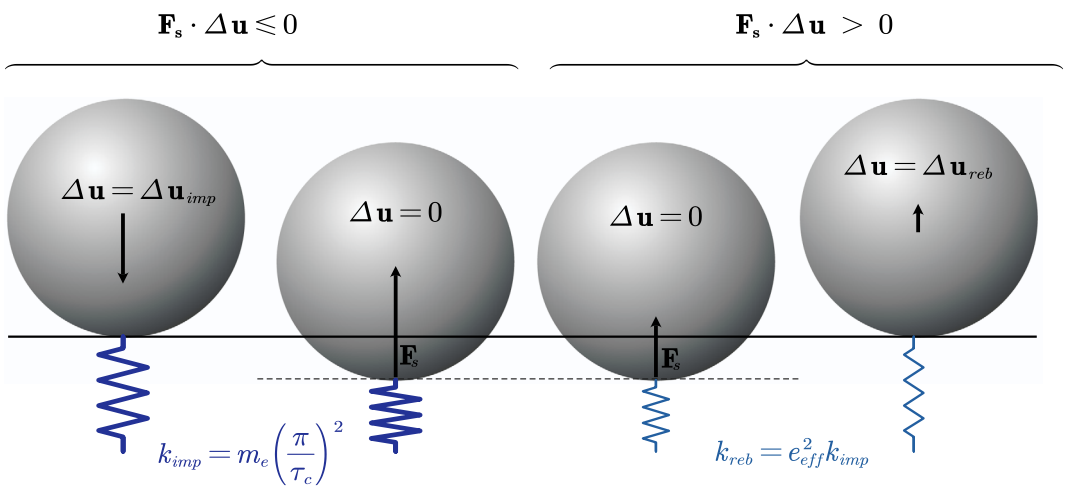

Fig. 3. Explanatory diagram of the collision model.

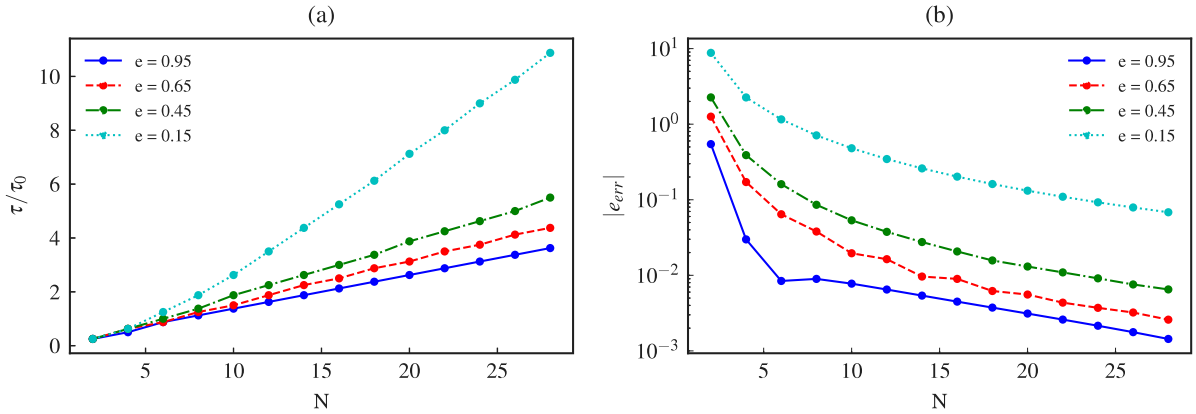

Fig. 4. (a) Evolution of the collision duration stretching factor as a function of N for different coefficients of restitution e. (b) Evolution of the integration error as a function of N for different coefficients of restitution e.

To alleviate the numerical constraints caused by the high viscosity ratios R_μ required by the viscous penalty method. The evaluation of the diffusive source term is implicited and computed with an Uzawa algorithm.

Regarding the calculation of the collision term $\mathbf{C}^{n+1}$, the distance δ_n (Eq. (10)) between the surfaces of each pair of particles p and q is calculated. If ($\delta_n < 0$) then a collision is detected and the force to be applied to each of these particles is calculated. According to the third Newton law of motion, the reaction force to be applied to the particle q is of equal intensity and opposite direction to the force applied to the particle p:

$$\mathbf{F}_{\mathbf{c},p\to q} = -\mathbf{F}_{\mathbf{c},q\to p} \tag{21}$$

The forces acting on the particle p are summed up and divided by the volume V_p of the particle p. The result is then applied to the appropriate solid cells thanks to the phase indicator function:

$$\mathbf{c}^{n+1} = I^n \sum_q \frac{\mathbf{F}_{\mathbf{c},q\to p}^{n+1}}{V_p} \tag{22}$$

The forces are calculated at each time step until no overlapping is observed ($\delta_n \geq 0$). The time integration of the collision force is done by a Semi Implicit Euler time scheme (SIE) to prevent numerical divergences caused by the Forward Euler scheme:

$$\mathbf{F}_{\mathbf{c},q\to p}^{n+1} = -k_i \delta_n^{n+1} \mathbf{n} \tag{23}$$

where $\mathbf{n}$ is given by Eq. (11) and δ_n^{n+1} is the distance separating the surface of the two colliding particles evaluated at the time $n+1$:

$$\delta_n^{n+1} = \left\| \left(\mathbf{x}_p^n - \mathbf{x}_q^n\right) + \Delta t \left(\mathbf{u}_p^n - \mathbf{u}_q^n\right) \right\| - \left(R_p + R_q\right) \tag{24}$$

As the coefficient N (Eq. (14)) is the only numerical parameter of our model, we discuss its influence in more detail in the following. The spring stiffness during the negative phase ($\Delta\mathbf{u} \cdot \mathbf{n} < 0$) is obtained by setting the collision duration $\tau_0 = N\Delta t$. However, when the spring stiffness is reduced in the positive phase ($\Delta\mathbf{u}\cdot\mathbf{n} > 0$), the collision period is stretched due to the oscillation period being inversely proportional to the spring stiffness. By noting that $T_{reb} = T_{imp}/e$ and:

$$\tau = \frac{1}{2}\left(\frac{T_{imp}}{2} + \frac{T_{reb}}{2}\right) \tag{25}$$

where T_{imp} and T_{reb} are the oscillation periods corresponding to the spring stiffness k_{imp} and k_{reb}, we can show that the stretching factor is equal to:

$$\frac{\tau}{\tau_0} = \frac{1}{2}\left(1 + \frac{1}{e}\right) \tag{26}$$

Fig. 4(a) illustrates the evolution of the stretching factor as a function of N for various coefficients of restitution e. We can see that the initial collision duration τ_0 is retrieved in the dry regime (high Stokes numbers corresponding to $e = 1$). In the asymptotic case where $e \to 0$, the collision duration tends to infinity, and no rebound is observed as the particles remain in permanent contact.

Considering the relationship between N and the collision duration τ, it is important to keep N as small as possible to maintain physical realism at high Stokes numbers. However, N must be high enough for the collision force to be accurately integrated, as integration errors increase when N decreases. In order to demonstrate this concept, we have numerically solved Eq. (12) using a semi-implicit Euler scheme. The spring stiffness of the system is defined by Eq. (19). Fig. 4(b) illustrates the evolution of the integration error, which is defined as $|e_{err}| = |e - e(N)|/e$, where $e(N)$ represents the coefficient of restitution obtained after numerically solving Eq. (12) with an Euler Semi-Implicit method.

In our work, we have set $N = 8$ similarly to Breugem (2010), Brändle de Motta et al. (2013), Costa et al. (2015). For this value, the integration error in the dry regime is less than 1 percent. However, due to our model's nonlinear nature, the integration error increases as the coefficient of restitution decreases. For e equal to 0.65, 0.45, and 0.15, the integration error is equal to 0.038, 0.085, and 0.71, respectively. To reduce the integration error at lower Stokes numbers, N can be increased (see Fig. 4(b)). However, this comes at the cost of losing physical realism at higher Stokes numbers. Alternatively, higher-order integration schemes can be used, but they come at the expense of computing time and memory consumption. In the collision validation section, we compared our simulation results to experimental data. We found that the overestimation of the rebound velocity introduced by the numerical integration scheme was negligible compared to the additional viscous damping effect exerted by the surrounding fluid. Therefore, we selected a value of $N = 8$ and the ESI scheme for the following simulations, as this choice was seen a good balance between computation time, accuracy, and physical realism.

In the case of a wall-particle collision, a virtual particle identical to the particle p is generated behind the wall as proposed in Glowinski et al. (1999). This strategy allows the calculation of the collisions force in the wall-particle collisions situation to be treated in an identical manner to the particle–particle scenario. The virtual particle's center of mass is positioned so that the contact point is displaced from the wall by a distance ε_{wp}. Due to numerical restrictions unique to our simulation code, which prohibit Lagrangian points from leaving the simulation domain, the use of this offset is necessary. It was observed that this numerical limitation may be overcome with hardly any impact on the accuracy of the simulations provided in the next section by taking ε_{wp} equal to one fourth of the simulation grid cell.

Once the contributions corresponding to each source term in Eq. (20) is known, the predicted velocity field $\mathbf{u}^*$ is then obtained by using an Euler Explicit (EE) time scheme:

$$\mathbf{u}^* = \mathbf{u}^n + \dot{\mathbf{u}}\Delta t \tag{27}$$

Then, an elliptic pressure equation is solved by a SSOR-preconditioned GCP solver to impose a divergence-free velocity field:

$$\nabla \cdot \left(\frac{1}{\rho^n} \nabla P^{n+1} \right) = \frac{1}{\Delta t} \nabla \cdot \mathbf{u}^* \tag{28}$$

From the resulting pressure field, we can compute the projected velocity field $\mathbf{u}^{n+1}$ by:

$$\mathbf{u}^{n+1} = \mathbf{u}^* - \frac{1}{\Delta t} \nabla P^{n+1} \tag{29}$$

The freshly obtained Eulerian velocity field is used to compute the velocity $\mathring{\mathbf{u}}_i$ at the position of Lagrangian nodes thanks to a tri-interpolation procedure $\mathcal{F}()$:

$$\mathring{\mathbf{u}}_i^{n+1} = \mathcal{F}\left(\mathring{\mathbf{x}}_i^n, \mathbf{u}^{n+1} \right) \tag{30}$$

The velocities of the Lagrangian nodes are used to compute a mean velocity of the interface $\mathring{\mathbf{u}}_m$:

$$\mathring{\mathbf{u}}_m^{n+1} = \frac{1}{\sum S_i} \sum S_i \mathring{\mathbf{u}}_i^{n+1} \tag{31}$$

Table 1
Physical parameters for a spherical particle settling in viscous fluid.

Case	ρ_s/ρ_f	ρ_f [kg m^{-3}]	μ_f [Pa s]	V_{inf} [m s^{-1}]	Re
1.1	1.115	970	0.373	0.038	1.5
1.2	1.161	965	0.212	0.060	4.1
1.3	1.164	963	0.113	0.091	11.6
1.4	1.167	960	0.058	0.128	31.9

The Lagrangian nodes are then translated with the mean interfacial velocity:

$$\mathring{\mathbf{x}}_i^{n+1} = \mathring{\mathbf{x}}_i^n + \Delta t \mathring{\mathbf{u}}_m^{n+1} \tag{32}$$

The phase indicator is integrated using the new front position by a geometrical procedure $\mathcal{G}()$:

$$I^{n+1} = \mathcal{G}\left(\mathring{\mathbf{x}}^{n+1} \right) \tag{33}$$

And finally the physical properties are updated:

$$\rho^{n+1} = I^{n+1}\rho_{solid} + (1 - I^{n+1})\rho_{fluid} \tag{34}$$

$$\mu^{n+1} = \begin{cases} \mu_{solid} & \text{if} \quad I^{n+1} = 1 \\ \mu_{fluid} & \text{if} \quad I^{n+1} < 1 \end{cases} \tag{35}$$

The algorithm is implemented in the TrioCFD code developed by CEA relying on the TRUST platform (formerly known as Trio_U). The code is fully parallel, written in C++ and has been widely used to simulate both single-phase and multi-phases (liquid/gas) flows (Toutant and Bataille, 2013; Aulery et al., 2015; Dupuy et al., 2018, 2019; du Cluzeau et al., 2019, 2020, 2022).

3. Canonical validation cases

In this section, the validity of the present method is demonstrated by comparing its performances to reproduce the experimental data of ten Cate et al. (2002) and Gondret et al. (2002).

3.1. Free-falling sphere

The first validation case considered to be the settling of spherical a particle in a three-dimensional box at different Reynolds numbers. The test case is based on the experimental configuration of ten Cate et al. (2002) where a single sphere, of diameter $dp = 15$ mm, is released at rest in an open quiescent container. This numerical benchmark was also done by Vincent et al. (2014), Zhou et al. (2017), Chen and Müller (2020). Reynolds numbers, $Re_t = \rho_f V_t R_p/\mu_f$ with V_t the terminal velocity, of 1.5, 4.1, 11.6 and 32.2 are considered by adjusting the fluid viscosity inside the box as shown in Table 1. The container dimensions are $0.1 \times 0.16 \times 0.1$ m^3 in the x, y and z-direction respectively. The gravity $g = 9.81$ m s^{-1} acts in the negative y-direction. The release position of the particle gravity center is positioned 12.75 cm above the bottom of the tank, and centered on the x and z directions. The density of the solid particle is $\rho_p = 1120$ kg m^{-3}.

Our numerical domain corresponds to the experimental container size. No-slip boundary conditions are imposed on the walls of the domain, while outflow boundary conditions (with a null reference pressure) is applied on the upper boundary. Initially, the fluid is at rest in the domain. The latter is divided into $100 \times 160 \times 100$ mesh cells, which leads to a mesh resolution of $Nd = 15$ grid cells per diameter. The viscosity ratio is set to $R_\mu = 1000$ for all the four cases. Finally, an integration time step equal to $\Delta t = 10^{-4}$ s is used for the pressure solver. Fig. 5 compares the evolution of the simulated particle vertical velocity and position to the experimental results. The velocity history of the particle highlights four different phases: (i) An acceleration phase – where the speed of the particle increases gradually until it reaches its terminal velocity –. (ii) A stationary phase – during which the particle

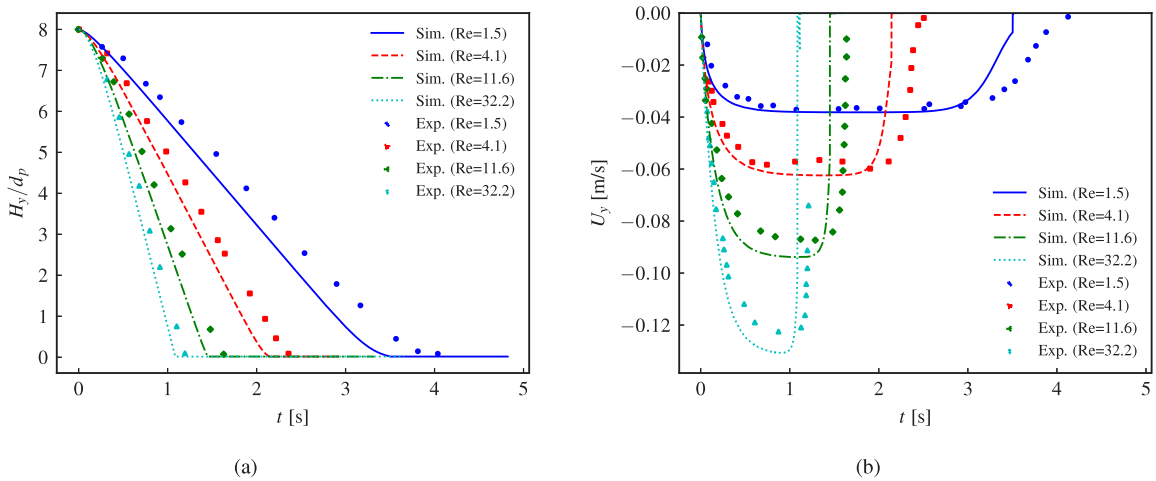

Fig. 5. Time histories of the vertical position and velocity for a particle settling in a small container: (a) Normalized gap height H_y/d_p; (b) Settling Velocity U_y. Symbols: experimental data (ten Cate et al., 2002), lines: present simulations.

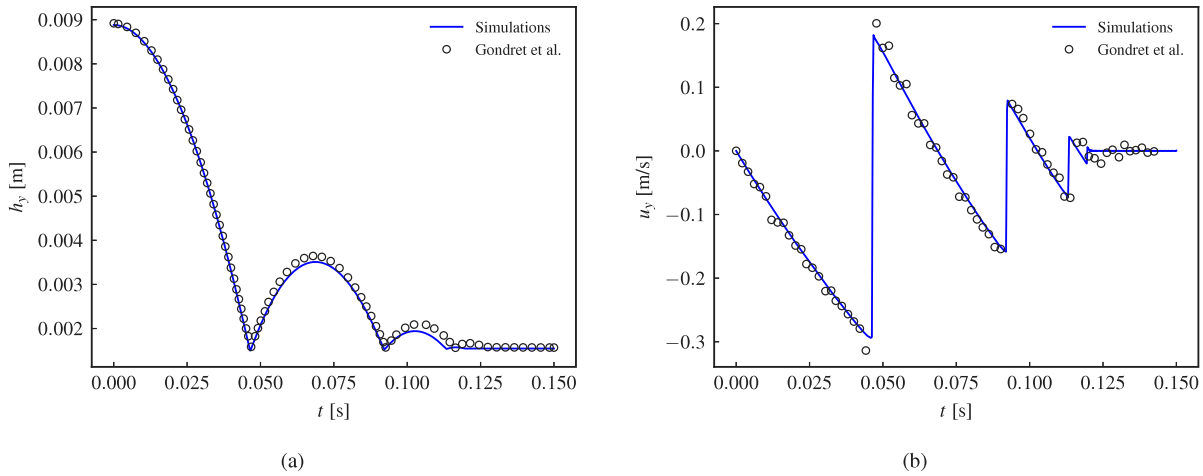

Fig. 6. Time histories of the vertical position and velocity for a 3 mm steel sphere colliding with a normal surface in silicon oil RV10: (a) Vertical position h_y; (b) Settling Velocity u_y. Symbols: experimental data (Gondret et al., 2002), lines: present simulations.

velocity remains constant –. (iii) A deceleration phase – as the particle gets closer to the bottom wall, its velocity decrease under the effect of the viscous constraints –. (iv) A contact phase when the motion of the particle ends. With our method, the acceleration and deceleration phases are qualitatively well captured. However the method seems to underestimate the drag constraints, as the computed terminal velocity in the equilibrium phase is systematically slightly higher than the reference. As a result, the collision with the bottom of the tank occurs earlier in our simulations. Moreover, at low Reynolds number, when the particle comes into contact with the wall, an abrupt change in the slope of the velocity is noticed.

Finally, by reproducing these cases, we demonstrate that our method is able to reproduce the settling of a solid sphere in a quiescent flow. This case allows, moreover, to validate the implementation of the rigid body motion in the particle and the collision model for the no-bouncing contact regime.

3.2. Bouncing motion of a solid sphere colliding onto a planar surface in a viscous fluid

the second validation case is dedicated to the bouncing collision regime. To this end, we reproduce the experimental data of Gondret et al. (2002) exploring the bouncing motion of a solid sphere colliding onto a planar surface in a viscous fluid as conducted. The same benchmark was also performed by Jain et al. (2019), Kidanemariam and Uhlmann (2014), Elghannay and Tafti (2016). A stainless steel particle is released in a tank filled with silicon oil RV10. Under the effect of gravity, the particle accelerates towards the bottom of the tank until multiple collisions are observed. The simulated time evolution of the trajectory and vertical velocity profiles are compared to the experimental data. The simulation is conducted in a $9 \times 12 \times 9$ mm^3 domain with a mesh resolution $d_p/\Delta x = 20$. The particle is 3 mm in diameter, and its center is positioned at the coordinates (4.5 mm, 8.88 mm, 4.5 mm). The densities of the fluid and the solid are equal to 935 and 7800 kg/m^3 respectively. The fluid viscosity is equal to 0.01 Pa s and the viscosity ratio R_μ is kept to 1000. No-slip boundary conditions are imposed on all the walls of the domain. The time step is equal to 5×10^{-5} s. The advection time, defined with the terminal velocity and the mesh size, is equal to 5×10^{-3} s. To decrease the numerical costs, the simulation begins at the second rebound of the (Gondret et al., 2002) experiments. This approach is justified because the impact of the fluid perturbation induced by the first rebound does not carry over to the following rebounds, as stated in Gondret et al. (2002).

Fig. 6 shows the time evolution of the particle gravity center and it's settling velocity. The simulated trajectory agrees convincingly with the experimental data during the initial settling phase. The trajectory after

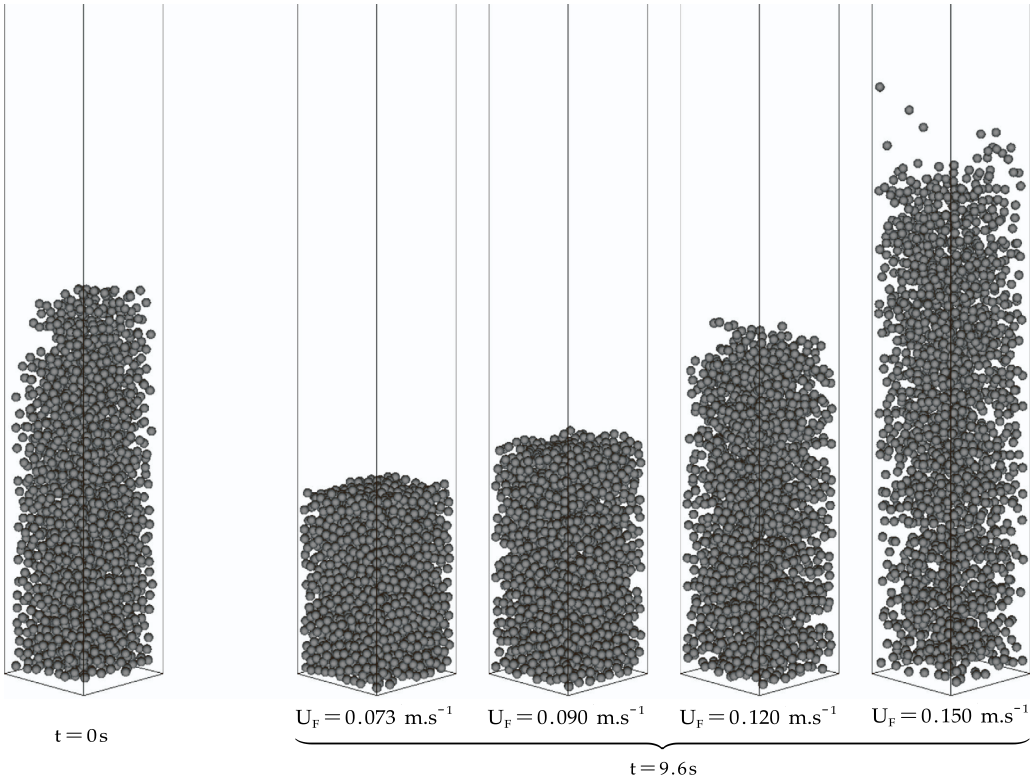

Fig. 7. 3D views of the particles' position distribution in the domain for $t = 0\,\mathrm{s}$ and $t = 9.6\,\mathrm{s}$ for the four fluidization velocities tested.

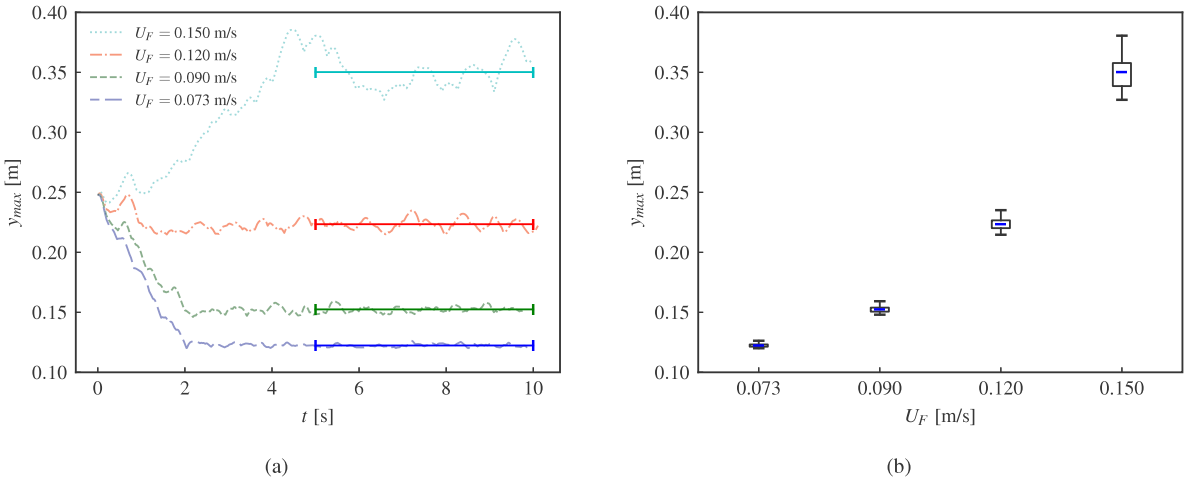

Fig. 8. (a): Time-evolution of maximum axial particle position at different fluidization velocities: $U_F = 0.15,\ 0.12,\ 0.09,\ 0.073$ m s^{-1}. The continuous lines represent the average mean value of y_{max} over the range $t = [5\,\mathrm{s}, 10\,\mathrm{s}]$ (b) Box plot of the distribution of y_{max} (m). The box represents the interquartile range (IQR), the line inside the box is the mean, the whiskers extend to the minimum and maximum values.

the first rebound is properly reproduced. However slight discrepancies are observed with the experimental data for the following rebounds. This is to be expected, as experimental data are more scattered at lower Stokes numbers (see Fig. 2). As the restitution coefficient underestimation accumulates over the successive rebounds, numerically the particle comes at rest slightly sooner than in the experiments. The Stokes numbers of the successive rebounds are respectively $St = 76.1$, $St = 41.2$, $St = 18.9$ and $St = 5.2$.

Finally, this case allows extending our validation of the collision model to the bouncing regime. As the particle–wall and particle–particle collisions are treated the same way in our model (see Section 2), we consider at this point our model validated and in the next section we assess its capability to model complex flows involving a large number of particles.

4. Particle resolved direct numerical simulation of a 2100 liquid–solid fluidized bed

In this section, our aim is to examine the overall accuracy of the framework to reproduce the global behavior of a dense fluid–particles suspension. To do so, we report simulation results of a 2100 particles fluidized bed at 4 different fluidization velocities. The parameters for the simulation are derived from the experiment of Aguilar-Corona (2008) who investigated the fluidization of 6 mm monodisperse spherical particles of Pyrex ($\rho_p = 2230$ kg/m^3) in a concentrated aqueous solution (65% w/w) of potassium thiocyanate ($\rho_f = 1400$ kg/m^3, $\mu_f = 3.8 \times 10^{-3}$ Pa s). The experimental setup was designed to facilitate the validation of numerical method. The refractive index matching of both

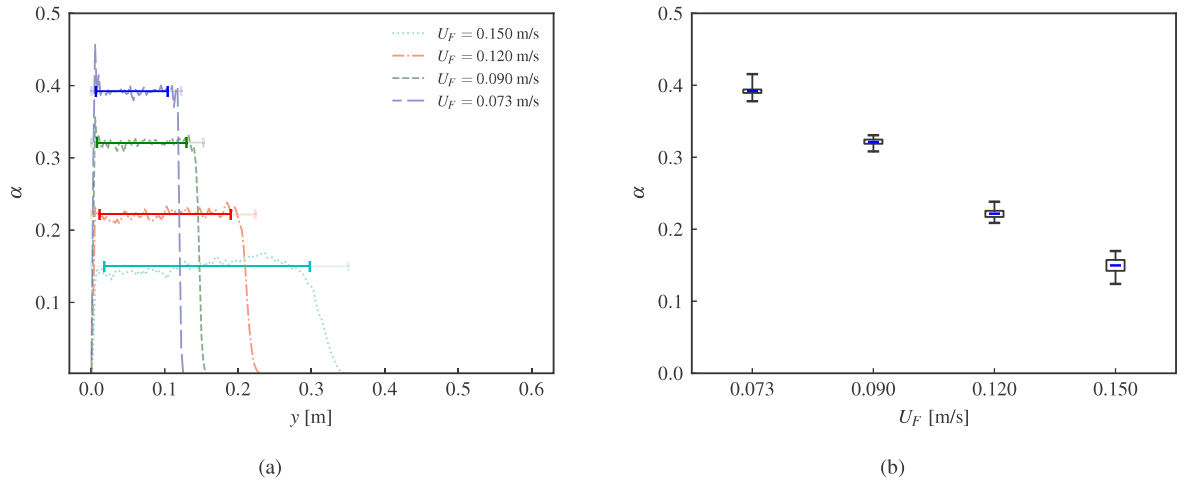

Fig. 9. (a) Time-section average of solid void fraction α as a function of height. The continuous lines represent the mean value of α over $y = [0.05\overline{y_{max}}, 0.95\overline{y_{max}}]$. (b) Box plot of the distribution of α. The box represents the interquartile range (IQR), the line inside the box is the mean, the whiskers extend to the minimum and maximum values.

phases allows the authors to use non-intrusive optical measurement technique (PIV) to characterize the fluid velocity field and the particles agitation. The particle terminal velocity is $V_t = 0.24\,\mathrm{m\ s^{-1}}$ (see Aguilar-Corona (2008)) and the associated Reynolds and Stokes numbers are 530 and 94, respectively. Note that Ozel et al. (2017) use a different definition of the Stokes number $St = \frac{8\rho_p}{3\rho_f Cd}$. With this definition, the Stokes number is equal to 5.3. The two definitions are equivalent if $Re \ll 1$ and consequently $Cd = 24/Re$. Both phases are contained in a cylindrical shaped tank.

This configuration was already studied numerically by Ozel et al. (2017) – using the Implicit Tensorial Penalty Method of Vincent et al. (2014) – with a mesh resolution of $Nd = 12$. To assess the performance of our approach, we reproduce in this section the numerical configuration of Ozel for four different fluidization velocities: $0.15\,\mathrm{m\ s^{-1}}$, $0.12\,\mathrm{m\ s^{-1}}$, $0.09\,\mathrm{m\ s^{-1}}$ and $0.073\,\mathrm{m\ s^{-1}}$. However, as our code does not handle O-grid mesh, the container geometry considered is a cuboid of dimensions $0.072 \times 0.648 \times 0.072$ (matching the experimental cross-section area). The simulations were performed on the same mesh resolution as Ozel, imposing $Nd = 12$. This is slightly coarser than the resolution used for the previous cases, but it appears to be a fair balance between computational cost and accuracy for this numerical case. The viscosity ratio is set to $R_\mu = 10000$. To speed up the initial transient in the simulations, particles are initially positioned so that the initial bed height approximately matches the one expected at stationary state (based on the results of Ozel et al. (2017) for a fluidization velocity of $U_F = 0.12\,\mathrm{m\ s^{-1}}$). Fig. 7 shows the initial position of the particles (left) and a snapshot at $t = 9.6$ s for the four fluidization velocities (right).

The time-evolution of the maximum particles position $y_{max}(t)$ at various fluidization velocities is shown in Fig. 8 along side of a box plot for the fluctuation of y_{max}. This quantity is calculated by tracking the maximum y-coordinate of the center of gravity for all particles. Since the expected height of the bed at $U_F = 0.12\,\mathrm{m\ s^{-1}}$ was used to initialize the position of the particles, the transient in this case is the shortest. We can see that y_{max} fluctuates around a mean value, and that the fluctuations amplitudes increase with the fluidization velocities. The height evolution shows that a statistical stationary state is reached, roughly after 2 s, for $U_F = 0.09\,\mathrm{m\ s^{-1}}$ and $U_F = 0.073\,\mathrm{m\ s^{-1}}$. However, even after 10 s of simulation, the bed-level oscillations are quite strong for $U_F = 0.15\,\mathrm{m\ s^{-1}}$. In this case, single particles are ejected much higher than the average bed height (see Fig. 7).

Fig. 9 shows the time averaged evolution of the solid fraction α as a function of the height y, alongside a box plot showing the spread of the values of the volume fraction relative to the mean. These profiles were obtained by taking cross sections of the domain at regular intervals and calculating the mean solid fraction over the cross section.

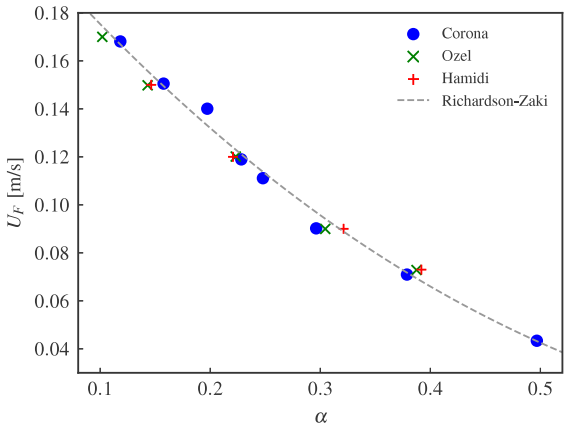

Fig. 10. Fluidization velocity with respect to the bed solid concentration.

The instantaneous profiles obtained were then time averaged over the period $[t_0 = 5\,\mathrm{s}, t_1 = 10\,\mathrm{s}]$ to obtain the time averaged profiles shown in Fig. 9. From both figures, One can see that the volume fraction is fairly uniform along the height of the bed; however, a transition zone appears between the bed itself and the pure fluid region. We can see that the thickness of this transition zone directly depend on the fluidization speed. The lower the fluidization velocity, the narrower the transition zone. Indeed, this transition zone is nothing but a time average of the fluctuation of the bed height observed on Fig. 7 and 8. The bed volume fraction is calculated by taking the spatial average along the y direction between $[0.05\overline{y_{max}}; 0.95\overline{y_{max}}]$ to eliminate the edge effects caused by the wide transition zone at high fluidization speeds. $\overline{y_{max}}$ is the time averaged maximal axial particle position given by:

$$\overline{y_{max}} = \frac{1}{t_1 - t_0} \int_{t_0}^{t_1} y_{max}(t)$$

The resulting average bed volume fraction is plotted against the fluidization velocity, on Fig. 10, and compared with the experimental data. of Aguilar-Corona (2008) the numerical results of Ozel et al. (2017) and the empirical correlation proposed by Richardson and Zaki (1954) (for $n = 2.4$ and $U_{F0} = 0.24\,\mathrm{m\ s^{-1}}$ as proposed by Aguilar-Corona (2008)) given by:

$$\frac{U_F}{U_{F0}} = (1 - \alpha)^n \tag{36}$$

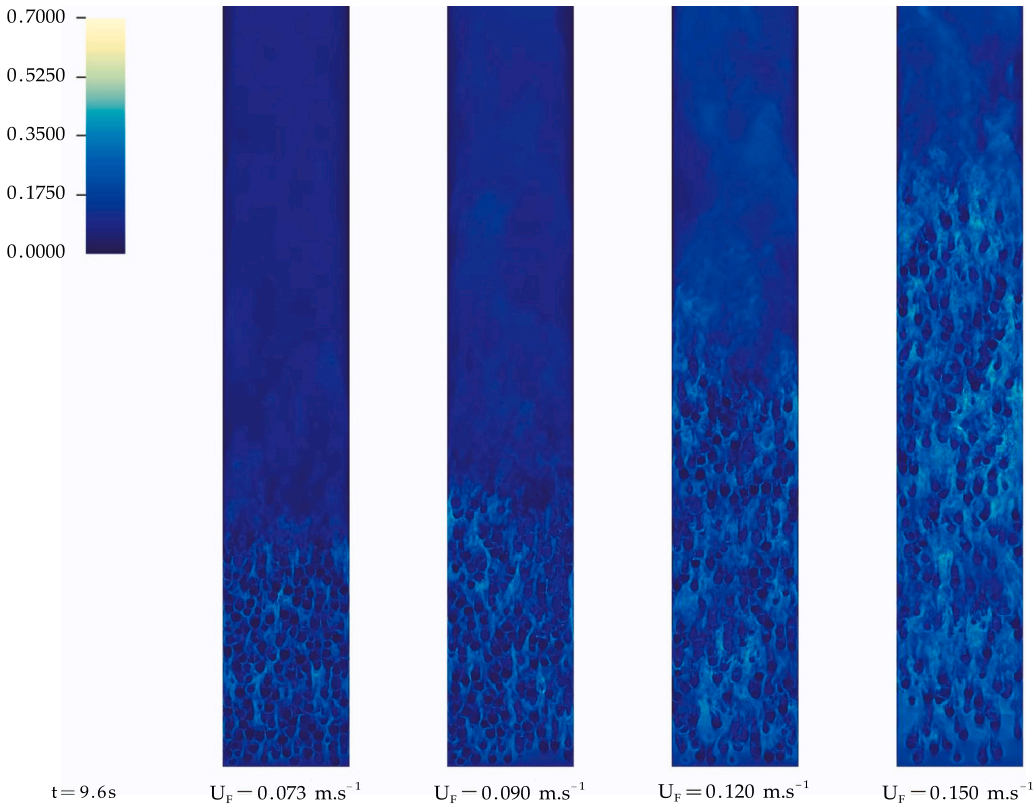

Fig. 11. Contours of the velocity magnitude, in a plane centered in the domain of the x-direction, in the established phase ($t = 9.6\,s$) and for the four fluidization velocities U_F.

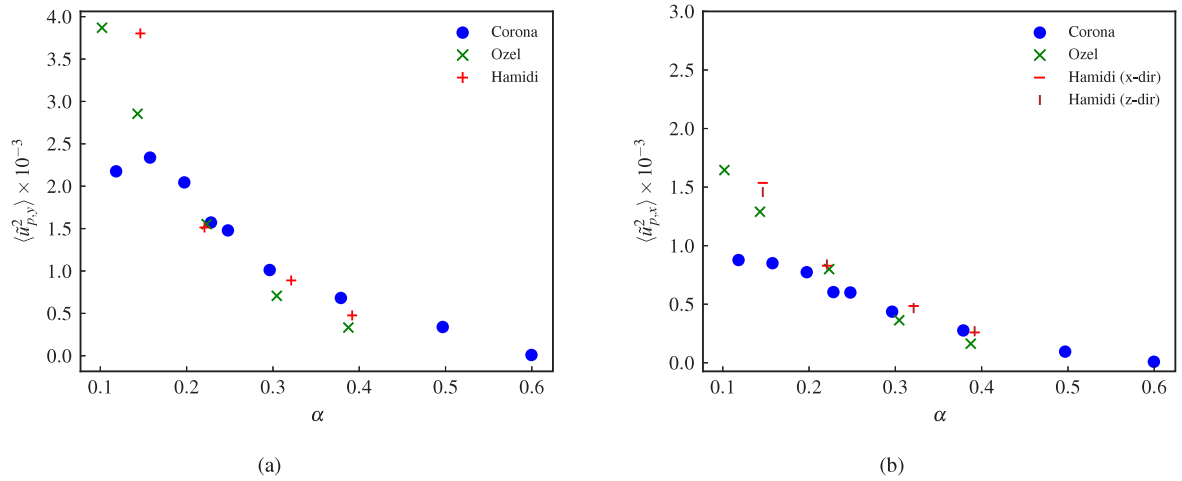

Fig. 12. Variance of axial (a) and transverse (b) particle velocity with respect to the bed solid concentration.

where U_F is the fluidization velocity, U_{F0} is the entrainment velocity and n is a function of Re_t.

$$\begin{cases} n = 4.65 & \text{if } Re_t < 0.2 \\ n = 4.4 Re_t^{0.03} & \text{if } 0.2 < Re_t < 1 \\ n = 4.45 Re_t^{0.1} & \text{if } 1 < Re_t < 500 \\ n = 2.4 & \text{if } Re_t > 500 \end{cases} \tag{37}$$

One can observe in Fig. 10 that our results are in good agreement with both the numerical and experimental references. All the evolutions were well predicted by the empirical correlation for the given n and U_{F0} values. Fig. 11 displays a color map of the velocity magnitude, at the center plan of the domain. One can observe that the velocity in the particles is one order of magnitude lower than the fluid velocities. As the fluidization velocities increase, larger pseudo-turbulent structures emerge behind the particles. The interaction of the developing wakes with the particles results in a complex flow dynamic. A more quantitative insight of this flow configuration is detailed in the following.

4.1. Solid phase agitation

A much challenging validation relies on the ability of the method to predict the velocity statistics of the solid phase and especially its agitation. Statistical quantities are computed using the same methodology

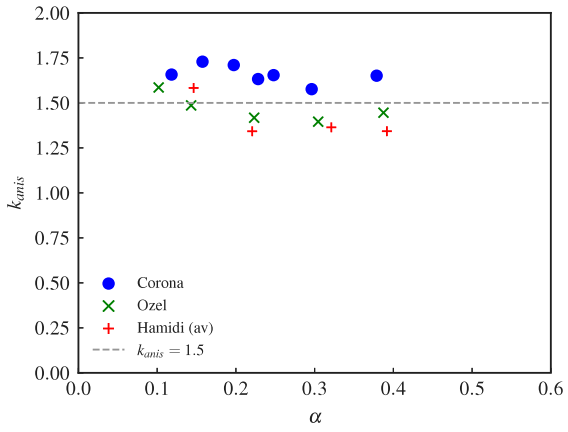

Fig. 13. Anisotropy coefficient of the particle velocity fluctuations as a function of the bed solid concentration.

as in the reference data. The instantaneous variance of particle velocity in each direction i are first calculated using Eq. (38):

$$\langle \tilde{u}_{p,i}^2 \rangle_p = \left\langle \left(u_{p,i} - \langle u_{p,i} \rangle_p \right)^2 \right\rangle_p \tag{38}$$

The notation $\langle \cdot \rangle_p$ denotes the particle phase average :

$$\langle \phi_p \rangle_p = \frac{1}{N_p} \sum_1^{N_p} \phi_p \tag{39}$$

where N_p is the total number of particles in the domain. Then, the time average of the variance of the particle velocities (Eq. (40)) is computed for all directions and shown in Fig. 12 alongside the previous experimental and numerical results.

$$\langle \tilde{u}_{p,i}^2 \rangle = \frac{1}{t_1 - t_0} \int_{t_0}^{t_1} \langle \tilde{u}_{p,i}^2 \rangle_p \tag{40}$$

We can see that our method allows to accurately predict the velocity variance, for the three components,for solid fractions $\alpha > 0.2$. The superimposition of the two transverse components, x and z, attest the convergence of the statistics. For the lowest volume fraction (highest fluidization speed), our simulation overestimates the variance of the three components and the two transverse components are no longer matching. Moreover, the variance of the velocity along the vertical axis is always higher than in the transverse direction whatever the solid fraction. This anisotropy can be characterized by a coefficient k_{anis}:

$$k_{\text{anis}} = \sqrt{\frac{\langle \tilde{u}_{p,y}^2 \rangle}{\frac{1}{2}\left(\langle \tilde{u}_{p,x}^2 \rangle + \langle \tilde{u}_{p,z}^2 \rangle \right)}} \tag{41}$$

The evolution of the anisotropy coefficient as a function of the volume fraction is plotted in Fig. 13. We can see that, even if the values obtained are slightly lower than (Ozel et al., 2017), as expected we find no dependence of the k_{anis} on the averaged particle volume fraction (overlooking the non-converged case which corresponds to the highest fluidization velocity $U_F = 0.15$ m s^{-1}). Based on this analysis, the accuracy of our approach is comparable to that of Ozel et al. (2017), Vincent et al. (2014).

5. Conclusion

We have implemented in the Front-Tracking framework a one-fluid method capable of performing Particle-resolved direct numerical simulations of dense fluid–particle flow.

The interactions between the fluid and the particles are taken into account by a combined viscous penalty method and a front tracking algorithm. Both collision and lubrication interactions are simultaneously modeled by soft sphere collision model similar to what Mohaghegh and Udaykumar (2019) proposed. During a collision, the spring stiffness of the model is adjusted to obtain the desired rebound velocity by using experimental correlation relating the impact Stokes number to the coefficient of restitution. This approach allows to avoid using additional closure laws for lubrication modeling, which results in a reduction of the number of numerical parameters in the models. The method has been tested against well-established experimental benchmarks of, and demonstrated good overall numerical consistency. The hydrodynamics was first validated by simulating the motion of a settling sphere in a fluid. The method showed qualitatively good results with the experiments on the range of terminal Reynolds numbers studied ($1.5 < Re < 32$). The collision modeling was then validated by reproducing the bouncing trajectory of a spherical particle colliding into a planar surface. The method proved to be quite capable of reproducing a physically realistic bouncing motion. Finally, the ability of the method to simulate granular flow with numerous particles (> 2000) was demonstrated by reproducing the experiments and Aguilar-Corona (2008). The results obtained showed quantitative consistency with the references for solid fraction ranging from 0.2 to 0.4. In this range, our method showed similar performances to the one developed by Ozel et al. (2017). Overall the proposed numerical approach does capture convincingly the physics of particles–fluid and inter-particle interactions and was shown to be valid over a wide range of Stokes/Reynolds numbers.

CRediT authorship contribution statement

Mohamed Salim Hamidi: Conception and design of study, Acquisition of data, Analysis and/or interpretation of data, Writing – original draft. **Adrien Toutant:** Conception and design of study, Analysis and/or interpretation of data, Writing – review & editing. **Samuel Mer:** Conception and design of study, Analysis and/or interpretation of data, Writing – original draft, Writing – review & editing. **Françoise Bataille:** Analysis and/or interpretation of data, Writing – review & editing.

Declaration of competing interest

The authors declare that they have no known competing financial interests or personal relationships that could have appeared to influence the work reported in this paper.

Data availability

Data will be made available on request

Acknowledgments

This work was granted access to the HPC resources of CINES under the allocation A0082B11441 made by GENCI (Grand Equipement National de Calcul Intensif, France). The author would like to thank the support team of The TrioCFD software for their assistance. All authors approved the version of the manuscript to be published.

References

Aguilar-Corona, A., 2008. Agitation des Particules Dans Un Lit Fluidisé Liquide. Etude Expérimentale (Ph.D. thesis). Institut National Polytechnique de Toulouse.

Ardekani, M.N., Costa, P., Breugem, W.P., Brandt, L., 2016. Numerical study of the sedimentation of spheroidal particles. Int. J. Multiph. Flow. 87, 16–34.

Aulery, F., Toutant, A., Bataille, F., Zhou, Y., 2015. Energy transfer process of anisothermal wall-bounded flows. Phys. Lett. A 379, 1520–1526.

Benoit, H., Pérez López, I., Gauthier, D., Sans, J.L., Flamant, G., 2015. On-sun demonstration of a 750 °C heat transfer fluid for concentrating solar systems: Dense particle suspension in tube. Sol. Energy 118, 622–633.

Biegert, E., Vowinckel, B., Meiburg, E., 2017. A collision model for grain-resolving simulations of flows over dense, mobile, polydisperse granular sediment beds. J. Comput. Phys. 340, 105–127.

Brändle de Motta, J.C., Breugem, W.P., Gazanion, B., Estivalezes, J.L., Vincent, S., Climent, E., 2013. Numerical modelling of finite-size particle collisions in a viscous fluid. Phys. Fluids 25, 083302.

Breugem, W.P., 2010. A combined soft-sphere collision/immersed boundary method for resolved simulations of particulate flows. In: ASME 2010 3rd Joint US-European Fluids Engineering Summer Meeting: Volume 1, Symposia – Parts A, B, and C. ASME, Montreal, Quebec, Canada, pp. 2381–2392. http://dx.doi.org/10.1115/FEDSM-ICNMM2010-30634.

Bunner, B., Tryggvason, G., 2003. Effect of bubble deformation on the properties of bubbly flows. J. Fluid Mech. 495, 77–118.

Caltagirone, J.P., Vincent, S., 2001. Sur une méthode de pénalisation tensorielle pour la résolution des équations de Navier–Stokes. C. R. de L'Acad. Des Sci. - Ser. IIB - Mech. 329, 607–613.

Calvin, C., Cueto, O., Emonot, P., 2002. An object-oriented approach to the design of fluid mechanics software. ESAIM: M2AN 36, 907–921.

Chen, Y., Müller, C.R., 2020. A Dirichlet boundary condition for the thermal lattice Boltzmann method. Int. J. Multiph. Flow. 123, 103184.

Cooley, M.D.A., O'Neill, M.E., 1969. On the slow motion generated in a viscous fluid by the approach of a sphere to a plane wall or stationary sphere. Mathematika 16, 37–49.

Costa, P., Boersma, B.J., Westerweel, J., Breugem, W.-P., 2015. Collision model for fully resolved simulations of flows laden with finite-size particles. Phys. Rev. E 92, 053012.

Costa, P., Picano, F., Brandt, L., Breugem, W.-P., 2016. Universal scaling laws for dense particle suspensions in turbulent wall-bounded flows. Phys. Rev. Lett. 117, 134501.

Cox, R.G., Brenner, H., 1967. The slow motion of a sphere through a viscous fluid towards a plane surface—II small gap widths, including inertial effects. Chem. Eng. Sci. 22, 1753–1777.

Cundall, P.A., Strack, O.D.L., 1979. A discrete numerical model for granular assemblies. Géotechnique 29, 47–65.

du Cluzeau, A., Bois, G., Leoni, N., Toutant, A., 2022. Analysis and modeling of bubble-induced agitation from direct numerical simulation of homogeneous bubbly flows. Phys. Rev. Fluids 7, 044604.

du Cluzeau, A., Bois, G., Toutant, A., 2019. Analysis and modelling of Reynolds stresses in turbulent bubbly up-flows from direct numerical simulations. J. Fluid Mech. 866, 132–168.

du Cluzeau, A., Bois, G., Toutant, A., Martinez, J.-M., 2020. On bubble forces in turbulent channel flows from direct numerical simulations. J. Fluid Mech. 882, A27.

Dupuy, D., Toutant, A., Bataille, F., 2018. Turbulence kinetic energy exchanges in flows with highly variable fluid properties. J. Fluid Mech. 834, 5–54.

Dupuy, D., Toutant, A., Bataille, F., 2019. Effect of the Reynolds number on turbulence kinetic energy exchanges in flows with highly variable fluid properties. Phys. Fluids 31, 015104.

Elghannay, H.A., Tafti, D.K., 2016. Development and validation of a reduced order history force model. Int. J. Multiph. Flow. 85, 284–297.

Esteghamatian, A., Hammouti, A., Lance, M., Wachs, A., 2017. Particle resolved simulations of liquid/solid and gas/solid fluidized beds. Phys. Fluids 29.

Feng, Z.G., Michaelides, E.E., Mao, S., 2010. A three-dimensional resolved discrete particle method for studying particle-wall collision in a viscous fluid. J. Fluids Eng. 132.

Flamant, G., Gauthier, D., Benoit, H., Sans, J.L., Garcia, R., Boissière, B., Ansart, R., Hemati, M., 2013. Dense suspension of solid particles as a new heat transfer fluid for concentrated solar thermal plants: On-sun proof of concept. Chem. Eng. Sci. 102, 567–576.

Flamant, G., Hemati, H., 2010. Dispositif collecteur d'energie solaire (device for collecting solar energy). p. 20, French Patent FR 1058565.

Foerster, S.F., Louge, M.Y., Chang, H., Allia, K., 1994. Measurements of the collision properties of small spheres. Phys. Fluids 6 (3), 1108–1115.

Fornari, W., Picano, F., Brandt, L., 2016. Sedimentation of finite-size spheres in quiescent and turbulent environments. J. Fluid Mech. 788, 640–669.

Ge, W., Wang, L., Xu, J., Chen, F., Zhou, G., Lu, L., Chang, Q., Li, J., 2017. Discrete simulation of granular and particle-fluid flows: From fundamental study to engineering application. Rev. Chem. Eng. 33, 551–623.

Glowinski, R., Pan, T.W., Hesla, T.I., Joseph, D.D., 1999. A distributed Lagrange multiplier/fictitious domain method for particulate flows. Int. J. Multiph. Flow. 25, 755–794.

Gondret, P., Lance, M., Petit, L., 2002. Bouncing motion of spherical particles in fluids. Phys. Fluids 14, 643.

Gueguen, R., Sahuquet, G., Mer, S., Toutant, A., Bataille, F., Flamant, G., 2021. Gas-solid flow in a fluidized-particle tubular solar receiver: Off-sun experimental flow regimes characterization. Energies 14, 7392.

Hertz, H., 1882. Über die Berührung Fester Elastischer Körper (on the contact of elastic solids). J. Reine Angew. Math. 1882, 156–171.

Izard, E., Bonometti, T., Lacaze, L., 2014. Modelling the dynamics of a sphere approaching and bouncing on a wall in a viscous fluid. J. Fluid Mech. 747, 422–446.

Jain, R., Tschisgale, S., Fröhlich, J., 2019. A collision model for DNS with ellipsoidal particles in viscous fluid. Int. J. Multiph. Flow. 120, 103087.

Johnson, K.L., 1985. Contact Mechanics. Cambridge University Press, Cambridge.

Joseph, G.G., Zenit, R., Hunt, M.L., Rosenwinkel, A.M., 2001. Particle–wall collisions in a viscous fluid. J. Fluid Mech. 433, 329–346.

Kempe, T., Fröhlich, J., 2012. Collision modelling for the interface-resolved simulation of spherical particles in viscous fluids. J. Fluid Mech. 709, 445–489.

Kidanemariam, A.G., Uhlmann, M., 2014. Interface-resolved direct numerical simulation of the erosion of a sediment bed sheared by laminar channel flow. Int. J. Multiph. Flow. 67, 174–188.

Kidanemariam, A.G., Uhlmann, M., 2017. Formation of sediment patterns in channel flow: Minimal unstable systems and their temporal evolution. J. Fluid Mech. 818, 716–743.

Legendre, D., Daniel, C., Guiraud, P., 2005. Experimental study of a drop bouncing on a wall in a liquid. Phys. Fluids 17 (9), 097105.

Legendre, D., Zenit, R., Daniel, C., Guiraud, P., 2006. A note on the modelling of the bouncing of spherical drops or solid spheres on a wall in viscous fluid. Chem. Eng. Sci. 61, 3543–3549.

Lucci, F., Ferrante, A., Elghobashi, S., 2010. Modulation of isotropic turbulence by particles of Taylor length-scale size. J. Fluid Mech. 650, 5–55.

Mohaghegh, F., Udaykumar, H.S., 2019. Modeling collisions of arbitrary-shaped particles in simulations of particulate flows. Powder Technol. 344, 756–772.

Müller, C.R., Holland, D.J., Sederman, A.J., Scott, S.A., Dennis, J.S., Gladden, L.F., 2008. Granular temperature: Comparison of magnetic resonance measurements with discrete element model simulations. Powder Technol. 184, 241–253.

Ozel, A., Brändle de Motta, J., Abbas, M., Fede, P., Masbernat, O., Vincent, S., Estivalezes, J.-L., Simonin, O., 2017. Particle resolved direct numerical simulation of a liquid–solid fluidized bed: Comparison with experimental data. Int. J. Multiph. Flow. 89, 228–240.

Pan, T.W., Joseph, D.D., Bai, R., Glowinski, R., Sarin, V., 2002. Fluidization of 1204 spheres: Simulation and experiment. J. Fluid Mech. 451, 169–191.

Picano, F., Breugem, W.P., Brandt, L., 2015. Turbulent channel flow of dense suspensions of neutrally buoyant spheres. J. Fluid Mech. 764, 463–487.

Puckett, E.G., Almgren, A.S., Bell, J.B., Marcus, D.L., Rider, W.J., 1997. A high-order projection method for tracking fluid interfaces in variable density incompressible flows. J. Comput. Phys. 130, 269–282.

Ray, S., Kempe, T., Fröhlich, J., 2015. Efficient modelling of particle collisions using a non-linear viscoelastic contact force. Int. J. Multiph. Flow. 76, 101–110.

Richardson, J.F., Zaki, W.N., 1954. The sedimentation of a suspension of uniform spheres under conditions of viscous flow. Chem. Eng. Sci. 3, 65–73.

Ritz, J., Caltagirone, J., 1999. A numerical continuous model for the hydrodynamics of fluid particle systems. Internat. J. Numer. Methods Fluids 30, 1067–1090.

Ruiz-Angulo, A., Hunt, M.L., 2010. Measurements of the coefficient of restitution for particle collisions with ductile surfaces in a liquid. Granul. Matter 12, 185–191.

Stevens, A.B., Hrenya, C.M., 2005. Comparison of soft-sphere models to measurements of collision properties during normal impacts. Powder Technol. 154, 99–109.

Sundaresan, S., Ozel, A., Kolehmainen, J., 2018. Toward constitutive models for momentum, species, and energy transport in gas–particle flows. Annu. Rev. Chem. Biomol. Eng. 9, 61–81.

Temam, R., Miranville, A., 2005. Mathematical Modeling in Continuum Mechanics, second ed. Cambridge University Press, Cambridge.

ten Cate, A., Nieuwstad, C.H., Derksen, J.J., Van den Akker, H.E.A., 2002. Particle imaging velocimetry experiments and lattice-Boltzmann simulations on a single sphere settling under gravity. Phys. Fluids 14, 4012–4025.

Thiam, E.I., 2018. Modélisation et Simulation Numérique Directe Des Transferts De Chaleur Dans Les Écoulements Fortement Chargés En Particules (Ph.D. thesis). UT3 Paul Sabatier.

Toutant, A., Bataille, F., 2013. Turbulence statistics in a fully developed channel flow submitted to a high temperature gradient. Int. J. Therm. Sci. 74, 104–118.

Tryggvason, G., Scardovelli, R., Zaleski, S., 2011. Direct Numerical Simulations of Gas-Liquid Multiphase Flows, 1. publ Cambridge Univ. Press, Cambridge.

Uhlmann, M., 2005. An immersed boundary method with direct forcing for the simulation of particulate flows. J. Comput. Phys. 209, 448–476.

Uhlmann, M., 2008. Interface-resolved direct numerical simulation of vertical particulate channel flow in the turbulent regime. Phys. Fluids 20, 053305.

Uhlmann, M., Doychev, T., 2014. Sedimentation of a dilute suspension of rigid spheres at intermediate galileo numbers: The effect of clustering upon the particle motion. J. Fluid Mech. 752, 310–348.

van der Hoef, M.A., Ye, M., van Sint Annaland, M., Andrews, A.T., Sundaresan, S., Kuipers, J.A.M., 2006. Multiscale modeling of gas-fluidized beds. In: Advances in Chemical Engineering, vol. 31, Academic Press, pp. 65–149.

Vincent, S., Brändle de Motta, J.C., Sarthou, A., Estivalezes, J.L., Simonin, O., Climent, E., 2014. A Lagrangian VOF tensorial penalty method for the DNS of resolved particle-laden flows. J. Comput. Phys. 256, 582–614.

Wan, D., Turek, S., 2006. Direct numerical simulation of particulate flow via multigrid FEM techniques and the fictitious boundary method. Internat. J. Numer. Methods Fluids 51, 531–566.

Wang, L.P., Ayala, O., Gao, H., Andersen, C., Mathews, K.L., 2014. Study of forced turbulence and its modulation by finite-size solid particles using the lattice Boltzmann approach. Comput. Math. Appl. 67, 363–380.

Willen, D.P., Prosperetti, A., 2019. Resolved simulations of sedimenting suspensions of spheres. Phys. Rev. Fluids 4, 014304.

Yang, F.L., Hunt, M.L., 2006. Dynamics of particle-particle collisions in a viscous liquid. Phys. Fluids 18, 121506.
Yao, Y., Criddle, C.S., Fringer, O.B., 2021. Competing flow and collision effects in a monodispersed liquid–solid fluidized bed at a moderate archimedes number. J. Fluid Mech. 927, A28.
Zhang, H., Benoit, H., Perez-Lopèz, I., Flamant, G., Tan, T., Baeyens, J., 2017. High-efficiency solar power towers using particle suspensions as heat carrier in the receiver and in the thermal energy storage. Renew. Energy 111, 438–446.
Zhou, Z., Jin, G., Tian, B., Ren, J., 2017. Hydrodynamic force and torque models for a particle moving near a wall at finite particle Reynolds numbers. Int. J. Multiph. Flow. 92, 1–19.

International Journal of Heat and Mass Transfer 241 (2025) 126687

Contents lists available at ScienceDirect

International Journal of Heat and Mass Transfer

journal homepage: www.elsevier.com/locate/hmt

Investigation of heat transfers with particle-resolved simulations: From Stokes flow to fluidized bed

E. Butaye *, R. Quintana, S. Mer, F. Bataille, A. Toutant *

PROMES Laboratory (UPR 8521), CNRS – University of Perpignan (UPVD), 66100 Perpignan, France

ARTICLE INFO

Keywords:
Fluid - particles flow
Fluidized bed
DEM
Fully resolved particles
PRS
Viscous penalization
Wall-to-bed heat transfer
Anisothermal flow

ABSTRACT

Particle-Resolved Simulations (PRS) of fluid–solid particles are conducted to study fluid–particle heat transfers and wall-to-bed heat transfers in an anisothermal liquid–solid fluidized bed. An overview of existing PRS methods to study anisothermal fluid–solid flows is presented. In the framework of fluidized bed simulations, the collision detection method is optimized using Verlet tables. The overall computation time is reduced by 20%. An original Lagrangian method to compute the fluid–particle heat transfers is presented for an isolate particle. A parametric study on the fluid–particle heat transfer is performed to assess well-known correlations of the literature for a settling particle in a quiescent fluid. 77 PRS are performed for Reynolds numbers between 1 and 32 and Prandtl number between 0.1 and 10 for a grid resolution of 20 meshes per particle diameter. For two of three correlations considered, the predicted heat flow is within 10% error. An anisothermal fluidized bed of 2 134 particles is finally studied. Four fluidization velocities are considered for a solid fraction comprised between 0.13 and 0.35. Three grid resolutions are carried out to assess the sensitivity of the mesh for the lowest fluidization velocity (12, 24 and 36 meshes per particle diameter). Results show that the macroscopic behavior of the bed is well retrieved even with a coarser grid as the solid fraction is well predicted. However, strong effects of the grid resolution are observed on the fluid–particle and the wall-to-bed heat transfers. The study of the velocity–temperature correlation shows that the parietal heat transfer is driven by the turbulent heat flow near the wall ($x^+ \sim 30$).

1. Introduction

The concept of fluidization is studied since a hundred years. In a recent review, Zhang et al. [1] highlighted that the first prototype of fluidization was introduced by Winkler et al. [2] in 1922 for water-gas production. Since then, it has been used in many industrial areas such as pneumatic conveying for powder transport [3] or methane cracking for hydrogen production with fluidized beds [4]. In the field of solar energy, fluidized beds are used as a new heat transfer fluid (HTF) in concentrated solar power (CSP) plants. In solar tower power plants, a panel of heliostats reflects solar radiation to a receiving surface located at the top of a solar tower. The HTF is exposed to the concentrated solar flux at the receiving surface so it received the solar flux. The HTF is then either transported in a thermal storage or injected into a thermodynamic Rankine cycle to convert its thermal energy into electricity [5]. Current CSP plants use molten salt as HTF. However, the main drawback is the limitation of the working temperature (<560 °C) due to the degradation of thermodynamic properties at high temperature as a result of chemical reactions [5–7]. To overcome this issue, the use of solid particles as a new HTF is of great interest. In particle-in-tube solar receiver, introduced by Flamant in 1982 [8], solid particles are fluidized in a dispenser with a primary air injection. With an imposed pressure gradient, the particles flow upward the tube. Finally, a secondary injection directly into the tube controls the mass flow rate and thus the fluidization regime. [7]. In a recent study, Gueguen et al. [7] succeeded in operating at 650 °C demonstrating a 50% increase of the wall-to-bed heat transfer in front of a mean operating temperature of the particles of 500 °C (see Fig. 13 in [7]). With such systems, the main limitation is no longer the temperature of the HTF but the solar receiver wall temperature. When very high temperatures are reached, the inhomogeneous solid fraction at the wall leads to a highly inhomogeneous heat transfer between the wall and the bed, resulting in high thermomechanical stresses. It is therefore required to characterize the flow inside the solar receiver for two reasons. First, to predict the wall-to-bed heat transfer as a function of the flow regime and physical properties of the fluid and the particles. It implies to understand the complex dynamic and thermal behavior of the fluid–particles flow. Then, to limit the thermomechanical stresses exerted on the wall of the solar receiver.

* Corresponding authors.
E-mail addresses: edouard.butaye@promes.cnrs.fr (E. Butaye), adrien.toutant@univ-perp.fr (A. Toutant).

https://doi.org/10.1016/j.ijheatmasstransfer.2025.126687
Received 19 July 2024; Received in revised form 17 December 2024; Accepted 6 January 2025

Nomenclature

α	Volumic presence rate [–]
Δt	Temporal discretization [s]
Δx	Spatial discretization [m]
δ_n	Overlapping during collision [m]
λ	Thermal conductivity [W m^{-1} K^{-1}]
$\mathbf{F_c}$	Vector collision force [N m^{-3}]
$\mathbf{g}$	Vector gravity acceleration [m s^{-2}]
$\mathbf{u}$	Vector velocity [m s^{-1}]
μ	Dynamic viscosity [Pa s]
Φ	Heat flux [W]
ρ	Density [kg m^{-3}]
τ_0	Collision time [s]
$_f$	Fluid
$_p$	Particle
$_w$	Wall
c_p	Heat capacity [J K^{-1} kg^{-1}]
D	Diameter [m]
e_{dry}	Dry restitution coefficient [–]
e_{eff}	Effective restitution coefficient [–]
e_{wet}	Wet restitution coefficient [–]
h	Heat transfer coefficient [W m^{-2} K^{-1}]
I	Volume phase indicator function [–]
k	Spring stiffness [N m^{-1}]
m	Mass [kg]
N_f	Facets number [–]
N_p	Particles number [–]
Nu	Nusselt number [–]
p	Pressure [Pa]
Pe	Peclet number [–]
Pr	Prandtl number [–]
Re	Reynolds number [–]
S	Surface area [m^2]
St	Stokes number [–]
T	Temperature [K]
T'	Fluctuating temperature [K]
U'	Fluctuating velocity [m s^{-1}]
CFD-DEM	Computational Fluid Dynamics - Discrete Element Method
CSP	Concentrated Solar Power
HTF	Heat Transfer Fluid
PR-DNS	Particle Resolved - Direct Numerical Simulation
PRS	Particle Resolved Simulation

Over the last decades, a number of experiments were conducted to study fluidized beds [9,10]. Flow regime transitions are now well characterized in terms of particle shape [11] and hydrodynamics [12,13]. Regarding heat transfers, Gueguen et al. showed that the wall-to-bed heat transfer increases with temperature and strongly depend on the fluidization regime. The aforementioned experimental studies have described the dynamic and thermal behavior of fluidized beds macroscopically. However, a local description of the flow is not possible through an experimental process without invasive methods and nearly impossible at high temperature. The prediction of the inhomogeneous behavior of parietal heat transfer is required to understand the thermomechanical stresses exerted on the wall of the solar receiver. The greater the particle agitation, the greater the heat transfer. Since the regime of interest for solar applications is turbulent fluidization [7], the inhomogeneous nature of heat transfer cannot be neglected. Therefore, numerical simulation is an excellent tool to fully characterize the flow inside the solar receiver. It enables to access local quantities of the fluid and particles such as physical properties, mean value and fluctuations of velocity, pressure and temperature, or the local solid fraction.

Numerical simulations of fluidized beds are challenging because of the multi-scale phenomenon occurring in the flow. In a particle-in-tube fluidized beds, the largest structures can be of the order of the meter and yet strongly depend on fluid–particle and particle–particle interactions at the particle scale [14]. At the particle scale - also referred to as microscopic scale-, the hydrodynamic force exerted by the fluid to the particles and particle–particle interactions operate. At the scale of several particle diameters (mesoscopic scale), the wake of the particle and the interaction with the wake of other particles must be considered. At a larger scale (macroscopic scale), particle assembly movements prevail, resulting in different flow regimes which depend on the fluidization velocity and the particle size. Different scales of resolution have emerged to study fluidized beds [1,14,15]. At the smallest scale, particle-resolved direct numerical simulation (PR-DNS) fully resolve the flow at the particle scale and thus capture all the aforementioned hydrodynamic interactions. This requires to capture the velocity and temperature gradients at the interface between the fluid and the particle. For a review of PR-DNS methods, the reader is referred to Tenneti and Subramanian [16], Maxey [17] and more recently Marchelli et al. [18]. The Eulerian grid resolution associated with PR-DNS is then more than 40 meshes per diameter for viscous flows and increase with the Reynolds number [19]. The numerical cost of PR-DNS limits its application to academic cases, thus excluding the possibility to study the collective effects of a large number of particles involving several hundreds of millions of particles. To study a large number of particles, Computational Fluid Dynamics - Discrete Element Method (CFD-DEM) simulations, also commonly referred to as Eulerian–Lagrangian methods in the literature, can be performed [20–22]. At this scale, particles are smaller than the Eulerian grid size, enabling to study the collective effects of a particle assembly. CFD-DEM resolve Navier–Stokes equations on an Eulerian grid and track particles in a Lagrangian way. Particles are transported by solving Newton equation. As the flow is not resolved at the particle scale in that case, correlations are employed to model the hydrodynamic forces exerted by the fluid to the particles (drag force, lift force, Basset's force...) [23,24]. If the solid fraction is sufficiently high, particles are not simply advected by the fluid (one-way coupling) and the force exerted by the particles to the fluid have to be considered (two-way coupling) as well as collision forces between particles (four-way coupling) [25]. CFD-DEM presents the advantage to track individually each particle and so to accurately compute the mean velocity and fluctuations of particles and solid fraction but models are required to considered mutual interactions exerted between the fluid and the particles. Closure models are obtained from PR-DNS simulations, as the hydrodynamic forces exerted by the fluid on the interface can be computed explicitly for each particle. Experience at a laboratory scale can be reproduced numerically. To study fluidized beds in an industrial context, the Euler–Euler method is most appropriate. It considered the fluid and the particles as two distinct and continuous phases [26,27]. Phase averaged Navier–Stokes equations are solved for each medium and interphase coupling is ensured via closure terms. CFD-DEM simulations can be harnessed to inform Euler–Euler simulations [28,29].

An intermediate scale between PR-DNS and CFD-DEM is Particle Resolved Simulation (PRS). PRS uses the same methodology as PR-DNS but with a coarser mesh because of the numerical costs associated with PR-DNS for a fluidized bed. Particles are therefore represented by a dozen meshes per diameter on the Eulerian mesh, which is not sufficient to fully resolved hydrodynamics and thermal gradients at the interface between the fluid and the particles. A first attempt to correct hydrodynamic gradients at the fluid–particle interface was presented in [19] for a single-particle Stokes flow. This correction will not be

studied or applied in the present work, as extensions of the method are needed to tackle the complex case of fluidized beds.

PRS are widely employed to compute drag force to inform Euler–Lagrange simulations [24,30,31]. However, due to high computational cost, the Eulerian mesh is coarse and hydrodynamic gradients are not fully resolved in the meaning of PR-DNS. Indeed, at least 5 Eulerian mesh cells in the boundary layer are required to accurately capture the gradients [30]. In the best cases, a mesh sensitivity is performed on macroscopic quantities such as the mean velocity, the drag force and the bed height [32]. In other scenarios, hydrodynamic forces were accurately computed on fixed beds, shallow fluidized beds, two-dimensional or very small three-dimensional fluidized beds [30,33–35]. To this day, the largest particle resolved simulation of a fluidized bed was performed by Dou et al. [36]. The authors computed a 3D particle resolved simulation of 115 200 particles in a shallow fluidized bed using a Lattice Boltzmann Method - Discrete Element Method (LBM-DEM) approach and GPU-based parallel computation. It is an impressive achievement for particle resolved simulation demonstrating the ability of their method to simulate multi-scale flows with relatively high accuracy (the lattice step was 20 times smaller than the particle diameter).

In the case of fluidized beds in solar receivers, heat transfers need to be considered. If numerical methods to study the hydrodynamic of fluidized beds with PRS are now well established, the consideration of heat transfers is much more recent. The first study to consider three-dimensional heat transfer on a single particle was conducted by Bagchi et al. [37] in 2001. Later, two-dimensional studies investigated heat transfers in a particle assembly. Feng and Michaelides [38] developed a numerical method to consider heat transfers with an Immersed Boundary Method (IBM) on a four-way coupling basis. Boussinesq hypothesis was assumed to consider density variation in the buoyancy term. Gan et al. [39] used the same hypothesis to study heat transfers with the Arbitrary Lagrangian Eulerian (ALE) finite-element method. Both authors demonstrated that the sedimentation process of particles is affected by the local temperature and buoyancy force. Gan et al. identified five sedimentation regimes defined by the Grashof number — which confronts buoyant force with viscous force. The authors demonstrated that the terminal velocity of a sedimenting particle depends on the Grashof number in a complex way. Yu et al. [40] employed the fictitious domain method and retrieved Gan results. It was later extended to three-dimensional simulations by Dan and Wachs [41] who performed the first three-dimensional study of a single particle in sedimentation in a semi-infinite channel.

Two types of heat transfers can be identified in particle-in-tube solar receiver: fluid–particle heat transfer and wall-to-bed heat transfer. In a review, Deen et al. highlighted the work of Tenneti et al. [42] and Tavassoli et al. [43] for the study of heat transfer in fixed array of spheres. Both authors computed the mean Nusselt number as a function of the void fraction to assess the validity of Gunn's correlation [44] up to Reynolds 100 for a Prandtl number of 0.72 [42] and 1 [43]. Deen et al. [45] refit Gunn's correlation based on the numerical data of the work of Tenneti and Tavassoli. In a following study, the authors extended their method to consider heat and mass transfer between the fluid and a fixed array of particles [46]. Three Reynolds numbers were studied (120, 180 and 240). The results are consistent with Gunn's correlation (within 4%), even if the resolution was rather coarse, with 24 meshes per particle diameter. Other studies investigated mass transfers in fixed and dynamic beds (fluidized beds with high inertia particles) [47], heat and mass transfers in a shallow fluidized bed [48]. Feng and Musong [48] pointed out that the simulation is partially under-resolved at Reynolds numbers above 200 when the resolution is only 15 meshes per particle diameter. Furthermore, the authors showed that the average particle Nusselt number increases with the fluidization velocity and the fluid-to-particle heat transfer decreases along the bed height. More recently, Chadil et al. [49,50] computed with a high-order interpolation method the fluid-to-particle heat transfer for each particle in a fixed assembly. Finally, one of the most recent work on heat transfer in fluidized beds was pursued by Thiam [51]. The authors realized an extensive study on the heat transfer in a small fluidized bed (1120 particles) with coarse mesh (16 meshes per particle diameter). An excellent agreement was found with Wen & Yu [52] correlation for the drag force and with Gunn's [44] correlation for heat transfers. The results obtained for the resolution of 16 meshes per particle diameter were confronted with those obtained with a resolution of 32 meshes per diameter for Reynolds numbers comprised between 15 and 50 and for a Prandtl number equals to 7. No significant deviations were observed for the hydrodynamic behavior. However, the authors showed that a mesh refinement would have been required to correctly predict heat transfers because of the high Prandtl number. In their work, periodic boundary conditions were applied so parietal heat transfers were not considered.

Wall-to-bed heat transfers were studied by Haid [53]. The author compared five correlations to predict the heat transfer coefficient on a database of more than 2500 experiments. As it gathers experiments with very different heater geometries, the mean relative error of all correlations lie in 67.2%. The best prediction is obtained with the correlation using 7 constants, for an error of 32.0%. For the simplest correlation, using 3 constants, the error is 34.4%. The author emphasizes that this correlation is a reasonable compromise between accuracy and complexity. More recent experiments on wall-to-bed heat transfers were conducted by Gueguen et al. [7] and Lee et al. [54].

To the best of our knowledge, there is no study of wall-to-bed and fluid-to-particle heat transfers, for a particle-in-tube fluidized bed with a PRS approach, in the literature. This study aims to clarify heat transfers in an anisothermal fluidized bed. The paper is organized as follows. First, the numerical and physical modeling are described in Section 2. Key aspects of the numerical analysis are presented in section. Section 3. Section 4 pertains a parametric study of the heat transfers on a isolate particle. Section 5 investigates fluid–particle and wall-to-bed heat transfers in an anisothermal liquid–solid fluidized bed. Finally, conclusions and outlooks are drawn in Section 6.

2. Physical and numerical modeling

The assumptions on which the model relies are described in Section 2.1. The simulations of the present study are performed with `TrioCFD` software. `TrioCFD`, previously named `Trio_U` is developed by the French atomic energy commission (CEA) since 1993 [55]. Since then, it has been widely used to study heat transfers [56], turbulence [57] and bubbly flows [58], to name but a few. In the present work, `TrioCFD` is used to investigate anisothermal fluid–solid flows. The numerical modeling of the particle-resolved approach on the Eulerian grid is presented in Section 2.2. The choices of the discretization schemes and solvers are detailed in Section 2.3.

2.1. General hypothesis

The computation of anisothermal fluidized beds requires to resolve the flow of the fluid and the particles trajectory. The model is based on a one-fluid formulation of the Navier–Stokes equations and particles are model as a highly viscous fluid. The numerical model is based on the following assumptions:

(i) both phases are incompressible. The fluid velocity is very small in front of the speed of sound. All physical properties of fluid and particles are assumed constants.
(ii) particles are considered spherical and non-deformable. Particle–particle and wall-particle collision velocities are too small to induce a deformation. The imposed temperature is sufficiently far from the melting temperature of the particles for dilation to be neglected. Only monodisperse fluidized beds are considered in the present study so all particles have the same diameter.

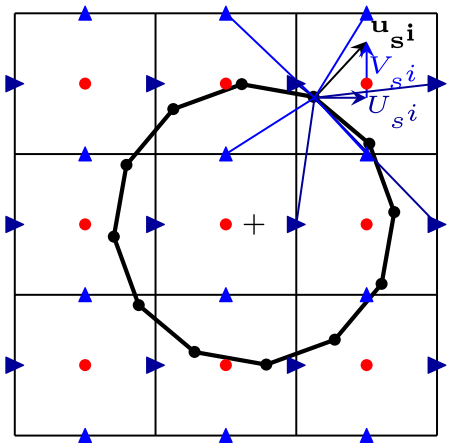

Fig. 1. Interpolation of Eulerian velocity on Lagrangian markers. $\mathbf{u}_s^i$ represents the velocity of the i-eme Lagrangian marker. •: pressure and temperature nodes, ▲/▶ : y / x velocity nodes, •: Lagrangian marker.

(iii) the temperature is constant inside the particles. A boundary condition imposes the constant temperature on their surfaces. The thermal conductivity of particles is several orders of magnitude larger than that of the fluid. Conduction can therefore be considered instantaneous in the particles. In aimed application, solid particles are in addition small (less than 100 μm). The Biot number is small enough to justify the hypothesis of homogeneous temperature.

(iv) the particles' temperature is constant in time and uniform for all the particles in the bed. The fluidized beds computed are not circulating. Particles are therefore considered as a thermal sink.

(v) radiative heat transfers are neglected in the present approach as well as contact thermal resistances as particles are maintained at a constant temperature (heat sink).

2.2. Particle-resolved numerical approach

Numerous studies have investigated the numerical modeling of PRS. One can identify, the fictitious domain methods [59], the lattice Boltzmann methods [60] and the Arbitrarian Lagrangian Eulerian - Finite Element Methods (ALE-FEM) [61]. The approach described below is a fictitious domain method. The `TrioCFD-1.9.1` one-fluid formulation of Navier–Stokes equation is employed to resolve the fluid flow (see Section 2.2.1). The surface of the particles is described with a Front-Tracking method [62]. Each particle is therefore represented by a set of Lagrangian markers (see Fig. 1). Hereinafter, Lagrangian facets will refer to the closed surface formed by three Lagrangian markers (in two-dimension, it refers to the segment formed by two Lagrangian markers). To enforce the solid-body motion, all Lagrangian markers of a particle are advected with the same velocity (see Section 2.2.2). Furthermore, spurious velocities in particles are damped with a viscous penalization. This method implicitly enforces fluid constraints on the interface and was early validated in [63,64]. A soft-sphere collision model was developed in [65] to tackle the collision process. The numerical approach was employed in [19,65] to study fluidized beds and to compute hydrodynamic forces exerted by the fluid to the particles.

2.2.1. Navier–Stokes equation and temperature energy equation

With the one-fluid formulation, the fluid and the particles movement are governed by the following mass, momentum and energy equations, respectively:

$$\nabla \cdot \mathbf{u} = 0 \tag{1}$$

$$\frac{\partial (\rho \mathbf{u})}{\partial t} + \nabla (\rho \mathbf{u} \otimes \mathbf{u}) = -\nabla p + \nabla \cdot \left(\mu \left(\nabla \mathbf{u} + \nabla^T \mathbf{u}\right)\right) + \rho \mathbf{g} + \mathbf{F_c} \tag{2}$$

$$\frac{\partial \left(\rho C_p T\right)}{\partial t} + \nabla \cdot \left(\rho C_p \mathbf{u} T\right) = \nabla \cdot (\lambda \nabla T) \tag{3}$$

$\mathbf{u}$ is the velocity, p the pressure, T the temperature, t the time, $\mathbf{g}$ the gravity vector, ρ the density, μ the viscosity. The definition of ρ and μ specific to the one-fluid formulation is defined in Section 2.2.3. A collision source term $\mathbf{F_c}$ is added to the classical formulation of the momentum equation to consider wall-particle and particle–particle interactions. $\mathbf{F_c}$ ensures the coupling between the Eulerian field on which Navier–Stokes equations are solved, and the Lagrangian approach employed to compute the collision forces. Velocity, pressure and temperature are solved on a staggered grid (see Fig. 1). Scalar quantities are computed at the center of Eulerian cells whereas vector quantities are computed component by component at the center of the faces of the element volume control (see Fig. 1).

Without phase change, there is no stress jump at the interface between the fluid and the particle [66,67]. Inside solid particles, the deformation tensor is null. This condition is achieved by imposing a high viscosity ratio between the fluid and the particles (viscous penalization).

For the energy equation, the boundary condition to impose is a Dirichlet condition ($T_p = 0\,\mathrm{K}$). The temperature is only solved for the fluid. As both phases are incompressible, physical properties are not temperature-dependent. Consequently, the value of 0 K does not refer to absolute zero, and only the temperature difference between the fluid and the solid should be considered. A ghost fluid method is employed to ensure it implicitly. The procedure is the following. First, the Lagrangian facets' normal is computed. Then, the temperature gradient is evaluated at the gravity center of all the Lagrangian facets by considering a pure diffusion model in the boundary layer of the particles. The gradient, computed in a Lagrangian manner, is distributed to purely fluid Eulerian cells close to the interface. A linear extrapolation is performed to extend the temperature gradient in solid cells. Finally, the convection and diffusion therms of the energy equation (see Eq. (3)) can be computed in the whole computational domain. A complete description of the procedure is detailed in Grosso et al. [56].

2.2.2. Transport of Lagrangian markers

Lagrangian markers that describe the particles' surface represent a mobile mesh overlying on the fixed Eulerian mesh. The interest of the method lies in its ability to represent accurately the position of the interface. The Front-Tracking (FT) method is often described as complex because of the remeshing procedures that are required for bubbles or drops. For solid particles – which are rigid by definition – no remeshing is required which drastically simplifies the FT algorithm. Nevertheless, it should be pointed out that, because of the data structure and the communications between Lagrangian and Eulerian meshes, the computation of the volume fraction in two-phase cells and the management of MPI operations for multiprocessor computing are rather complex.

The interface is advected by a transport equation:

$$\frac{\partial \chi}{\partial t} + \mathbf{u} \cdot \nabla \chi = 0 \tag{4}$$

where χ is the phase indicator function. $\chi = 0$ in the solid phase and $\chi = 1$ in the fluid phase (see Fig. 2).

To solve this equation numerically, a trilinear interpolation of the Eulerian velocity field is computed at each Lagrangian marker (see Eq. 1). The velocity is then computed at the gravity center of each Lagrangian marker. The velocity of a particle p writes:

$$\mathbf{u_p} = \frac{1}{S_p} \sum_{\text{facets}} S_i \mathbf{u_i} \tag{5}$$

where S_p is the particle surface, S_i and $\mathbf{u_i}$ the surface and velocity of the facet i. The Lagrangian markers are transported with the velocity $\mathbf{u_p}$:

$$\mathbf{x_i^{t+1}} = \mathbf{x_i^t} + \mathbf{u_p} \Delta t \tag{6}$$

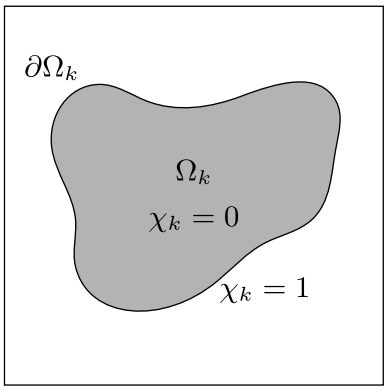

Fig. 2. Phase indicator function.

where $\mathbf{x_i}$ denotes the position of the Lagrangian marker i and Δt is the time step of the simulation. As mentioned in [19], the Lagrangian makers are not physical points of the interface. Consequently, if the particle is rotating, a given marker does not represent the same physical point at two different instants. This is possible because the particle is spherical. The projection of its shape onto the Eulerian mesh remains unchanged by pure rotation. The rotational motion of a particle is only considered when solving the Navier–Stokes equation, and would result from a local sheared flow. This phenomenon can be observed by looking at a cross-section of the velocity field inside the particle. The rotational motion of a particle cannot result directly from a collision. For non-spherical particles, the equation of angular momentum conservation must be resolved.

2.2.3. Defining the one-fluid properties

In the one-fluid formulation of Navier–Stokes equation, physical properties are defined by the presence rate of each phase in an Eulerian cell. In each Eulerian cell of volume V, the volume indicator function is defined as:

$$I = \int_V \chi dV \tag{7}$$

The density is computed with an arithmetic average (see Eq. (8)) whereas the viscosity is computed with a harmonic average (see Eq. (9)).

$$\rho = I\rho_f + (1 - I)\rho_p \tag{8}$$

$$\mu = \frac{\mu_f \mu_p}{I\mu_p + (1 - I)\mu_f} \tag{9}$$

The thermal conductivity is only defined in purely fluid cells as temperature is not solved inside the particle ($T_p = 0\,\mathrm{K}$).

2.2.4. Collision modeling

The soft-sphere collision model of Hamidi et al. [65] is used to model solid–solid interactions. As the collision time is of the order 10^{-9} s, the resolution of solid–solid interaction with strain laws is impossible as it would drastically constrain the simulation time step. Thus, the collision is spread over several time steps of the fluid solver. Collision forces are computed using a Lagrangian approach. Each collision force exerted on a particle is discretized on the Eulerian field in the corresponding purely solid meshes. The coupling between the Eulerian approach and the Lagrangian approach is achieved by the number of the particle. Indeed, at each time step, a correspondence is performed between the Lagrangian and the Eulerian number of the particles. The model developed by Hamidi et al. [65] is briefly described hereinafter.

The contact force is modeled with a harmonic oscillator and writes:

$$F_c = -k\delta_n \mathbf{n} \tag{10}$$

where δ_n is the particle–wall or particle–particle overlapping, k is the spring stiffness constant and $\mathbf{n}$ is the normal vector to the plan of collision. δ_n is described by the following equation:

$$m_e\ddot{\delta}_n + k\delta_n = 0 \tag{11}$$

where m_e is the effective mass. $m_e = \frac{m_p}{2}$ for a particle–particle collision and $m_e = m_p$ for a particle–wall collision.

The collision process is divided in two steps: the impact step corresponds to the decrease of the particle velocity during a collision while the rebound step starts when the particle's velocity changes sign. During the impact:

$$k = m_e\left(\frac{\pi}{\tau_0}\right)^2 \tag{12}$$

where τ_0 represents the collision time. During the rebound:

$$k = e_{eff}^2 m_e\left(\frac{\pi}{\tau_0}\right)^2 \tag{13}$$

where e_{eff} is the effective restitution coefficient and is another input parameter of the model. e_{eff} is the ratio of the particle velocity after impact to the particle velocity before impact. $e_{eff} = e_d e_{wet}$. e_d is the dry coefficient that models the energy loss during the collision by elastic deformation of the particle and vibration. e_{wet} models the (unresolved) lubricating force that dissipates kinetic energy through viscosity. According to Legendre et al. [68]:

$$e_{wet} = exp\left(-\frac{35}{St}\right) \tag{14}$$

The Stokes number is defined by $St = \frac{1}{9}\frac{\rho_p}{\rho_f}Re$ and the Reynolds number is defined by $Re = \frac{\rho U D_p}{\mu_f}$. The input parameters of the collision model are the dry coefficient and the collision time.

2.3. Discretization schemes and solvers

An explicit first-order Euler scheme is used to discretize the time derivatives of the mass, momentum and energy equations and to advect Lagrangian markers. An implicit treatment of diffusion relaxes the time step. Spatial derivatives of convection and diffusion terms are discretized using a second-order centered scheme. A prediction correction algorithm is used to solve the momentum equation. The Poisson equation is then solved by the conjugate gradient method with a symmetrical successive overrelaxation preconditioner (ssor).

3. Numerical tool optimization and post-processing

PRS of fluidized beds is challenging because it requires to detect and model all collisions separately. The computation time to detect the particles in collisions increases with the square of the particle number because all particle pairs are tested. Thus, it limits the number of particles to be studied without a careful treatment of the algorithm of detection. This issue is addressed in Section 3.1. The assets of PRS-DEM approach lie in its ability to (i) track particles in their movement, (ii) compute the hydrodynamic force exerted by the fluid and the heat flux received on the particles surface. A description of the heat flux computing procedure is provided in Section 3.2. The post-processing of fluidized bed simulations is complex because of the large amount of data generated. The post-processing methodology is presented in Section 3.3.

3.1. Optimization of collision detection

One of the numerical challenges to fluidized beds computation is the detection of collision. The simplest algorithm to implement is to compute the distance to center for all particle pairs in the domain [65]. This procedure is realized by each CPU of the simulation and is therefore not optimized. Furthermore, the computational complexity scales

as $\mathbb{O}\left(\frac{N_p(N_p+1)}{2}\right)$. However, not all collisions are likely to occur, as two particles may be located several diameters apart. It is therefore essential to have efficient collision detection processing to handle several thousand or even tens of thousands of particles at reasonable cost.

An alternative procedure, namely the Verlet algorithm [69], is implemented in this paper. This method is widely employed for collision detection [64,70] in granular media. It is based on the Verlet table, which records the particles with which each particle may collide during a given time step. The algorithm is described in Appendix C.

This procedure is very similar to the one detailed by Fang et al. [70]. For all the simulations, ϵ_v is set to 30% of the particle diameter and $\Delta t^{max} = 50\Delta t_{simu}$ with Δt_{simu} the computational time step. The computational efficiency of the approach is presented in for a fluidized bed of 2134 particles, three mesh resolutions (12, 24 and 36 meshes per particle diameter) and four solid fractions. One can see that for the coarser mesh, the computational time of the collision process is scaled by a factor comprised between 12.2 and 13.6. The lower the solid volume fraction, the more efficient the method as less collision occurs. For finest grid resolutions (24 and 36 meshes per particle diameter), one can note that the computational time of the collision process is comprised between 1.0% and 1.3% which shows the high scalability of the method. One should point out that the collision detection does not depend on the grid resolution. However, the finer the mesh, the longer the CPU time to complete a time step (due to increased CPU communications). As a result, the relative time devoted to collision detection over a time step decreases with grid resolution. For these resolutions, the simulations were only performed for the Verlet algorithm due to its computational cost.

For the coarser mesh, the overall simulation time is reduced by 20%. A parametric study on the distance ϵ_v and the time Δt^{max} would be required to have the optimal pair of parameters. For the sake of simplicity, we propose to define Δt^{max} as the time required for a particle to travel half the distance ϵ_v at the median velocity of all particles. Indeed, Δt^{max} in only used as a safety factor. It must therefore be neither too small, as this would considerably increase computation time, nor too large, as some collisions might not be detected.

The order of the Verlet method is $\mathbb{O}\left(\frac{N_p(N_p+1)}{2}\right)$ every Δt_{maj} time steps and $\mathbb{O}(N)$ otherwise. Some preliminary tests on a fluidized bed of 8536 particles showed that with Verlet algorithm, the computation time of the collision force represents 14% of the time it takes to complete a time step. Therefore, one suggests combining the Verlet Algorithm with the Link Cell (LC) method as proposed by Fang et al. [70]. The algorithm is currently under development and will not be presented in the present paper. The LC method was previously employed in the literature [64,71]. It consists to search for potential collision in sub-domains close to a given one. In [64] and [71], a sub-domain matches the domain of a CPU or a GPU. Therefore, potential collisions between long-distance particles are not computed.

The efficiency of collision detection does not necessarily justify the implementation of a complex algorithm, especially if only a few particles are being investigated. Furthermore, LC algorithms require communication between Central Processing Units (CPUs), which can also increase computation time. The choice of the algorithm therefore depends on the number of particles and the solid fraction of the bed. More precisely, it depends on the number of particles contained in each sub-domain and therefore on the choice of domain partitioning between CPU or GPU for a given solid fraction. The denser the bed, the larger the number of collisions to be handled. As it is difficult to define a criterion considering these two parameters, we propose the following classification:

- $N_p = \mathbb{O}(1) - \mathbb{O}(10)$: classical algorithm
- $N_p \mathbb{O}(10) - \mathbb{O}(10^3)$: Verlet algorithm [69]
- $N_p \geq \mathbb{O}(10^4)$: Fang algorithm [70]

Table 1
Collision force computation time as a percentage of the total time it takes to complete a time step. α is the solid volume fraction, D_p, Δx are the particle diameter and the spatial discretization step, respectively. $\frac{D_p}{\Delta x}$ represents the spatial resolution as a function of the particle diameter.

	$\frac{D_p}{\Delta x}$ \ α	0.36	0.29	0.20	0.13
Verlet algorithm	12	1.8	1.7	1.7	1.4
	24	1.3	1.1	1.1	-
	36	1.0	-	-	-
Classic algorithm	12	22	22	21	19

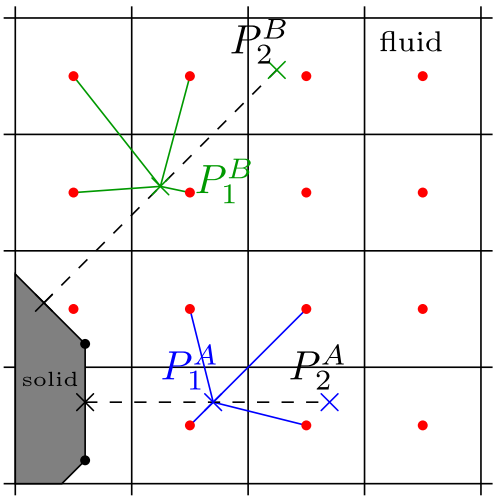

Fig. 3. Diagram of the heat flux computing.
Source: Figure extracted from [19].

3.2. Fluid–particle heat flux postprocessing

The computation of the heat flux follows the method developed in [19] for the hydrodynamic force. The heat flux received by the particle writes:

$$\Phi_p = \iint_{S_p} \lambda_f \nabla \mathbf{T} \cdot \mathbf{n} dS \tag{15}$$

with λ_f the thermal conductivity of the fluid, $\mathbf{n}$ the normal to the interface and S_p the particle surface. Eq. (15) is discretized on the Lagrangian mesh as follows:

$$\Phi_p = \sum_i^{N_f} \lambda_f \nabla \mathbf{T}_i \cdot \mathbf{n_i} S_i \tag{16}$$

where Nf is the number of Lagrangian facets of a particle and S_i is its surface area. For each Lagrangian facets, two interpolation points are defined at a distance δ and 2δ along the normal (see Fig. 3). The distance δ is chosen equals to Δx as defined in [19], where Δx is the Eulerian mesh size. The temperature is evaluated in all points P_1 and P_2 with a tri-linear interpolation from the Eulerian mesh. The temperature gradient is computed with a second order upwind scheme as follows:

$$\nabla \mathbf{T}_i = \lambda \frac{-T_{P_2} + 4T_{P_1} - 3T_p}{2\delta} S_i \tag{17}$$

where T_p is the temperature of the particle. The reader is referred to [19] for a complete description of the interpolation procedure.

3.3. Post-processing methodology

The post-processing of the simulations of fluidized bed is rather complex because of the amount of data generated. For the finest

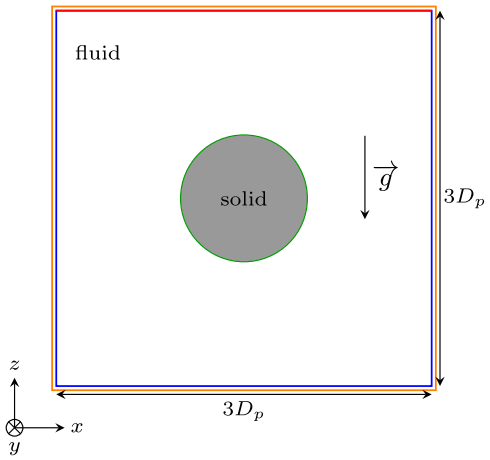

Fig. 4. Two-dimensional diagram of the configuration of the sedimentation of a particle in an infinite medium. The boundary conditions are as follows: –: Imposed pressure walls, –: Imposed velocity walls, –: Imposed temperature walls, –: Imposed temperature interface.

mesh, containing 181 million meshes, more than 1 Terabyte of data was generated for $10\,s$ of simulated flow. Post-processing such a large quantity of data requires specific treatment. A brief description of the procedure is detailed hereinafter for the Lagrangian statistics on one hand, and on the Eulerian statistics on the other hand. More details are also given in Appendices A and B.

Lagrangian statistics include the velocity and position of each particle, as well as the hydrodynamic force exerted by the fluid on the particle surface and the heat flux received by the particle. Data is recorded for all particles every 0.01 s of physical simulated time, which represents a good compromise between the accuracy of particle tracking, the simulation time spent writing the data and the computation time for post-processing the statistics. The supercomputer on which the computations were performed requires a maximum execution time of 24 h per simulation. Each complete simulation is therefore divided into 24 h simulation folders. Each folder contains a single file including the Lagrangian quantities of all the particles for each time step. For each folder, the velocity, position, hydrodynamic force and heat flux are extracted using `bash` commands and `GNU Parallel` [72]. Each variable is saved in an independent `csv` file. The data is then concatenated for all the folders of the simulation and saved in `HDF` format for faster rereading. Finally, the void fraction, bed height, position and velocity statistics are computed using `Python` multiprocessing tools.

Eulerian fields include the pressure, the velocity, the temperature and the solid volume fraction. The fields are written by `TrioCFD` software in a `lata` format at the same frequency as for the Lagrangian data. The files are first converted to the `vtk` format using `GNU parallel` [72] and `Visit` software. The `Vtk` files are loaded into `Python` using the module `Pyvista` [73]. The variables of interest are averaged for each 24 h simulation folder using `Pyvista` and `Pandas` modules coupled with `Python` multiprocessing tools and saved in `HDF` format. Finally, the data is concatenated for all the folders of the simulation and Eulerian statistics are computed. The computation of Eulerian averages on planes parallel and transverse to the flow is detailed in Appendix A. Finally, the wall heat transfer coefficient computation is explained in Appendix B.

4. Heat transfers on an isolated particle

The present method was validated in [19,65] for the hydrodynamic of the flow. A parametric study of the heat transfer computation is presented on the sedimentation of a particle at very small Reynolds under Stokes assumption (see Section 4.1) and on the sedimentation of a sphere in a quiescent fluid (see Section 4.2).

Table 2
Physical parameters of Stokes configuration.

Re	Pr	$\frac{\rho_p}{\rho_f}$	$\frac{\mu_p}{\mu_f}$	D_p	ΔT
$7.8.10^{-2}$	6	10	10^3	$5.2.10^{-6}$ m	5 K

4.1. Sedimentation of a particle in an infinite medium with heat transfer

The aim of this section is to study temperature diffusion in a case where it is predominant compared to convection. For this purpose, the configuration described in [19] was reproduced and adapted to study heat transfer (see Fig. 4). A cubic domain of section $3\,D_p$ is considered. The theoretical velocity and pressure fields of Stokes sedimentation are imposed at the boundaries (see Tab. 1 in [19]). A fixed temperature T_w is imposed on the lateral walls. The thermal boundary condition at the inlet is also an imposed temperature at T_w. The solid temperature is initialized at T_p and remains constant during the simulation. The initial fluid initial is T_w. Due to the heat transfer with the particle, a boundary layer develops around the particle (see Fig. 5).

The heat flux received by the sphere is computed with two methods. The first one is described in Section 3.2 and the second relies on a heat balance at the boundaries of the domain. It writes:

$$\boldsymbol{\Phi}_p = \boldsymbol{\Phi}_i + \boldsymbol{\Phi}_l - \boldsymbol{\Phi}_o \tag{18}$$

with respectively $\boldsymbol{\Phi}_p$, $\boldsymbol{\Phi}_i$, $\boldsymbol{\Phi}_l$ and $\boldsymbol{\Phi}_o$, the heat flux at the particle, the inlet, the lateral boundaries and the outlet. The Nusselt number is computed as follows:

$$Nu_p = \frac{hD_p}{\lambda_f} \tag{19}$$

and the heat transfer coefficient writes:

$$h = \frac{\boldsymbol{\Phi}_p}{S_p(T_\infty - T_p)} \tag{20}$$

with S_p, the particle surface and T_∞ the undisturbed temperature of the fluid ($T_\infty = T_w$).

The physical and numerical parameters of the simulation are summarized in Table 2. A mesh convergence study of the particle Nusslet number is presented in Table 3 for the method which uses the heat balance at the boundaries. This method presents the advantage of providing the flux actually received by the particle during the simulation, in contrast to the first method described in Section 3.2. The relative error to the finest mesh, $\frac{D_p}{\Delta x} = 50$ which is considered as the exact solution, is 3.5% for the coarser mesh while it drops down to 0.17% for a mesh resolution of $\frac{D_p}{\Delta x} = 20$. Snapshots of the steady-state temperature field are presented in Fig. 5 for two mesh resolutions (5 and 40 meshes per diameter). Even with the coarser mesh, the boundary layer of the particle is well captured. The particle Nusselt number computed with the finest mesh is compared to well-known correlations of the literature listed below:

- Ranz and Marshall [74]

$$Nu = 2 + 0.6Pr^{1/3}Re^{1/2} \tag{21}$$

for $2 \leq Re \leq 10^4$, $Pr \geq 0.6$

- Whitaker [75]:

$$Nu = 2 + (0.4Re^{1/2} + 0.06Re^{2/3})Pr^{2/5} \tag{22}$$

for $0.71 \leq Pr \leq 380, 3.5 \leq Re \leq 7.6.10^4$

- Feng and Michaelides [76]

$$Nu = 0.992 + Pe^{1/3} + 0.1Pe^{1/3}Re^{1/3} \tag{23}$$

for $0.1 \leq Re \leq 4000, 0.2 \leq Pe \leq 2000$.

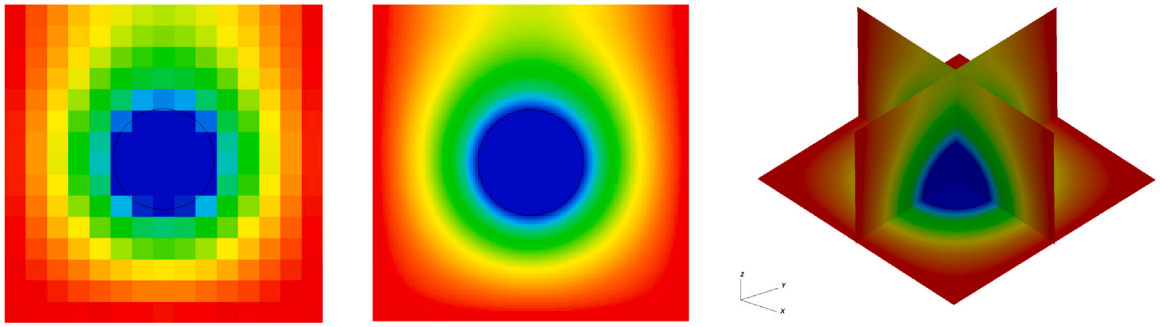

$\frac{D_p}{\Delta x} = 5$ – XZ plane $\frac{D_p}{\Delta x} = 40$ – XZ plane $\frac{D_p}{\Delta x} = 40$ – three-dimensional slice

Fig. 5. Temperature field of a Stokes flow past a sphere.

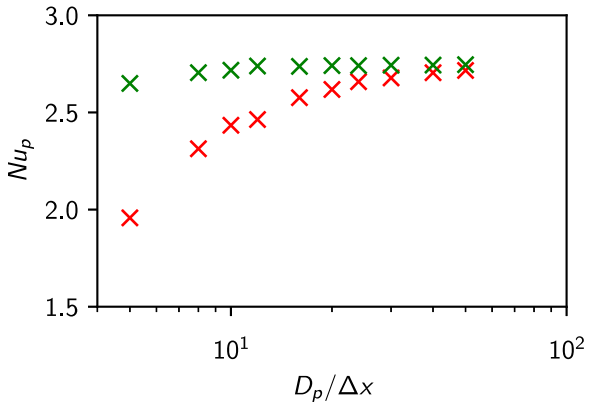

Fig. 6. Mesh convergence of the Nusselt number computed with two methods. x: heat balance at the boundaries, x: interpolation method.

Table 3
Particle Nusselt number computed with the heat flux obtained with a heat balance at the boundaries.

$D_p/\Delta x$	5	8	10	12	16
Nu_p	2.647	2.704	2.716	2.738	2.736
$D_p/\Delta x$	20	24	30	40	
Nu_p	2.740	2.740	2.742	2.742	

Table 4
Relative error of the prediction of the Nusselt number compared to the value computed with PR-DNS.

Reference value	Nusselt number	Relative error
PR-DNS	2.74	–
Ranz and Marshall	2.30	16.1%
Whitaker	2.25	17.8%
Feng and Michaelides	1.80	34.3%

The relative error of the correlations to the computed value with PR-DNS is presented in Table 4. The error is larger than 15% for all correlations. It can be explained by the fact that the Reynolds number of the simulation is too low and the correlations are not adapted for this flow regime. In addition, the error could be related to a confinement effect, as the domain is small compared to the particle diameter. The fixed temperature imposed on the boundaries may also alter the shape of the thermal boundary layer.

The heat balance method for calculating the flux received by the particle is only possible because the calculation domain contains only one particle. For multi-particle system, the use of the interpolation method (see Section 3.2) is required even though for resolution or collision reasons, the calculated flux might deviate from the exact heat flux received by the particle. A mesh convergence of the heat flux computed with this method is presented in Fig. 6. The interpolation method and the heat balance method both converge to the same value. The relative deviation falls below 4% for resolutions greater than 20 meshes per particle diameter. The interpolation method is therefore validated and will be employed to compute the flux received by the particle in the next section.

Table 5
Fluid properties of Cate's et al. experiment [77].

Case number	ρ_f [kg m^{-3}]	μ_f [Pa s]	Re
$E1$	970	0.373	1.50
$E2$	965	0.212	4.10
$E3$	962	0.113	11.6
$E4$	960	0.058	31.9

4.2. Settling sphere in a quiescent viscous fluid with heat transfer

A particle in sedimentation in a quiescent fluid is considered to assess the method at higher Reynolds numbers. The isothermal case of Cate's et al. experiment [77] is adapted to study fluid–particle heat transfer. The domain is a rectangular parallelepiped with square cross-section, sides 6.67 D_p and height 10.67 D_p. The particle diameter is 15 mm. The fluid properties are reported in Table 5. This configuration was previously studied by [65] with the same method without considering the heat transfer. The position and velocity profiles were in good agreement with the experimental data even with a coarse mesh of 15 meshes per particle diameter.

4.2.1. Assessment of the sedimentation trajectory

A fixed wall condition is applied on lateral and bottom boundaries. A pressure imposed condition is applied at the top. The temperature is imposed at 10 K at the wall and at 0 K at the particle surface. Initially, the fluid is at 10 K. Three mesh resolutions are investigated: 20, 30 and 40 meshes per particle diameter. It required respectively 200, 490 and 1088 CPUs. Four fluid viscosities were considered by Cate et al. to compute different flow regimes. Reynolds numbers based on the terminal settling velocity – in a infinite medium – are 1.50, 4.10, 11.6 and 31.9. The temporal evolution of the vertical position and velocity of the particle are represented in Fig. 7. It should be noted that the simulation was terminated before the particle reached the bottom of the tank in cases where the Reynolds number is below 4.10. For all Reynolds number, the numerical results are converged with the mesh resolution of 20 meshes per diameter, as all curves completely overlap. This avoided excessive computation costs when the simulated trajectory already correctly predicted the experiment. The curves representing the different meshes are superimposed. It shows that the mesh resolution of 15 meshes per particle diameter of Hamidi et al. [65] was too coarse to fully capture the hydrodynamic force exerted by the fluid

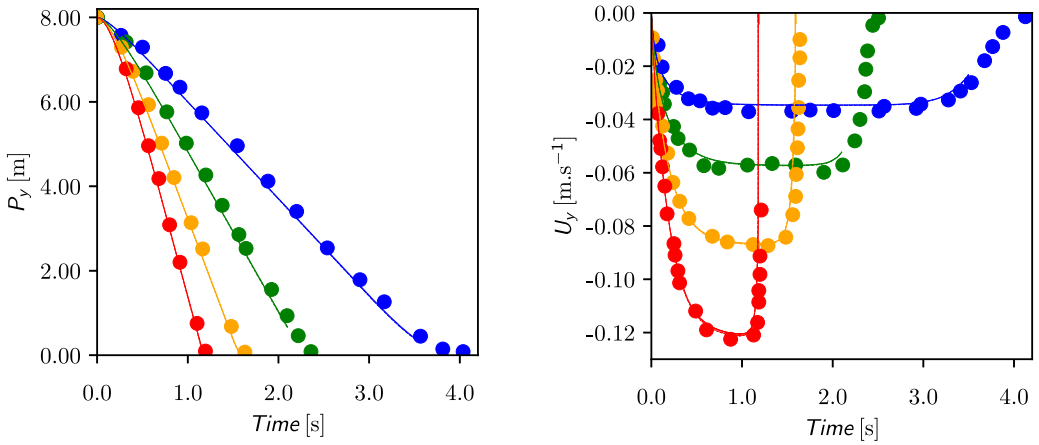

Fig. 7. Temporal evolution of the particle vertical position (left) and velocity (right). —: $\frac{D_p}{\Delta x} = 20$, – –: $\frac{D_p}{\Delta x} = 30$, – • : $\frac{D_p}{\Delta x} = 40$, • : experimental data [77]. —: $Re = 1.50$, —: $Re = 4.10$, —: $Re = 11.6$, —: $Re = 31.9$. For a given Reynolds number, all mesh resolutions are superimposed.

Table 6
Nusselt number for various Reynolds and Prandtl number. Nu^{RM}, Nu^{W} and Nu^{FM} are the Nusselt number computed with the correlation of Ranz and Marshall [74], Whitaker [75] and Feng and Michaelides [76], respectively. Nu^{PR-DNS} is the simulated value of the Nusselt number. ϵ is the relative error of the correlation to the simulated value: $\epsilon = (Nu_p^{correlation} - Nu_p^{PRS})/Nu_p^{PRS}$.

Pe	Re	Pr	Nu_p^{PRS}	Nu_p^{RM}	Nu_p^{W}	Nu_p^{FM}	ϵ^{RM} [%]	ϵ^{W} [%]	ϵ^{FM} [%]
0.67	1.33	0.5	2.23	2.55	2.40	1.96	14.3	7.86	−12.0
1.33	1.33	1	2.35	2.69	2.53	2.21	14.5	7.80	−5.86
1.94	3.88	0.5	2.47	2.94	2.71	2.44	18.8	9.54	−1.55
2.66	1.33	2	2.58	2.87	2.70	2.53	11.2	4.71	−2.04
3.88	3.88	1	2.77	3.18	2.94	2.81	14.7	5.87	1.33
5.50	11.0	0.5	3.04	3.58	3.23	3.15	17.8	6.31	3.68
7.76	3.88	2	3.18	3.49	3.24	3.28	9.74	1.76	3.26
11.0	11.0	1	3.55	3.99	3.63	3.71	12.4	2.09	4.56
15.0	29.9	0.5	4.01	4.61	4.10	4.22	14.7	2.04	5.15
22.0	11.0	2	4.21	4.51	4.15	4.42	7.12	−1.56	4.99
29.9	29.9	1	4.84	5.28	4.77	5.06	9.11	−1.54	4.53
59.8	29.9	2	5.87	6.14	5.65	6.12	4.50	−3.76	4.20

to the particle. This further explains the slight discrepancy with the experiment observed by the authors on particle velocity at the highest sedimentation velocity.

4.2.2. Assessment of fluid–particle heat transfer

In this section, the Nusselt number is computed with the method based on the interpolation from the nearest Eulerian fluid points. For each fluid viscosity considered in the previous section, three Prandtl numbers were studied ($Pr \in \{0.5, 1, 2\}$). In each case, one can compute the Nusselt number as a function of the time. However, the method required the boundary layer to be fully developed for the interpolation of the gradient to be accurate. Therefore, the transient phase from the start of the simulation cannot be studied. In each case, one can compute the Nusselt number of the particle when it has reached its terminal velocity. The data are presented in Table 6. The minimum relative error of the three correlations to the computed value is below 8% for all the computed cases. Ranz and Marshall correlation [74] always overestimates the particle Nusselt number and appeared less adapted than the correlations developed by Whitaker [75] and Feng and Michaeliedes [76]. One cannot define the most appropriate correlation between Whitaker and Feng and Michaelides, as neither appears to predict more accurately the Nusselt number than the other.

The parametric study is extended to a wider range of Peclet numbers ($Pe = RePr = D_p U_t/\alpha$, with U_t the particle terminal velocity and α the thermal diffusivity). 77 simulations with a resolution of 20 meshes per particle diameter. 7 Reynolds numbers and 11 Prandtl numbers were considered. Reynolds numbers are defined by the viscosity of the fluid and correspond to the Reynolds number reached by the particle when it reaches its terminal sedimentation velocity ($Re \in \{1, 2, 3, 4, 5, 12, 32\}$). Prandtl numbers are defined by the thermal conductivity of the fluid ($Pr \in \{0.1, 0.2, 0.25, 0.33, 0.5, 1, 2, 3, 4, 5, 10\}$). In the context of flows in solar receivers, Reynolds numbers are of the order of unity and the Prandtl number is approximately 0.7 for air. Peclet numbers are therefore very low. The parametric study focuses on these flow regimes. In each case, one value of the particle Nusselt number is computed when the thermal boundary layer is fully developed. The value given by the three correlations is computed with the corresponding Reynolds and Prandtl numbers. One can plot the Nusselt number obtained with the correlations as a function of the Nusselt number computed with PR-DNS (see Fig. 8). The closer the points to the identity curve, the more accurate the correlation. The correlations of Whitaker [75] and Feng and Michaelides [76] are both within the 10% confidence interval of the PR-DNS values. This demonstrates that they are both appropriate for predicting heat transfer between the fluid and an isolated particle at low Peclet numbers.

An attempt was made to optimize the coefficients of Whitaker [75] and Feng and Michaelides correlations [76]. The following equations were considered:

$$Nu^{opt\_W}(Pr, Re) = a_1 + (b_1 Re^{c_1} + d_1 Re^{e_1}) Pr^{f_1} \tag{24}$$

$$Nu^{opt\_FM}(Pe, Re) = a_2 + b_2 Pe^{c_2} + d_2 Pe^{e_2} Re^{f_2} \tag{25}$$

where $\{a_i..f_i\}$ are constant coefficients determined with the least square method (see Table 7). Both new correlations are represented on Fig. 8. It should be emphasized that the plots are superimposed, even if the equation is not in the same form. It suggests that there are too many degrees of freedom in determining the correlation coefficients. In addition, these correlations fail to predict the Nusselt value when the Reynolds number tends to zero. Indeed, for a sphere in a stationary fluid, the Nusselt number equals 2 [78]. A possible explanation is the fact that the computational domain is too small in front of the particle

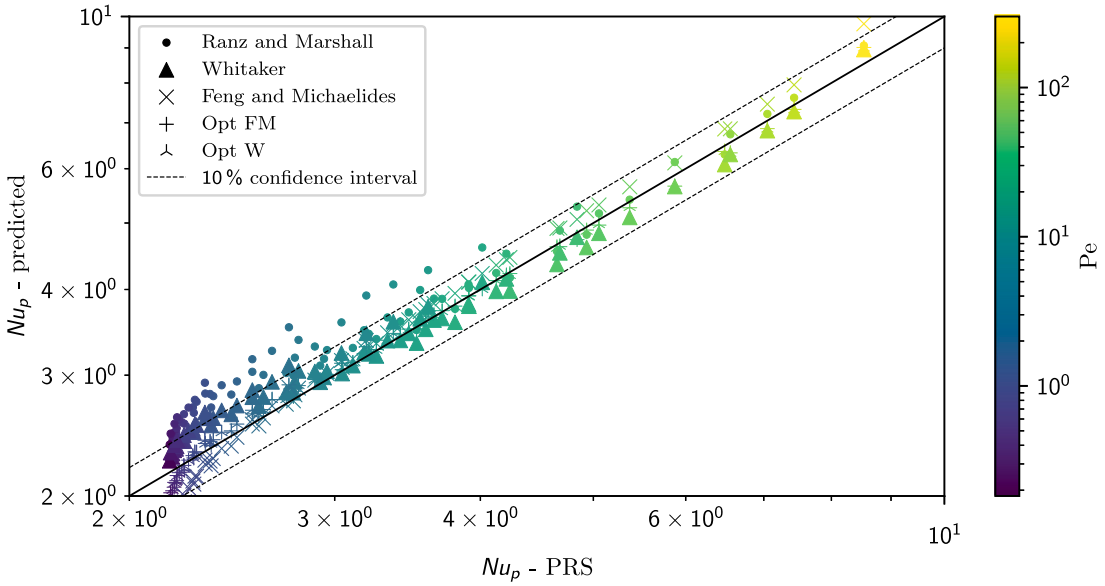

Fig. 8. Assessment of the correlation of Whitaker and Feng and Michaelides with the data produced with PRS. *Opt FM* and *Opt W* refers to the correlations obtained with optimized coefficients of Feng and Michaelides, and Whitaker correlations, respectively.

Table 7
Coefficients obtained with the least square method for Eqs. (24) and (25). W: coefficients of Whitaker's correlation [75], FM: coefficients of Feng & Michaelides's correlation [76].

	a_i	b_i	c_i	d_i	e_i	f_i
$i = 1$	1.5	0.072	−2.5	0.73	0.44	0.37
$i = 2$	1.5	0.64	0.38	0.10	0.34	0.30
W	2	0.4	0.5	0.06	2/3	2/5
FM	0.992	1	1/3	0.1	1/3	1/3

diameter. At low Peclet numbers, the thermal diffusion is predominant in front of the thermal convection and the thermal boundary layer is thicker than the dynamic one for low Prandtl number. Thus, the influence of the domain boundaries is higher at low Peclet numbers and could explain the discrepancy.

5. Study of an anisothermal liquid–solid fluidized bed

In this section, an anisothermal liquid–solid fluidized bed is studied. The physical configuration is described in Section 5.1. The numerical method is validated by confrontation with experimental [79] and numerical [80] work of the literature in Section 5.2. Fluid–particle heat transfer and wall-to-bed heat transfer are addressed in Sections 5.3 and 5.4 respectively. Finally, velocity–temperature correlations are discussed in Section 5.5.

5.1. Description of the physical configuration

The simulation reproduces the experimental work of Corona [79, 81]. The author investigated an isothermal liquid–solid fluidized bed in a cylindrical vessel. The working fluid is a concentrated aqueous solution of Potassium Thiocyanate (KSCN, 64% w/w). The particles are 6 mm Pyrex spheres. The fluid viscosity is 3.8×10^{-3} Pa s. A viscosity ratio of 10^4 is imposed as in [65]. The density of the fluid and the particles is, respectively, 1400 kg m^{-3} and 2230 kg m^{-3}. In the experiment, the cylindrical vessel is made of glass. The column is 8 cm in diameter and 60 cm height. The exponent of the Richardson–Zaki fluidization law [82] was measured experimentally by the authors as equal to 2.41. The terminal velocity of the particles in the fluid is 0.23 m s^{-1} and the minimum fluidization velocity is estimated to 0.03 m s^{-1} based on Fig. 2.24 of [79].

To numerically reproduce the experiment, a parallelipedic domain is defined with the same cross section area (see Fig. 9). The square cross-section is slightly larger than the circular cross-section by 3.1%. A no-slip boundary condition is imposed on the lateral walls. The fluid is injected at the bottom of the tank with a velocity U_f. A pressure imposed boundary condition is applied to the outlet section. The wall temperature is imposed 10 K higher than that of the particles. In the present work, all particles remain at a constant temperature. The entrance temperature of the fluid is that of the particles so only wall-to-bed heat transfer is considered. The thermal conductivity and the heat capacity of the fluid are constant in the whole domain (λ_f = 3.8 W m^{-1} K^{-1}, $c_{p,f}$ = 1000 J kg^{-1} K^{-1}). The thermal properties of the fluid were selected so that the Prandtl number equals 1. Four fluidization velocities were studied, $U_f \in \{0.073, 0.090, 0.120, 1.150\}$ m s^{-1}. Three mesh resolutions were considered for the lowest fluidization regime ($\frac{D_p}{\Delta x} \in \{12, 24, 36\}$), whereas two mesh resolutions were investigated for the fluidization velocities of 0.090 m s^{-1} and 0.120 m s^{-1} ($\frac{D_p}{\Delta x} \in \{12, 24\}$). Finally, one mesh resolution is considered for the highest fluidization velocity ($\frac{D_p}{\Delta x} = 12$). The numerical configuration of each case is detailed in Table 8. The height of the computation domain was shortened for the lowest fluidization velocities in order to reduce the numerical cost of the simulation. Preliminary tests showed that it did not affect the bed height, the solid volume fraction or the particle velocity variances. The computational time step depends on the grid resolution and the fluidization velocity. For all the simulations, Δt_{simu} lies between $5 \cdot 10^{-5}$ s and $1 \cdot 10^{-4}$ s.

5.2. Hydrodynamic behavior

The numerical method was previously validated by Hamidi et al. [65] for the same configuration of the fluidized bed with a mesh resolution of $\frac{D_p}{\Delta x} = 12$. The authors studied the bed height, the mean solid fraction as well as velocity variances and its anisotropy. The method has evolved since the `TrioCFD-1.7.9` version used in [65]. A harmonic viscosity model is employed in the present work compared to the *on-off* model employed in [65]. The on-off viscosity model implicitly define an effective diameter smaller than the real diameter for the computation of the diffusive term in the momentum equation. For coarse meshes, the consideration of the real diameter lead to an overestimation of the drag force [64]. However, the harmonic viscosity model should be employed to compute the stress tensor as it was proved

Table 8
Numerical configuration of fluidized beds.

Studied case	Dimensions (L/D_p)	Resolution ($D_p/\Delta x$)	Nb Eulerian cells	Nb CPU's	Physical simulated time (s/24 h computation)
$v < 0,15\,\mathrm{m\ s^{-1}}$	$12 \times 54 \times 12$	12 24	$13.4 \cdot 10^6$ $107 \cdot 10^6$	288 1152	1.74 0.8
$v = 0.073\,\mathrm{m\ s^{-1}}$	$12 \times 27 \times 12$	36	$181 \cdot 10^6$	3888	0.35
$v = 0.15\,\mathrm{m\ s^{-1}}$	$12 \times 108 \times 12$	12	$26.9 \cdot 10^6$	544	1.45

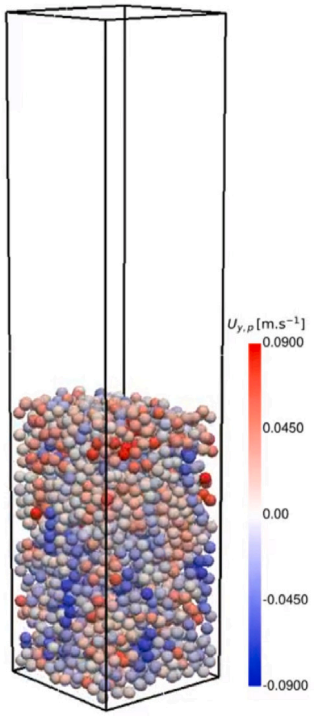

Fig. 9. Snapshot of a simulation at the highest solid fraction ($\alpha = 0.36$, $U_f = 0.073\,\mathrm{m\ s^{-1}}$).

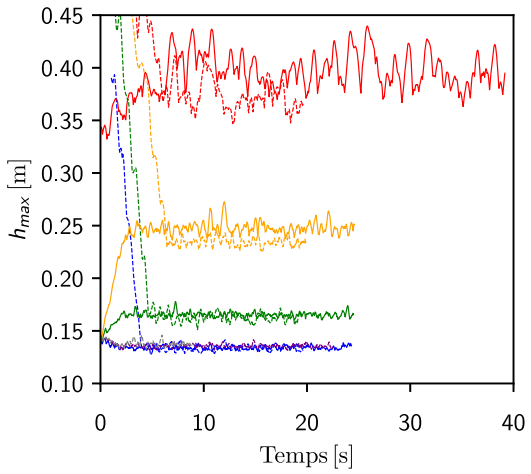

Fig. 10. Time evolution of the bed height for different fluidization velocities and mesh resolutions. —: present work, - - -: numerical work of Ozel [80]. —: $U_f = 0.15\,\mathrm{m\ s^{-1}}$ - $\frac{D_p}{\Delta x} = 12$, —:$U_f = 0.12\,\mathrm{m\ s^{-1}}$ - $\frac{D_p}{\Delta x} = 12$, —:$U_f = 0.09\,\mathrm{m\ s^{-1}}$ - $\frac{D_p}{\Delta x} = 12$, —:$U_f = 0.073\,\mathrm{m\ s^{-1}}$ - $\frac{D_p}{\Delta x} = 12$, —:$U_f = 0.073\,\mathrm{m\ s^{-1}}$ - $\frac{D_p}{\Delta x} = 24$, —:$U_f = 0.073\,\mathrm{m\ s^{-1}}$ - $\frac{D_p}{\Delta x} = 36$. For $U_f = 0.073\,\mathrm{m\ s^{-1}}$, all mesh resolutions are superimposed.

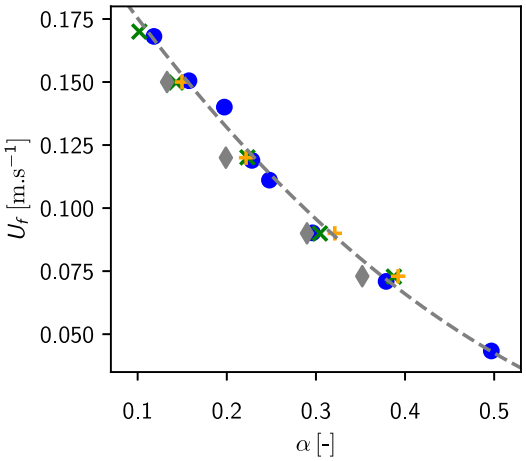

Fig. 11. Fluidization law. •: experiment of Corona [79], - - -: Richardson–Zaki law [82] x: numerical work of Ozel [80], +: numerical work of Hamidi [65], ♦: present work for $\frac{D_p}{\Delta x} = 12$.

to converge with the grid resolution [67]. For the simulations performed in this paper, with Reynolds numbers above 460 for meshes of up to 36 meshes per diameter, mesh convergence is not achieved. This leads to a slight overestimation of the drag force, which consequently results in an underestimation of the presence rate compared to Hamidi et al. [65] and Corona [79] experimental data. For this reasons, the numerical method is further evaluated against the experimental work of Corona [79] and the numerical work of Ozel [80]. Ozel et al. employed the Implicit Tensorial Penalty Fictitious Domain Method (ITPM) of Vincent et al. [64] for their simulations. A parallelipedic domain was considered and a Darcy penalty method was employed to add a wall boundary condition in the momentum equation and thus consider a cylindrical column. A grid resolution of 12 meshes per diameter was defined by the authors. The temporal evolution of the bed height is represented in Fig. 10. The bed height closely matches the simulation conducted by Ozel for the lowest fluidization velocities with the same grid resolution. The higher the fluidization velocity, the larger the fluctuations in bed height. The mesh sensitivity is represented in the figure for the lowest fluidization velocity. As shown in the figure, the bed height is slightly affected by the grid resolution. The discrepancy observed for the highest fluidization velocities could be explained by the fact that the cross-section area differs of 3.1% between both computational domain. It could also be explained by the difference in the geometry of the cross-section as a square is defined in the present work whereas a disk is defined in the work of Ozel [80]. The average solid fraction is computed between 5% and 85% of the bed height to avoid any boundary effects. It is represented in Fig. 11 as a function of the fluidization velocity. The fluidization law is well predicted and closely matches the experimental work of Corona [79] and the numerical work of Ozel [80] and Hamidi [65]. The slight deviation observed is explained by the choice of the harmonic viscosity model as detailed above. A reduced diameter of Δx was defined in [64] and employed in [80]. The viscosity model defined in [65] mimics

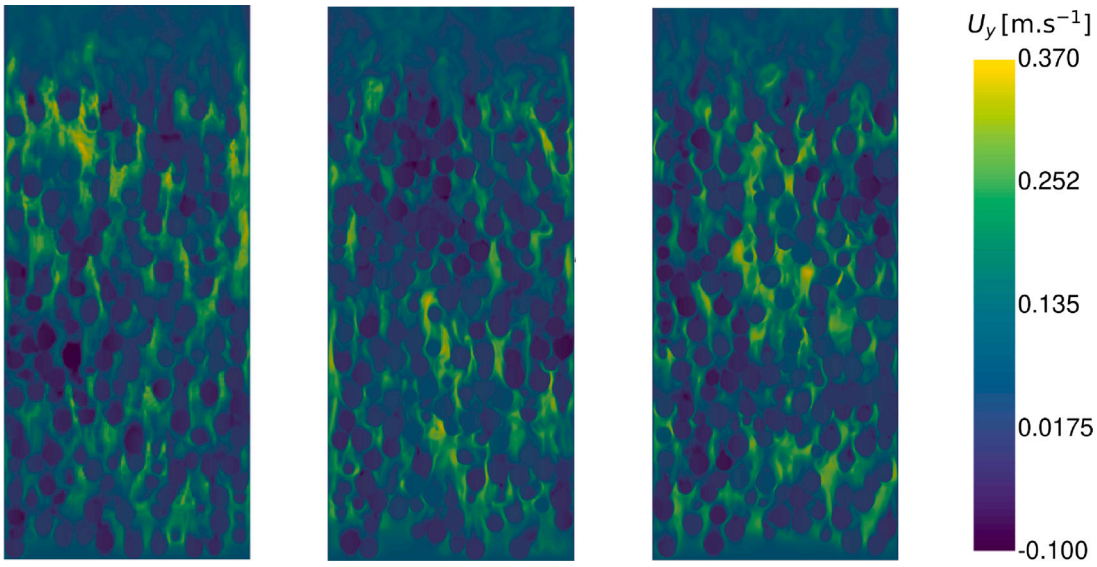

Fig. 12. Instantaneous visualization of the streamwise velocity field. $U_y = 0.073\,\mathrm{m\ s^{-1}}$. Left: $\frac{D_p}{\Delta x} = 12$, Middle: $\frac{D_p}{\Delta x} = 24$, Right: $\frac{D_p}{\Delta x} = 36$.

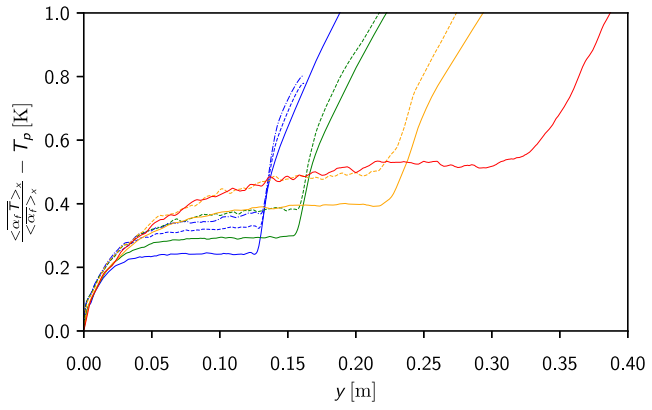

Fig. 13. Mean temperature profile along the bed height for different fluidization velocities U_f and mesh resolutions $\frac{D_p}{\Delta x}$. —: $U_f = 0.073\,\mathrm{m\ s^{-1}}$, —: $U_f = 0.09\,\mathrm{m\ s^{-1}}$, —: $U_f = 0.12\,\mathrm{m\ s^{-1}}$, —: $U_f = 0.15\,\mathrm{m\ s^{-1}}$. —: $\frac{D_p}{\Delta x} = 12$, – –: $\frac{D_p}{\Delta x} = 24$, – •: $\frac{D_p}{\Delta x} = 36$.

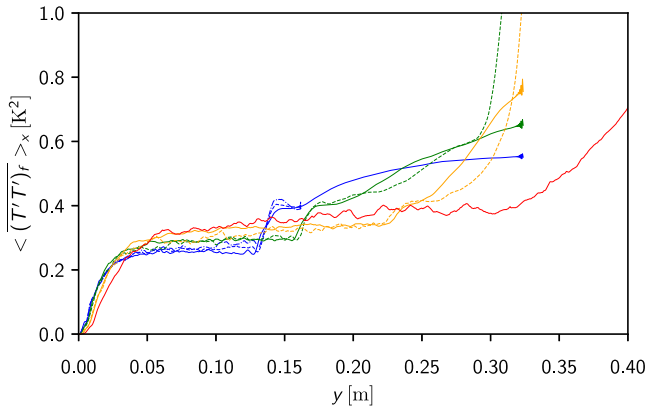

Fig. 14. Profile of the double temperature correlation along the bed height for different fluidization velocities U_f and mesh resolutions $\frac{D_p}{\Delta x}$. —: $U_f = 0.073\,\mathrm{m\ s^{-1}}$, —: $U_f = 0.09\,\mathrm{m\ s^{-1}}$, —: $U_f = 0.12\,\mathrm{m\ s^{-1}}$, —: $U_f = 0.15\,\mathrm{m\ s^{-1}}$. —: $\frac{D_p}{\Delta x} = 12$, – –: $\frac{D_p}{\Delta x} = 24$, – •: $\frac{D_p}{\Delta x} = 36$. For all mesh resolution, curves are superimposed along the bed height.

the reduced diameter of the penalty method. In the present work, the harmonic viscosity model was employed as it is expected to converge with the grid resolution.

Instantaneous visualization of the streamwise velocity field is shown in Fig. 12. The whole domain is represented for the grid resolutions of 24 and 36 grid per particle diameter while the domain is cropped for the coarsest grid to confront the above grid resolutions. The particle wake appears to be more accurately captured for the 24-mesh resolution than for the 12-mesh resolution. On the other hand, few differences are visible between the resolutions of 24 and 36 meshes per diameter.

5.3. Fluid–particle heat transfer

The mean temperature profiles along the height of the column are represented in Fig. 13 for the four fluidization velocities. For details on the way this quantity is computed from the simulations results, the reader is referred to Appendix A. For hereinafter, the notation $\langle A \rangle_{i,j}$ denotes for the spatial average of the quantity A in directions i, j and $\overline{A}$ denotes for the time average. In the figure, one can observe that the lower the fluidization velocity, the more homogenous the fluid temperature in the bed. Indeed, the particles act as a heat sink in the simulations and the lower the fluidization velocity, the denser the fluidized bed and therefore the more homogeneous the temperature field. Particles thus limit the increase in fluid temperature. One can point out that the bed height can be identified by the change in the slope of the temperature profile along the height of the column. Above the later, the fluid is simply heated by the walls and the temperature variation with y significantly rises. One can point out that a grid resolution of 12 meshes per particle diameter is too coarse to accurately capture the temperature evolution along the column height. A large discrepancy is observed between the evolution of the fluid temperature for grid resolutions of 12 and 24 meshes per diameter. However, the evolution of the fluid temperature for grid resolutions of 24 and 36 meshes per particle diameter, closely match. Therefore, for this configuration, at least 24 meshes per particle diameter is required to predict the mean temperature profiles.

The double correlation of temperature temporal fluctuations are represented with respect to the bed height and the wall distance in Figs. 14 and 15, respectively. The computation of $\langle \overline{(T'T')_f} \rangle_x$ and

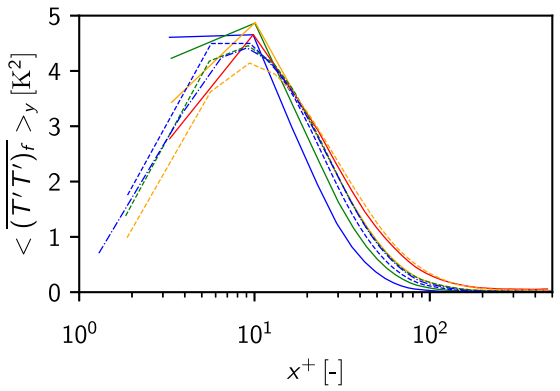

Fig. 15. Profile of the double temperature correlation as a function of x^+ for different fluidization velocities U_f and mesh resolutions $\frac{D_p}{\Delta x}$. —: $U_f = 0.073$ m s^{-1}, —: $U_f = 0.09$ m s^{-1}, —: $U_f = 0.12$ m s^{-1}, —: $U_f = 0.15$ m s^{-1}. —: $\frac{D_p}{\Delta x} = 12$, – –: $\frac{D_p}{\Delta x} = 24$, – ∘: $\frac{D_p}{\Delta x} = 36$.

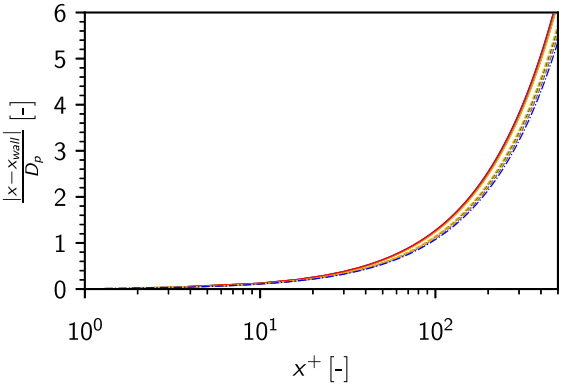

Fig. 16. Relation between x^+ and the wall distance normalized by the particle diameter. The legend is the same as for Fig. 15.

$\langle\overline{(T'T')}_f\rangle_y$ is detailed in Appendix A. One can notice in Fig. 14 that the higher the Reynolds number, the higher the temperature variance. The influence of the lack of resolution for coarse grid has less effects than for the mean temperature profiles (see Fig. 13). In addition, when the fluid leaves the bed, temperature variance increase strongly. This can be explained by the destruction of fluid agitation by pseudo-turbulence. Once exiting the bed, turbulence develops, generating strong spatial and temporal fluctuations in the temperature field. The effect of the lack of resolution of near-wall flow is more visible in Fig. 15. In the figure, x^+ is a dimensionless distance to the wall. $x^+ = \frac{|x-x_{wall}|u^*}{\nu_f}$, $u^* = \frac{\tau_w}{\rho_f}$ and $\tau_w = \mu_f \frac{\partial u_y}{\partial x}$. The link between x^+ and the wall distance scaled by the particle diameter is described in Fig. 16. In Fig. 15, the horizontal lines for low values of x^+ are due to the under-resolved discretization. All values of the double correlation of the temperature are 0 at the wall. Contrary to what is observed in Fig. 14, the maximum values of the correlation do not appear to depend on the Reynolds number. The correlation peak is located approximately at $x^+ = 10$, which correspond to a distance below 10% of the particle diameter. It emphasizes the necessity to refine the mesh at the wall. It is confirmed by the significant influence of the mesh resolution on the location of the correlation peak. The temperature variance falls to zero in the center of the bed, as the fluid and particles are at the same temperature.

The mean Nusselt number is defined as follows:

$$\langle\overline{Nu_f}\rangle_{0D} = \frac{\langle\overline{h_f}\rangle_{0D} D_p}{\lambda_f} \tag{26}$$

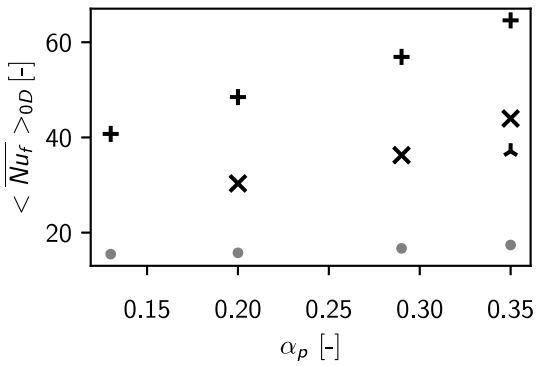

Fig. 17. Nusselt number as a function of the solid fraction. +: $\frac{D_p}{\Delta x} = 12$, ×: $\frac{D_p}{\Delta x} = 24$, 人: $\frac{D_p}{\Delta x} = 36$. ∘: Gunn's correlation [44].

where h_f is the heat transfer coefficient, D_p is the particle diameter and λ_f is the thermal conductivity of the fluid. h_f writes:

$$\langle\overline{h_f}\rangle_{0D} = \frac{\boldsymbol{\Phi}_{f\to p}}{N_p S_p (T_p - \langle\overline{T_f}\rangle_{0D})} \tag{27}$$

where $\boldsymbol{\Phi}_{f\to p}$ is the total heat flux received by the particles. $\boldsymbol{\Phi}_{f\to p}$ is computed with a heat balance at the boundaries as described in Section 4.1. N_p is the number of particles in the bed, T_p is the temperature of the particles and $\langle\overline{T_f}\rangle_{0D}$ is the mean fluid temperature in the bed. Therefore, one can express the Nusselt number as follows:

$$\langle\overline{Nu_f}\rangle_{0D} = \frac{\boldsymbol{\Phi}_{f\to p}}{N_p \lambda_f \pi D_p (T_p - \langle\overline{T_f}\rangle_{0D})} \tag{28}$$

The Nusselt computed for each fluidization velocity and each mesh grid resolution is represented in Fig. 17. The computed Nusselt number increases with the solid fraction. A large discrepancy is observed with the correlation of Gunn [44] even for the mesh grid resolution of 24 and 36 meshes per particle diameter. In such configuration, the fluid is injected at the same temperature as the particles and is only heated by the lateral walls. Thus, near-wall particles are submitted to a mean temperature gradient. Gunn's correlation [44] was not developed to describe such fluid-to-particle heat transfer. To assess Gunn's correlation [44] in the present case, the mean heat flux received by the particles ($\boldsymbol{\Phi}_{f\to p}$) should only be computed in the homogeneous part of the fluidized bed. However, the fluid-to-particle heat flux was not post-processed on a Lagrangian way for each particle in the current version of the code. Only the mean particle-to-fluid heat flux is available for post-processing. Nevertheless, it should be noted that Gunn's correlation always underestimates the fluid–particle heat transfer, which is expected as it was originally developed for fixed bed configurations. The same results were observed in [51]. Thus, as shown in Fig. 17, Gunn's correlation is not suitable to predict the overall convective heat transfer in the present configuration. Furthermore, even with 36 meshes per particle diameter, the mesh grid resolution is too coarse for the studied regime. Indeed, the particle Reynolds number defined as $Re = \frac{\rho_f U_f D_p}{\alpha_p \mu_f}$ is 461 for the lowest fluidization velocity and $Pr = 1$ and thus the Peclet number equals the Reynolds number. Consequently, a complete resolution of the thermal boundary layer would require more than a hundred meshes per particle diameter.

5.4. Wall-to-bed heat transfer

The wall-to-bed heat transfer is computed for the four walls of the parallelepipedic domain with a first order upwind scheme. The computation of the heat transfer coefficient is detailed in Appendix B. Instantaneous visualization of the heat transfer coefficient is shown in Fig. 18 for various mesh resolutions. The thermal wake is more

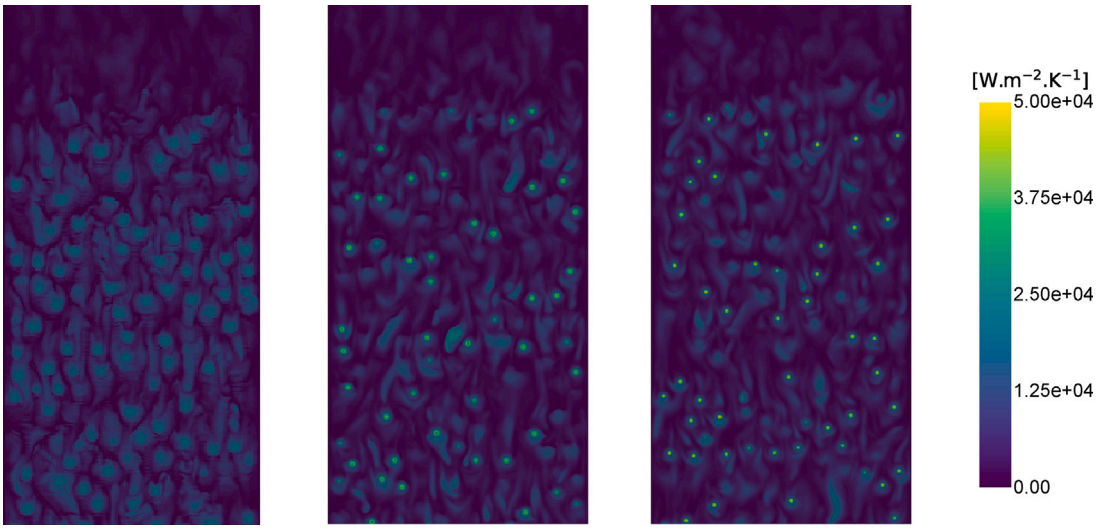

Fig. 18. Instantaneous wall-to-bed heat transfer coefficient. From left to right, the grid resolution is 12, 24 and 36 meshes per particle diameter.

spread out for the coarser grid than for the others and the magnitude of the heat transfer is lower. A large discrepancy is observed between the grid resolutions of 12 and 24 meshes per particle diameter. Even though the thermal wake of the particles is thinner for the finest grid, few differences are observed between the two finest grid resolutions, suggesting mesh convergence.

The mean heat transfer coefficient is represented in Fig. 19. The wall-to-bed heat transfer decreases with the fluid fraction. This behavior is in agreement with the correlation of Haid [53]. The author defined the Nusselt number as a function of the Reynolds number, the Prandtl number and the solid fraction (see Eq. (29)).

$$Nu_p = 0.0734 Re_p^{0.75} Pr^{0.63} \alpha_p^{0.25} \left(1-\alpha_p\right)^{-1} \tag{29}$$

To assess the correlation, the Reynolds number is computed with the velocity corresponding to a given solid fraction according to the Richardson–Zaki law [82]. One can point out an important effect of the mesh resolution on the wall-to-bed heat transfer coefficient. For the lowest fluid fraction, corresponding to the lowest fluidization velocity, the computed coefficient start to falls within the 30% confidence interval for the finest mesh. The finer the grid resolution, the less intense the heat transfer, contrary to what Fig. 18 suggests. Indeed, even if the points of contact with the wall are subject to high instantaneous values of the heat transfer coefficient, the contact zone and the collision time are very small. The higher coefficient computed for the coarser grid resolutions is therefore due to the more extensive thermal wake than for the finer resolutions. This results from the lack of resolution of pseudo-turbulence dissipation. An unexpected result is that the error is smaller for the largest fluid fractions and therefore, for the highest fluidization velocities. Indeed, for the fluidization velocity of $U_f = 0.12\,\mathrm{m\ s^{-1}}$ ($1-\alpha = 0.8$), the heat transfer coefficient falls within the confidence interval for a grid resolution of 24 meshes per particle diameter. It should be noted, however, that the current configuration does not fall within the range of validity of the correlation. Indeed the correlation is valid for a Prandtl number between 1.65 and 7700, whereas in the present simulations $Pr = 1$.

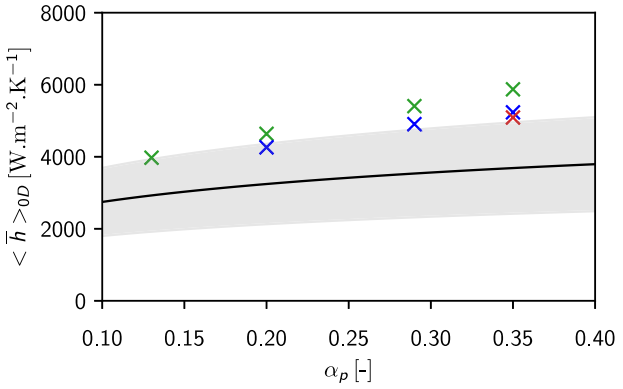

Fig. 19. Space–time averaged wall-to-bed heat transfer coefficient. x: $\frac{D_p}{\Delta x} = 12$, x: $\frac{D_p}{\Delta x} = 24$, x: $\frac{D_p}{\Delta x} = 36$. —: Haid correlation [53] and its confidence interval of 34.4%.

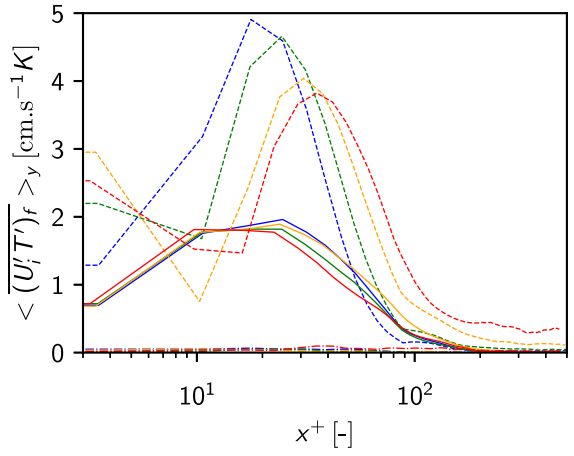

Fig. 20. Fluidization velocity effect on the near wall evolution of space–time average of the velocity–temperature correlation. $\frac{D_p}{\Delta x} = 12$. —: $U_f = 0.073\,\mathrm{m\ s^{-1}}$, —: $U_f = 0.09\,\mathrm{m\ s^{-1}}$, —: $U_f = 0.12\,\mathrm{m\ s^{-1}}$, —: $U_f = 0.15\,\mathrm{m\ s^{-1}}$. - -: streamwise velocity, —: normal wall velocity, - •: wall tangent velocity.

5.5. Velocity–temperature correlation

Velocity–temperature correlations are investigated to study heat transfers. The mean and bulk temperatures are computed along the cross-section of the flow. The bulk temperature is defined in Appendix A. The mean and bulk temperature profiles along the cross-section area are represented in Fig. 21. The higher the velocity, the hotter the mean temperature of the fluid along the cross-section area. Indeed, the higher the velocity, the less cooled the fluid by the particles along the bed height (see Fig. 13). Strong spatial variations of the temperature are observed along the transverse direction to the flow as the fluid

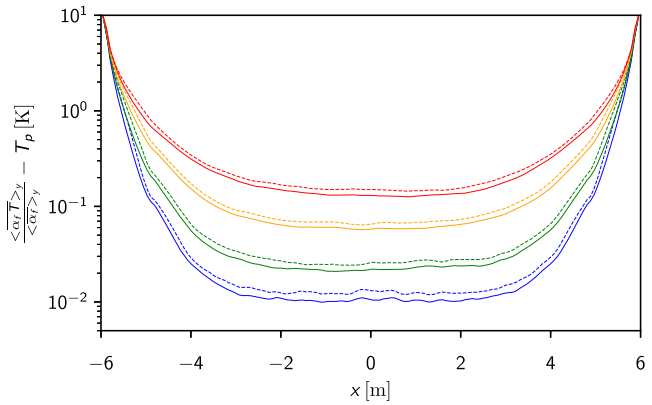

Fig. 21. Mean and bulk fluid temperature along the cross-section area. $\frac{D_p}{\Delta x} = 12$. ▬: mean temperature, ▬ ▬: bulk temperature, ▬: $U_f = 0.073\,\mathrm{m\ s^{-1}}$, ▬: $U_f = 0.09\,\mathrm{m\ s^{-1}}$, ▬: $U_f = 0.12\,\mathrm{m\ s^{-1}}$, ▬: $U_f = 0.15\,\mathrm{m\ s^{-1}}$.

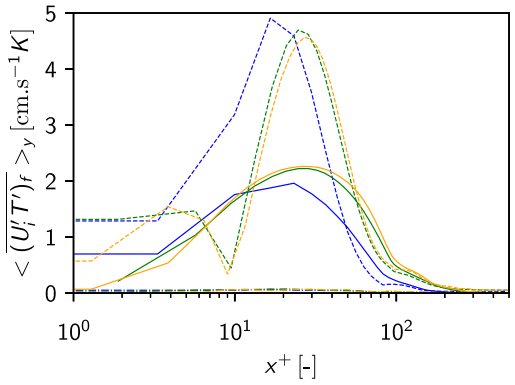

Fig. 22. Resolution effect on the near wall evolution of space–time average of the velocity–temperature correlation. $U_f = 0.073\,\mathrm{m\ s^{-1}}$, ▬: $\frac{D_p}{\Delta x} = 12$, ▬: $\frac{D_p}{\Delta x} = 24$, ▬: $\frac{D_p}{\Delta x} = 36$. The components of the velocity are described with the same representation than that of Fig. 20.

is only heated at the wall. The computation of velocity–temperature correlation $\langle\overline{(U'T')_f}\rangle_y$ is detailed in Appendix A.

Fig. 20 represents this correlation, for the four fluidization velocities, along the cross-section area. The fluid Reynolds number can be defined as $Re = \frac{U_f L_x}{\nu_f \alpha_f}$. From the lowest to the highest fluidization velocity, the Reynolds number is respectively 2980, 3360, 3980 and 4970. The extremum of the double correlation is located further into the bed when the Reynolds number increases. The main component of the turbulent movement is obtained with the streamwise velocity. One can note that the turbulent agitation associated with the normal wall velocity is less than a third of the intensity of that of the streamwise velocity. The correlation peak associated with the normal wall velocity is located further into the bed than that of the streamwise component. Furthermore, the location of the correlation peak differs from that of the temperature variance (see Fig. 15) which was located at $x^+ \sim 10$. For both studied correlation, it corresponds to a distance less than half of the particle diameter. Finally, the velocity tangent to the wall does not contribute to the turbulent heat flow. Results on the average of each velocity component showed that the mean normal wall velocity is almost zero. Therefore, the mean convective heat flux, computed as $\rho_f c_{p,f} \langle\overline{u_x}\rangle_{0D} \langle\overline{T}\rangle_{0D}$, is very small in front of the term $\rho_f c_{p,f} \langle\overline{u_x' T'}\rangle_{0D}$. Wall-to-bed heat transfer is therefore driven by the turbulent convective heat flux. One should note that it is not the case for the streamwise mean convective heat flux as the mean fluid velocity is equal to the fluidization velocity divided by the mean fluid fraction. However, for heat transfer enhancement in the bed, it is the convective heat flux associated to the normal wall velocity that needs to be considered. Mesh resolution has a strong influence on the location of the agitation peak, as shown in Fig. 22. Indeed, the agitation peak associated with the streamwise component is located at $x^+ = 16$ for the mesh resolution of 12 meshes per particle diameter whereas it is located at $x^+ = 27$ for the mesh resolution of 36 meshes per particle diameter. The intensity of the turbulent heat flow is slightly affected by the grid resolution.

6. Concluding remarks

The objective of this study was to study the dynamic and the heat transfers in a fluidized bed. For this purpose, the numerical method was first validated on the study of an isolate particle in sedimentation in an infinite medium. A method to compute the heat flux received by the particle was developed, inspired by the method of hydrodynamic force computation of Butaye et al. [19]. Then a parametric study of the particle Nusselt number of a particle in sedimentation in quiescent fluid was performed. An excellent agreement with existing correlation of the literature was found except for very low Peclet numbers (below 1) which could be explained by the influence of the lateral boundaries at these regimes.

A study of a liquid–solid anisothermal fluidized bed showed that the macroscopic behavior of the bed was well predicted based on the bed height and the solid fraction. However, for coarse grid ($D_p/\Delta x = 12$), the method fails to predict the thermal behavior of the flow. A finer mesh ($D_p/\Delta x = 24$) was required to predict the heat transfer at a reasonable cost. The fluid Nusselt number increases with the solid fraction, in accordance with Gunn's correlation [44]. Finally, regarding the wall-to-bed heat transfer, the heat transfer coefficient increases with the solid fraction. The deviation from Haid's correlation [53] increases with the solid fraction, which is unexpected since, for the same grid resolution, the resolution of the flow decreases as the velocity increases. The velocity–temperature correlations are strongly affected by the grid resolution. Finally, it was shown that the wall-to-bed heat transfer is driven by the turbulent convective heat flux associated with the normal wall velocity.

The perspectives to this work would be to study anisothermal gas-solid fluidized beds. In such configurations, the particle diameter is less than a hundred micrometers and the fluid studied is air.

CRediT authorship contribution statement

E. Butaye: Writing – original draft, Visualization, Software, Methodology, Investigation, Formal analysis, Data curation, Conceptualization. **R. Quintana:** Formal analysis, Data curation. **S. Mer:** Writing – review & editing, Visualization, Validation, Supervision, Methodology, Investigation, Formal analysis, Conceptualization. **F. Bataille:** Writing – review & editing, Validation, Supervision. **A. Toutant:** Writing – review & editing, Visualization, Validation, Supervision, Methodology, Investigation, Formal analysis, Conceptualization.

Declaration of competing interest

The authors declare that they have no known competing financial interests or personal relationships that could have appeared to influence the work reported in this paper.

Acknowledgment

This work was granted access to the HPC resources of CINES under the allocation 2023-A0142B11441 made by GENCI. The authors gratefully acknowledge the CEA for the development of the TRUST platform. The technical support of TRUST/TrioCFD team was also greatly appreciated. The authors would like to thank Dr. Ali Ozel for providing the simulation data.

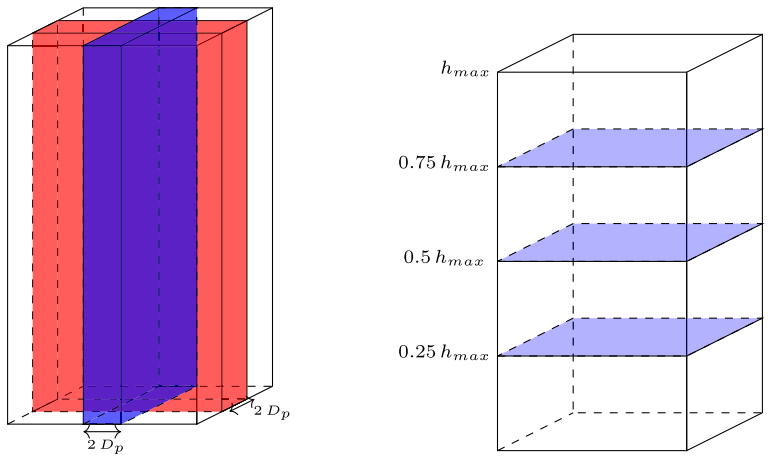

Fig. A.23. Diagram of planes employed in the spatial average. Along streamwise direction (left) and along the cross-section area (right).

Appendix A. Computation of Eulerian statistics

The mean Eulerian properties of the flow are computed with a space–time average. Two configurations can be distinguished. The first is an average over planes parallel to the flow and the second is an average over the cross-section area (see Fig. A.23). For the first configuration, all the planes at the centre of the domain are considered over a thickness of two particle diameters and along the two transverse directions. Thus, for resolutions of 12, 24 and 36 meshes per diameter, we consider 48, 96 and 144 planes respectively. Three cross-sections are considered for the second configuration, at a height of 25%, 50% and 75% of the mean bed height.

For a field A, the space–time average in a two-dimensional plane $\overline{\langle A \rangle}$ is computed as follows:

$$\overline{\langle A \rangle}(x,y) = \frac{1}{N_t}\sum_t \left(\frac{1}{N_{planes}} \sum_{planes} A(x,y,z,t) \right)$$

where N_t is the number of timesteps considered in the simulation and N_{planes} is the number of planes.

The zero-dimensional average of the quantity $\overline{\langle A \rangle}(x,y)$ is then computed on a section of the two-dimensional plane. To avoid any boundary effects, cells located at a distance of $3D_p$ near the fluid injection are not taken into account, nor are cells located at a distance of one particle diameter near the corners. In addition, as only the characteristics of the fluid inside the bed are studied, cells located above the average height of the bed are not taken into account in the average. Then, the $0D$ average writes:

$$\langle \overline{A} \rangle_{0D} = \int_{3\,D_p}^{h_{bed}} \int_{-L_x/2+D_p}^{L_x/2-D_p} \overline{\langle A \rangle}(x,y) dx dy$$

One dimensional space–time average in the direction x or in the direction y are computed as follows:

$$\langle \overline{A} \rangle_y = \int_{3\,D_p}^{h_{bed}} \overline{\langle A \rangle}(x,y) dy$$

$$\langle \overline{A} \rangle_x = \int_{-L_x/2+D_p}^{L_x/2-D_p} \overline{\langle A \rangle}(x,y) dx$$

The mean fluid temperature is computed over the planes parallel to the streamwise direction of the flow and writes:

$$\overline{\langle T \rangle}_{f,0D} = \frac{\langle \overline{\alpha_f T} \rangle_{0D}}{\langle \alpha_f \rangle_{0D}}$$

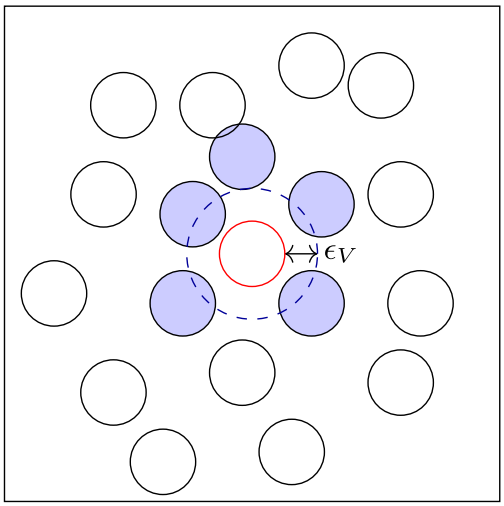

Fig. C.24. Diagram of the Verlet algorithm (not to scale).

The bulk temperature writes:

$$\overline{\langle T_b \rangle}_{f,0D} = \frac{\langle \overline{\alpha_f V T} \rangle_{0D}}{\langle \overline{\alpha_f V} \rangle_{0D}}$$

where V stands for the streamwise velocity.

Double correlation for field A and field B are computes as follows:

$$\langle \overline{(A'B')_f} \rangle_y = \frac{\langle \overline{\alpha_f AB} \rangle_y}{\langle \overline{\alpha_f} \rangle_y} - \frac{\langle \overline{\alpha_f A} \rangle_y \langle \overline{\alpha_f B} \rangle_y}{\langle \overline{\alpha_f} \rangle_y^2}$$

$$\langle \overline{(A'B')_f} \rangle_x = \frac{\langle \overline{\alpha_f AB} \rangle_x}{\langle \overline{\alpha_f} \rangle_x} - \frac{\langle \overline{\alpha_f A} \rangle_x \langle \overline{\alpha_f B} \rangle_x}{\langle \overline{\alpha_f} \rangle_x^2}$$

Appendix B. Computation of the wall-to-bed heat transfer

The mean heat transfer coefficient is computed as follows:

$$\overline{h} = \frac{1}{N_t}\sum_{N_t} \frac{1}{4} \sum_i \frac{1}{S_w^i} \iint_{S_w^i} h_t^i(x,y,z)\, dS \tag{B.1}$$

where N_t is the number of timesteps considered for the time-average, S_w^i is the surface of the lateral wall i and depends on the bed height,

$h_t^i(x, y, z)$ is the heat transfer coefficient at the position (x,y,z) of the lateral wall i at the time t.

Appendix C. Verlet algorithm

1. **Construction of the Verlet tables** At the start of the calculation, for each particle i, the distance d_{ij} with all the other particles is computed. If d_{ij} is below a given threshold ϵ_v, the particle j is identified as a potential candidate for collision for particle i and saved in its Verlet table. The algorithm is schematized in Fig. C.24
2. **Identifying the fastest particle** The speed of the fastest particle is identified as $v_{p,max}$.
3. **Computation of the update time** A characteristic time of the table update is constructed based on the time two particles at $v_{p,max}$, distant by ϵ_v and traveling in the opposite direction, need to collide $\Delta t_V = \frac{\epsilon_v}{2v_{p,max}}$. A numerical security Δt^{max} is also considered to avoid excessively long time intervals without update. The final update time is $\Delta t_{upd} = min\left(\Delta t_V, \Delta t_{max}\right)$.
4. **Update fo the tables** Every Δt_{upd} the Verlet tables are recalculated

Data availability

Data will be made available on request.

References

[1] Y. Zhang, J. Xu, Q. Chang, P. Zhao, J. Wang, W. Ge, Numerical simulation of fluidization: Driven by challenges, Powder Technol. 414 (2023) http://dx.doi.org/10.1016/j.powtec.2022.118092.

[2] F. Winkler, Verfahren zum Herstellen von Wassergas, (DE437970C) 1922, https://patents.google.com/patent/DE437970C/de.

[3] T. Suppan, M. Neumayer, T. Bretterklieber, S. Puttinger, H. Wegleiter, A model-based analysis of capacitive flow metering for pneumatic conveying systems: A comparison between calibration-based and tomographic approaches, Sensors 22 (2022) http://dx.doi.org/10.3390/s22030856.

[4] N. Muradov, Hydrogen via methane decomposition: an application for decarbonization of fossil fuels, Int. J. Hydrog. Energy 26 (2001) http://dx.doi.org/10.1016/S0360-3199(01)00073-8.

[5] G. Flamant, D. Gauthier, H. Benoit, J.-L. Sans, R. Garcia, B. Boissiere, R. Ansart, M. Hemati, Dense suspension of solid particles as a new heat transfer fluid for concentrated solar thermal plants: On-sun proof of concept, Chem. Eng. Sci. 102 (2013) http://dx.doi.org/10.1016/j.ces.2013.08.051.

[6] M. Castro-Quijada, D. Faundez, R. Rojas, A. Videla, Improving the working fluid based on a $NaNO_3 - KNO_3 - NACl - KCl$ molten salt mixture for concentrating solar poser energy storage, Sol. Energy 231 (2022) http://dx.doi.org/10.1016/j.solener.2021.11.058.

[7] R. Gueguen, G. Sahuquet, M. Tessoneaud, J.-L. Sans, E. Guillot, A.L. Gal, R. Garcia, S. Mer, A. Toutant, F. Bataille, G. Flamant, Heat transfer in a fluidized bed tubular solar receiver. On-sun experimental investigation, Sol. Energy 265 (2023) http://dx.doi.org/10.1016/j.solener.2023.112118.

[8] G. Flamant, Theoretical and experimental study of radiant heat transfer in a solar fluidized-bed receiver, AIChE J. 28 (1982) http://dx.doi.org/10.1002/aic.690280402.

[9] R. Gueguen, G. Sahuquet, S. Mer, A. Toutant, F. Bataille, G. Flamant, Gas-solid flow in a fluidized-particle tubular solar receiver: Off-sun experimental flow regimes characterization, Energies 14 (2021) http://dx.doi.org/10.3390/en14217392.

[10] B. Boissiere, R. Ansart, D. Gauthier, G. Flamant, M. Hemati, Experimental study of gas-particle dense suspension upward flow for application as a new heat transfer and storage fluid, Can. J. Chem. Eng. 93 (2014) http://dx.doi.org/10.1002/cjce.22087.

[11] D. Geldart, Types of gas fluidization, Powder Technol. 7 (1973) http://dx.doi.org/10.1016/0032-5910(73)80037-3.

[12] R. Gueguen, S. Mer, A. Toutant, F. Bataille, G. Flamant, Effect of temperature on the hydrodynamics of a fluidized bed circulating in a long tube for a solar energy harvesting application, Chem. Eng. Sci. 281 (2023) http://dx.doi.org/10.1016/j.ces.2023.119218.

[13] R. Gueguen, G. Sahuquet, S. Mer, A. Toutant, F. Bataille, G. Flamant, Fluidization regimes of dense suspensions of Geldart group A fluidized particles in a high aspect ratio column, Chem. Eng. Sci. 267 (2022) http://dx.doi.org/10.1016/j.ces.2022.118360.

[14] M.V. der Hoef, M. Ye, M. van Sint Annaland, A.A. IV, S. Sundaresan, J. Kuipers, Multiscale modeling of gas-fluidized beds, Adv. Chem. Eng. 31 (2006) http://dx.doi.org/10.1016/S0065-2377(06)31002-2.

[15] F. Alobaid, N. Almohammed, M.M. Farid, J. May, P. Rößger, A. Richter, B. Epple, Progress in CFD simulations of fluidized beds for chemical and energy process engineering, Prog. Energy Combust. Sci. 91 (2022) http://dx.doi.org/10.1016/j.pecs.2021.100930.

[16] S. Tenneti, S. Subramaniam, Particle-resolved direct numerical simulation for gas-solid flow model development, Annu. Rev. Fluid. Mech. 46 (2014).

[17] M. Maxey, Simulation methods for particulate flows and concentrated suspension, Annu. Rev. Fluid. Mech. 49 (2017) http://dx.doi.org/10.1146/annurev-fluid-122414-034408.

[18] F. Marchelli, L. Fiori, R. Di Felice, Cohesive particle-fluid systems: An overview of their CFD simulation, Can. J. Chem. Eng. (2024) http://dx.doi.org/10.1002/cjce.25269.

[19] E. Butaye, A. Toutant, S. Mer, F. Bataille, Development of particle resolved - subgrid corrected simulations: Hydrodynamic force calculation and flow sub-resolution corrections, Comput. & Fluids 267 (2023) http://dx.doi.org/10.1016/j.compfluid.2023.106071.

[20] H.A. Khawaja, CFD-DEM simulation of minimum fluidisation velocity in two phase medium, Int. J. Multiphys. 5 (2011) http://dx.doi.org/10.1260/1750-9548.5.2.89.

[21] Y. Dufresne, V. Moureau, E. Masi, O. Simonin, J. Horwitz, Simulation of a reactive fluidized bed reactor using CFD/DEM, in: Center for Turbulence Research Summer Program 2016, Vol. 26, 2016.

[22] L. Zhou, W. Lv, L. Bai, Y. Han, J. Wang, W. Shi, G. Huang, CFD-DEM study of gas-solid flow characteristics in a fluidized bed with different diameter of coarse particles, Energy Rep. 8 (2022) http://dx.doi.org/10.1016/j.egyr.2022.01.174.

[23] S. Tenneti, R. Garg, S. Subramaniam, Drag law for monodisperse gas–solid systems using particle-resolved direct numerical simulation of flow past fixed assemblies of spheres, Int. J. Multiph. Flow 37 (2011) http://dx.doi.org/10.1016/j.ijmultiphaseflow.2011.05.010.

[24] R. Beestra, M.V. der Hoef, J. Kuipers, Drag force of intermediate Reynolds number flow past mono- and bidisperse arrays of spheres, AIChE J. 53 (2007) http://dx.doi.org/10.1002/aic.11065.

[25] B. Vowinckel, Incorporating grain-scale processes in macroscopic sediment transport models, Acta Mech. 232 (2022) http://dx.doi.org/10.1007/s00707-021-02951-4.

[26] A. Ozel, P. Fede, O. Simonin, Development of filtered Euler–Euler two-phase model for circulating fluidised bed: High resolution simulation, formulation and a priori analyses, Int. J. Multiph. Flow 55 (2013) http://dx.doi.org/10.1016/j.ijmultiphaseflow.2013.04.002.

[27] D. Dupuy, Y. Badran, R. Ansart, O. Simonin, Calibrating the frictional-pressure model from two-fluid simulation of fluidised beds in the defluidisation regime, Powder Technol. (2024) http://dx.doi.org/10.1016/j.powtec.2024.119776.

[28] N. Deen, M.V.S. Annaland, M.V. der Hoef, J. Kuipers, Review of discrete particle modeling of fluidized beds, Chem. Eng. Sci. 62 (2007) http://dx.doi.org/10.1016/j.ces.2006.08.014.

[29] D. Dupuy, R. Ansart, O. Simonin, Investigation of near-wall particle statistics in CFD-DEM simulations of dense fluidised beds and derivation of an Eulerian particle dynamic wall boundary condition, J. Fluid Mech. 982 (2024) http://dx.doi.org/10.1017/jfm.2024.36.

[30] M.-A. Chadil, S. Vincent, J.-L. Estivalezes, Accurate estimate of drag forces using particle-resolved direct numerical simulations, Acta Mech. 230 (2018) http://dx.doi.org/10.1007/s00707-018-2305-1.

[31] A. Esteghamatian, M. Bernard, M. Lance, A. Hammouti, A. Wachs, Micro/meso simulation of a fluidized bed in a homogeneous bubbling regime, Int. J. Multiph. Flow 92 (2017) http://dx.doi.org/10.1016/j.ijmultiphaseflow.2017.03.002.

[32] A. Esteghamatian, A. Hammouti, M. Lance, A. Wachs, Particle resolved simulations of liquid/solid and gas/solid fluidized beds, Phys. Fluids 29 (2017) http://dx.doi.org/10.1063/1.4979137.

[33] N. Deen, S. Kriebitzsch, M.V. der Hoef, J. Kuipers, Direct numerical simulation of flow and heat transfer in dense fluid-particle systems, Chem. Eng. Sci. 81 (2012) http://dx.doi.org/10.1016/j.ces.2012.06.055.

[34] S. Kriebitzsch, M.V. der Hoef, J. Kuipers, Fully resolved simulation of a gas-fluidized bed: A critical test of DEM models, Chem. Eng. Sci. 91 (2013) http://dx.doi.org/10.1016/j.ces.2012.12.038.

[35] K. Luo, J. Tuan, Z. Wang, J. Fan, Particle-resolved direct numerical simulation of gas–solid dynamics in experimental fluidized beds, AIChE J. 62 (2016) http://dx.doi.org/10.1002/aic.15186.

[36] J. Dou, L. Wang, W. Ge, J. Ouyang, Effect of mesoscale structures on solid phase stress in gas-solid flows, Chem. Eng. J. 455 (2023) http://dx.doi.org/10.1016/j.cej.2022.140825.

[37] P. Bagchi, M. Ha, S. Balachandar, Direct numerical simulation of flow and heat transfer from a sphere in a unifrm cross-flow, J. Fluid Eng. 123 (2001) http://dx.doi.org/10.1115/1.1358844.

[38] Z.-G. Feng, E. Michaelides, Heat transfer in particulate flows with Direct Numerical Simulation, Int. J. Heat Mass Transfer 52 (2009) http://dx.doi.org/10.1016/j.ijheatmasstransfer.2008.07.023.

[39] H. Gan, J. Chang, J. Feng, H. Hu, Direct numerical simulation of the sedimentation of solid particles with thermal convection, J. Fluid Mech. 481 (2003) http://dx.doi.org/10.1017/S0022112003003938.

[40] Z. Yu, X. Shao, A. Wachs, A fictitious domain method for particulate flows with heat transfer, J. Comput. Phys. 217 (2006) http://dx.doi.org/10.1016/j.jcp.2006.01.016.

[41] C. Dan, A. Wachs, Direct numerical simulation of particulate flow with heat transfer, Int. J. Heat Fluid Flow 31 (2010) http://dx.doi.org/10.1016/j.ijheatfluidflow.2010.07.007.

[42] S. Tenneti, B. Sun, R. Garg, S. Subramaniam, Role of fluid heating in dense gas-solid flow as revealed by particle-resolved direct numerical simulation, Int. J. Mass. Transf. 58 (2013) http://dx.doi.org/10.1016/j.ijheatmasstransfer.2012.11.006.

[43] H. Tavassoli, S. Kriebitzsch, M.V. der Hoef, E. Peters, J. Kuipers, Direct numerical simulation of particulate flow with heat transfer, Int. J. Multiph. Flow. 57 (2013) http://dx.doi.org/10.1016/j.ijmultiphaseflow.2013.06.009.

[44] D. Gunn, Transfer of mass and heat to particles in fixed and fluidized beds, Int. J. Heat Mass Transfer 21 (1978) http://dx.doi.org/10.1016/0017-9310(78)90080-7.

[45] N. Deen, E. Peters, J. Padding, J. Kuipers, Review of direct numerical simulation of fluid-particle mass, momentum and heat transfer in dense gas-solid flows, Chem. Eng. Sci. 116 (2014) http://dx.doi.org/10.1016/j.ces.2014.05.039.

[46] N. Deen, J. Kuipers, Direct numerical simulation of fluid flow accompanied by coupled mass and heat transfer in dense fluid-particle systems, Chem. Eng. Sci. 116 (2014) http://dx.doi.org/10.1016/j.ces.2014.05.036.

[47] J. Derksen, Simulations of solid-liquid mass transfer in fixed and fluidized beds, Chem. Eng. J. 255 (2014) http://dx.doi.org/10.1016/j.cej.2014.06.067.

[48] Z.-G. Feng, S. Musong, Direct numerical simulation of heat and mass transfer of spheres in a fluidized bed, Powder Technol. 262 (2014) http://dx.doi.org/10.1016/j.powtec.2014.04.019.

[49] M.-A. Chadil, S. Vincent, J.-L. Estivalezes, Novel method to compute drag force and heat transfers for motions around spheres, Thermodyn. Interfaces Méc. Fluides 2 (2018) http://dx.doi.org/10.21494/ISTE.OP.2018.0299.

[50] M.-A. Chadil, S. Vincent, J.-L. Estivalezes, Gas-solid heat transfer computation from particle-resolved direct numerical simulations, Fluids 7 (2022) http://dx.doi.org/10.3390/fluids7010015.

[51] E. Thiam, Modélisation et Simulation Numérique Directe des Transferts de Chaleur dans les Écoulements Fortement Chargés en Particules (Ph.D. thesis), Université de Toulouse, 2018.

[52] C. Wen, Y. Yu, Mechanics of fluidization, Chem. Eng. Prog. Symp. Ser. 162 (1966).

[53] M. Haid, Correlations for the prediction of heat transfer to liquid-solid fluidized beds, Chem. Eng. Process. 36 (1997) http://dx.doi.org/10.1016/S0255-2701(96)04177-3.

[54] M. Lee, S. Kim, S. Kim, Experimental investigation of wall-to-bed heat transfer of carbon nanotubes in a fluidized bed, Int. J. Heat Mass Transfer 204 (2023) http://dx.doi.org/10.1016/j.ijheatmasstransfer.2023.123858.

[55] C. Calvin, O. Cueto, P. Emonot, An object-oriented approach to the design of fluid mechanics software, Math. Model. Numer. Anal. 36 (2002) http://dx.doi.org/10.1051/m2an:2002038.

[56] M. Grosso, G. Bois, A. Toutant, Thermal boundary layer modelling for heat flux prediction of bubbles at saturation: A priori analysis based on fully-resolved simulations, Int. J. Heat Mass Transfer 222 (2024) http://dx.doi.org/10.1016/j.ijheatmasstransfer.2023.124980.

[57] Y. Benarafa, O. Cioni, F. Ducros, P. Sagaut, RANS/LES coupling for unsteady turbulent flow simulation at high Reynolds number on coarse meshes, Comput. Methods Appl. Mech. Engrg. 195 (2006) http://dx.doi.org/10.1016/j.cma.2005.06.007.

[58] A. Toutant, E. Labourasse, O. Lebaigue, O. Simonin, DNS of the interaction between a deformable buoyant bubble and a spatially decaying turbulence: a priori tests for LES two-phase flow modelling, Comput. & Fluids 37 (2008) http://dx.doi.org/10.1016/j.compfluid.2007.03.019.

[59] R. Glowinsky, T. Pan, T. Hesla, D. Jospeh, J. Périaux, A fictitious domain approach to the direct numerical simulation of incompressible viscous flow past moving rigid bodies: Application to particulate flow, J. Comput. Phys. 169 (2001) http://dx.doi.org/10.1006/jcph.2000.6542.

[60] A. Ladd, Numerical simulations of particulate suspensions via a discretized Boltzmann equation. Part 1. Theoretical foundation, J. Fluid. Mech. 271 (1994) http://dx.doi.org/10.1017/S0022112094001771.

[61] H.H. Hu, N. Patankar, M. Zhu, Direct numerical simulations of fluid-solid systems using the arbitrary Lagrangian-Eulerian technique, J. Comput. Phys. 169 (1992) http://dx.doi.org/10.1006/jcph.2000.6592.

[62] S. Unverdi, G. Tryggvason, A front-tracking method for viscous, incompressible, multi-fluid flows, J. Comput. Phys. 100 (1992) http://dx.doi.org/10.1016/0021-9991(92)90307-K.

[63] J. Ritz, J. Caltagirone, A numerical continuous model for the hydrodynamics of fluid particle systems, Internat. J. Numer. Methods Fluids 30 (1999) http://dx.doi.org/10.1002/(SICI)1097-0363(19990830)30:8<1067::AID-FLD881>3.0.CO;2-6.

[64] S. Vincent, J.B. de Motta, A. Sarthou, J.-L. Estivalezes, O. Simonin, E. Climent, A Lagrangian VOF tensorial penalty method for the DNS of resolved particle-laden flows, J. Comput. Phys. 256 (2014) http://dx.doi.org/10.1016/j.jcp.2013.08.023.

[65] S. Hamidi, A. Toutant, S. Mer, F. Bataille, Assessment of a coupled VOF-Front Tracking/DEM method for simulating fluid-particles flows, Int. J. Multiph. Flow 165 (2023) http://dx.doi.org/10.1016/j.ijmultiphaseflow.2023.104467.

[66] J. Delahaye, Jump conditions and entropy sources in two-phase systems. Local instant formulation, Int. J. Multiph. Flow 1 (1974) http://dx.doi.org/10.1016/0301-9322(74)90012-3.

[67] A. Toutant, Modélisation Physique des Interactions Entre Interfaces et Turbulences (Ph.D. thesis), Institut National Polytechnique de Toulouse, 2006.

[68] D. Legendre, R. Zenit, C. Daniel, P. Guiraud, A note on the modelling of the bouncing of spherical droplets or solid spheres on a wall in viscous fluid, Chem. Eng. Sci. 61 (2006) http://dx.doi.org/10.1016/j.ces.2005.12.028.

[69] L. Verlet, Computer 'experiments' on classical fluids. I. Thermodynamical properties of Lennard-Jones molecules, Phys. Rev. 159, http://dx.doi.org/10.1103/PhysRev.159.98.

[70] X. Fang, J. Tang, H. Luo, Granular damping analysis using an improved discrete element approach, J. Sound Vib. 308, http://dx.doi.org/10.1016/j.jsv.2007.07.034.

[71] A. Xu, B.-T. Li, Particle-resolved thermal lattice Boltzmann simulation using OpenACC on multi-GPUs, Int. J. Heat Mass Transfer 218 (2024) http://dx.doi.org/10.1016/j.ijheatmasstransfer.2023.124758.

[72] O. Tange, GNU parallel - The command-line power tool, USENIX Mag. 36 (1) (2011) 42–47, URL http://www.gnu.org/s/parallel.

[73] C.B. Sullivan, A. Kaszynski, PyVista: 3D plotting and mesh analysis through a streamlined interface for the visualization toolkit (VTK), J. Open Source Softw. 4 (37) (2019) 1450, http://dx.doi.org/10.21105/joss.01450.

[74] W. Ranz, W. Marshall, Evaporation from drops - Part 1, Chem. Eng. Prog. 48 (1952).

[75] S. Whitaker, Forced convection heat transfer correlations for flow in pipes, past flat plates, single cylinders, single spheres, and for flow in packed beds and tube bundles, AIChE J. 18 (1972) http://dx.doi.org/10.1002/aic.690180219.

[76] Z.-G. Feng, E. Michaelides, A numerical study on the transient heat transfer from a sphere at high Reynolds and Peclet numbers, Int. J. Heat Mass Transfer 43 (2000) http://dx.doi.org/10.1016/S0017-9310(99)00133-7.

[77] A.T. Cate, C. Nieuwstad, J. Derksen, H.V. den Akker, Particle imaging velocimetry experiments and lattice-Boltzmann simulations on a single sphere settling under gravity, Phys. Fluids 14 (2002) http://dx.doi.org/10.1063/1.1512918.

[78] R. Bird, W. Stewart, E. Lightfoot, Transport phenomena, 1960.

[79] A.A. Corona, Agitation des Particules dans un Lit Fluidisé (Ph.D. thesis), Institut National Polytechnique de Toulouse, 2008.

[80] A. Ozel, J.B. de Motta, M. Abbas, P. Fede, O. Masbernat, S. Vincent, J.-L. Estivalezes, O. Simonin, Particle resolved direct numerical simulation of a liquid–solid fluidized bed: Comparison with experimental data, Int. J. Multiph. Flow 89 (2017) http://dx.doi.org/10.1016/j.ijmultiphaseflow.2016.10.013.

[81] A.A. Corona, R. Zenit, O. Masbernat, Collisions in a liquid fluidized bed, Int. J. Multiph. Flow 37 (2011) http://dx.doi.org/10.1016/j.ijmultiphaseflow.2011.02.004.

[82] J. Richardson, W. Zaki, The sedimentation of a suspension of uniform sphere under conditions of viscous flow, Chem. Eng. Sci. 3 (1954) http://dx.doi.org/10.1016/0009-2509(54)85015-9.

Conclusions et perspectives

Les travaux de recherche exposés dans ce mémoire portent sur les écoulements diphasiques et les transferts thermiques associés dans les technologies solaires à concentration. Ils s'inscrivent à l'interface de trois domaines scientifiques complémentaires : la mécanique des fluides, la thermique et le génie des procédés. Fondés sur une démarche multiéchelle, ils combinent des approches expérimentales et numériques afin d'étudier les phénomènes physiques mis en jeu dans ces procédés. Ces recherches ont permis d'apporter une contribution originale à la compréhension des écoulements diphasiques et des transferts de chaleur dans les technologies solaires à concentration. Les avancées obtenues ouvrent des perspectives prometteuses en vue d'améliorer l'efficacité énergétique des centrales CSP et de soutenir la décarbonation de l'industrie par l'hybridation solaire.

Mes activités de recherche couvrent une large gamme d'échelles – du procédé solaire lui-même jusqu'aux plus petites échelles d'un écoulement turbulent diphasique – et s'articulent entre *recherche appliquée* et *recherche fondamentale*. Le *"curseur"* se déplace, d'un projet à l'autre, en fonction du niveau de détail requis et des objectifs scientifiques visés. Je considère que cette double casquette constitue une force : les problématiques appliquées permettent de révéler les limites des modèles intégrés dans les codes commerciaux, tandis que les études plus fondamentales contribuent à une meilleure compréhension des phénomènes physiques et à l'élaboration de modélisations plus pertinentes. Par ailleurs, la complémentarité des approches expérimentales et numériques que je développe permet de confronter efficacement ces deux mondes, tout en produisant des bases de données expérimentales indispensables à la validation rigoureuse des modèles. Ce positionnement, à la fois multi-échelles et multi-approches, est relativement original dans les communautés internationales des CST et de la mécanique des fluides, auxquelles je m'inscris. J'espère – et je pense – qu'il permettra d'y apporter une contribution originale dans les années à venir.

Les trois principaux axes de recherche développés au cours de ces travaux ont été présentés dans les chapitres 2 à 4. Souhaitant poursuivre le développement de ces trois thématiques dans les années à venir, ce dernier chapitre est structuré en trois sections. Chacune d'elles propose un récapitulatif des travaux réalisés à ce jour, suivi des perspectives de recherche qui leur sont associées.

Écoulement bouillant horizontaux dans les récepteurs à Génération Directe de Vapeur

Les travaux menés sur les récepteurs à Génération Directe de Vapeur (GDV) ont permis de mieux caractériser les régimes d'écoulement bouillant susceptibles d'apparaître dans ces dispositifs, ainsi que leur influence sur les transferts thermiques. L'approche adoptée combine simulations numériques et développement expérimental.

L'outil de simulation thermohydraulique mis en place, basé sur les modèles développés dans l'industrie nucléaire, a été adapté aux conditions de fonctionnement spécifiques des récepteurs GDV. Son couplage à un solveur solide permet de prédire les champs de température dans la paroi et d'identifier les zones de fort gradient susceptibles de générer des contraintes thermomécaniques. Il constitue un outil puissant pour l'optimisation de la géométrie et des conditions de fonctionnement des récepteurs, et a déjà permis d'évaluer l'effet de l'inclinaison du récepteur sur les régimes d'écoulement.

En parallèle, le banc expérimental ConBo a été développé pour étudier en détail les régimes d'écoulement bouillant à basse pression dans une configuration représentative des récepteurs linéaires. Du fait de l'importante puissance requise pour évaporer un débit d'eau, peu ou pas de dispositifs semblables existent dans la littérature. L'instrumentation déployée (ombroscopie, mesures de température et de pression) permet d'établir une première cartographie des régimes en fonction des conditions opératoires.

Dans un futur proche, je souhaite poursuivre le développement de ConBo – notamment pour étoffer son instrumentation – et confronter l'outil de simulation thermohydraulique à la base de données constituée. Cela permettra d'évaluer finement la pertinence des modèles de fermeture sur lesquels repose Neptune_Cfd. Étant encore jeune au sens de l'ANR – et ce malheureusement pour la dernière année – j'ai déposé le projet JCJC SteamSun à l'AAPG2025 de l'ANR. Ce projet vient d'être accepté. Son programme de recherche constitue les perspectives à moyen terme pour cet axe et sera l'occasion de consolider des collaborations notamment avec C. Colin de l'IMFT et W. Benguigui et N. Merigoux d'EDF.

Ainsi, je souhaite faire évoluer l'instrumentation de ConBo pour mesurer le champ de fraction volumique en sortie de la TS, ainsi que les contraintes thermomécaniques auxquelles celle-ci est soumise. La mesure de fraction volumique passera par l'achat d'un *WireMesh Sensor (WMS)* commercialisé par le HZDR. Il s'agit d'un dispositif de mesure de pointe, qui donne un accès résolu en espace et en temps à α_{vap} dans un plan. Pour les mesures thermomécaniques, des jauges de contrainte seront mises en place sur la TS. Compte tenu des variations de température auxquelles elle est soumise, cette mesure devra être entreprise avec précaution. R. Reoyo Prats (MCF recrutée en 2022) apportera son expertise sur ce point. Ces développements permettront de cartographier finement tous les régimes d'écoulement, l'efficacité des transferts thermiques qui y sont associés, ainsi que les contraintes qu'ils engendrent sur le tube.

Parallèlement, l'outil de simulation thermohydraulique – basé sur un couplage entre Neptune_Cfd et Syrthes – sera utilisé pour reproduire la base de données expérimentale. Les modèles de fermeture de l'approche Euler–Euler pourront ainsi être évalués – et améliorés si nécessaire. Les champs de température obtenus dans le solide alimenteront le solveur thermomécanique Code_Aster. Les contraintes et déformations obtenues numériquement pourront alors être confrontées aux mesures expérimentales.

Lits fluidisés comme fluide caloporteur dans les CST

Sur le deuxième axe, détaillé dans le chapitre 3, les travaux menés ont permis le développement de deux bancs expérimentaux dédiés, permettant d'abord la caractérisation hydrodynamique, puis l'évaluation des performances thermiques d'un récepteur solaire innovant utilisant un lit fluidisé en circulation ascendante comme fluide caloporteur.

Dans un premier temps, l'hydrodynamique du système a été étudiée à température ambiante à l'aide du banc RALF, permettant une identification fine des régimes de fluidisation et de leurs transitions. Cette étude a posé les bases nécessaires à l'interprétation du comportement du système dans des conditions thermiques réalistes.

Grâce au dispositif RALFI, conçu pour fonctionner sous irradiation solaire concentrée, les régimes d'écoulement ont pu être observés en fonctionnement réel, et leur dépendance à la température mise en évidence. L'analyse dynamique a montré que les fluctuations de la ressource solaire peuvent être finement et dynamiquement compensées par un ajustement du débit d'aération.

Enfin, les performances thermiques du récepteur ont été évaluées. Le coefficient de transfert thermique adimensionnel $H_{\text{paroi,part}}$ a permis de comparer les performances associées aux différents régimes de fluidisation. Il ressort que le régime de fluidisation turbulente offre les meilleures performances en termes d'évacuation de la chaleur. Ce régime est donc à privilégier pour l'exploitation de ce type de récepteur.

Les perspectives à moyen terme associées à cet axe concernent principalement le volet numérique de mes recherches. Dans le cadre des projets européens P2P et ANR SICSUN, nous prévoyons d'adapter l'outil de simulation thermohydraulique présenté dans le chapitre 2 aux écoulements gaz-particules. En effet, NEPTUNE_CFD est également utilisé, notamment par la communauté IMFT/LGC toulousaine initiée par O. Simonin, pour simuler des lits fluidisés. Dans ce contexte, les modèles de fermetures interfaciaux se limitent à une traînée et à des équations de transport pour les variables scalaires et les grandeurs turbulentes (modèle $q_p - q_{fp}$, par exemple) [4]. Les modèles implémentés dans NEPTUNE_CFD permettent de reproduire le comportement de particules de tailles relativement élevées – de type B selon la classification de Geldart [26]. En revanche, pour des particules plus fines – de type A selon Geldart, telles que celles utilisées pour les expériences du chapitre 3 – l'approche actuelle tend à surestimer l'expansion du mélange [79]. Pour contourner ce problème – induit par les plus petites échelles de l'écoulement – nous introduirons un terme sous-maille appliqué aux mélanges gaz-particules. Plus précisément, un terme de vitesse de dérive sous-maille est ajouté pour corriger la vitesse relative entre les phases utilisée dans la loi de traînée. Cette correction permet de reproduire de manière satisfaisante l'expansion de lit pour des particules de type A [73, 19].

Le couplage thermo-hydraulique avec SYRTHES n'a toutefois jamais été mis en place, à notre connaissance. L'aptitude de l'outil à reproduire la base de données consolidée dans le chapitre 3 sera donc évaluée. Si nécessaire, la modélisation du coefficient d'échange thermique entre le lit fluidisé et la paroi pourra être ajustée dans NEPTUNE_CFD.

Par ailleurs, dans le cadre de l'ANR SICSUN, un postdoctorat débutera à l'automne 2025 pour mettre en place cet outil et simuler des récepteurs solaires tubulaires en carbure de silicium (SiC), qui seront testés expérimentalement dans le cadre du projet. Sans entrer dans les détails, le SiC est un matériau céramique réfractaire capable de supporter des températures très élevées. La conception d'un récepteur solaire en SiC devrait ainsi permettre d'atteindre des températures

de sortie des particules avoisinant $800\,°C$. Aucune simulation thermo-hydraulique de ce genre de récepteur n'existe dans la littérature à notre connaissance.

En parallèle, la thèse de K. Bachir-Brahim – débutée en novembre 2024, financé par les projets UE P2P et PEPR SHIP4D et co-encadrée avec A. Toutant et R. Ansart du LGC – participera à mise en place de cet outil pour optimiser géométriquement l'échangeur de chaleur qui transfère l'énergie des particules chaudes au fluide de travail du cycle thermodynamique dans une centrale CSP (voir Fig. 1.1). Cet échangeur, basé sur une architecture de type tube-calandre, est conçu de manière à ce que les particules fluidisées s'écoulent à travers différents compartiments successifs, où elles échangent de la chaleur avec un faisceau de tubes dans lequel circule le fluide de travail. L'objectif applicatif de la thèse est d'optimiser numériquement la répartition géométrique des tubes afin de maximiser les transferts thermiques.

Modélisation résolue d'écoulement fluide-particules anisotherme

Enfin, dans le chapitre 4, nous avons présenté les travaux menés autour du développement d'un modèle numérique dédié à la simulation résolue d'écoulements fluide-particules anisothermes. L'approche, implémentée dans le code Trio_CFD, repose sur une méthode originale combinant une description eulérienne du fluide avec une représentation lagrangienne des particules via un suivi d'interface de type *Front-Tracking*.

L'ensemble des briques numériques nécessaires à la simulation d'écoulements fluide-particules complexes a été progressivement mis en place : modification de la méthode de suivi d'interfaces pour les objets non déformables, pénalisation visqueuse pour imposer un tenseur des taux de déformation nul dans les particules, modélisation des collisions entre particules et entre particules et parois, et enfin prise en compte des effets thermiques. Ces développements ont été validés sur une large base de cas tests issus de la littérature, allant de la sédimentation d'une particule isolée à la simulation d'un lit fluidisé comportant plus de 2000 particules.

Les méthodes développées ont été appliquées à trois échelles de modélisation différentes dites :

- ▷ *Particle Resolved – Direct Numerical Simulation* (PR-DNS),
- ▷ *Particle Resolved – Subgrid Corrected Simulation* (PR-SCS),
- ▷ *Particle Resolved Simulation* (PRS).

Dans un objectif de remontée d'échelle, l'approche intermédiaire baptisée PR-SCS a été développée pour des cas mono-particule. Elle permet de corriger les biais introduits par la sous-résolution des gradients hydrodynamiques et thermiques autour de la particule, tout en maintenant un coût numérique raisonnable. Plusieurs verrous de modélisation empêchent encore son utilisation pour des cas multi-particules. Une approche PRS a donc été appliquée pour simuler des des lits fluidisés anisothermes liquide solide. Cette approche a permis de prédire avec une bonne précision les transferts thermiques à la paroi et au sein du lit, en accord avec les corrélations de la littérature.

Ces travaux posent les fondations d'une approche prédictive pour l'analyse fine des transferts de quantité de mouvement et de chaleur dans les suspensions gaz-particules représentatives des récepteurs solaires détaillés dans le chapitre 3.

Les perspectives associées à ces travaux sont nombreuses. Elles peuvent être décomposées en deux volets : un volet de développement méthodologique – visant à inclure autant que possible

les phénomènes physiques prépondérants pour les récepteurs solaires dans nos simulations – et un volet d'études physiques – visant à caractériser et comprendre les transferts dans les lits fluidisés gaz-solides utilisés dans les récepteurs solaires grâce à l'outil mis en place.

Sur le volet méthodologique, plusieurs axes d'amélioration sont envisagés :

- ▷ Actuellement, les particules représentent un puits thermique dans nos simulations. Leur température est homogène et invariante dans le temps. Pour retranscrire le chauffage des particules par les parois dans un récepteur solaire, nous souhaitons faire évoluer la description thermique des particules. Bien que la température d'une particule reste homogène spatialement, elle pourra désormais varier au cours du temps en fonction du flux de chaleur local reçu. Cela nécessite de mesurer précisément le flux de chaleur reçu par chaque facette d'une particule, de les sommer pour calculer le flux net absorbé par la particule, et de faire évoluer sa température en conséquence (en tenant compte de son inertie thermique).
- ▷ Toujours sur le plan thermique, nous souhaitons évaluer l'importance des transferts radiatifs dans nos configurations d'écoulement. La distribution de flux de chaleur extrait à la paroi présentée en Fig. 4.8 ne prend en compte que les transferts conducto-convectifs. *Quelle est l'importance relative des transferts radiatifs ? Dans ce milieu opaque, jusqu'à quelle distance caractéristique de la paroi une particule échange-t-elle par rayonnement ? Comment cette distance évolue-t-elle avec la fraction volumique de particule et donc la vitesse de fluidisation ?* Pour apporter des éléments de réponse à ces questions, nous utiliserons le logiciel de simulation Monte Carlo Stardis [9]. Pour une distribution spatiale donnée de particules, nous chercherons à évaluer le flux radiatif net échangé entre chaque particule et la paroi. Dans un premier temps, nous supposerons que la paroi et les particules sont des corps noirs, puis nous adapterons la description pour les représenter comme des corps gris qui n'absorbent qu'une partie de l'énergie reçue. En fonction du temps de calcul associé à ces simulations, un couplage dynamique entre les deux codes pourra être envisagé.
- ▷ Jusqu'à présent, nous n'avons simulé que des particules sphériques. Or, les particules utilisées dans les lits fluidisés – généralement obtenues par concassage puis broyage – sont loin de l'être. De plus, la méthode de *Front-Tracking* que nous utilisons pour le suivi d'interface est particulièrement bien adaptée – grâce au maillage lagrangien suivant l'interface – pour traiter des objets de formes quelconques. Nous souhaitons donc adapter notre outil pour qu'il puisse simuler des particules de forme ellipsoïdale. Les deux principaux défis associés à cette modification sont : (i) la détection efficace des collisions entre deux ellipsoïdes et (ii) l'adaptation du traitement des collisions pour tenir compte du moment engendré par ces interactions sur les particules.

Ces différentes perspectives sont d'ores et déjà initiées dans le cadre respectif de la thèse d'A. Labat, du postdoctorat de J. Djeumegni (en collaboration avec C. Caliot – CR LMAP) et du postdoctorat de T. Devos (en collaboration avec S. Abides – Pr. Univ. Nice).

Parallèlement à ces développements méthodologiques, l'outil mis au point permet désormais de réaliser des simulations massivement parallèles de configurations physiques complexes d'écoulement fluide-particules anisotherme. Nous souhaitons ainsi étudier les transferts thermiques (au minimum conducto-convectifs) dans les lits fluidisés gaz-solides dans le cadre de la thèse d'A. Labat. Pour ce faire, des lits fluidisés impliquant jusqu'à 8000 particules seront simulés. Les statistiques issues de ces simulations permettront d'évaluer l'hydrodynamique ainsi que les transferts thermiques lit–paroi et gaz-particule dans ces configurations. À plus long terme, ces

résultats pourront alimenter, par remontée d'échelle, les simulations gaz-particules réalisées avec NEPTUNE_CFD dans le volet précédent. Enfin, dans le cadre du postdoctorat de T. Devos, l'effet de la non-sphéricité des particules sur la dynamique d'un lit fluidisé et sur les transferts thermiques associés sera évalué.

Bibliographie

[1] I. Aguilera-Cortes, A. Toutant et S. Mer – 2025 – *"Numerical investigation of tilt angle effect on a Direct Steam Generation solar receiver"* – Solar Energy , 287

[2] A. K. Araújo, J. C. Passos, T. P. Ferreira et C. W. van der Geld – 2024 – *"Heat transfer characteristics of horizontal flow boiling with uniform and non-uniform circumferential heat flux"* – International Journal of Heat and Mass Transfer , 228

[3] F. M. Beckett, H. M. Mader, J. C. Phillips, A. C. Rust et F. Witham – 2011 – *"An experimental study of low-Reynolds-number exchange flow of two Newtonian fluids in a vertical pipe"* – Journal of Fluid Mechanics , 682

[4] H. Benoit, R. Ansart, H. Neau, P. Garcia Triñanes, G. Flamant et O. Simonin – 2018 – *"Three-dimensional numerical simulation of upflow bubbling fluidized bed in opaque tube under high flux solar heating"* – AIChE Journal , 64

[5] B. Bigot, T. Bonometti, L. Lacaze et O. Thual – 2014 – *"A simple immersed-boundary method for solid-fluid interaction in constant- and stratified-density flows"* – Computers and Fluids , 97

[6] E. Butaye, R. Quintana, S. Mer, F. Bataille et A. Toutant – 2025 – *"Investigation of heat transfers with particle-resolved simulations : From Stokes flow to fluidized bed"* – International Journal of Heat and Mass Transfer , 241

[7] E. Butaye, A. Toutant et S. Mer – 2023 – *"Euler–Euler multi-scale simulations of internal boiling flow with conjugated heat transfer"* – Applied Mechanics , 4

[8] E. Butaye, A. Toutant, S. Mer et F. Bataille – 2023 – *"Development of Particle Resolved - Subgrid Corrected Simulations : Hydrodynamic force calculation and flow subresolution corrections"* – Computers and Fluids , 267

[9] C. Caliot, L. D'Alençon, S. Blanco, V. Forest, R. Fournier, F. Hourdin, F. Retailleau, R. Schoetter et N. Villefranque – 2024 – *"Coupled heat transfers resolution by Monte Carlo in urban geometry including direct and diffuse solar irradiations"* – International Journal of Heat and Mass Transfer , 222

[10] A. T. Cate, C. Nieuwstad, J. Derksen et H. V. den Akker – 2002 – *"Particle imaging velocimetry experiments and lattice-Boltzmann simulations on a single sphere settling under gravity"* – Physics of Fluids , 14

[11] M.-A. Chadil, S. Vincent et J.-L. Estivalezes – 2018 – *"Accurate estimate of drag forces using particle-resolved direct numerical simulations"* – Acta Mechanica , 230

[12] M. Colombo et M. Fairweather – 2025 – *"Prediction of bubbly flow and flow regime development in a horizontal air-water pipe flow with a morphology-adaptive multifluid CFD model"* – International Journal of Multiphase Flow , 184

[13] T. Conroy, M. N. Collins et R. Grimes – 2020 – *"A review of steady-state thermal and mechanical modelling on tubular solar receivers"* – Renewable and Sustainable Energy Reviews , 119

[14] A. A. CORONA, R. Zenit et O. Masbernat – 2011 – *"Collisions in a liquid fluidized bed"* – International Journal of Multiphase Flow , 37

[15] P. Coste – 2013 – *"A large interface model for two-phase CFD"* – Nuclear Engineering and Design , 255

[16] G. Davy, E. Reyssat, S. Vincent et S. Mimouni – 2022 – *"Euler–Euler simulations of condensing two-phase flows in mini-channel : Combination of a sub-grid approach and an interface capturing approach"* – International Journal of Multiphase Flow , 149

[17] N. Deen, M. V. S. Annaland, M. V. der Hoef et J. Kuipers – 2007 – *"Review of discrete particle modeling of fluidized beds"* – Chemical Engineering Science , 62

[18] R. Denèfle, S. Mimouni, J.-P. Caltagirone et S. Vincent – 2015 – *"Multifield hybrid approach for two-phase flow modeling - Part 1 : Adiabatic flows"* – Computers and Fluids , 113

[19] Y. Deng, F. Sabatier, R. Dewil, G. Flamant, A. Le Gal, R. Gueguen, J. Baeyens, S. Li et R. Ansart – 2021 – *"Dense upflow fluidized bed (DUFB) solar receivers of high aspect ratio : Different fluidization modes through inserting bubble rupture promoters"* – Chemical Engineering Journal , 418

[20] J. Dirker, H. Scheepers et J. P. Meyer – 2022 – *"The effect of circumferentially non-uniform heat flux on flow boiling heat transfer in a horizontal tube"* – International Journal of Heat and Mass Transfer , 185

[21] D. Dupuy, R. Ansart et O. Simonin – 2024 – *"Investigation of near-wall particle statistics in CFD-DEM simulations of dense fluidised beds and derivation of an Eulerian particle dynamic wall boundary condition"* – Journal of Fluid Mechanics , 982

[22] D. Dupuy, Y. Badran, R. Ansart et O. Simonin – 2024 – *"Calibrating the frictional-pressure model from two-fluid simulation of fluidised beds in the defluidisation regime"* – Powder Technology , 441

[23] L. Favre, C. Colin, S. Pujet et S. Mimouni – 2023 – *"An updated force balance approach to investigate bubble sliding in vertical flow boiling at low and high pressures"* – International Journal of Heat and Mass Transfer , 211

[24] Z.-G. Feng et E. Michaelides – 2000 – *"A numerical study on the transient heat transfer from a sphere at high Reynolds and Peclet numbers"* – International Journal of Heat Mass Transfer , 43

[25] S. Fleau, S. Mimouni, N. Merigoux et S. Vincent – 2016 – *"Validation of a multifield approach for the simulations of two-phase flows"* – Computational Thermal Sciences , 7

[26] D. Geldart – 1973 – *"Types of Gas Fluidization"* – Powder Technology , 7

[27] L. Gilman et E. Baglietto – 2017 – *"A self-consistent, physics-based boiling heat transfer modeling framework for use in computational fluid dynamics"* – International Journal of Multiphase Flow , 95

[28] P. Gondret, M. Lance et L. Petit – 2002 – *"Bouncing motion of spherical particles in fluids"* – Physics of Fluids , 14

[29] B. Grange, A. Ferrière, D. Bellar, M. Vrinat, R. Couturier, F. Pra et Y. Fan – 2011 – *"Thermal Performances of a hight temperature air solar absorber based on compact heat exchange technology"* – Journal of Solar Energy Engineering , 133

[30] M. Grosso, G. Bois et A. Toutant – 2024 – *"Thermal boundary layer modelling for heat flux prediction of bubbles at saturation : A priori analysis based on fully-resolved simulations"* – International Journal of Heat Mass Transfer , 222

[31] R. Gueguen, S. Mer, A. Toutant, F. Bataille et G. Flamant – 2023 – *"Effect of temperature on the hydrodynamics of a fluidized bed circulating in a long tube for a solar energy harvesting application"* – Chemical Engineering Science , 281

[32] R. Gueguen et al. – 2023 – *"Heat transfer in a fluidized bed tubular solar receiver. On-sun experimental investigation"* – Solar Energy , 265

[33] M. Haid – 1997 – *"Correlations for the prediction of heat transfer to liquid-solid fluidized beds"* – Chemical Engineering and Processing: Process Intensification , 36

[34] M. S. Hamidi, A. Toutant, S. Mer et F. Bataille – 2023 – *"Assessment of a coupled VOF-Front-Tracking/DEM method for simulating fluid–particles flows"* – International Journal of Multiphase Flow , 165

[35] S. Hansch, D. Lucas, E. Krepper et T. Hohne – 2012 – *"A multi-field two-fluid concept for transitions between different scales of interfacial structures"* – International Journal of Multiphase Flow , 47

[36] B. K. Hardik et S. V. Prabhu – 2016 – *"Boiling pressure drop and local heat transfer distribution of water in horizontal straight tubes at low pressure"* – International Journal of Thermal Sciences , 110

[37] M. van der Hoef, M. Ye, M. van Sint Annaland, A. A. IV, S. Sundaresan et J. Kuipers – 2006 – *"Multiscale modeling of Gas-Fluidized Beds"* – Advances in Chemical Engineering , 31

[38] A. Hoffmann, E. Schleicher, L. Keller, J. León Alonso et R. Pitz-Paal – 2018 – *"Application of a single wire-mesh sensor in a parabolic trough facility with direct steam generation"* – Solar Energy , 159

[39] T. Höhne, E. Krepper, D. Lucas et G. Montoya – 2019 – *"A Multiscale Approach Simulating Boiling in a Heated Pipe Including Flow Pattern Transition"* – Nuclear Technology , 205

[40] T. Höhne, E. Krepper, G. Montoya et D. Lucas – 2017 – *"CFD-simulation of boiling in a heated pipe including flow pattern transitions using the GENTOP concept"* – Nuclear Engineering and Design , 322

[41] ID Partner. Austenitic or ferritic stainless steel, induction heating efficiency. - . Accessed : 2025-02-10. 2025.

[42] International Renewable Energy Agency. Renewable energy technologies : capacity and generation. - . Accessed : 2025-03-25. 2022.

[43] IPCC – Climate Change 2023: Synthesis Report. Contribution of Working Groups I, II and III to the Sixth Assessment Report of the Intergovernmental Panel on Climate Change , 2023

[44] M. Ishii et T. Hibiki – Thermo-Fluid Dynamics of Two-Phase Flow , 2006

[45] D. D. Joseph, R. Bai et K. P. Chen – 1997 – *"CORE-ANNULAR FLOWS"* – Annual Review of Fluid Mechanics , 29

[46] R. R. Kerswell – 2011 – *"Exchange flow of two immiscible fluids and the principle of maximum flux"* – Journal of Fluid Mechanics , 682

[47] H. A. Khawaja – 2011 – *"CFD-DEM Simulation of Minimum Fluidisation Velocity in Two Phase Medium"* – International Journal of Multiphysics , 5

[48] N. Kurul et M. Z. Podowski in: Proceeding of International Heat Transfer Conference 9 , 1990

[49] Kyotherm. Vapeur Solaire pour la brasserie Heineken de Valence (Espagne) - . 2024.

[50] A. Le Gal, B. Grange, M. Casanova, A. Perez, W. Baltus, M. Tessonneaud et G. Flamant – 2023 – *"Experimental results for a MW-scale fluidized particle-in-tube solar receiver in its first test campaign"* – Solar Energy , 262

[51] D. Legendre, R. Zenit, C. Daniel et P. Guiraud – 2006 – *"A note on the modelling of the bouncing of spherical droplets or solid spheres on a wall in viscous fluid"* – Chemical Engineering Science , 61

[52] Q. Li, N. G. de Tourville, I. Yadroitsev, X. Yuan et G. Flamant – 2013 – *"Micro-channel pressurized-air solar receiver based on compact heat exchanger concept"* – Solar Energy , 91

[53] D. H. Lobón, E. Baglietto, L. Valenzuela et E. Zarza – 2014 – *"Modeling direct steam generation in solar collectors with multiphase CFD"* – Applied Energy , 113

[54] J. Magnaudet, H. Bruhier, S. Mer et T. Bonometti – *"Rational constitutive law for the viscous stress tensor in incompressible two-phase flows : Derivation and tests against a benchmark experiment"*, submitted

[55] F. Marchelli, L. Fiori et R. D. Felice – 2024 – *"Cohesive particle-fluid systems : An overview of their CFD simulation"* – The Canadian Journal of Chemical Engineering , 103

[56] M. Maxey – 2017 – *"Simulation Methods for Particulate Flows and Concentrated Suspension"* – Annual Review of Fluid Mechanics , 49

[57] S. Mer, D. Fernandez, J. P. Thibault et C. Corre – 2016 – *"Optimal design of a Thermodynamic Vent System for cryogenic propellant storage"* – Cryogenics , 80

[58] S. Mer, O. Praud, J. Magnaudet et V. Roig – 2019 – *"Emptying of a bottle : How a robust pressure-driven oscillator coexists with complex two-phase flow dynamics"* – International Journal of Multiphase Flow , 118

[59] S. Mer, O. Praud, H. Neau, N. Merigoux, J. Magnaudet et V. Roig – 2018 – *"The emptying of a bottle as a test case for assessing interfacial momentum exchange models for Euler-Euler simulations of multi-scale gas-liquid flows"* – International Journal of Multiphase Flow , 106

[60] S. Mer, J.-P. Thibault et C. Corre – 2016 – *"Active Insulation Technique Applied to the Experimental Analysis of a Thermodynamic Control System for Cryogenic Propellant Storage"* – Journal of Thermal Science and Engineering Applications , 8

[61] S. Mer, J.-P. Thibault et C. Corre – 2017 – *"Influence of non-condensable gases on self-pressurization and thermodynamic control experiments in a tank filled with a liquid and its vapor"* – Journal of Thermal Science and Engineering Applications , 10

[62] E. Montanet, S. Rodat, Q. Falcoz et F. Roget – 2023 – *"Influence of topography on the optical performances of a Fresnel linear asymmetrical concentrator array : The case of the eLLO solar power plant"* – Energy , 274

[63] G. Montoya, D. Lucas, E. Baglietto et Y. Liao – 2016 – *"A review on mechanisms and models for the churn-turbulent flow regime"* – Chemical Engineering Science , 141

[64] National Renewable Energy Laboratory. Concentrating Solar Power Projects Operational - . Accessed : 2025-05-05.

[65] A. Ozel, P. Fede et O. Simonin – 2013 – *"Development of filtered Euler–Euler two-phase model for circulating fluidised bed : High resolution simulation, formulation and a priori analyses"* – International Journal of Multiphase Flow , 55

[66] R. K. Pal et K. Ravi – 2021 – *"Thermo-hydrodynamic modeling of flow boiling through the horizontal tube using Eulerian two-fluid modeling approach"* – International Journal of Heat and Mass Transfer , 168

[67] R. K. Pal et K. Ravi – 2021 – *"Two-fluid modeling of direct steam generation in the receiver of parabolic trough solar collector with non-uniform heat flux"* – Energy , 226

[68] G. Pianet, A. T. Cate, J. Derksen et E. Arquis – 2007 – *"Assessment of the 1-fluid method for DNS of particulate flows : Sedimentation of a single sphere at moderate to high Reynolds numbers"* – Computers and Fluids , 36

[69] M. Ploquin, S. Mer, A. Toutant et F. Roget – 2022 – *"CFD investigation of level fluctuations in steam accumulators as thermal storage : A direct steam generation application"* – Solar Energy , 245

[70] W. Ranz et W. Marshall – 1952 – *"Evaporation from drops - Part 1"* – Chemical Engineering Progress , 48

[71] C. Reiss, A. Gerschenfeld et C. Colin – 2024 – *"Heat flux partition based on onset of significant void"* – International Journal of Multiphase Flow , 181

[72] J. Ritz et J. Caltagirone – 1999 – *"A numerical continuous model for the hydrodynamics of fluid particle systems"* – International Journal for Numerical Methods in Fluids , 30

[73] F. Sabatier, R. Ansart, H. Zhang, J. Baeyens et O. Simonin – 2020 – *"Experiments support simulations by NEPTUNE CFD Code in a Upflow Bubbling Fluidized Bed reactor"* – Chemical Engineering Journal , 385

[74] H. Sweeney, R. R. Kerswell et T. Mullin – 2013 – *"Rayleigh-Taylor instability in a finite cylinder : Linear stability analysis and long-time fingering solutions"* – Journal of Fluid Mechanics , 734

[75] Y. Taitel et A. E. Dukler – 1976 – *"A model for predicting flow regime transitions in horizontal and near horizontal gas-liquid flow"* – AIChE Journal , 22

[76] S. Tenneti et S. Subramaniam – 2014 – *"Particle-Resolved Direct Numerical Simulation for Gas-Solid Flow Model Development"* – Annual Review of Fluid Mechanics , 46

[77] TOPCSP. UE - Horizon - MSCA - Doctoral Network (101072537) - . 2022.

[78] S. Vincent, J. B. de Motta, A. Sarthou, J.-L. Estivalezes, O. Simonin et E. Climent – 2014 – *"A Lagrangian VOF tensorial penalty method for the DNS of resolved particle-laden flows"* – Journal of Computational Physics , 256

[79] J. Wang – 2009 – *"A Review of Eulerian Simulation of Geldart A Particles in Gas-Fluidized Beds"* – Industrial and Engineering Chemistry Research , 48

[80] S. Whitaker – 1972 – *"Forced convection heat transfer correlations for flow in pipes, past flat plates, single cylinders, single spheres, and for flow in packed beds and tube bundles"* – AIChE Journal , 18

[81] L. Wojtan, T. Ursenbacher et J. R. Thome – 2005 – *"Investigation of flow boiling in horizontal tubes : Part I - A new diabatic two-phase flow pattern map"* – International Journal of Heat and Mass Transfer , 48

[82] L. Wojtan, T. Ursenbacher et J. R. Thome – 2005 – *"Investigation of flow boiling in horizontal tubes : Part II - Development of a new heat transfer model for stratified-wavy, dryout and mist flow regimes"* – International Journal of Heat and Mass Transfer , 48

[83] Z. Yang, X. F. Peng et P. Ye – 2008 – *"Numerical and experimental investigation of two phase flow during boiling in a coiled tube"* – International Journal of Heat and Mass Transfer , 51

[84] M. Zastawny, G. Mallouppas, F. Zhao et B. Wachem – 2012 – *"Derivation of drag and lift force and torque coefficients for non-spherical particles in flows"* – International Journal of Multiphase Flow , 39

[85] T. Zhang, Z. J. Ooi, M. Skrzypek et C. S. Brooks – 2020 – *"A multi-dimensional dataset for two-phase instability in low pressure natural circulation based on direct transient local measurement"* – International Journal of Heat and Mass Transfer , 151

[86] L. Zhou, W. Lv, L. Bai, Y. Han, J. Wang, W. Shi et G. Huang – 2022 – *"CFD-DEM study of gas-solid flow characteristics in a fluidized bed with different diameter of coarse particles"* – Energy Reports , 8

Annexes

Annexe A

Curriculum Vitae détaillé

A.1 Renseignements généraux

Nom Mer
Prénom Samuel (♂)
Né le 27 mai 1990 à Annonay (07) – France
Pacsé, 2 enfants

Grade Maître de Conférences - CN
CNU Section 62 – Energétique, génie des procédés
Université de Perpignan Via Domitia
Département Science Physiques pour l'Ingénieur
Laboratoire PROMES-CNRS – UPR 8521
04 68 68 22 38
samuel.mer@univ-perp.fr

HAL 19638
ORCID 0000-0001-7915-3146
ResearchGate Samuel_Mer

A.2 Déroulement de carrière & Formation

2024 – 2027 Récipiendaire de la prime **RIPEC-C3**

2019 – prés. **Maître de conférences,** 🏛 Université de Perpignan Via Domitia
Laboratoire : PROMES – UPR CNRS 8521 – Site de Perpignan
Thème de recherche : Centrales Solaires de Prochaines Générations (CSPG)
En intégrant le laboratoire PROMES, mes activités de recherche ont évolué pour se concentrer sur l'étude des écoulements diphasiques dans les récepteurs solaires.

2019 **Post-doctorat II** – 6 mois – 🏛 Institut de Mécanique des Fluides de Toulouse
Modélisation d'écoulements diphasiques visqueux en configuration instable dans une conduite verticale.
Collab. : T. Bonometti & J. Magnaudet – Financ. : Institut Carnot ISIFoR

2017 – 2018 **Post-doctorat I** – 24 mois – 🏛 Institut de Mécanique des Fluides de Toulouse.
Hydrodynamique de cavités immergées.
Collab. : O. Praud, J. Magnaudet & V. Roig – Financ. : Naval Group

2013 – 2016 🎓 **Doctorat en Mécanique des fluides et énergétique** – 36 mois
🏛 Université Grenoble Alpes – Laboratoire LEGI
Stockage d'ergol cryogénique pour l'exploration spatiale : étude expérimentale, modélisation et optimisation d'un système de contrôle thermodynamique à échappement.
Encad. : J.P. Thibault & C. Corre – Financ. : CNES & ALAT

2010 – 2013 🎓 **Diplôme d'ingénieur** – mention Bien, *Mécanique et Energétique*,
🏛 École Nationale Supérieure de l'Energie, l'Eau et l'Environnement (ENSE^3) – Grenoble INP

2011 – 2012 **Master 1**, *Fluid Mechanics*, 🏛 Lund University – LTH, Suède.

A.3 Synthèse des activités d'enseignements

Depuis mon arrivée à l'UPVD j'interviens dans quatre formations du département *Science Physiques pour l'Ingénieur (SPI)* : l'école d'ingénieur Sup'EnR, le master énergie solaire, la licence 3 (SPI/PC) et le master international EUREC basé à Odeillo. Comme le montre la Fig. A.1, mes enseignements portent principalement sur l'informatique et les outils numériques (programmation en python et différences finies), la thermique (stockage thermique et TP), l'énergétique (conversion thermique de l'énergie solaire et TP) et la mécanique des fluides (TD et TP et un nouveau cours CM/TD depuis cette année). Cette représentation met également en évidence la répartition CM/TD/TP pour chaque année. Ma charge moyenne annuelle s'élève à $212\,h/an$.

J'utilise dans mes enseignements différentes méthodes de pédagogie active pour stimuler l'intérêt des étudiants. Afin de favoriser un processus d'amélioration continue, chacun de mes cours se conclut par une enquête de satisfaction. De plus, je participe activement au développement du pool de TP mécanique et énergétique - notamment en collaboration avec M. Perier-Muzet. Nous avons ainsi acheté des nouveaux banc de TP et produit les sujets associés mais également créé et remis à jours des bancs de TP en collaboration avec les collègues de l'atelier de PROMES et du département SPI. Nous avons également mis en place une collaboration avec le lycée technique de Prades pour la conception de châssis de TP solaire.

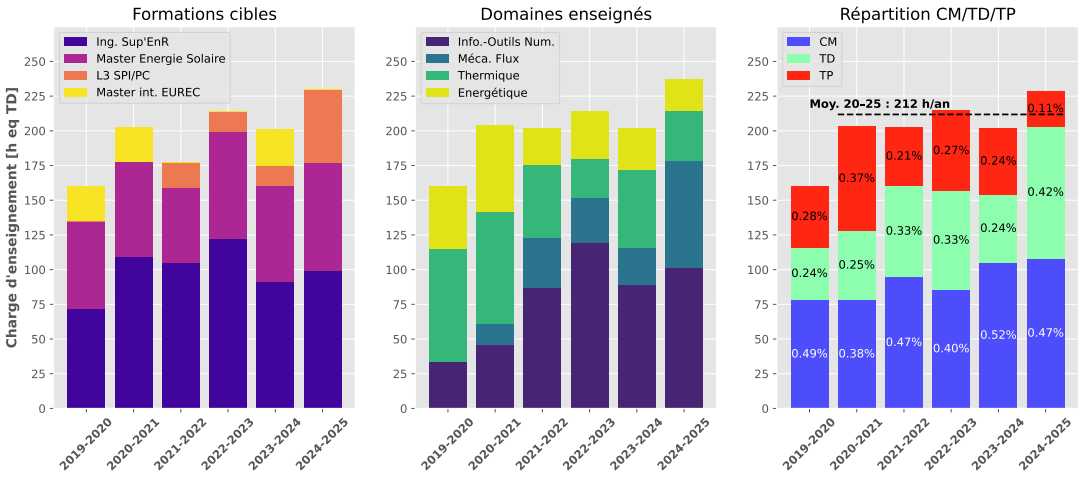

FIGURE A.1 – Représentation graphique de l'évolution de ma charge d'enseignement à l'UPVD

Enfin, j'ai à cœur de participer activement à la vie des formations où j'enseigne. Ainsi, comme le montre la Sec. A.4.1, je m'implique dans les taches d'intérêt général associées au bon fonctionnement de chacune d'elles.

A.4 Synthèse des responsabilités collectives et d'intérêt général

A.4.1 Liées à l'enseignement

Responsabilités administratives

2022 – prés. **Responsable de l'alternance et de la formation continue** à **Sup'EnR**. Ouveture de la 5ème année au contrat de professionnalisation depuis la rentré 2024. Un cursus alternant sur le cycle ingénieur complet ouvrira à la rentrée 2026.

2023 – prés. Membre du **Comité de Direction** de l'école d'ingénieur **Sup'EnR** – *Freq. : 1 CoDir par mois*

2024 – 2025 Participation au montage du projet **MECENE** (France 2030 CMA), porté par l'Université de Montpellier et l'École Centrale Méditerranée, qui vise à **développer l'offre de formation en lien avec l'éolien off-shore (EOF)** – de BAC-3 à BAC+5 – sur le pourtour méditerranéen. Le projet regroupe 7 partenaires académiques, 3 campus métier, un CFA, un lycée, un ITE, et des partenaires industriels. L'aide totale demandée est de 10 M€ dont 450 k€ pour le montage d'un module de formation EOF à **Sup'EnR** – *[déposé en phase 2 en mars 2025]*

Responsabilités pédagogiques

2020 – prés. Membre du **jury du M1 & du M2 Energie Solaire** UPVD - *Freq. : 2 jury par semestre*

2022 – prés. **Tuteur académique** de 2 alternants/an du **Master Energie Solaire** de l'UPVD - *Freq. : 3 visites de suivi par an et par alternant*

Investissement dans la vie des formations

2024 – 2025 Membre du **groupe de travail** sur la refonte de la maquette du cycle ingénieur Sup'EnR

2023 Membre du **groupe de travail** sur la refonte de la maquette de la L3 SPI-EM

2023 – 2024 Membre actif de la mise en place de la **valorisation de l'engagement associatif** des étudiants à **Sup'EnR** - *2 réunions avec les étudiants et préconisation au CoDir*

2023 – prés. Membre actif de la mise en place de l'**approche par compétence** au **master Energie Solaire** – **Référent compétence : BC03** - *Freq. : 3 réunion par semestre*

2019 – prés. Développement actif du pool de Travaux Pratiques de la **plateforme de TP Mécanique Energétique** de Sup'EnR et du master Energie

Rayonnement des formations

2024 – 2025 Promotion de l'école d'ingénieur **Sup'EnR** au salon InfoSup - Toulouse

2023 – 2024 Promotion de l'école d'ingénieur **Sup'EnR** au salon EnerGaïa - Montpellier

2022 – 2024 **Représentant** de **Sup'EnR** au **Comité de pilotage Numérique INSA Partenaires** dans le cadre du projet INSA2025 dédié entre autres aux **pédagogies innovantes** et au développement de **services numériques globaux pour l'apprenant** – *Freq. : 1 CoPil par trimestre*

2020 – 2021 **Partenariat** avec la filière *Bac pro modélisation et prototypage 3D* du lycée professionnel *Charles Renouvier* de Prades (66) pour la **conception de châssis pour des TP solaires**

A.4.2 Liées à la recherche

Responsabilités administratives

2025 – prés. **Membre** de l'équipe KCT (*Knowledge Creation Teams*) de l'UPVD – pour la thématique *"gestion des ressources naturelles dans le contexte du changement global, y compris l'invention, le développement et l'application de nouvelles technologies"* – au sein du projet Européen **ACROSS** pour le partage des savoirs transfrontaliers

2023 – prés. **Co-Responsable** de la Cellule d'Animation Scientifique et de Communication Interne (**CASCI**) du laboratoire PROMES - *Organisation d'un séminaire par mois*

2021 – prés. **Représentant élu** des Chercheurs et Enseignants-Chercheurs permanents (45 pers.) au **Conseil d'Unité** du laboratoire PROMES

Rayonnement

2023 **Organisation** de la réunion de lancement du projet européen **TOPCSP** les 16 et 17 Octobre 2023 - 24 participants - Programme

2022– prés. **Membre** du **GdR TansInter**

2024– prés. **Membre** du **GdR Tamarys**

2018 Membre du comité d'**organisation** de la **conférence** *Dispersed Two-Phase Flows* organisée par V. Roig et M. Guingo avec la Société Hydrotechnique de France à Toulouse du 17 au 19 Septembre 2018

Vulgarisation scientifique

2023 **Création et animation** d'un **atelier** pour la **Fête de la science** intitulé : Du sable sous le soleil : Récepteur solaire à lit fluidisé en circulation ascendante

2022 - 2023 **Organisation** d'une **visite du four solaire** d'Odeillo pour les étudiants de 2ème année du département *Mécanique des fluides* de l'**ENSEEIHT** de Toulouse (62 étudiants + 2 enseignants)

Expertise scientifique

2017 – prés. **12 Révisions d'articles** pour des journaux internationaux : *Cryogenics, Chemical Engineering process, Applied Thermal Engineering, International Journal of Thermal Sciences, Nuclear Engineering and Design, Fractal and fractional, Fluids*

A.5 Encadrement doctoral et scientifique

Pour chacune des thèses encadrées, je précise la date de démarrage (⌛), l'équipe d'encadrement ainsi que mon implication dans celle-ci (👥) et les publications associées (📝).

A.5.1 Thèses de doctorat [6]

A.5.1.1 En cours [3]

K. Bachir *Modélisation d'un échangeur de chaleur à lit fluidisé pour intégration dans une centrale solaire*
⌛ : Novembre 2024, Financement : UE - P2P & PEPR SHIP4D
👥 : **S. Mer**, A. Toutant, R. Ansart – taux d'encadrement : 33%

A. Labat *Modélisation et simulation numérique des transferts thermiques pariétaux en écoulements gaz-particules dans les récepteurs solaires.*
⌛ : Octobre 2024, Financement : ED305 UPVD
👥 : **S. Mer**, A. Toutant, F. Bataille – taux d'encadrement : 33%

I. Aguilera *Ecoulements diphasiques turbulents dans un récepteur solaire à génération directe de vapeur*
⌛ : Juin 2023, Financement : UE - MSCA- DN : TOPCSP
👥 : **S. Mer**, A. Toutant, F. Lecat – taux d'encadrement : 33%
📝 : 1 articles, 3 conf. int., 3 posters

A.5.1.2 Soutenues [3]

E. Butaye *Modélisation et simulations résolues d'écoulement fluide-particules : du régime de Stokes aux lits fluidisés anisothermes*
⌛ : Soutenue le 09/12/2024, Financement : ED305 UPVD
👥 : **S. Mer**, F. Bataille, A. Toutant – taux d'encadrement : 33%
📝 : 3 articles , 3 conf. int., 2 posters

S. Hamidi *Simulations numériques directes d'un écoulement dense fluide-particules*
⌛ : Soutenue le 07/02/2024, Financ. : ED305 UPVD – 1 an de césure
👥 : **S. Mer**, F. Bataille, A. Toutant – taux d'encadrement : 33%
✍ : 1 article

R. Gueguen *Écoulement et transfert de chaleur dans les récepteurs solaires tubulaires à lits fluidisés*
⌛ : Soutenue le 20/07/2023, Co-financ. : Labex SOLSTICE & Sandia Lab.
👥 : **S. Mer**, F. Bataille, G. Flamant – taux d'encadrement : 50%
✍ : 6 articles, 4 conf. int., 3 posters

A.5.1.3 Encadrement de stage doctoral : 1

Dans le cadre du projet TOPCSP, j'ai accueilli en 2024 un doctorant de l'UC3M pour un stage doctoral de 3 mois.

V. Safari *Thermomechanical study of central solar receivers working with high temperature heat transfer fluids (HTS) using state-of-the-art numerical models and experiments.*
⌛ : Mai – Juillet 2024, Financement : UE - MSCA-DN : TOPCSP
🏛 : Universidad Carlos Tercero – Madrid - Spain

A.5.2 Post-doctorat [2]

J. Djeumegni *Simulations des transferts radiatifs dans les lits fluidisés pour le solaire concentré*
⌛ : Janvier 2025, Financement : Labex Solstice
👥 : **S. Mer**, A. Toutant

T. Devos *Simulations numériques fines des transferts thermiques dans les lits fluidisés avec particules de formes complexes - Application aux centrales solaires à concentration*
⌛ : Mars 2025, Financement : Fonds propres
👥 : **S. Mer**, A. Toutant, S. Abide

A.5.3 Encadrement de stages [15]

A.5.3.1 Stages longs [$> 5\,mois$] : 9

2025 **A. Saha** – M2 DENSYS BarcelonaTech – 5 mois – *Etude paramétrique d'un récepteur solaire horizontal pour la production directe de vapeur* – Co-encadrement : 33%
2025 **A. Kundu** – M2 Univ. Grenoble Alpes – 5 mois – *Simulations d'écoulements anisothermes fluide-particules* – Co-encadrement : 33%
2024 **D. Kafeh** – M2 Energie Solaire UPVD – 5 mois – *Simulation thermique et optimisation thermodynamique d'un procédé de stockage thermique par changement de phase : Intégration dans un moteur Ericsson* – Co-encadrement : 50%
2024 **G. Ologaray** – M2 DET Univ. Paul Sabatier – 5 mois – *Simulations d'écoulements anisothermes fluide-particules* – Co-encadrement : 33%

2022 **L. Jaunasse** – M2 ISAE ENSMA – 6 mois – *Écoulement bouillant eau-vapeur : expérimentation et modélisation multi-échelles dans un formalisme à deux fluides* – Co-encadrement : 50%

2021 **E. Butaye** – M2 ISAE ENSMA – 6 mois – *Simulations gaz-liquide multi-échelles des écoulements dans les centrales solaires à concentration reposant sur la génération directe de vapeur* – Co-encadrement : 50% – ✎ : 1 article

2021 **M. Ploquin** – M1 INSA-Lyon – 5 mois – *Stockage thermique eau/vapeur de la centrale solaire eLLo : modélisation des fluctuations de niveau liquide durant le déstockage.* – Co-encadrement : 50% – Financement : SUNCNIM – ✎ : 1 article

2020 **H. Vernier** – M2 ISAE ENSMA – 5 mois – *Simulations gaz-liquide multi-échelles des écoulements dans les centrales solaires à concentration reposant sur la génération directe de vapeur* – Co-encadrement : 50%

2020 **G. Sahuquet** – M2 UPVD – 6 mois – *Étude des écoulements solide-gaz fluidisés dans des tubes de grand rapport de forme* – Co-encadrement : 50%

A.5.3.2 Stages courts [$< 3\,mois$] : 6

2024 **F. Hertrich** – M1 énergie solaire – 2 mois – *Simulations d'écoulements anisothermes fluide - particules pour les récepteurs solaires* – Encadrement : 33%

2023 **R. Quintana** – L3 Sup'EnR – 2.5 mois – *Simulations d'écoulements anisothermes fluide - particules* – Encadrement : 33% – ✎ : 1 article

2023 **E. Flahaut** – L3 SPI UPVD – 2.5 mois – *Écoulement bouillant eau-vapeur en conduite horizontale : Conception Assistée par Ordinateur (CAO) d'un banc expérimental et modélisation 1D des régimes d'écoulement* – Encadrement : 50%

2018 **C. Barutel** – L3 ENS Rennes – 2 mois – *Mesure de la fraction volumique équivalente dans une bouteille durant sa vidange par mesure de pression couplée à une technique d'ombroscopie.* – Co-encadrement : 50%

2018 **T. Briand** – M1 ENSEEIHT – 2 mois – *Calibration d'une sonde résistive de mesure de taux de vide moyennée par section.* – Co-encadrement : 50%

2017 **D. Velasco** – M1 int. ENSEEIHT – 3 mois – *Etude expérimental de l'influence des paramètres de contrôle de la vidange d'une bouteille.* – Co-encadrement : 50%

A.6 Financement de la recherche et responsabilités scientifiques

Pour financer mes travaux de recherche, j'ai participé à 13 projets de recherche institutionnels et 3 collaborations industrielles. Ceux-ci sont détaillés ci-après.

A.6.1 Projets européens : 2

2023–2027 **Membre** du projet **UE - Horizon CL5** – *Powder2Power P2P : MW-scale fluidized particle-driven CSP prototype demonstration* - Encadrant de la thèse de K. Bachir : « Modélisation et optimisation d'un échangeur thermique pour lit fluidisé » – 2,29 M€ Project website

2022–2026 **Responsable scientifique** à PROMES du projet **UE - HORIZON - MSCA Doctoral Network** intitulé *Towards Competitive, Reliable, Safe and Sustainable Concentrated Solar Power (CSP) Plants doctoral network* – **TOPCSP**
Coordination : C. Sobrino - Université Carlos III de Madrid
Consortium : **6 Universités** (Madrid, Brescia, Sevilla, Politecnico di Milano, Aachem, Perpignan) – **5 Organismes de recherche** (CNRS, CIEMAT, DLR, ENEA, The Cyprus Institute) – **7 Industriels** du solaire concentré (Virtual Mech, John Cockerill, Brembana, Acerinox, Europa Media, Synhelion, Solarlite)
Budget total : 2,6 M€ Budget PROMES : 282 k€ Project website

A.6.2 Projets nationaux : 5

2025–2029 **Coordinateur scientifique** du projet **ANR JCJC** – *SteamSun : Génération Directe de Vapeur dans les technologies solaires à concentration* – 400 k€

2023–2027 **Responsable du Work Package 4** (*Modèle numérique - écoulements, transferts couplés et contraintes thermomécaniques*) du projet **ANR PRME** – *SiC-Sun : Récepteur solaire en carbure de silicium pour procédés gaz-particules à haute température* – 600 k€

2024–2025 **Responsable de la tache :** *Modelling of a phase change thermal storage* du projet **Eurocluster GEMSTONE** – *POWERJOOL* – **Collab. :** ExtraJool, Alma Consulting, I2M Bordeaux, PLACAMAT Bordeaux – 8 k€ pour PROMES

2023–2024 **Responsable de la tache :** *Modélisation du stockage thermique* du projet **PEPS Cellule Energie 2023** – *TESS :Exploitation des chaleurs sensible et latente de LiOH dans un système de stockage thermique ultra-compact : conception & réalisation* – **Collab. :** I2M Bordeaux, PLACAMAT Bordeaux – 25 k€ dont 5 k€ pour PROMES

2023 **Responsable** du projet *Simulation Euler-Euler de récepteurs solaires à Génération Directe de Vapeur* à l'**IDRIS** : 1.8 Mh CPU sur la machine Jean-Zay et au **CINES** : 1 Mh CPU sur la machine Adastra Genoa– 17 k€

A.6.3 Projets régionaux : 1

2019 **Responsable** du projet **CALMIP** – *Ecoulements gaz-liquide multi-échelles dans les centrales solaires à concentration* : 1.3 Mh CPU sur la machine Olympe du supercalculateur régional CALMIP à Toulouse – 13 k€

A.6.4 Projets locaux (université/laboratoire) : 6

2024 **Allocation doctorale de l'ED 305** - *Modélisation et simulation numérique des transferts thermiques pariétaux en écoulements gaz-particules dans les récepteurs solaires* – 36 mois – Alexandre Labat

2023 **Co-Responsable** du projet **Action Incitative Recherche Enseignement** de PROMES - Collab. ExtraJool, I2M Bordeaux : Financement d'un stage M2 pour la mise en place d'une batterie thermique dans un moter Ericsson – 6 k€

2021 **Allocation doctorale de l'ED 305** - *Modélisation et simulations résolues d'écoulement fluide-particules : du régime de Stokes aux lits fluidisés anisothermes* – 36 mois – Edouard Butaye

2021 **Responsable** du projet **Action Incitative Recherche Enseignement** de PROMES – *CSP Gen-V* : mise en place d'un banc expérimental pour l'étude de la génération directe de vapeur – 5 k€

2020 **Responsable** de l'allocation **Jeune Chercheur** du laboratoire PROMES – *Simulations d'écoulements diphasiques dans les centrales solaires à concentration par approche Euler-Euler* – 15k€

2020 **Responsable** du projet **Bonus Qualité Recherche** de l'UPVD – *Écoulements gaz-liquide multi-échelles dans les centrales solaires à concentration* – 15 k€

A.6.5 Collaborations industrielles : 3

2024 – prés. ExtraJool – Conception d'un stockage thermique, à base de matériaux à changement de phase (LiOh), intégré à un moteur Ericsson afin de stocker l'énergie excédentaire du réseau électrique :
- Collaboration : Univ. Bordeaux et Univ. Pau
- Participation à l'encadrement du stage de D. Kafeh

2021 – prés. eLLO – Étude des écoulement bouillant dans les centrales solaires GDV et des problématiques de stockage associées :
- Participation à l'encadrement de la thèse de I. Aguilera (2023-2026)
- Financement du stage de M. Ploquin en 2021

2016 – prés. EdF - Chatou – Participation au dévellopement du code Euler-Euler NEPTUNE_CFD :
- Interactions régulières avec l'équipe de développement du code
- Mise en place d'une convention entre EdF, l'IMFT et le laboratoire PROMES pour intégrer le laboratoire au consortium de développement

A.7 Listes des publications

Dans les listes ci-dessous, mon nom apparaît en gras et je souligne le nom des étudiants que j'ai encadré. Des liens directs vers les documents en ligne, matérialisés par les logos des plateformes d'hébergements, sont mis à disposition dès que possible. Pour les conférences, le nom de l'orateur ayant présenté le travail est indiqué par (*) dans la liste des auteurs.

A.7.1 Articles dans des revues à comité de lecture [18]

18. J. Magnaudet, H. Bruhier, **S. Mer**, T. Bonometti - Rational constitutive law for the viscous stress tensor in incompressible two-phase flows : Derivation and tests against a benchmark experiment - Physical Review Fluids - **accepted** **ArXiv preprint**

17. I. Aguilera, A. Toutant, **S. Mer** – Numerical investigation of tilt angle effect on a Direct Steam Generation solar receiver – J. Sol. Ener., 287 – 2025 HAL

16. E. Butaye, R. Quintana, **S. Mer**, F. Bataille, A. Toutant – Investigation of heat transfers with particle-resolved simulations : from Stokes flow to fluidized bed – Int. J. Heat Mass Trans., 241 – 2025 HAL
15. R. Gueguen, G. Sahuquet, M. Tessonneaud, J.L. Sans, E. Guillot, A. Le Gal, R. Garcia, **S. Mer**, A. Toutant, F. Bataille, G. Flamant – Heat transfer in a fluidized bed tubular solar receiver. On-sun experimental investigation – J. Sol. Ener., 265 – 2023 HAL
14. E. Butaye, A. Toutant, **S. Mer**, F. Bataille – Development of Particle Resolved - Subgrid Corrected Simulations : Hydrodynamic force calculation and flow sub-resolution corrections – Comput. & Fluids., 267 – 2023 HAL
13. R. Gueguen, **S. Mer**, A. Toutant, F. Bataille, G. Flamant – Effect of temperature on the hydrodynamics of a fluidized bed circulating in a long tube for application to solar energy harveting – Chem. Eng. Sci, 281 – 2023 HAL
12. R. Gueguen, G. Sahuquet, **S. Mer**, A. Toutant, F. Bataille, G. Flamant – Experimental Study of an upflow Fluidized Bed : Identification of Fluidization Regimes – MATEC Web Conf., 379 – 2023 OPEN ACCESS
11. S. Hamidi, A. Toutant, **S. Mer**, F. Bataille – Assessment of a coupled VOF - Front-Tracking/DEM method for simulating fluid-particles flows – Int. J. Multiph. Flow, 165 – 2023 HAL
10. E. Butaye, A. Toutant, **S. Mer** – Euler-Euler multi-scale simulations of internal boiling flow with conjugated heat transfer – Appl. Mech., 4, 191-209 – 2023 OPEN ACCESS
9. R. Gueguen, G. Sahuquet, **S. Mer**, A. Toutant, F. Bataille, G. Flamant – Fluidization regimes of dense suspensions of Geldart group A fluidized particles in a high aspect ratio column – Chem. Eng. Sci 267, 118360 – 2023 OPEN ACCESS
8. M. Ploquin, **S. Mer**, A. Toutant, F. Roget – CFD investigation of level fluctuations in steam accumulators as thermal storage : A direct steam generation application – J. Sol. Ener. 245, 11-18 – 2022 HAL
7. R. Gueguen, G. Sahuquet, **S. Mer**, A. Toutant, F. Bataille, G. Flamant – Gas-Solid Flow in a Fluidized-Particle Tubular Solar Receiver : Off-Sun Experimental Flow Regimes Characterization – Energies 14, 7392 – 2021 OPEN ACCESS
6. R. Gueguen, B. Grange, F. Bataille, **S. Mer**, G. Flamant – Shaping High Efficiency, High Temperature Cavity Tubular Solar Central Receivers – Energies 13, 4803 – 2020 OPEN ACCESS
5. **S. Mer**, O. Praud, J. Magnaudet, V. Roig – Emptying of a bottle : How a robust pressure-driven oscillator coexists with complex two-phase flow dynamics – Int. J. Multiph. Flow 118, 23-36 – 2019 HAL
4. **S. Mer**, O. Praud, H. Neau, N. Merigoux, J. Magnaudet, V. Roig – The emptying of a bottle as a test case for assessing interfacial momentum exchange models for Euler-Euler simulations of multi-scale gas-liquid flows – Int. J. Multiph. Flow 106, 109-124 – 2018 HAL
3. **S. Mer**, J.P. Thibault, C. Corre – Influence of non-condensable gases on thermodynamic control on-ground experiments using a substitute fluid – J. Thermal Sci. Eng. Appl. 10, 021006 – 2017 HAL
2. **S. Mer**, D. Fernandez, J.P. Thibault, C. Corre – Optimal design of a thermodynamic vent system for cryogenic propellant storage – Cryogenics 80, 127–137 – 2016 HAL
1. **S. Mer**, J.P. Thibault, C. Corre – Active insulation technique applied to the experimental analysis of a thermodynamic control system for cryogenic propellant storage – J. Thermal Sci. Eng. Appl. 8, 021024 – 2016 HAL

A.7.2 Congrès internationaux [26]

A.7.2.1 Présentation orale

20. I. Aguilera*, C. Colin, S. Cazin, A. Toutant, **S. Mer**. Study of Horizontal Water Boiling Flow Patterns via Shadowgraphy for Enhancing Direct Steam Generation Solar Receivers. 31th SolarPaces, September 2025 - Almeria, Sp.
19. I. Aguilera*, A. Toutant, **S. Mer**. Numerical investigation of two-phase flow in DSG solar receivers : an Euler-Euler modelling approach. 30th SolarPaces, October 2024 - Rome, It.
18. I. Aguilera*, A. Toutant, **S. Mer**. Numerical analysis of two phase flow in DSG solar receivers uing an Euler-Euler modelling technique. EU-Solaris 18th Sollab Doctoral Colloquium, July 2024 - Odeillo, Fr.
17. E. Butaye*, R. Quintana, A. Toutant, **S. Mer**, F. Bataille. Particle – Resolved Simulation of anisothermal fluidized beds. 9th International Conference on Momentum, Heat and Mass Transfer (ICMHMT), April 2024 - London, UK.
16. R. Gueguen, **S. Mer**, A. Toutant, F. Bataille, G. Flamant*. Managing Heat Transfer Intensity in a Fluidized Particle-in-Tube Solar Receiver. 29th SolarPaces, October 2023 - Sydney, Australia.
15. G. Sahuquet, R. Gueguen, L Fontalvo, **S. Mer**, A. Toutant, F. Bataille, G. Flamant*. Particle flow heterogeneity in fluidized-particles multitube solar receiver. 28th SolarPaces, September 2022 - Albuquerque, USA.
14. R. Gueguen*, G. Sahuquet, **S. Mer**, A. Toutant, F. Bataille, G. Flamant. Influence of temperature on gas-solid flow in fluidized-particle tubular solar receiver. 28th SolarPaces, September 2022 - Albuquerque, USA.
13. E. Butaye*, **S. Mer**, A. Toutant, F. Bataille. Direct numerical simimulation of fluid-solid particles flows using front-tracking approach. IUTAM Symposium : From Stokesian suspension dynamics to particulate flows in turbulence, September 2022 - Toulouse, France.
12. E. Butaye*, M. Ploquin, **S. Mer**, A. Toutant, F. Bataille. Euler-Euler multi-scale simulations of internal turbulent boiling flow with conjugated transfer. Dispersed two-phase flow - SHF, October 2021 - Online Event.
11. G. Sahuquet*, R. Gueguen, A. Toutant, **S. Mer**, F. Bataille, G. Flamant. Control of particle mass flowrate in a fluidized bed solar receiver. SFERA III 2nd Doctoral Colloqium, Octorber 2021 - Almeria, Spain.
10. R. Gueguen*, G. Sahuquet, A. Toutant, **S. Mer**, F. Bataille, G. Flamant. Identification and characterization of the fluidization regimes in a fluidized bed solar receiver. SFERA III 2nd Doctoral Colloqium, Octorber 2021 - Almeria, Spain.
9. **S. Mer***, O. Praud, J. Magnaudet, V. Roig, Experimental characterization of the gas phase during bottle emptying, 10th International Conference on Multiphase Flow ICMF2019, May 2019 - Rio de Janeiro, Brazil.
8. **S. Mer***, O. Praud, J. Magnaudet, V. Roig, Simulating the emptying of a water bottle with a multi-scale two-fluid approach, Proceedings of ASME 2018 5th Joint US-European Fluids Engineering Division Summer Meeting, July 2018 - Montréal, CANADA.
7. **S. Mer***, O. Praud, N. Mérigoux, J. Magnaudet, V. Roig, Assessment of multi-scale two-fluid approach by simulating the emptying of a bottle, Dispersed Two-Phase Flow 2018 - SHF, September 2018 - Toulouse, France.
6. **S. Mer***, O. Praud, N. Mérigoux, J. Magnaudet, V. Roig, Simulating the emptying of a water bottle with a multi-scale two-fluid approach, 2nd International Workshop of Non-Invasive Experimental Tools and Numerical Methods for the Investigation of Non-Reactive and Reactive Gas-Liquid Flows - TU Hambourg, June 2018 - Hambourg, Germany.
5. **S. Mer***, O. Praud, N. Mérigoux, H. Neau, J. Magnaudet, V. Roig, Multi-scale gas/liquid simulations of the glug-glug emptying process of a water bottle, 1st NEPTUNE_CFD User Meeting - EdF R&D, April 2018 - Saclay, France.

4. **S. Mer***, J.P. Thibault, C.Corre, Thermodynamic control system for cryogenic propellant storage : experimental and analytical performance assessment, APS - Division of Fluid Dynamics conference, November 2016 - Portland, USA.
3. **S. Mer***, J.P. Thibault, C.Corre, Optimal design of a thermodynamic control system for cryogenic propellant storage, 1st International IIR Conference, June 2016 - Bucarest, Roumania.
2. **S. Mer***, J.P. Thibault, C. Corre, Experimental analysis of a thermodynamic control system for cryogenic propellant storage, 26th Space and Cryogenics Workshop, June 2015 - Phoenix, USA.
1. J.P. Thibault*, C. Corre, L. Demeure, **S. Mer**, Thermodynamic control systems for cryogenic propellant storage during long mission, Proceedings of ASME 2014 4th Joint US-European Fluids Engineering Division Summer Meeting, August 2014 - Chicago, USA.

A.7.2.2 Poster

6. I. Aguilera, A. Toutant, **S. Mer**. Thermo-hydraulic and thermo-mechanical evaluation of a Direct Steam Generation solar receiver using conjugate simulations. 31th SolarPaces, September 2025 - Almeria, Sp.
5. I. Aguilera, C. Colin, S. Cazin, A. Toutant, **S. Mer**. Experimental investigation of water boiling flow patterns in horizontal and slightly tilted large diameter tube. 12th International Conference on Multiphase Flow, May 2025 - Toulouse, Fr.
4. I. Aguilera, H. Duval, J.J. Huc, E. Hernandez, A. Toutant, **S. Mer**. Experimental investigation of Direct Steam Generation for horizontal or slightly tilted solar receivers. 30th SolarPaces, October 2024 - Rome, It.
3. I. Aguilera, A. Toutant, **S. Mer**. Turbulent two phase flow in direct steam generation solar receiver. 3rd NEPTUNE_CFD User Meeting - EdF R&D, October 2023 - Saclay, France.
2. M. Ploquin, E. Butaye, F. Roget, **S. Mer**, A. Toutant. Thermal water-steam storage for CSP : modelling and identification of liquid level fluctuations during unloading phases. 26th SolarPaces, September 27 - October 1 2020 - Online Event.
1. G. Sahuquet, R. Gueguen, **S. Mer**, A. Toutant, F. Bataille, G. Flamant. Particle Flow Stability in Tubular Fluidized Bed Solar Receivers. 26th SolarPACES, September 28 - October 2 2020 - Online Event.

A.7.3 Congrès nationaux [7]

A.7.3.1 Présentation orale

4. I. Aguilera*, C. Colin, S. Cazin, A. Toutant, **S. Mer**. Study of horizontal water boiling flow patterns based on a shadowgraphy technique : optimizing Direct Steam Generation Solar Receiver. 26ème Congrès Français de Mécanique, Août 2025 - Metz, France.
3. I. Aguilera*, H. Neau, A. Toutant, **S. Mer**. Thermomechanical analysis of a Direct Steam Generation receiver based on conjugate fluid-solid simulations. 26ème Congrès Français de Mécanique, Août 2025 - Metz, France.
2. R. Gueguen*, G. Sahuquet, **S. Mer**, A. Toutant, F. Bataille, G. Flamant. Etude expérimentale et isotherme d'un "lit fluidisé à circulation ascendante" : identification des régimes de fluidisation. Congrès de la Société Française de Génie des Procédés, Novembre 2022 - Toulouse, France OPEN ACCESS
1. **S. Mer***, J.P. Thibault, C. Corre, Etude expérimentale d'un système de contrôle TVS pour les réservoirs d'ergols cryogéniques, 22ème Congrès Français de Mécanique, Août 2015 - Lyon, France.

A.7.3.2 Poster

3. D. Kafeh, **S. Mer**, N. Mazet, R. Olives, P. Neveu, M. Perier-Muzet. Modélisation et optimisation thermodynamique du couplage entre un stockage thermique MCP et un moteur ERICSSON pour favoriser l'intégration des EnR sur le réseau électrique. Journées Nationales de l'Energie Solaire, Juin 2024 - Anglet, France
2. G. Ologaray, E. Butaye, A. Toutant, **S. Mer**, F. Bataille. Anisothermal gas–particle flow simulations for concentrated solar applications. 32ème Congrès Français de Thermique, Juin 2024 - Strasbourg, France
1. R. Gueguen, G. Sahuquet, E. Delorme, **S. Mer**, A. Toutant, F. Bataille, G. Flamant. Régimes d'ecoulement dans les récepteurs solaires tubulaires à lits fluidisés. Journées Nationales de l'Energie Solaire, Aout 2021 - Odeillo, France

A.7.4 Séminaires invités [11]

11. *Two-phase heat transfer fluids in Concentrated Solar Technologies (CST)* - TOPCSP European project Training Course - Cyprus - Juillet 2025.
10. *Fluides de transfert thermique diphasiques dans les technologies solaires à concentration (CST)* - Laboratoire de Modélisation Pluridisciplinaire et Simulations (LAMPS) - Perpignan - Juin 2025.
9. *Modélisation et simulations hautes performances d'écoulements diphasiques dans les technologies solaires à concentration (CST)* - Atelier *"Simulation et modélisation thermique pour les EnR"* du 33ème Congrès français de thermique - Chambéry - Juin 2025.
8. *Modélisation de type Simulation des Grandes Echelles d'écoulements anisothermes fluide – particules* - 5ème séminaire TrioCFD - Saclay - Oct. 2023 (*présenté par E. Butaye*).
7. *Simulations of anisothermal fluidized beds resolved to a scale smaller than the particle diameter* - Séminaire ANR MUSCAT - IFPEN, Lyon - Mars 2024 (*présenté par A. Toutant*).
6. *Euler-Euler multi-scale simulations of internal turbulent boiling flow with conjugated heat transfer* - Rencontres IUSTI - PROMES, Perpignan - Décembre 2021.
5. *Simulation numérique de la vidange d'une bouteille d'eau par approche multi-échelle* - Laboratoire de Mécanique des Fluides et d'Acoustique (LMFA), Lyon - Juin 2018.
4. *Simulation numérique de la vidange d'une bouteille d'eau par approche multi-échelle* - Laboratoire des Ecoulements Géophysique et Industriel (LEGI), Grenoble - Mars 2018.
3. *Évaluation des modèles de transfert de quantité de mouvement pour les écoulements liquide/gaz multi-échelles* - Rencontre EdF - FERMaT, Toulouse - Novembre 2017.
2. *Contrôle thermodynamique d'ergol cryogénique : étude expérimentale et optimisation numérique de performances* - Laboratoire de Mécanique des Fluides et d'Acoustique (LMFA), Lyon - Mai 2016.
1. *Analysis of a Thermodynamic Vent System for long-duration space missions* - Department of Aerospace Science & Technology, Politecnico de Milan, Italie - Janvier 2016 (*présenté par C. Corre*).

A.7.5 Séminaires internes [8]

8. Journée des thématiques du laboratoire PROMES, Odeillo, Janvier 2024
7. Séminaire à la montagne de l'équipe F&P de l'IMFT, Ercé, Mars 2018
6. Séminaire d'équipes ASI/F&P de l'IMFT, Toulouse, Juin 2018
5. Séminaire des doctorants du LEGI, Grenoble, Mars 2016
4. Séminaire CoopExpé du LEGI (Coopération Expérimentateurs), Grenoble, Novembre 2015
3. Séminaire interne de l'équipe EDT du LEGI, Grenoble, Novembre 2015
2. Séminaire aux Journées CNES Jeunes Chercheurs, Cité de l'espace de Toulouse, Octobre 2015
1. Séminaire aux Journées Jeunes Chercheurs DLA-CNES, Paris, Juin 2014